From single cell mechanics and intercellular forces to collective aggregate dynamics

Individual cell-based modeling of cell cultures for tissue engineering

Bart SMEETS

Supervisory Committee:
Prof. Dr. ir. Maurice De Proft, chair
Prof. Dr. ir. Herman Ramon, supervisor
Prof. Dr. ir. Hans Van Oosterwyck, co-supervisor
Dr. ir. Paul Van Liedekerke, co-supervisor
(INRIA, France)
Prof. Dr. ir. Wouter Saeys
Dr. Engelbert Tijskens
Prof. Dr. ir. Liesbet Geris
(Université de Liège and KU Leuven)
Dr. ir. Romaric Vincent
(CEA, LETI, MINATEC, France)

Dissertation presented in partial fulfillment of the requirements for the degree of Doctor in Bioscience Engineering

April 2016

Doctoraatsproefschrift nr. 1350 aan de faculteit Bio-ingenieurswetenschappen van de KU Leuven

Uitgegeven in eigen beheer, Bart Smeets
Kasteelpark Arenberg 30 bus 2456, B-3001 Leuven (Belgium)

Dankwoord

Een doctoraat vertegenwoordigt meer dan een boekje, of een paar publicaties met wat nieuwe ideeën. In de eerste plaats vormt het een persoonlijk rijpingsproces dat met name wordt bepaald door de mensen die je omringen, in professionele maar ook in de persoonlijke context. Vandaar is het ook gepast om vooraan in dit doctoraatsproefschrift kort de tijd te nemen om hiervoor mijn dank uit te drukken.

In de eerste plaats wil ik mijn promotor, Prof. Herman Ramon, bedanken. De haast onvoorwaardelijke steun die ik genoot doorheen heel mijn doctoraat, en de ongelimiteerde wetenschappelijke vrijheid waar ik over beschikte, waren voor mij heel belangrijk. Voor een grote (en grootse) visie bent u er altijd geweest, maar voor de precieze invulling en de technische uitwerking kreeg ik alle vrijheid van de wereld. Het grote voordeel daarvan is niet alleen dat ik zonder remmingen van alles kon proberen — en daar draait het in de wetenschap nog steeds vaak om — maar ook dat de weg die men zelf vindt met veel meer overtuiging en toewijding bewandeld zal worden. Dat die weg na wat omzwervingen uiteindelijk terugkeert naar de door u voorspelde windrichting getuigt van de doeltreffendheid van de "onzichtbare hand". Bewonderenswaardig is dat u ook in zeer woelige tijden erin slaagde met vastberadenheid en volle inzet in deze richting te blijven duwen. Mijn co-promotor, Prof. Hans Van Oosterwyck, wil ik bedanken voor de inspiratie, het enthousiasme, de grote wetenschappelijke betrokkenheid, en de strategische raad op de meest cruciale momenten, zoals tijdens het aanvragen van een beurs en het herwerken van een publicatie.

Verder gaat mijn dank uit naar Dr. Engelbert Tijskens, voor de eerste fundamenten te leggen in de ontwikkeling van de software waar wij al jaren met plezier aan verder werken, en Dr. Paul Van Liedekerke, voor me mee te helpen introduceren in het reilen en zeilen van de fysische wetenschappen en het modelleren. Ook dank ik graag de juryleden in mijn doctoraatscommissie: Prof. Liesbet Geris en Prof. Wouter Saeys, die beiden voor mij een voorbeeldfunctie vervullen, en de voorzitter van mijn examencommissie, Prof. Maurice De Proft, voor deze taak op zich te nemen.

Het Agentschap voor Innovatie door Wetenschap en Technologie (IWT) wil ik bedanken

voor de financiële steun die werd geboden aan dit onderzoek. Ik apprecieer het vertrouwen dat hiermee in mij werd gesteld, en ik hoop dat ik met dit werk mijn steentje heb bijgedragen aan de wetenschap in Vlaanderen.

My research stay in Barcelona, while only lasting for three months, made an important mark on my doctoral project, and constituted a greatly enriching life experience. Therefore, I would like to thank Prof. Xavier Trepat and his team, for welcoming me in the lab, and Ignacio and Ricard, for enthusiastically helping me with the ambitious task that I embarked upon. My special gratitude goes to Dr. Romaric Vincent, who is also willing to be a jury member in my supervisory committee, for making me ask the right questions when thinking about cells, for providing me with powerful new ideas, distilled from reading an uncountable numbers of papers, and mostly for your immense personal generosity in all aspects of your life.

Also my colleagues closer to home earn my profound gratitude. I'm grateful that I could be part of Prometheus. Its diverse composition has broadened my thinking and it has always offered a platform for exchanging ideas, be it at the weekly data sessions, or the yearly retreat or symposium. Moreover, it offers a beautiful example of how to reconcile fundamental research with straightforward practical goals that try to address real-world problems. In particular I would like to thank Yann. Working with you has been a truly enjoyable experience, and I appreciated the laid-back yet very efficient "working" style during my short visits in Liège. I'm also indebted to the MAtrix team: I learned a great deal from our in-depth discussions, where no stone from a cell's cytoskeleton would be left unturned.

Dan zijn er natuurlijk mijn collega's van MeBioS en "den dertig": bedankt voor de Alma-uitjes, de barbecues, de onvergetelijke kerstfeestjes, het bierproeven, de loop- en gymsessies, en voor het voorzien van een gemoedelijke werksfeer die moeilijk kan worden geëvenaard! Ook het secretariaat mag niet worden vergeten: Uiteindelijk zorgen zij ervoor dat zelfs in een kluwen van administratieve regeltjes, er toch niet steeds tijd kan worden besteed aan echt onderzoek. Mijn bureaugenootjes en ex-bureaugenootjes, Elien, Maxim, Jorina, Jirka, Simon, Ramesh, Kristina, wil ik bedanken voor de immer coöperatieve werkomgeving, voor de gedeelde onderzoekspassie, voor discussies zonder heilige huisjes en voor de hilarische sfeer (bonuspunten gaan naar Simon voor dat laatste).

Een speciale vermelding is op zijn plaats voor Tim Odenthal. Tim, Dein Beitrag zu dieser Arbeit als Freund und Kollege ist enorm wertvoll. Schon in 2009 als ich bei Dir meine Masterarbeit angefangen habe, hast Du mir geholfen zu Programmieren und Schreiben und wir suchten zusammen nach kreative Lösungen - manchmal auch zu Problemen die eigentlich gar keine waren. Durch unsere enge Zusammenarbeit konnten wir uns auf für uns unbekanntes wissenschaftliches Terrain wagen und neue Ideen und Konzepte entwickeln. Ich bin stolz auf uns!

Ik wil mijn vrienden bedanken om het net niet de hele tijd te hebben over doctoraten, of over de wetenschap, zodat ik even aan deze beslommeringen kon ontsnappen, en me niet zou verliezen aan gevaarlijk tunneldenken. Rodrigo — je wordt vermeld in deze categorie — bedankt voor de uiterst uiteenlopende gesprekken, voor de confronterende analyses en voor onze sportieve verwezenlijkingen.

Mijn grootste dank gaat tenslotte uit naar mijn familie. De onstuitbare werklust, de flexibiliteit en het optimisme van mijn ouders zijn een bron van inspiratie voor mij. Ik wil hen bedanken voor de jarenlange steun die ervoor gezorgd heeft dat ik sta waar ik nu sta. Bedankt, Dirk, om zeker tijdens mijn doctoraat, er te zijn als een “grote broer” op vele vlakken. Als allerlaatste vermeld ik Katrien. Met een soms door werk geobsedeerde doctorandus samenzijn is niet altijd even gemakkelijk, zeker als dat af en toe alle mentale energie opslorpt. Eerst en vooral ben ik dus dankbaar voor het begrip dat je had voor mijn “out”-momenten. Daarnaast wil ik je bedanken voor aan mijn zijde te staan en samen met mij het persoonlijk project uit te bouwen dat parallel met een doctoraatsproject plaatsgrijpt.

Abstract

The mechanisms that biological cells exploit to organize themselves into multicellular aggregates and tissue-like structures are based on fundamental physical principles. Yet, the natural emergence of complexity in biological systems, while of great importance for many applications in biology and medicine, is still poorly understood. For this, mathematical models can be of great help by identifying key components and mechanisms that govern a system, and based on these, predict the inception of complex pattern formation. Individual cell-based models consider cells as distinct entities that interact with each other, and describe the dynamics and structure of multicellular systems by integrating an equation of motion. By doing so, they can help elucidate the interplay between mechanical forces, active cell behavior and the properties of cell aggregates.

In this dissertation, new developments and applications of individual cell-based models are presented. The central aim is to quantify the collective dynamics of cell aggregates, based on the mechanical properties of single cells, and the specific shape of intercellular forces. One of the predominant difficulties in individual cell-based modeling lies in properly taking into account cell shape. In order to address this, a novel methodology is established here for representing arbitrary cell shapes and modeling mechanical forces on the intercellular interface in great detail.

First, a general computational theory is introduced for accurately calculating contact forces between any two arbitrary shapes. For this, an expression for the contact pressure is integrated over the surface of an intersection polygon, to come up with net normal and tangential contact forces. When the shape is rounded, i.e. the radius of curvature varies smoothly between adjacent discretization points, a mechanistic contact model is obtained that can make use of shape independent material properties and a pressure formulation from classical Hertz theory. The usage of this new methodology is demonstrated in simulations at the macro scale of granular material using the Discrete Element Method. By implementing a pressure formulation from Maugis-Dugdale theory in order to model cell adhesion, and adding an approximate model for the mechanical behavior of the cytoskeleton, a deformable cell model is obtained. By

performing simulations that use this model, the fundamental power laws governing initial cell spreading are analyzed. Finally, a coupling with computational fluid dynamics is realized by making use of the Immersed Boundary Method. Simulations of human periostium derived cells inside a bioreactor show the various mechanical effects of perfusion flow on cells cultured for Tissue Engineering purposes. In the future, individual cell-based models using these deformable cells can serve to relate detailed intercellular forces at the cell interface to multicellular organization.

In order to model the collective behavior of large cell numbers, more simple cell shapes are adopted, for which an explicit equation of motion is integrated. By adding a morphological description for cell division, a model is obtained that can be used to simulate proliferation in *in vitro* cell culture. It is shown that for cells growing on spherical microbeads, a sudden increase in mechanical stress is expected upon reaching confluence. Finally, simulations of large monolayer cultures of epithelial cells were performed in order to construct a diagram of physical phases. It is demonstrated that two cell properties are critical in governing phase behavior and the appearance of emergent complex structures: cell-cell contractile energy and the strength of contact inhibition of locomotion. The latter is shown to give rise to large-scale collective migration, as experimentally seen monolayer sheet expansion, and polarized structures with liquid-like behavior. By classifying multicellular structures in physical phases, the groundwork is provided of a structured framework for explaining the emergence of complex *in vitro* and *in vivo* tissue architectures.

Samenvatting

De mechanismen waarmee biologische cellen zichzelf organiseren in multicellulaire aggregaten en weefselstructuren zijn gebaseerd op fundamentele fysische principes. Ondanks het belang ervan voor toepassingen in de biologie en de medische wetenschappen is het natuurlijk ontstaan van complexiteit in biologische systemen nog niet voldoende begrepen. Hiervoor kunnen wiskundige modellen erg behulpzaam zijn, omdat ze de belangrijkste fysische ingrediënten kunnen identificeren die het systeemgedrag bepalen, en omdat ze op basis hiervan kunnen voorspellen hoe complexe patronen kunnen ontstaan. Individuele-celgebaseerde modellen beschouwen cellen als afzonderlijke entiteiten die met elkaar in interactie treden, en ze beschrijven de dynamica en structuur van multicellulaire systemen door middel van een bewegingsvergelijking, die expliciet wordt geïntegreerd. Hiermee kunnen ze licht laten schijnen op de wisselwerking tussen mechanische krachten, actief celgedrag en de eigenschappen van meercellige aggregaten.

In dit proefschrift worden nieuwe ontwikkelingen in, en toepassingen van individuele-celgebaseerde modellen gepresenteerd. Het hoofddoel is de karakterisatie van de collectieve dynamica in celaggregaten, als functie van de mechanische eigenschappen van individuele cellen, en de specifieke kenmerken van intercellulaire krachten. Eén van de belangrijkste moeilijkheden voor individuele-celgebaseerde modellen vormt het in rekening brengen van celvorm. Daartoe wordt hier een nieuwe methodologie voorgesteld om willekeurige celvormen voor te stellen en mechanische krachten tussen cellen op een gedetailleerde manier te modelleren.

Vooraleerst wordt een nieuwe computationele theorie geïntroduceerd, die gebruikt kan worden om contactkrachten te berekenen tussen twee willekeurige vormen. Hiervoor wordt een uitdrukking voor de mechanische druk geïntegreerd over het oppervlak van de veelhoek die de doorsnede aflijnt tussen de twee lichamen. Het resultaat hiervan is een totale normale en tangentiële contactkracht. Als de lichamen afgerond zijn, dit wil zeggen dat de curvatuurstraal geleidelijk varieert tussen twee naburige discretisatiepunten, wordt een mechanistisch contactmodel bekomen dat gebruik kan maken van vorm-onafhankelijke materiaaleigenschappen en een drukformulering

uit de klassieke Hertz-theorie. Het gebruik van deze nieuwe methodologie wordt gedemonstreerd in macro-schaal simulaties van granulair materiaal met behulp van de discrete-elementenmethode. Voor het modelleren van adhesie kan een drukformulering op basis van Maugis-Dugdale-theorie worden gebruikt. Als tenslotte een benaderende beschrijving voor het mechanisch gedrag van het cytoskelet wordt toegevoegd, wordt een model bekomen voor vervormbare biologische cellen. Simulaties op basis van dit model worden vervolgens gebruikt om de fundamentele schalingswetten van de uitspreiding van cellen op een substraat (of op andere cellen) bloot te leggen. Een koppeling met modellen voor computationele vloeistofdynamica wordt bewerkstelligd met behulp van de "Immersed Boundary Method". Simulaties van stamcellen — afkomstig uit het menselijk periost — in een bioreactor worden gebruikt om verscheidene mechanische effecten van perfusiestroom in celcultuur voor weefselengineering te onderzoeken. In de toekomst kunnen individuele-celgebaseerde modellen gebruik maken van de hiervoor genoemde beschrijving van celvorm, om de gevolgen van zeer lokale intercellulaire krachten op de organisatie van meercellige aggregaten te voorspellen.

Om het collectief gedrag van een groot aantal cellen te modelleren worden eenvoudigere celvormen aangewend, die uitgaan van een cirkel- of bolvormige symmetrie van de interactiepotentiaal. Door een morfologische beschrijving voor de celdeling toe te voegen, wordt een model bekomen dat kan gebruikt worden om de proliferatie te simuleren in *in vitro* celcultuur. Voor cellen die groeien op "microbeads" — bolvormige draagstructuren die gebruikt worden als substraat voor 3D celcultuur in weefselengineering — wordt aangetoond dat een plotse toename van mechanische stress kan worden verwacht zodra de celbedekking confluentie bereikt. Ten slotte worden simulaties van grote tweedimensionale cultuursystemen voor epitheelcellen uitgevoerd. Met deze simulaties wordt dan een fysisch fasediagram opgesteld. Er wordt aangetoond dat twee fysische celeigenschappen cruciaal zijn in het bepalen van faselandschap en in het ontstaan van emergente complexe structuren: cel-cel contractiliteit, en contactinhibitie van celbeweging. Dat laatste zorgt voor grootschalig collectief migratiegedrag, zoals experimenteel wordt waargenomen bij "monolayer sheet expansion", en gepolariseerde structuren met vloeistofachtige eigenschappen. Door multicellulaire structuren te classificeren in fysische fasen worden de fundamenten gelegd voor een raamwerk dat de emergentie van complexe *in vitro* en *in vivo* weefselstructuren kan helpen verklaren.

Contents

Chapter 1

Introduction

Understanding the fundamental driving mechanisms which allow single cells to organize themselves into tissue-like structures – and ultimately, into large and complex multi-cellular organisms – remains one of the key challenges in the natural sciences. Developmental processes demonstrate that this organization is highly robust and remarkably well conserved across various species [117]. At first sight, this high degree of order appears to contrast with the seemingly random organization that can be observed in *in vitro* cell culture of immortal cell lines, colonies of single-celled organisms, and tumors. Still, the inherent robustness and ubiquitousness of cell organization, as well as the likeness of its constituents — single cells — suggest that it must rely on similar fundamental physical principles that can as well produce these disordered states. In the same vein, complex patterns at the tissue-scale may arise as emergent phenomena from a much more restricted lower (cellular) scale.

A full physical description of individual cells, including various cell organelles, the complex cytoskeleton and the tremendous number of biological pathways will remain unattainable for many years to come. At this moment, scientists are still trying to unravel the behavior of its most basic components such as the interaction between networks of actin fibers and myosin motors in small, well defined domains. Yet, the overall dynamics of cells can in principle be deduced from the net interaction between the cells and their environment. For this, we are provided with a natural point of interest: the cell's physical boundary. Mechanically, the complex passive and active behavior of the cytoskeleton generates net forces which are transmitted on its boundary to other cells or the extracellular matrix (ECM), typically on well-defined transmission points such as focal adhesions (FAs) – see Fig. 1.1(a). In that fashion, many intracellullar processes – which might not even be fully understood – can still be parameterized in a relatively small set of fundamentally distinct cell activities. Examples of these are the

random walk behavior as a result of cell migration, the generation of adhesive tension and the net modification of the activity of its neighborhood.

Tissue engineering aspires the production of bio-artificial tissues through a combination of (stem) cells, biomaterials and biochemical stimuli such as growth factors [110]. Although its objectives are of practical nature, the innate necessity for understanding how multicellular aggregates can be controlled has spurred substantial fundamental research on intercellular dynamics and self-organization. The latter is a key aspect in the principle of developmental engineering [117, 118], in which concepts from embryonic development are applied to robustly manufacture microtissues and as much as possible limit the need of external interference. For example, in bone tissue engineering, it can be pursued to mimic the developmental process of endochondral ossification, in which a spatial and temporal gradient of cells at different stages of differentiation is induced to obtain a growth plate-like structure. Difficulties in the consistent *in vitro* production of viable threedimensional cell aggregates have exposed the need for a better understanding of how cell fate is affected by characteristics of its microenvironment. Here, mathematical modeling can play an important role by identifying the most important mechanisms of action as well as offering a very practical tool that can be used to optimize *in vitro* processes.

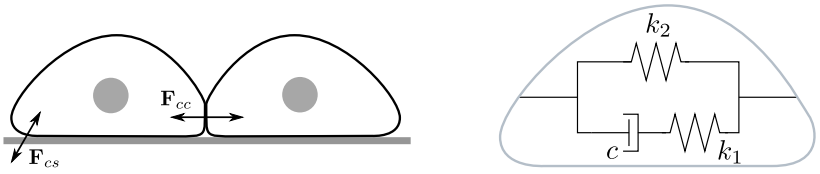

(a) (b)

Figure 1.1: (a): The force diagram of an individual cell is established from the total interaction with its environment, i.e. cell-substrate forces ($\mathbf{F}_{cs}$, for example the extracellular matrix) and cell-cell forces ($\mathbf{F}_{cc}$). Both $\mathbf{F}_{cs}$ and $\mathbf{F}_{cc}$ can be of active origin, i.e. effected by energy-consuming cytoskeletal activity. (b): Strongly simplified representation of the cell's effective mechanical behavior. The spring-like k_1 represents the cells' passive mechanical response to external forces, while the damper c accounts for the plasticity as a result of (active) cytoskeletal remodeling. The spring-like k_2 represents the cell's active tensile modulus, where contractile myosin activity increases with cell strain.

1.1 Mathematical modeling of multicellular dynamics

Model-based research of cellular behavior has known an explosive growth over the last two decades, because of an increased focus on the integration of physical principles

into biological systems. Mathematical models can be used to test hypotheses with respect to an observed phenomenon by separating processes that are significant for the phenomenon from processes that only cause side-effects[1]. Moreover, by reducing the biological complexity and by offering highly controllable settings, they lead to an improved structured insight into the underlying biological processes. Hence, *in silico* models also help generating new hypotheses on the mechanisms that determine cell fate.

A wide spectrum of modeling techniques (mathematical and computational) has been used to describe components of cellular systems. Here, we give a brief overview of the principal axes along which they can vary. More detailed information can be found in [5], [152] and [217].

1.1.1 Meso-scale models

Commonly, three scales of models are distinguished for modeling biological systems. At the smallest scale, the nano-scale, the activity of individual molecules (often proteins) accomplishes specific cellular functions. For example, the precise arrangement of amino acid residues in enzymes determines its catalytic action, and the architecture of actin networks together with the presence of myosin motors determine the local rigidity and contractility of the cytoskeleton. At the highest scale, the tissue- or macro-scale, mean field approaches become feasible, even for complex cellular system, and classical continuum descriptions can be used that capture gradients of field variables in partial differential equations. For example, the Finite Element Method (FEM) has been used to simulate the mechanical resistance of bones or tendons under load. Many physical systems can be sufficiently characterized at one of these two scales, depending on the required information. Additionally, in multi-scale techniques, mathematical formalisms are used to couple both scales, potentially yielding a powerful tool that describes "large" systems yet still captures the effects of microscopic features.

However, cellular structures manifest a natural third, intermediate scale: the meso-scale. Cells are spatially well defined entities that are delimited by a cell membrane, a clear boundary at which they sense their environment and respond to it (biochemically as well as mechanically). Hence, it makes sense to compose models that make abstraction of the molecular scale, and even of the entire complex intracellular machinery, but still do not approximate multicellular systems as continuum "fields". Such an approach has two main benefits. Firstly, it allows to quantify forces or chemical concentrations that

[1] Redundancy is common in biological systems: A multitude of equilibrium points are created that give the system the capacity to cope with (extremely) varying environmental conditions. In that sense, one can speak of side effects only related to a specific equilibrium point around which the system is operating. When this system is driven into a new equilibrium point, e.g. by changing environmental conditions, some side effect could suddenly play a more prominent role.

are experienced by individual cells, thereby enabling predictions of their effect on cell fate. Secondly, the discrete nature of the model entities (individual cells) facilitates the inclusion of stochasticity in cell behavior. The latter has been shown in some systems – and is suspected in many others – to be involved in processes that give rise to increasing complexity, e.g. in development [151], or to influence the overall physical properties of aggregates [133]. Moreover, through the explicit inclusion of stochastic effects, the model may naturally capture critical or near-critical behavior, when small microscopic fluctuations tend to determine large-scale system properties. Such behavior cannot be captured in classical "mean field" approaches.

1.1.2 Continuum versus Discrete models

For various spatial scales, continuum and discrete models can be used to describe spatial variability in cellular systems – see Fig. 1.2.

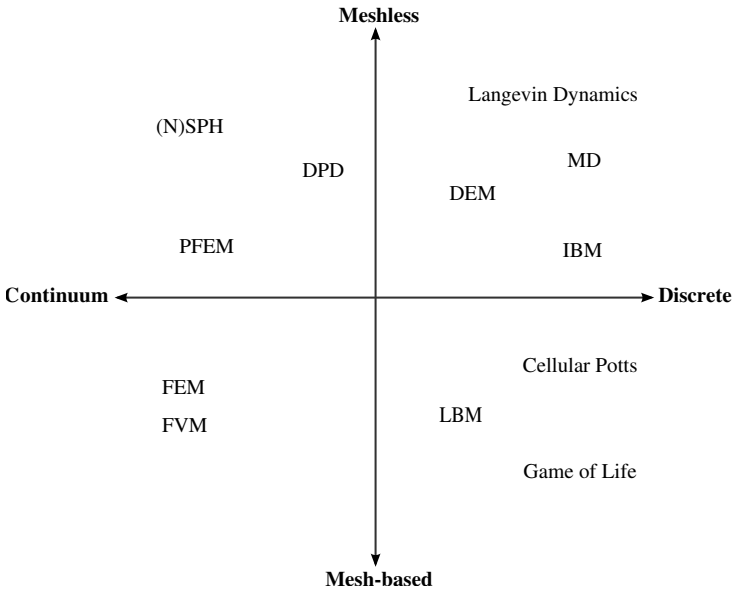

Figure 1.2: Non-exhaustive list of various computational modeling techniques, sorted according to their spatial mathematical description – continuum or discrete – and their numerical discretization in the space – meshless or mesh-based. **SPH**: Smoothed Particle Hydrodynamics, **DPD**: Dissipative Particle Dynamics, **FEM,FVM**: Finite Element and Finite Volume Method, **PFEM**: Particle Finite Element Method, **LBM**: Lattice Boltzmann Method, **DEM**: Discrete Element Method, **MD**: Molecular Dynamics and **IBM**: Individual cell-based models (not to be confused with Immersed Boundary Method, for which the same abbreviation is used in chapter 6).

Mathematically, continuum models are usually formulated as a set of partial differential equations (PDEs) and are solved by numerical schemes such as the Finite Difference/Element/Volume Method. Discontinuities must be represented by explicit boundary conditions, or are smoothened out into steep gradients. Discrete models explicitly describe the dynamics of spatially distinct entities, and are generally mathematically formulated in sets of ordinary differential equations (ODEs) or stochastic differential equations (SDEs). An example of the latter is the Langevin equation (see further, Eq. 1.4), which is commonly used to model the thermal motion of particles in a heat bath [116].

1.1.3 Meshless versus Mesh-based methods

Irrespective of their mathematical description (continuum or discrete), numerical models can vary in how their spatial variables are discretized. Here, we distinguish between meshless and mesh-based methods. Mesh-based methods make use of a spatial grid (mesh) on which variables of interest are computed using a numerical integration scheme or heuristic rules based on its (fixed) neighborhood. This grid can be either fixed in space (Eulerian description) or move along with the motion or deformation of the bodies of interest (Lagrangian description). Due to their high accuracy, their intrinsic computational efficiency and ease of parallelization, these methods are ubiquitous in almost all computational fields. Nonetheless, they can have difficulties in capturing free boundaries or ruptures and the grid itself commonly introduces numerical artifacts (which can be controlled by e.g. sophisticated meshes).

Meshless methods are often used to address these issues. They use free moving nodes or "particles" which can represent real particles but can also be merely virtual integration points for solving PDEs. In any case, local or long range interactions are defined with other particles, and the local neighborhood (or connectivity) of these particles can freely change. When the number of particles becomes very large, the efficient computation of this connectivity becomes an important bottleneck in simulations[2]. Computer programs which address these issues with more clever algorithms (e.g. grid-based contact detection, see chapter 2 and further), and provide a framework for meshless simulations are called particle simulators. It should be no surprise that these particle simulators can be used for simulating a wide range of mathematical models and can be applied to various applications at different spatial scales. In this PhD project, I employed and extended the particle-based simulation framework Mpacts (formerly called DEMeter), which is being developed within the division of Mechatronics, Biostatistics and Sensors (MeBioS) of KU Leuven. Mpacts is written

[2]For example, the naive "brute-force" approach where one checks each iteration all possible particle pairs, scales like the square of the number of particles. Simulations would already become unfeasible for more than 10^5 particles.

as a generic and extensible collection of C++ modules which are connected using an interface in Python.

Fig. 1.2 shows a number of popular computational modeling techniques according to their mathematical description (continuum or discrete) and their numerical discretization of space (mesh-based or meshless). Clearly, not all continuum descriptions are mesh-based, and not all discrete descriptions are meshless. Moreover, techniques exist that take advantage of two description methods. For example, the particle finite element method (PFEM) uses free particles as degrees of freedom, and only constructs a "virtual" mesh to help integrate the constitutive equations. Particle simulators are particularly well suited for meshless methods, but also for methods which make use of meshes but enable freely changing connectivity.

In this research we make use of discrete mathematical models that describe cellular systems at the meso-scale. While mostly meshless – see chapter 2 and 7 – they will be supplemented with meshed representations of contact surfaces – see chapter 3, 4 and 5. Moreover, a continuum model for fluid flow is added in chapter 6, through a coupling using the immersed Boundary Method.

1.1.4 Developments in individual cell-based modeling

Here, a compendiary overview of the state of the art in individual cell-based modeling techniques[3] at the start of this PhD project is given. Briefly, the field of single cell-based modeling can be classified in two major approaches: On the first hand, there are lattice-based techniques which are usually variants of cellular automata. On the other hand there exists a family of meshless/off-lattice methods.

Cellular automata make use of a fixed lattice, in which each lattice site is updated based on the properties of its neighbors. A classical example of cellular automata is "Conway's Game of Life" [64], which demonstrates how complex behavior and patterns can naturally emerge from very simple rules. These rules can be chosen in such a way that the time evolution of the lattice sites simulates the proliferative behavior of tissue and cellular structures [38]. Cellular Potts Models (CPM), or "extended large-q Potts models" were first proposed by Graner and Glazier in 1992 [67], as a generalization of the Potts model, which describes the interaction between "spins" on a crystalline lattice. The latter has been used to model for example the behavior of ferromagnets. Each lattice can take q different values for the spin, which are uniformly distributed over the circle at angles θ_n:

$$\theta_n = \frac{2\pi n}{q}, \tag{1.1}$$

[3] which are essentially all meso-scale models as discussed in section 1.1.1

for the n-th possible value of the spin. The total interaction energy of the system is then described by a Hamiltonian H:

$$H = J\sum_{i,j}\cos(\theta_i - \theta_j), \tag{1.2}$$

for all neighboring lattice sites i and j. The constant J determines the interaction strength. In CPM, the spin of a lattice sites reflects its (biological) cell index. A complete cell is defined as a continuous domain of connected lattice sites with the same spin. At every iteration, the spin values of each lattice site are recomputed based on probabilistic rules (e.g. sampled from a Boltzmann distribution). For example, the Hamiltonian of a hypothetical system with three different cell types could be expressed as:

$$H = \sum_{i,j} J\left(\tau(\sigma_i),\tau(\sigma_j)\right)\left[1-\delta_{\sigma_i,\sigma_j}\right] + \sum_{\text{type}\,\sigma}\left[a(\sigma)-A_{\tau(\sigma)}\right]^2\theta(A_{\tau(\sigma)}), \tag{1.3}$$

in which τ is an identifier for the cell type, $J(\tau,\tau')$ the surface energy between lattice spins of type τ and τ', and $\delta_{\sigma_i,\sigma_j}$ the Kronecker delta, which becomes one when $\sigma_i = \sigma_j$ and zero otherwise. The second term in Eq. 1.3 ensures that the cell surface area $a(\sigma)$ will grow and approach a reference surface area A_τ. One of the advantages of CPM is that they can be easily adapted to mimic a very wide range of biological phenomena, and often will naturally lead to the emergence of complex patterns and structures which are present in biological tissue. This, together with their computationally favorable formalism, has made CPM a very popular choice in the last two decades for cell-based modeling of biological systems. For example, the CPM has been used extensively to model the growth, invasion and evolution of tumors [203], as well as angiogenesis [33]. An extensive overview of applications and developments of CPM is given in [185]. Nonetheless, one must realize that discrete iterations in CPM simulations do not represent a time evolution but are merely Monte Carlo steps. As such, an *a priori* definition of timescale is not possible, and a clear separation of timescale with respect to a dominant phenomenon is required. Moreover, CPM approaches are not well suited for taking into account mechanics (i.e. describing the force balance which governs the dynamics of the system) because an equation of motion is never explicitly formulated. Since this PhD project tries to describe the relationship between mechanical forces and multicellular dynamics, CPM are not an ideal choice for a modeling technique.

A second major approach for single-cell based models consists of meshless methods, which consider single cells as discrete entities that can move and deform in space and for which an explicitly formulated equation of motion is solved. The fundamental concepts for this methodology are derived from long established techniques for modeling the physics of colloidal systems. Already in 1967, L. Verlet spearheaded the use of computer simulations — in a method that was later labeled Brownian Dynamics (BD) — to study the thermodynamical properties of systems with interacting particles [220].

Generally, the equation of motion for such systems will be a sub-class of the Langevin equation [116]:

$$m\frac{\mathrm{d}^2\mathbf{x}}{dt^2} = -\lambda\frac{\mathrm{d}\mathbf{x}}{dt} + \eta(t), \tag{1.4}$$

in which particles with mass m have positional degrees of freedom $\mathbf{x}$ and experience a viscous force with damping coefficient λ. The term $\eta(t)$ is δ-correlated white noise and its autocorrelation function, traditionally proportional to the thermal energy in BD [116], is scaled with the random components of cell movement. It should be noted that Eq. 1.4 in its given form is ill formulated in the strict mathematical sense: Due to the δ-correlated noise term $\eta(t)$, the derivative $\mathrm{d}\mathbf{x}/\mathrm{d}t$ is not defined in the limit. For a proper interpretation and justification, we refer to a reading of Itô calculus [214]. Since the Reynolds number for typical cellular systems is very low [167], the inertial term on the left hand side of Eq. 1.4 can be neglected, i.e.

$$m\frac{\mathrm{d}^2\mathbf{x}}{dt^2} \approx \mathbf{0}, \tag{1.5}$$

and we arrive at the equation of motion for an overdamped system (see further, e.g. Eq. 2.2). In their influential work [221], Vicsek *et al.* introduced an important class of models for "self-propelled particles" (SPP) which describe particles with a persistent active velocity $\mathbf{v}$:

$$\mathrm{dx} = \mathbf{v}\,\mathrm{d}t, \tag{1.6}$$

and a motion angle (polarization) θ:

$$\theta = \langle\theta\rangle_r + \Delta\theta, \tag{1.7}$$

where $\langle\theta\rangle_r$ denotes the average velocity direction of neighboring particles up to a radius r, and $\Delta\theta$ represents a noise term. Meanwhile, models of SPP have been widely used to investigate the collective dynamics of many active matter systems, including animal groups, cytoskeletal components, colonies of bacteria and cell groups [163]. A similar model will be adopted in chapter 7 in order to model the persistent motility of active migrating cells. In the early nineties, D. Drasdo pioneered the use of models based on Eq. 1.4 to study the dynamics and interactions of multicellular systems [45], thereby initiating the field of meshless individual cell-based modeling (IBM).

By the time of the start of this PhD, IBMs had been successfully applied to describe the dynamics of various biological systems, for example the *in vitro* growth of tumors [87], mesenchymal stem cell differentiation [106], growth and apoptosis of epithelial cell populations [61], and the *in vivo* regeneration of liver sinusoids [88]. Moreover, important methodological advances had been realized, such as the interaction of discrete cells with continuum fields, descriptions of important events in the cell cycle and cell

migration, attempts at representing complex non-spherical shapes, and different ways of solving the equations of motion [5, 20]. For the purposes of this PhD research, which heavily focuses on the action of mechanical forces, the latter two were found to be insufficient: No description for arbitrary cell shapes was available that properly accounts for mechanical forces at the (irregular) cell interface (see section 1.1.5), and an efficient method for solving the equation of motion in a deterministic way in friction-dominated systems was lacking[4]. Novel methodological developments that try to address these problems are presented further in this PhD manuscript.

1.1.5 On the importance of cellular shape

Simulations describing the collective dynamics of a large number of cells – see chapter 7 – usually consider the cell shape to be spherical or discoidal, or equivalently, the active or passive intercellular potential forces to on average act on a uniform sphere of influence[5]. By doing so, these models implicitly assume a clear separation of scale (time and space) between the duration and location of specific asphericities (if present) and the timescale and size of multicellular dynamics.

However, such an approach fails to account for persistent effects that rely on the non-spherical shape of the cells. For example, nematic behavior can arise naturally from the geometrical alignment of elongated particles alone [10]. Furthermore, while they can predict the global "average" mechanical state of a cell, they fail to meaningfully describe the highly localized forces which give rise to mechanotransduction events. Focal adhesions are well known centers of mechanotransduction, and the forces they experience are highly dependent on the local architecture of the cell, and specifically, the local geometry of the cell-substrate contact interface [47, 183].

To address these issues, various attempts have been made to complicate models with more detailed cell shapes – see e.g. [5]. Of particular merit is the subcellular element model as introduced by T.J. Newman, which describes cells as a collection of subcellular elements, of which the deformation is governed by an explicitly calculated "internal energy" [146]. In a Discrete Element Method framework, properly accounting for shape has been an important research question on itself for many years. Hence, the rigorous developments regarding geometrical contact calculations and contact force formulation can be considered important results by themselves – see chapter 3, 4 and 5. While mathematically very similar, these results can potentially contribute to wildly different research fields, such as complex particle behavior in macro-scale systems. Building on this, we develop a detailed deformable cell model that explicitly

[4] Performant Monte-Carlo-like methods as proposed in [45] are insufficient here since they assume *a priori* a local relaxation of mechanical stresses [5].

[5] Because they localize the (translational) degrees of freedom on the spherical center point, these models are often called "center-based models".

focuses on the interface between the cell and its environment, the rationale for this being that the collection of mechanical forces acting on the interface fully characterizes the translational and deformational behavior of the cell. Moreover, we accept that a detailed model of cytoskeletal behavior in a complete cell will remain unfeasible for the time being and therefore make use of simple approximations of cytoskeletal mechanics which can be easily "projected" on the cell surface – see chapter 5.

1.2 The timescales of cell dynamics

The mechanical response of a cell to an external force is highly dependent on the timescale of the measurement. In their seminal work, Fabry *et al.* determined the scaling laws that govern the microrheology of living cells, and identified the cytoskeleton as a soft glassy material close to the glass transition [48]. By modulating the effective noise temperature, cytoskeletal proteins can regulate the mechanical properties of the cell. For an active (living) cell, this implies that on short timescales (or high frequencies) the cell behaves like an elastic solid, and can be reasonably characterized by an instantaneous Young's modulus. This property can be measured using fast and precise experimental techniques like Atomic Force Microscopy (AFM). However, at larger timescales, cells flow more like a liquid that can be crudely characterized by an apparent viscosity. A lack of activity (or "noise") will return the cell to a glassy state, thereby maintaining its structural integrity. Moreover, it has been shown that the total contractile activity of myosin motors increases linearly[6] with increasing cell strain, producing an active tensile modulus of the cell, which determines its stress-strain relationship at very large timescales [223].

Very roughly – and neglecting the intricacies of soft glassy materials – the cell's mechanical response is summarized in Fig. 1.1(b). The instantaneous stiffness of the cell is represented by a spring-like k_1 which is in series with a damper with viscosity c, that is related to the constant remodeling of the cytoskeleton. For active cells, it can be assumed that c is sufficiently low to allow for flow-like behavior, and large deviations from the spherical shape. Hence, at the timescale of the transcriptional response of the cell, k_1 has little influence on the dynamics of cell movement and deformation. On the other hand, the active tensile modulus can be associated with an effective spring-like k_2, which is in parallel to both c and k_1. Indeed, the linear increase of tensile force with strain is very much analogous to a linear spring. On large epithelial monolayers, this contractile force results in a net intercellular tension which can be experimentally measured using traction force microscopy (TFM) [9, 212].

[6] Some scientists consider this linearity to be boring, but we rather enjoy its beauty and appreciate how it facilitates formulating simplified models for the physical behavior of cells.

From a modeler's perspective, awareness of the appropriate timescales for the system of interest is of utmost importance, not only when formulating a mathematical model, but also when interpreting the model's parameters. For example, a quick calculation can show that the instantaneous Young's modulus of the cell can impose a severe constraint on the timestep used in a simulation, yet has very little influence on the dynamics on the scale of days or weeks. However, when investigating mechanotransduction due to forces at focal adhesions (FAs), which operates on the timescale of seconds to minutes, the rigidity of the cell has a dominant influence on the local deformation in the integrin complexes, and can be an essential model parameter.

1.3 General Objectives

The central objective in this PhD project is to use computational models in order to investigate how single cell mechanical properties, combined with active cell behavior, give rise to intercellular forces, and on a larger scale, the collective dynamics of cellular aggregates. Specifically, we are interested in how the mechanical microenvironment of individual cells in *in vitro* cell cultures is affected by the general system conditions (e.g. cell density, substrate properties, etc.) as well as by the intrinsic biological activity of individual cells. As explained above, individual cell-based modeling provides an ideal tool to help expose the relationship between the most fundamental mechanical constituents in cellular systems.

Working towards this main objective, we define several technical objectives and subjectives, which are outlined below. These either involve methodological advancements towards representing accurate cells shapes, or using IBM methodology in order to help understand collective behavior of multicellular systems. A flow chart that visually illustrates the tasks delineated for this PhD project is given in Fig. 1.3.

Objective 1 Establishment of a particle-based simulation framework for modeling the dynamics and mechanics of cell aggregates

Individual cell-based modeling platforms which are general purpose, performant and properly account for motion and mechanics at the cellular scale are still lacking. Due to its very generic understructure, the Mpacts particle-based simulation software is ideally suited for this task. During this project, a framework is to be established that properly describes motion at the low Reynolds number environment that cells live in. Moreover, tools should be implemented that account for the most important morphological aspects of cell behavior and intercellular interactions. These include, but are not limited to, a description of the cell cycle, intercellular forces including the effect of adhesion, viscosity and contractility, and realistic (biased) random walk models to describe cell migration. It should be noted that for this task, I could rely on the previous work during

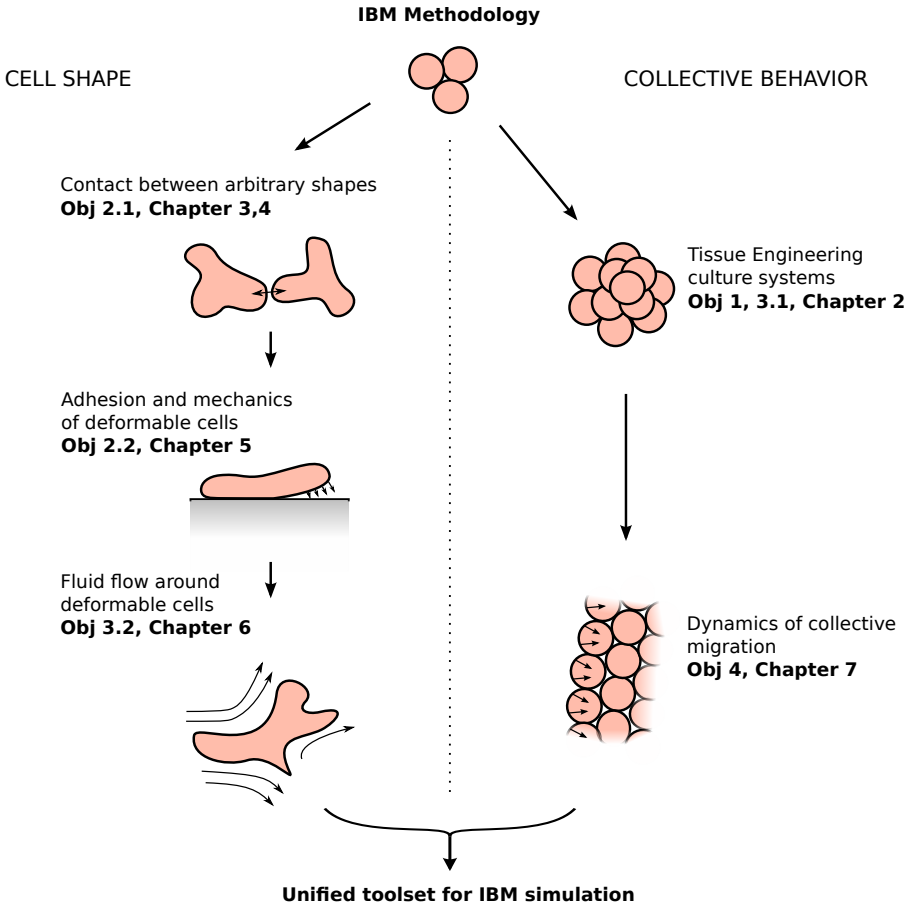

Figure 1.3: Illustrative flow chart of the work outlined for this PhD project. Starting from existing IBM methodology, two main pillars of progress can be distinguished: modeling cell shape, and modeling collective cell behavior (using more simple cell shapes). For each element, which represents a specific task and an independent result, the corresponding PhD objectives (**Obj.**) and the **Chapters** in which it is presented are indicated. Ultimately, the result is a unified framework — both in concept and in implementation — for IBM simulations, in which simulations of the collective behavior of highly detailed deformable cells are possible (see further in chapter 8).

my master's thesis [193], and in the PhD project of Dr. Tim Odenthal [152], which laid the foundations for solving equations of motion for cell movement in overdamped regimes. The results for this objective are showcased mainly in chapter 2 and 7, where

various added framework components are demonstrated.

Objective 2 Development of a generic and mechanistic method to account for shape and deformation of interacting cells

As explained in section 1.1.5, accounting for arbitrary cell shapes in individual cell-based models is important for linking local intercellular forces to mechanotransduction processes, hence to their effect on cell fate. Therefore, a deformable cell model is to be formulated, which takes into account local forces and pressures and provides a detailed description of cell shape. Since the establishment of a deformable cell model is generic and encompasses a large part of this PhD project, objective 2 is divided into the following two sub-objectives:

2.1 Mechanistic contact description for arbitrary meshed bodies.

One of the most common – and efficient – ways to account for arbitrary shapes is by making use of (triangulated) surface meshes. However, a general method to describe contact between triangulated meshes has not been described yet. The aim here is to derive a local formulation for the general contact between the mesh's primitive geometry elements (i.e. triangles, or in general, polygons). In order to achieve this, we would like to make use of well established contact models that already have been used for spherical contacts. The results for these tasks constitute an important development for DEM modeling in general. They will be described in detail in chapters 3 and 4. We hope that the reader, who is interested in models of cellular systems, will not be discouraged by the presented applications in macro-scale systems, but rather appreciates the universality of mathematical modeling which readily transcends narrowly defined scientific fields.

2.2 Conception of a new adhesion model for deformable cells.

Contacts at the cellular scale are distinguished from macroscopic contacts by the dominant importance of surface adhesion forces – for a complete overview, see [184]. For cellular models, adhesion theories like Johnson-Kendall-Roberts (JKR, see further, Eq. 2.3) are commonly used. However, due to the divergence of the pressure at the edge of a contact surface, JKR theory cannot be readily used to compute adhesion forces between triangulated surfaces. In order to model adhesion between arbitrarily shaped deformable cells, a suitable mechanistic (i.e. based on adhesion energy as a physical surface property) adhesion model must be formulated for the contact between triangles. The results of this task, together with the presentation of the deformable cell model, are provided in chapter 5. Moreover, the newly developed adhesion model is applied to investigate the universal dynamics of initial cell spreading.

Objective 3 Using computational models, investigate how cell culture conditions affect the mechanical micro-environment in the context of bone tissue engineering

By predicting how process settings of cell culture systems affect the mechanical micro-environment of individual cells, we hope to help optimize the production of multicellular aggregates of suitable quality for use in bone tissue engineering applications. In particular, the following study cases are defined:

3.1 Quantify the mechanical microenvironment on microcarrier systems during cell expansion.

Evidence suggests that the first steps towards cell fate determination are already established during the initial cell expansion phase of a tissue engineering process. One of the influencing factors affecting cell fate is the mechanical microenvironment [70, 175]. Consequently, already from the very first steps, tissue engineering processes should be designed with respect to the physical microenvironment. Here, we intend to use individual cell-based modeling techniques to predict the mechanical microenvironment in one possible cell culture system: microcarrier cell expansion. This will constitute a case study, but also provide a proof-of-concept for using such modeling techniques to address practical process design questions. The detailed results of this work are provided in chapter 2.

3.2 Quantify the mechanical effect of flow on cells in perfusion bioreactors

Perfusion bioreactors – see further in section 6.1 – are used in dynamic culturing systems to transport sufficient oxygen, nutrients and growth factors to the cells, and provide mechanical stimulation. The contribution of the latter can be investigated using the deformable cell model described above. For this, the deformable cell model must be coupled to a computational solver for the fluid flow in the cells' local environment. Such a coupling can be realized using the Immersed Boundary Method. These developments, the result of a close collaboration with Dr. Y. Guyot, together with calibration experiments using AFM, are provided in chapter 6.

Objective 4 Unravel how single cell behavior and intercellular interactions establish the physical properties of large multicellular aggregates

Whereas the previous objectives are either technical in nature (i.e. model developments) or address specific, practical problems (e.g. in the context of tissue engineering), the developed methodology can contribute to an enhanced insight in the fundamental physics of collective cell behavior in general. More specifically, we hypothesize that active multicellular structures can be classified in terms of physical phases, and that changes between these phenotypes are analogous to physical phase transitions.

Therefore, the final objective is to construct, borrowing from ideas from colloid physics, a minimal model that is able to capture the most crucial aspects of intercellular interactions and cell activity. Doing so will provide a universal framework, from which specific cell aggregate and tissue phenotypes are derived. The results from this work are presented in chapter 7.

Chapter 2

The mechanics of microbead cell expansion

Adapted from [195]:

Smeets, B., Odenthal, T., Tijskens, E., Ramon, H., Van Oosterwyck, H. (2013). Quantifying the Mechanical Micro-environment during Three-dimensional Cell Expansion on Microbeads by means of Individual Cell-based Modelling. Computer Methods in Biomechanics and Biomedical Engineering, 16 (10), 1071-1084.

2.1 Introduction

Developmental processes are inherently robust. Cells are guided from one stable equilibrium state — or attractor basin — to another by a combination of micro-environmental influences that change over time [102, 117]. These influences include biochemical agents — autocrine, endocrine and paracrine factors — but also the physical nature of the cell micro-environment. The robustness of a developmental process implies that small or transient changes in these influences will not change the stable outcome of the overall process.

However, *in vitro* cell culture has only achieved limited success in recapitulating these developmental processes. In fact, even in the cell expansion phase cell cultures typically exhibit considerable necrosis and/or loss of differentiation potential in a large number of cells [216]. Especially in large three-dimensional cell culture systems, local differences in cell behavior can be important.

In Tissue Engineering, where the desired cell number is typically very high and a high level of control of cell fate is required, these problems place serious limitations on the quality of obtained constructs. As Tissue Engineering applications often deal with very heterogeneous cell populations and high cell senescence, it is highly challenging to quantify the amount of biological heterogeneity introduced by the culturing conditions. Merely adding external chemical cues like growth factors and cytokines might not be enough to improve the quality of in vitro three-dimensional cell cultures. In order to achieve this, the physical micro-environment has to be carefully tuned to guide cell differentiation in each stage of the *in vitro* process. Specifically, this micro-environment must fulfil at least two main functions:

The first is to provide a spatial structure that facilitates the formation of inter-cellular communication. The micro-environment should allow the cells to interact with each other and should have well adjusted mass transport properties that mimic the spatial and temporal scale of the analogous developmental process.

The second function is to provide a proper mechanical environment for the cells. The mechanical properties of the substrate or scaffold are important determinants of forces that each cell will be exposed to [141], and of how it will rearrange its cytoskeleton and change its shape.

Through mechanotransduction pathways, cytoskeletal forces can be translated into molecular activation [91, 94], ultimately leading to changes in cell fate. Studies have shown that substrate stiffness and cell contractility can modulate cell differentiation, demonstrating their importance for Tissue Engineering and regenerative medicine [47, 66, 92].

Various scaffolds and biomaterials that try to optimize the cell micro-environment and allow for three-dimensional growth while limiting necrosis due to mass transport limitations have been developed [36, 46, 78]. Macro-porous scaffolds and micro- or nano-porous carriers such as biodegradable hydrogels can be used to accommodate cells in a three-dimensional environment. Alternatively, cells can be seeded and expanded on spherical microcarriers which can be clustered in order to create three-dimensional cellular aggregates. The advantage of this method is that the available surface to volume ratio can be much higher than for traditional two-dimensional cell expansion. It is also much easier to obtain uniform cell seeding and using microcarriers can prevent strong spatial gradients in cell densities by providing more efficient mass transport. However, in order to improve control of cell culture conditions at the individual cell level and bearing in mind the importance of the mechanical environment on cell fate, a better understanding of the complex interplay between this environment and culture conditions is crucial [175]. Measuring inter-cellular mechanics is highly challenging or even impossible, especially when it concerns multicellular, three-dimensional systems, such as aggregates.

Model-based research can help in quantifying the (inter-)cellular mechanical environment and — in combination with experimental data — unraveling its effect on cell fate [44, 105]. By reducing the biological complexity and by offering highly controllable settings, mathematical models can lead to an improved insight into underlying mechanisms of action [60]. Tissue-level models that describe cell aggregates in terms of cell densities lack the capacity to describe complex inter-cellular (mechanical) interactions at the single cell level [177]. Agent-based models try to address these problems by introducing cells as discrete entities. These entities can be "point masses", or more complex three-dimensional structures if shape and mechanics are taken into account – for a good overview see also [5]. These mesoscale models aim to describe both mechanical and biochemical inter-cellular interactions in (parts of) tissues.

In this chapter we demonstrate the potential of a framework for individual cell-based models (IBM) for quantifying the mechanical micro-environment in growing three-dimensional cell cultures. We make use of a Discrete Element Method based platform in which cells are considered as (mechanically) interacting particles [210]. These particles exert forces on each other and move and grow over time. The IBM is used for simulating expansion of osteochondroprogenitor cells (i.e. cells that can differentiate towards the osteogenic and chondrogenic lineage) on spherical, non-porous microbeads. A simple measure for mechanical stress on each individual cell is introduced to quantify the mechanical micro-environment. Using this stress measure as model output, we first characterize model robustness by analyzing the sensitivity of the model output to small changes in model input parameters. Secondly, changes in process design and cell culture dependent model parameters on the same model output measure are investigated.

2.2 Model Description

A lattice-free IBM is used in which cells are considered as deformable spherical particles. To calculate the movement of the cells over time, a discrete element-like method is employed. For this, we explicitly determine the forces on each cell at every time step. These forces can be external forces — body forces — or cell-cell and cell-substrate interaction forces — contact forces. The only body force we consider for the situation we want to model is a force representing Brownian motion — although for cells of diameter 12 μm, its effect is very small.

Section 2.2.2, details how contact forces are calculated and in section 2.2.3 the special interaction force assigned for cytokinesis is explained. In preliminary simulations, a small "random walk" force was added to the cells, but since it had very little effect, we neglected it for the first present analysis.

We begin by providing an overview of the way these forces act in our system in section 2.2.1:

2.2.1 Equation of motion

In the equation of motion, all the mechanical forces that are exerted on a cell are summed up. As cells move in a low-Reynolds number environment, inertial forces can be neglected. As a result of that, a first order equation is obtained that can be solved for the cell velocity **v**. Subsequently, the cell positions **x** are calculated using explicit Euler integration. The equation of motion for cell i in the system reads as follows:

$$\sum_{j\in\mathcal{N}} \mathbf{F}_{ij} + \mathbf{F}_{i,s} + \mathbf{F}_{i,\text{division}} + \mathbf{F}_{i,\text{Brownian}} = \Gamma_{iw}\mathbf{v}_i + \Gamma_{is}\mathbf{v}_i + \sum_{j\in\mathcal{N}} \Gamma_{ij}(\mathbf{v}_i - \mathbf{v}_j). \quad (2.1)$$

At the left hand side of Eq. (2.1) we recognize the contact forces between direct neighbouring ($\mathcal{N}$) cells j and cell i, contact forces between cell and substrate, cell division (cytokinesis) and a force representing Brownian motion. The velocity dependent terms are at the right hand side of Eq. (2.1): a viscous drag force due to suspension in liquid, $\Gamma_{iw}\mathbf{v}_i$, cell-substrate friction forces and the cell-cell friction forces between contacting cells. Eq. (2.1) can be rewritten as:

$$\mathbf{\Gamma}\cdot\mathbf{v} = \mathbf{F}, \quad (2.2)$$

in which all non-velocity dependent forces — both contact forces and body forces — are summed up at the right hand side. $\mathbf{\Gamma}$ at the left hand side is a friction matrix that contains all the cell-substrate, cell-cell and cell-liquid friction or drag constants. As most cells are only in contact with a relatively small number of other cells, the positive definite matrix $\mathbf{\Gamma}$ is typically diagonally dominated and very sparse in structure. Therefore Eq. (2.2) can be efficiently solved for **v** using an iterative method such as the conjugate gradient method (CGM).

2.2.2 Contact mechanics

The mechanical behavior of a cell — the way the cell will react to and adapt to external mechanical forces — is largely determined by the properties of the cytoskeleton. The components of the cytoskeleton will actively adapt to external forces by remodeling and can exert pulling forces on the anchoring points of the environment [95]. The IBM simulates the mechanical interactions of a multicellular system over a timespan that is long compared to cytoskeletal changes. It has been shown by [44] that for individual-cell based models, the precise formulation (e.g. Hertz including adhesion or JKR, see below) of the interaction forces does not significantly affect predictions of

growth behavior on longer timescales, as long as the key aspects — viscous dissipation and elastic contact interaction — are expressed in the model.

Therefore, the mechanical behavior of cells is approximated by a simple formulation: cells are considered deformable elastic spheres with an indentation dependent contact force described by the Johnson-Kendall-Roberts (JKR) model [97, 98]. This approximation has been successfully validated in experiments on living cells by e.g. [25]. The repulsive part of the JKR model is purely elastic: for a given indentation a repulsive force can be calculated analytically. Additionally, the JKR model also includes an adhesive force, proportional to the adhesion energy $K_{a,ij}$. Compared to the Hertz force with an additional adhesive term, the force from JKR has the advantage that it also incorporates hysteresis: adhesive forces remain active when cells are pulled apart because of already formed molecular bonds (due to adhesion molecules) until a final break-off point. For JKR, an expression for the magnitude of the contact force between two elastic, spherical cells can be derived as:

$$F_{ij} = \frac{4\hat{E}}{3\hat{R}} a^3 - \sqrt{8\pi K_{a,ij} \hat{E}\, a^3}, \tag{2.3}$$

in which

$$\hat{E} = \left(\frac{1-\nu_i^2}{E_i} + \frac{1-\nu_j^2}{E_j} \right)^{-1} \text{ and } \hat{R} = \left(\frac{1}{R_i} + \frac{1}{R_j} \right)^{-1}. \tag{2.4}$$

E_i and E_j are the Young's moduli [Pa], ν_i and ν_j the Poisson numbers [-], and R_i and R_j are the radii of cells i and j. $K_{a,ij}$ is the adhesion energy [J/m^2] for cells in contact i and j. Finally, the radius of the contact area a in Eq. (2.3) can be obtained iteratively from the sphere-sphere overlap δ [157]:

$$\delta = \frac{a^2}{\hat{R}} - \sqrt{\frac{2\pi\sigma}{\hat{E}}} a. \tag{2.5}$$

The JKR model takes the deformation of the cell due to contact into account: F_{ij} in Eq. (2.3) is dependent on the radius of the contact area, which changes on deformation according to Eq. (2.5). In reality, progenitor cells that attach on a substrate are not spherical but will flatten out substantially. However, as soon as multiple cell layers emerge and a three-dimensional aggregate is formed, the cell shape will again start to become more spherical [16]. Moreover, although cells can actively remodel their cytoskeleton in order to counteract mechanical stress, the space in dense three-dimensional aggregates is limited and eventually elastic mechanical stress will build up. As the model considers spherical microbeads, the JKR model is easily applicable as well for modeling repulsive and adhesive interaction between the cells and the microcarrier [142].

In order to accurately describe the dynamics of cellular contact, the IBM also incorporates velocity dependent friction forces. Two types of these friction forces are included in the model:

On the one hand there is a force perpendicular to the connecting vector between the two cells, $\mathbf{n}_{ij}$, counteracting sliding motion of two contacting cells. Physically, this force mainly results from the time dependent behavior of binding and unbinding events when a cell slides with respect to another cell in close contact.

On the other hand there is a force parallel to $\mathbf{n}_{ij}$, accounting for modified Stokes' forces close to other cells – similar to the near-field interactions in Stokesian Dynamics [17] — and velocity dependent energy dissipation due to deformation of the cell's cortex and due to the formation of adhesive bonds [29, 112].

In order to calculate which cells are interacting with each other, an advanced contact detection algorithm based on [79] is used that determines which particles (cells vs. cells or cells vs. bead) have a positive overlap δ.

2.2.3 Cell cycle

For small aggregate sizes, cell growth can be considered exponential and in a first approach the availability of resources such as glucose and oxygen is considered unlimited. Because the main focus of the IBM is related to mechanics, the cell cycle is simplified to a morphological description and is broken up into two distinct stages: increase of cell volume (representing interphase) and cytokinesis. When growing, the rate of volume increase over time is considered constant [54, 168], yielding the following formula for the cell radius r:

$$\frac{\mathrm{d}r}{\mathrm{d}t} = K_g \left(\frac{r_o}{r}\right)^2. \tag{2.6}$$

in which K_g is a growth constant and r_o the initial radius of the cell just after it finished the previous cytokinesis. For the cytokinesis we use a dumb-bell approximation as previously described in [44].

We assume that the total cytoplasmic volume of the two overlapping spheres which represent the division complex, remains constant. As the distance between the centers of the spheres, d, increases, the radii of the individual spheres, r, decrease (see Fig. 2.1). From the assumption of constant volume and the initial volume V_i, a relationship between r and d can be obtained:

$$r = \frac{d^2}{16C_A} - \frac{d}{4} + C_A, \tag{2.7}$$

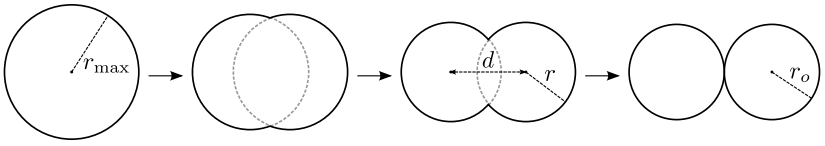

Figure 2.1: Dumb-bell approach for modeling geometry of binary fission. $r_{\max}$: final radius of the cell at which cytokinesis is initiated, d: distance between the centers of the spheres that make up the cytokinesis complex, r: radius of the spheres that make up the cytokinesis complex, r_o: cell radius just after it finishes cytokinesis.

with

$$C_A = \left(\frac{3\,\mathrm{V_i}}{8\pi} + \sqrt{\frac{9\,\mathrm{V_i}^2}{64\pi^2} + \frac{3\,\mathrm{V_i}\,d^3}{256\pi}} + \frac{d^3}{64} \right)^{1/3}. \tag{2.8}$$

The derivation of Eq. (2.7) and Eq. (2.8) can be found in [193]. From the perspective of a particle-based model, the cell undergoing cytokinesis is composed out of two interacting particles lacking contact forces in between them. In order to make sure that the relative movement of these particles corresponds to Eq. (2.7), the IBM includes a "division force". The division force is not a constant force but a force that adapts to the mechanical environment of the cell. Cytokinesis can be mechanically inhibited if the division force exceeds a predefined threshold force $F_{d,\max}$, but no additional biological contact inhibition [62] is taken into account here. In the model, the division force is calculated as:

$$F_d = K_d\,(d_r - d), \tag{2.9}$$

in which K_d is a gain factor that is chosen sufficiently high so that the division force ensures that cytokinesis finishes as prescribed, and $d_r - d$ the difference between the reference distance d_r and the actual distance d. The reference distance is defined to increase linearly in time during cytokinesis, until the spheres have no more overlap and make up two independent cells.

Aside from the cytokinesis time, the model also sets a growth time, i.e. the time in between two cytokinesis events — which for a given initial cell radius also defines the maximum cell radius at the end of the interphase through Eq. (2.6). Using a fixed growth time, the cell cycles would be exactly synchronized, giving rise to unrealistic forces and stress levels. In reality, cell cycles within an aggregate are at least partially asynchronous. Therefore we introduce a normal distribution on the maximum cell radius that a cell will achieve before starting cytokinesis. For a given cell, the growth time is determined on the one hand by the initial radius of the cell, and on the other hand by the maximum radius before initiating division. As a result, the normal distribution imposed on the maximum radius before cytokinesis will lead to a normal distribution on

the growth times. The reason for choosing the maximum cell radius for randomization is that its value is easy to obtain from microscopy images of growing cells.

2.2.4 Stress calculation

In order to quantify the mechanical micro-environment and to assess the influence of model parameters on simulation results, a simple measure for the mechanical stress on each cell is introduced that expresses the compressive or tensile nature of the environment in which the cell resides. For spherical cells, contact forces always act on a contact point at the edge of the sphere, and are defined in the direction of the vector between the contact point and the cell center. Contact forces pointing towards the cell center are of compressive nature and forces pointing away from the cell center are of tensile nature. Therefore, a simple measure of the mechanical stress on a cell can be obtained by summing up all magnitudes of contact forces a cell feels — counting forces towards the cell-center as positive and tensile forces (away from the cell-center) as negative. This force is divided by the total area of the cell in order to obtain a measure of the mechanical stress on a cell, further denoted by P, which is useful to compare the distribution of stresses in the different simulation scenarios investigated in this work.

The distribution of mechanical stress does not follow a normal distribution but is skewed towards the compressive side (see further, e.g. Fig. 2.3). Therefore, when comparing the distribution of stresses on a microcarrier between different scenarios, we do not use the commonly used Student's t-test. Instead, we use the Kruskal-Wallis one-way analysis of variance, which determines whether distinct samples come from the same distribution [107].

2.2.5 Sensitivity Analysis and Latin Hypercube Sampling

The IBM gives a basic theoretical description of the main mechanical actors involved in microcarrier cell culture systems. In order to use the IBM to make qualitative predictions of the effect of process design parameters on the mechanical conditions of the cell, we first have to assess the model sensitivity. A Sensitivity Analysis (SA) assesses how variation in model output can be apportioned to different sources of variation, such as uncertainty in the input variables [181]. In this study, it is being applied to quantify how uncertainty in the IBM's input parameters will affect the variation in the mechanical stress values. For this, we choose a design point — a combination of cell dependent and microcarrier dependent model parameters — and estimate (based on literature data) the standard deviations on the model input parameters as described in Table 2.1.

The sensitivity analysis investigates how sensitive the model output for this specific design point will be to small changes of input parameters. Ideally, in order for the model to be a valuable tool for process optimization, a low sensitivity of model output (in this case mechanical stress values) is desired. If not, process optimization with respect to the mechanical micro-environment would be very hard, as the unavoidable uncertainty in process specific parameters could result in vastly different predicted mechanical micro-environments, thereby rendering model-based optimization inappropriate.

To sample the multidimensional parameter space required for a sensitivity analysis efficiently, there are a number of sampling methods available. For N samples, Latin Hypercube Sampling (LHS) divides the range of each input variable into N intervals, resulting in N non-overlapping realizations for each of the input variables [181]. We use LHS and assume that every input parameter follows a normal distribution.

2.2.6 Model Parameters

The model parameters used for the simulations are listed in Table 2.1. This set represents the standard conditions for cell expansion of osteochondroprogenitors on spherical microbeads and the values are derived or estimated from data in the literature [86, 105, 106, 114, 147].

2.3 Results and Discussion

2.3.1 Sensitivity Analysis

Five parameters are varied in the simulations for the SA: cell Young's modulus (E), perpendicular and parallel friction coefficients ($\gamma_\perp$ and $\gamma_\parallel$), cell-cell adhesion ($K_{a,cc}$) and cell-bead adhesion ($K_{a,cb}$). On the one hand, these parameters are chosen since they are important measurable biological or mechanical parameters that vary depending on the materials or cell type in use. On the other hand, in preliminary simulations a few parameters such as the bead's Young's modulus E_b (section 2.3.3) and the Poisson's ratios were found to be of minor relevance for the stress predictions and therefore not varied in the SA. This is a commonplace procedure ("screening experiments") to limit the computational effort for the sensitivity analysis [181].

The Latin Hypercube Design resulted in 100 samples, i.e. 100 simulations. For each sample, two quantities are calculated as output variables:

Table 2.1: Base parameter set for the individual-based model. Unless stated otherwise, these values are used in the results section. $\hat{\sigma}$(Value) gives estimations of standard deviations used in the sensitivity analysis (section 2.3.1).

Parameter	Symbol	Units	Value	$\hat{\sigma}$(Value).
timestep	Δt	s	0.001	
simulation time	T_{end}	s	0.125e6	
conjugate gradient precision	$e_{\max}$	m/s	5e-12	
division controll stiffness	K_d	N/m	60e-5	
initial size	r_o	m	4.5e-6	
division size	$r_{\max}$	m	6.0e-6	
division size sdev	δ_{div}	m	0.1e-6	
division force threshold	$F_{d,\max}$	N	0.5e-9	
division time	T_d	s	5e3	
bead radius	R_b	m	35e-6	
growth time	T_g	s	57.6e3	
adhesion energy cell-cell	$K_{a,cc}$	J/m^2	10e-6	2e-6
adhesion energy cell-bead	$K_{a,cb}$	J/m^2	15e-6	2e-6
Youngs modulus cell	E_c	Pa	500	
Poisson's ratio cell	ν_c		0.4	
perp fric coef cell-cell	$\gamma_\perp$	kg/s	10e-6	2e-6
par fric coef cell-cell	$\gamma_\parallel$	kg/s	10e-6	2e-6
Youngs modulus bead	E_b	Pa	1e3	0.2e-3
Poisson's ratio bead	ν_b		0.5	
perp fric coef cell-bead	$\gamma_{\perp,s}$	kg/s	10e-6	2e-6
par fric coef cell-bead	$\gamma_{\parallel,s}$	kg/s	10e-6	2e-6
viscosity	μ	Pa·s	3e-3	
temperature	T	K	310	

The first is the mean compressive mechanical stress measure $\bar{P}$ [Pa] (see section 2.2.4), which indicates whether the average stress on a cell is compressive (positive) or tensile (negative).

The second quantity is the standard deviation of the compressive mechanical stress, which is a measure for the heterogeneity of the cells' mechanical environment. In order to avoid confusion between stress heterogeneity and its standard deviation between different simulations, this quantity will be denoted further on as H_p [Pa].

For each sample, the output values are calculated both before the cells reach confluency on the bead and after the cells have become confluent, that is when they cover the entire surface of the microcarrier. Fig. 2.2 shows the predicted outcome of the mean mechanical stress values $\bar{P}$ in function of the five varying model parameters. As can be seen in Fig. 2.2, the IBM is more sensitive to small changes of input parameters

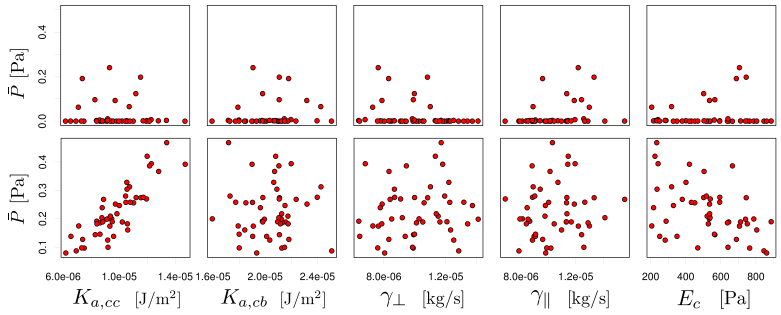

Figure 2.2: Predicted values of the mean mechanical stress measure $\bar{P}$ [Pa] as a function of five input parameters: cell-cell adhesion energy $K_{a,cc}$, cell-bead adhesion energy $K_{a,cb}$, perpendicular friction coefficient $\gamma_\perp$, parallel friction coefficient $\gamma_\parallel$ and cell Young's modulus E_c. One data point represents the mean mechanical stress $\bar{P}$ before (top row) and after (bottom row) confluency for a specific Latin Hypercube Sample.

after confluency is reached on the microcarrier: the total variance of the predictions increases strongly on confluency.

The uncertainty analysis, reported in Table 2.2 gives us the expected value and variance of the output variables mean compressive (mechanical) stress $\bar{P}$ and stress heterogeneity, H_p after confluency. Both for $\bar{P}$ and H_p, the standard deviation (or $\sqrt{V}$) is significantly lower than the expected value. As these data are for the worst case scenario — confluency, where the highest output variance was observed — it can be concluded that the modelled theoretical system itself is not very sensitive to small changes in input parameters. From Fig. 2.2 it is already obvious that most of the variance in the predicted values of $\bar{P}$ is caused by changes in the cell-cell attraction constant $K_{a,cc}$. To quantify the relative importance of these input parameter uncertainties, a standardized linear model is constructed that describes the mean stress measure as a linear combination of the model input parameters:

$$\bar{P} = a_0 + a_1 E_c + a_2 \gamma_\perp + a_3 \gamma_\parallel + a_4 K_{a,cc} + a_5 K_{a,cb}.$$

The coefficients of the linear model are given in Table 2.3. The values of these coefficients indicate how much of the output variance can be explained by their respective model parameter. For the data after confluency, we find significance (Student's t-test, $p < 0.001$) for parameters E_c, the cells Young's modulus and $K_{a,cc}$, the cell-cell adhesion energy. For the data before confluency is reached, no significance was found with any input parameter.

In other words, after the cells become confluent on the carrier, the parameters that the predicted mean stress values are most sensitive to are the cell-line dependent parameters: cell adhesion and Young's modulus.

Table 2.2: Uncertainty analysis for Latin Hypercube Sample design of IBM simulations. Expected value and Variance are given for two model output variables: mean compressive mechanical stress $\bar{P}$ and standard deviation on compressive mechanical stress H_p — a measure for mechanical heterogeneity of the cells. Data is time-averaged after the cells reach confluency on the microcarrier over a period of 2000 seconds.

	Expected value (E)	Variance (V)
$\bar{P}$	0.2153	0.0088
H_p	0.6393	0.0267

Table 2.3: Standardized coefficients of the linear model: $\bar{P} = a_0 + a_1 E_c + a_2 \gamma_\perp + a_3 \gamma_\parallel + a_4 K_{a,cc} + a_5 K_{a,cb}$. Data is time-averaged after the cells reach confluency on the microcarrier.

i	Coefficient	Estimate (a_i)	Std. Error	T value	Pr ($>\|t\|$)	$p < 0.001$
0	Intercept	1.392e-16	6.753e-02	0.000	1.000	
1	E_c	-3.191e-01	7.338e-02	-4.348	8.56e-05	*
2	$\gamma_\perp$	-7.386e-02	7.251e-02	-1.019	0.314	
3	$\gamma_\parallel$	2.841e-02	6.829e-02	0.416	0.679	
4	$K_{a,cc}$	7.813e-01	7.266e-02	10.753	1.23e-13	*
5	$K_{a,cb}$	1.111e-01	6.956e-02	1.597	0.118	

2.3.2 Dynamics of the mechanical micro-environment

The IBM gives the opportunity to monitor the mechanical micro-environment at all time points: from the start when the cells are seeded until after the cells become confluent on the microbead. In Fig. 2.3(a) the temporal evolution of the mean mechanical stress $\bar{P}$ is plotted as well as the mechanical heterogeneity as indicated with dotted lines (average $\pm$ standard deviation).

The filled red area indicates the complete range of the mechanical stress values in the aggregate. Furthermore, the cell density (defined as total number of cells in the aggregate per microcarrier surface area) as a function of time is plotted. Both tensile and compressive mechanical stresses are present. The mean compressive stress as well as the stress heterogeneity generally build up over time and both strongly increase at the point where the cells become confluent on the carrier at around 30h. The cells which are initially perfectly synchronized will not all start dividing at the same time (see section 2.2.3). Therefore, the increase in cell number during the cytokinesis cycles has a sigmoidal shape instead of a step shape (as visible at the start of the simulation, where all cells are perfectly synchronized). As cell proliferation progresses, the discrete

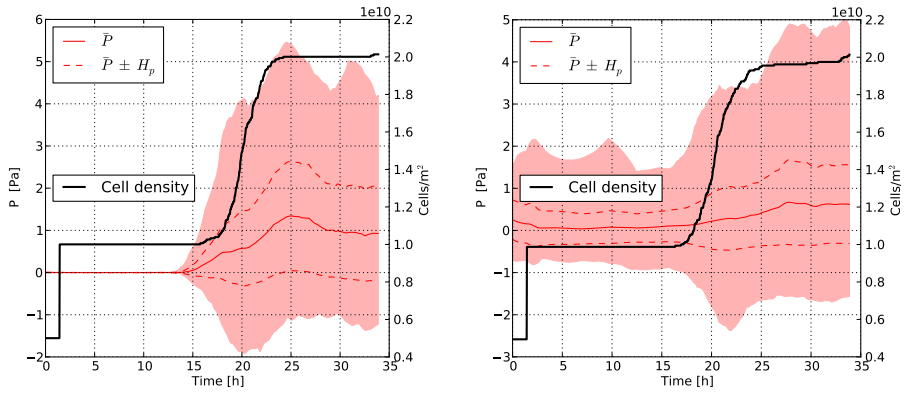

Figure 2.3: Average mechanical stress and cell density vs time for cell expansion on a microbead. $\bar{P}$: mean compressive stress, H_p: standard deviation on mean compressive stress. The filled red area denotes the complete range of the stress values. Bead diameter: 70 μm **(a)** Initial cell seeding is random and no cells are in contact with any neighbouring cells. **(b)** initially, cells are seeded in small clusters on the bead.

doubling cycles will change towards a continuous exponential growth curve. During phases with a relatively large number of cytokinesis events — in which the cell number quickly goes up — the mechanical stress in the aggregate increases. During interphase — in which each individual cell grows in volume but the cell number does not increase — a small stress relaxation can be observed.

The cells are seeded randomly on the microbead with the restriction that cells can not overlap. Therefore, initially none of the cells are in contact with other cells. As a result of that, initially $\bar{P}$ is close to zero. Fig. 2.3(b) shows $\bar{P}$ in function of time for a situation in which the cells are seeded in small clusters, instead of completely isolated. The effect is that the mechanical stress on the cell is initially much higher. However, the stress around confluency is not affected: at the time of maximal stress, there is no significant difference in the stress distribution (Kruskal-Wallis one-way analysis of variance, $p > 0.001$). Therefore, we use the simpler, non-clustered seeding algorithm for all following cases.

In the following parts, we will identify which physical properties of the system are responsible for the increase in heterogeneity in mechanical stress. First, we assess how much variation in the mechanical stress is caused by purely stochastic effects related to the initial cell distribution. In order to quantify this, 10 simulations were performed with the same model parameters but with a different random seed — the

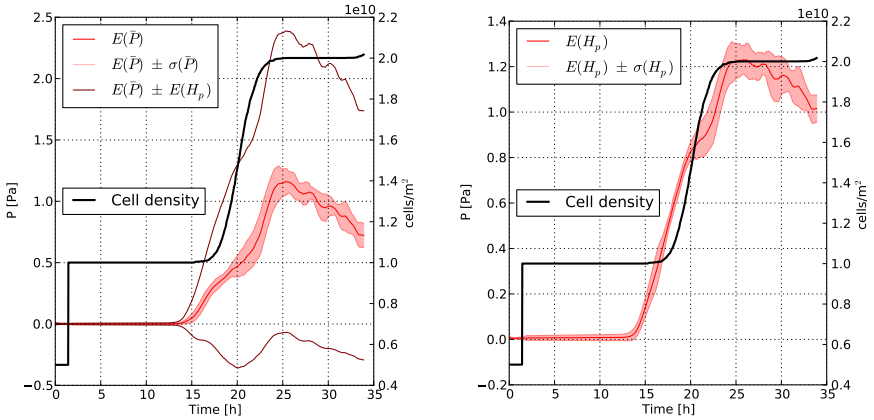

Figure 2.4: Influence of initial random seeding on the mean compressive mechanical stress $\bar{P}$ and the stress heterogeneity H_p. The cell densities are initially identical, and remain nearly the same because of the identically applied growth law. **(a)** Temporal evolution of mechanical stress values for simulations using different random seedings of cells (N=10). $E(\bar{P})$ and $\sigma(\bar{P})$: expected value and standard deviation on mean mechanical stress across different simulations, $E(H_p)$ expected value of stress heterogeneity. **(b)** Temporal evolution of stress heterogeneity. $E(H_p)$ and $\sigma(H_p)$: expected value and standard deviation of stress heterogeneity across different simulations.

initial positions of the cells on the microcarrier were randomly changed.

The outcome of these simulations is summarized in Fig. 2.4. As can be observed, the difference in $\bar{P}$ and H_p across simulations is small. From this, it can be concluded that the variation in predicted stress values in a given aggregate is mainly caused by effects not related to cell seedings. Also, performing simulations with different random seeding distributions is not required. The predicted stress evolution using one specific random seed is sufficient to assess the mean stress evolution with time.

2.3.3 Effect of microcarrier properties on the mechanical environment

In section 2.3.1 the general sensitivity of the model to small deviations from our base parameter set (Table 2.1) was investigated. Here we will look at how comparatively large variations in the mechanical properties of the microcarriers themselves influence the mechanical micro-environment. Again, both the mean mechanical stress $\bar{P}$ and the standard deviation on the mechanical stress H_p will be calculated from simulations.

The mechanically relevant design properties of the microbead are its stiffness E_b and its cell adhesion coefficient $K_{a,cb}$. The first property can be modified e.g. by modulating the degree of cross-linking (in case of a hydrogel microcarrier), changing the material properties of the microcarrier. The latter can be modified e.g. by applying a different surface coating, or by using a different concentration of adhesive biomolecules in the coating [114].

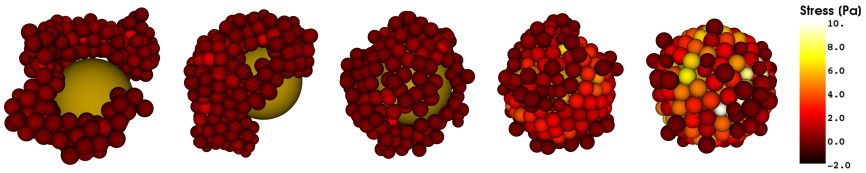

(a) (b) (c) (d) (e)

Figure 2.5: Simulated microcarrier cell expansion on microbeads with different cell-substrate adhesion values at the same time point at the end of the simulation. **(a)** $K_{a,cb}$ = 2.5e-6 J/m^2, **(b)** $K_{a,cb}$ = 5e-6 J/m^2, **(c)** $K_{a,cb}$ = 10e-6 J/m^2, **(d)** $K_{a,cb}$ = 20e-6 J/m^2, **(e)** $K_{a,cb}$ = 40e-6 J/m^2

In Fig. 2.5, the positions and stresses of the cells are shown for different cell-bead adhesion values. Not only does the spatial distribution of the cells change, but also the magnitude of the compressive stress changes with $K_{a,cb}$. It should be pointed out that in the cases of very small $K_{a,cb}$, the cells won't attach properly to the bead and will likely die or wash off in *in vitro* experiments.

In Fig. 2.6, the temporal evolution of the mean compressive mechanical stress $\bar{P}$ is shown for different cell-bead adhesion values $K_{a,cb}$. At confluency, $\bar{P}$ is strongly influenced by $K_{a,cb}$. Generally, high values of cell-bead adhesion energy lead to high mean compressive stress values and a higher rate of stress increase around the point of confluency. Fig. 2.6(b) shows the distribution of the stress values around confluency. For this, we use an averaging window of 1000 s around the peak stress (see SI in [195]). Statistically, the effect of cell-bead adhesion on stress distribution is significant (Kruskal-Wallis one-way analysis of variance $p < 0.001$).

Additionally, we performed simulations of cell expansion on microbeads for different Young's moduli of the beads. The distribution of mechanical stresses on the cells is not as strongly influenced by the Young's modulus of the bead than its surface adhesion properties (Fig. 2.7).

Spherical microcarriers exist in a wide range of sizes. The radius of non-porous microbeads is usually around 75 μm[1]. The production of very small microbeads

[1] Porous microbeads are typically larger than non-porous microbeads, as the former can also accommodate cells inside the bead.

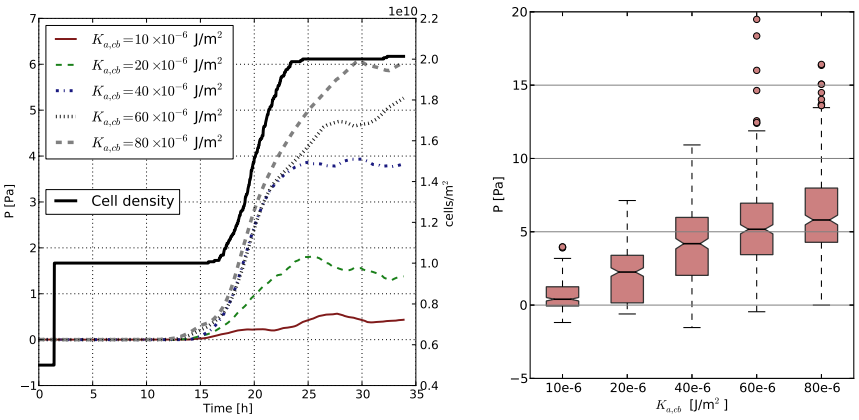

(a) (b)

Figure 2.6: **(a)** Temporal evolution of mean stress level $\bar{P}$ in simulated microcarrier cell expansion for different cell-substrate adhesion values. The cell densities are initially identical, and remain nearly the same because of the identically applied growth law. **(b)** Boxplot for stress levels P on cells for different cell-bead adhesion values. The stress distribution was assembled around the peak mean stress $\bar{P}$, i.e. at confluency ($\pm$500 s). The effect of cell-bead adhesion on stress distribution is significant (Kruskal-Wallis one-way analysis of variance $p < 0.001$).

is more difficult because technical limitations exist for reducing the diameter of the extrusion device (personal communication from Dr. Y.-C. Chai, KU Leuven). In this study, simulations were performed to investigate the effect of microbead size on the mechanical micro-environment. Only the lower range of microbeads is being considered because computational limitations make simulations of large beads containing a very large number of cells very time-consuming. The radii of the beads were varied between 15 μm and 75 μm. The effect of microbead size on the mechanical micro-environment is summarized in Fig. 2.8. Since we are investigating size dependency, artifacts stemming from all cells having the same size should be avoided. Therefore we use asynchronous cell cycles (see section 2.3.4).

Large bead sizes correspond to a larger increase in $\bar{P}$ when the cells reach confluency on the microcarrier. As the bead size (indicated by the bead radius R_b) increases, the temporal evolution of the mechanical stress starts becoming more similar. Not only $\bar{P}$ increases with bead size, but also the stress heterogeneity H_p, as can be observed in Fig. 2.8(b).

An explanation for the increase in $\bar{P}$ for higher values of R_b can be given from purely geometric effects: when the curvature of the substrate gets larger, cells have more space

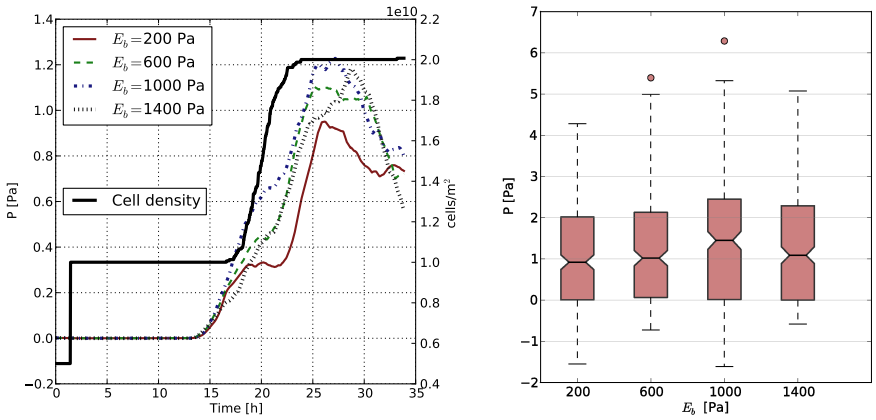

Figure 2.7: **(a)** Temporal evolution of mean stress level $\bar{P}$ in simulated microcarrier cell expansion for different microbead Young's moduli E_b. The cell densities are initially identical, and remain nearly the same because of the identically applied growth law. **(b)** Boxplot for stress levels P on cells for different values of E_b. The stress distribution was assembled around the peak mean stress $\bar{P}$, i.e. at confluency ($\pm$500 s). The effect of E_b on mechanical stress distribution is not significant (Kruskal-Wallis one-way analysis of variance $p > 0.001$).

to grow "outwards" from the bead and by doing that release built up mechanical stress, i.e. the cell are less compressed since there is more space available. This explanation is consistent with the observation that the temporal evolution of the mechanical stress seems to asymptotically approach a maximum. As the curvature of the substrate decreases, the available space into which the cells can grow decreases until it approaches the flat plane.

2.3.4 Effect of cell cycle synchronization on the mechanical environment

Although cells used in *in vitro* cell expansion typically exhibit some degree of cell cycle synchronization, cell cycles are initially never perfectly synchronized. In the simulations however, the perfectly synchronized cells will undergo their first cytokinesis all at the same time, resulting in a step-wise increase in cell number (e.g. Fig. 2.3). In order to investigate the effect of cell synchronization and to assess how much this initial step increase in cell number would affect the mechanical micro-environment, simulations were performed with varying degrees of initial cell cycle synchronization.

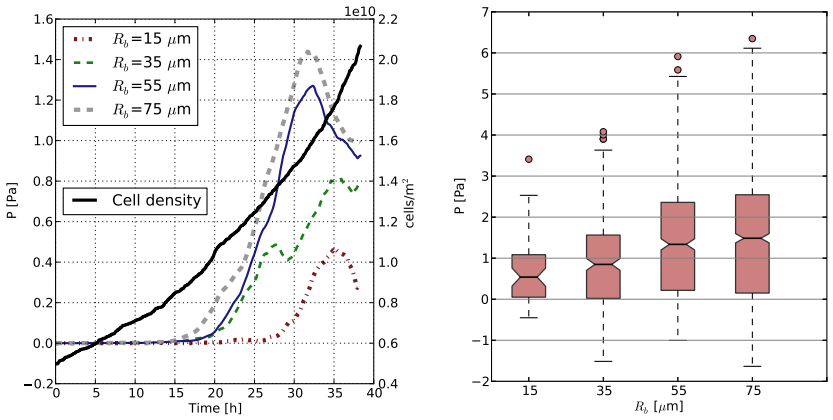

(a) (b)

Figure 2.8: **(a)** Temporal evolution of mean stress level $\bar{P}$ in simulated microcarrier cell expansion for different microbead radii R_b. The cell densities are initially identical, and remain nearly the same because of the identically applied growth law. For clarity reasons, cell density is shown for $R_b = 75\mu$m only. **(b)** Boxplot for stress levels P on cells for different bead radii. The stress distribution was assembled around the peak mean stress $\bar{P}$, i.e. at confluency ($\pm$500 s). The effect of R_b on mechanical stress distribution is significant (Kruskal-Wallis one-way analysis of variance $p < 0.001$).

In the extreme case it was assumed that the cell cycles are completely asynchronous. This implies that the number of cells initiating cytokinesis is constant over time. In order to achieve this, the initial cell radii were randomly chosen from a uniform distribution between r_o, the initial radius of the cells just after cytokinesis, and $r_{\max}$, the cell radius at which cells will initiate cytokinesis. Cell cycles can also be partially desynchronized. In this case, the initial cell radii were randomly chosen from a normal distribution around $(r_o + r_{\max})/2$. The standard deviation on this normal distribution, σ, is a measure for how asynchronous the initial cell cycles are. Low values of σ indicate strongly synchronized cell cycles, and high values indicate asynchronous cell cycles.

The results of these simulations are summarized in Fig. 2.9. For the normal distribution with $\sigma = 0.05$ μm, the cell cycles are still strongly synchronized. In the case of $\sigma = 0.15$ μm, the cell cycles are partially synchronized, and for the uniform distribution on the initial radii, the cell cycles are completely asynchronous. As the cell cycles become more asynchronous, the growth curve changes from stepwise increases to a continuous exponential-looking curve. The temporal evolution of the mean mechanical stress $\bar{P}$ changes when the initial cell cycles become more asynchronous, but the magnitude of the mean stress does not change significantly. In Fig. 2.9(b), the stress distribution around the peak mean stress $\bar{P}$ is shown for different levels of initial cell

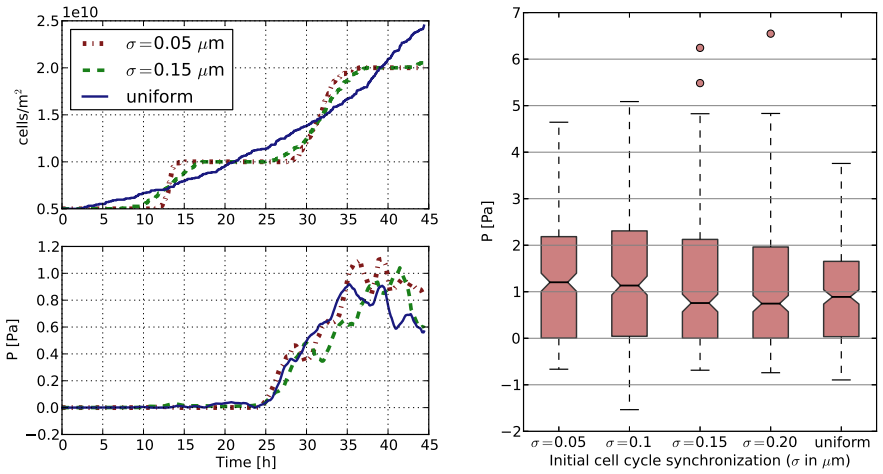

(a) (b)

Figure 2.9: **(a)** top: Temporal evolution of cell number and bottom: temporal evolution of mean stress level $\bar{P}$ in simulated microcarrier cell expansion for different levels of initial cell cycle synchronization. Partially synchronized cells have a mean initial radius of 5.25 μm $\pm$ a given standard deviation σ. Large values of σ indicate more asynchronous cell cycles. In the extreme case — a uniform distribution between $r_{\min}$ and $r_{\max}$ — the cell cycles are completely asynchronous. **(b)** Boxplot of the distribution of P around the peak mean stress $\bar{P}$ ($\pm$500 s) for different levels of cell cycle synchronization. The effect of cell cycle synchronization on mechanical stress distribution is not significant (Kruskal-Wallis one-way analysis of variance $p > 0.001$).

cycle synchronization. No significant difference between the calculated means ($\bar{P}$) and heterogeneity H_p was observed.

2.3.5 Comparison to experimental stress determination

Direct measurements of intercellular forces for cells cultured on microbeads have not been reported so far in the literature. Current cell mechanical techniques allow to measure mechanical properties of single cells, adhesion energies between a cell and a substrate and adhesion energy between two cells. In fact, data from such measurements was used as input for corresponding model parameters (see Table 2.1). Traction force microscopy (TFM) allows to measure forces exerted by a single cell on a deformable substrate. The technique has recently been extended to also estimate intercellular forces within a cell monolayer. To this extent, the monolayer is considered as a

continuous material with a given thickness, on which tractional forces (as measured by TFM) act as external forces. By solving a stress balance for each cell with the monolayer, intercellular forces can be estimated [187, 206]. The authors reported intercellular stresses up to 300 Pa during collective cell migration of epithelial as well as endothelial monolayers. Although challenging, one may think of extending this technique to monolayers on spherical surfaces, in this way providing a means to validate the simulated intercellular stresses. Such techniques may be complemented by means of genetically encoded molecular force sensors that rely on force-induced Förster Resonance Energy Transfer (FRET). Such FRET sensors are able to measure forces in the 1-10 pN range and can be inserted into specific proteins that are e.g. part of the cytoskeleton or adhesion complexes [228]. Such a sensor has been recently developed and applied to measure actomyoson-generated tensional forces exerted on the cytoplasmic part of E-cadherin cell-cell adhesion receptors [14]. One should notice though that cytoskeleton-generated tensional forces are at the heart of all these techniques. As these have not been incorporated yet in our model, it presents a limitation for the applicability and experimental validation of our current modeling approach.

It must be emphasized that the mechanical stress values P obtained by our simple measure are useful to compare mechanical stress between different cells in the same aggregate and between similar aggregates, but cannot be directly compared to actual local mechanical stress on the cell membrane due to cell-cell or cell-substrate contact. The measure for the mechanical stress P used throughout the present work is normalized using the complete cell's surface area. The local JKR contact areas would be an equally arbitrary normalization choice, since the JKR model regards only passive deformation of the cells and can not account for active cytoskeletal remodeling. If that choice were taken, stress levels would be higher by a factor relating the sphere-surface area to the typical JKR contact area. In our simulations, for a typical cell surrounded by other cells, this local cell stress level is around 200 times higher (using the force and effective JKR contact area for a single contact) than the measure P and therefore in the order of 100 Pa.

2.4 Conclusion and Outlook

In this chapter, an individual cell-based model of cell expansion on spherical microcarriers was described. The aim was to investigate how the mechanical micro-environment of the cell is influenced by the mechanical and geometrical properties of the carrier system. This was achieved by considering a simplified theoretical model, excluding biological differences between the cells. The study gives a proof of principle that theoretically, large biological heterogeneity is not required for a strongly heterogeneous micro-environment. As cell behavior and cell fate are

strongly influenced by the mechanical micro-environment, one can assume that a large phenotypic heterogeneity might occur purely due to spatial and mechanical phenomena. Simulations revealed that a substantial heterogeneity of mechanical stresses can be expected, even for a completely homogeneous cell source. As strongly adhering cells expand on a microbead, compressive stresses gradually build up and will peak when the proliferating cells reach confluency.

The geometric and mechanical properties of the microbead play a major role in determining the mechanical stresses on individual cells. Adhesive properties of the bead — determined by the surface coating that is applied — strongly influence the mechanical stress levels after confluency. On the other hand, the Young's modulus of the beads has a minor direct influence on the mean mechanical stress levels or stress heterogeneity. In vitro experiments have demonstrated that depending on the cell type in question, a stiffer substrate increases cell-tension [40], and cell tension can be directly related to cell stiffness as well [226]. Thereby cell stiffness can be increased by increased substrate stiffness [207]. As we demonstrated that intercellular stress levels were sensitive to the cells' Young's modulus, substrate stiffness may therefore have an indirect effect on stress levels, which is not captured in the present work.

The size of the microbead is expected to strongly affect the mechanical micro-environment of the cells as well. We hypothesize that this can be explained mainly from purely geometrical effects: as the curvature of the surface on which the cells grow increases, the cells can more easily detach from the substrate when they compete for space on the carrier. By doing that, the mechanical stresses that were built up can be dissipated and the mean stress level will be lower.

Additionally, we looked at the effect of the amount of cell cycle synchronization on mechanical stress. Although a slightly different temporal evolution of $\bar{P}$ was observed, the mean stress levels around confluency are not significantly different for different levels of cell cycle synchronization. Cell seeding, as shown in Fig. 2.4, does not influence $\bar{P}$ or H_p at confluency.

The benefit of the model lies in a quantification of the mechanical microenvironment for which at this stage an experimental alternative is hard to find. The importance of mechanics for cell fate is beyond any doubt, meaning that in the long term we hope to be able to relate the mechanical findings to cell behavior (e.g. in terms of proliferation and differentiation). It is clear that there is still a long way to go for the valorization of such models in e.g. a tissue engineering context, which again would require some sort of experimental validation on the biological meaningfulness of the calculations. Interestingly, FRET sensors, have also been used to study mechanics-induced activation of specific kinases that are involved in mechanotransduction, such as Src [145, 227]. One could envision that in the future cell generated forces, such as intercellular forces that arise during expansion, could be related to intracellular molecular events that are indicative for e.g. cell differentiation.

In order to further characterize how inter-cellular interactions in three-dimensional aggregates influence cell fate, we believe an integrative modeling approach should be developed. In this approach, mechanical and biochemical signaling should be both considered, as well as the spatial properties of the cellular system. This study proposes a framework for modeling cell aggregates at the individual cell level. The focus in this platform is the explicit description of cells as interacting agents in a three-dimensional environment. The time dependent behavior of these agents is not based on empirical "rules" but on physical forces acting on the cells. Although the presented model mainly focuses on cell mechanics and only includes biological aspects of the system in a rudimentary way, cell metabolism and signaling must be included in the future. Ultimately, meso-scale cellular models will combine the simulated conditions at the cell boundary with changes in cell behavior, and by doing that, eventually predict how cell fate is regulated in cellular aggregates.

Acknowledgements

This work is part of Prometheus, the Leuven Research & Development Division of Skeletal Tissue Engineering of the Katholieke Universiteit Leuven: www.kuleuven.be/prometheus.

Bart Smeets acknowledges the *Agency for Innovation by Science and Technology in Flanders (IWT)* for financial support.

Chapter 3

Mechanistic contact model for arbitrary rounded shapes

Adapted from [194]:

Smeets, B., Odenthal, T., Keresztes, J., Vanmaercke, S., Van Liedekerke, P., Tijskens, E., Saeys, W., Van Oosterwyck, H., Ramon, H. (2014). Modeling contact interactions between triangulated rounded bodies for the discrete element method. Computer Methods in Applied Mechanics and Engineering, 277, 219-238.

3.1 Introduction

A correct model of particle shape in the discrete element method (DEM), is not only a model that approximates the volume taken up by the particle, but also the normal direction at each point on the particle's surface. The latter is crucial for calculating correct contact forces as it determines the direction of both normal and tangential contact forces. Classical contact theories such as the Hertz model [83] impose a third requirement: the radius of curvature at the point of contact. From the perspective of DEM, the most straightforward particle shape is a perfect sphere[1]. The normal direction at a given contact point is trivial to calculate and the radius of curvature is directly given by the sphere's radius.

Representing arbitrary particle shapes in DEM while accounting for these three requirements remains a challenge. Various other shape models have been used, such as ellipsoids [170, 234, 239], poly-ellipsoids [160], superquadric surfaces [166,

[1] or a disk in two dimensions

230], polyhedra [52, 164] and convex bodies [224]. These more complex shape descriptions allow for DEM simulations of a wide range of non-spherical particles. However, calculating contact properties and contact forces in general requires extensive computational effort. Furthermore, formulations for obtaining proper contact forces can not always be directly related to mechanistic contact theories, nor to the intrinsic mechanical properties of the particle, such as the Young's modulus. In the case of two contacting polyhedra, the overlapping volume can be assumed to be proportional to the stored elastic energy, but deriving an appropriate contact force from this energy requires classification between various types of contact [164].

Another approach for representing arbitrary shapes is by making use of composite geometries: multiple shape primitives are connected in a rigid or non-rigid fashion to approximate more complex geometries [49]. By connecting spheres of various sizes, the volume as well as the surface normal direction of arbitrary smoothed shapes can be accurately represented, if the spheres are chosen carefully [53, 127]. The local curvature, however, cannot be correctly accounted for as constraints on the sphere size can be imposed by the volume representation. Also, the approximation is made that the local curvature is spherical, where in reality the principal radii of curvature are not necessarily equal and can even be negative. Because of this, locally linearized contact force models are often used. Furthermore, adjustments have to be made to account for the occurrence of multiple simultaneous contacts between two particles, which otherwise may lead to non-physical collision behavior [89, 132].

In this work, a new way of representing arbitrary particle shapes in DEM is presented. By accounting for the volume, as well as the normal direction and the local average curvature, it tries to improve on the method of sphere composites. The new shape model is introduced based on the Hertz model for the contact between elastic spheres. In principle, Hertz-like models can describe contact between smooth surfaces – even with cusps – almost exactly in an asymptotic sense. Surfaces with asperities will fail only if the Hertz model itself breaks down.

Section 3.2 details how contact forces between triangulated rounded bodies can be calculated for DEM simulations. In Section 3.3, the model is first validated by showing convergence upon mesh refinemenent towards the Hertz solution for spherical bodies. Next, the error made in contact force calculation for non-spherical curvatures is estimated and the model is compared to an indentation experiment of a pear-shaped object. Finally, an example DEM simulation is given where gravitational packing is compared for spheres, meshed spheres, pear-shaped and gummy bear-shaped objects.

3.2 Model description

The purpose of this work is to demonstrate a new method for modeling arbitrary shapes in DEM. The solution is derived from classical contact theory and based on the following ideas:

1. The arbitrary shape is represented as a triangulated surface. Each triangle in this surface has a well-defined local curvature (see Section 3.2.1). Therefore, each triangle can be associated with a unique spherical surface that has the local radius of curvature as radius and intersects with all three triangle points.
2. For each contact candidate an effective overlap distance is calculated. If the effective overlap distance is positive, a non-zero contact force can be expected (see Section 3.2.3).
3. Contact forces are determined by explicitly integrating the pressure from classical Hertz contact theory over the contact area between two rounded shapes (see Section 3.2.4).

3.2.1 Local curvature of a triangulated surface

Each point on a smooth rounded surface can be characterized by two principal radii of curvature. As fitted spheres are used, the assumption is made that the principal radii of curvature are equal. This forms one of the major drawbacks of the method, as an error is made for strongly anisotropic curvatures (see Section 3.3.2). In principle, both radii of curvature can be calculated on a triangulated surface mesh [65, 180]. For obtaining only the mean radius of curvature at a node i of the triangulation, the Laplace-Beltrami operator $\mathbf{K}$ suffices [139]:

$$\mathbf{K}(\mathbf{x}_i) = \frac{1}{2\mathcal{A}_i} \cdot \sum_{j \in \mathcal{N}_i} \left[\cot(\alpha_{ij}) + \cot(\beta_{ij})\right](\mathbf{x}_i - \mathbf{x}_j)\,. \tag{3.1}$$

Its L^2-norm is twice the mean curvature, while it points to the outward direction at this node. The variables in Eq. (3.1) are defined in Fig. 3.1(c) and the sum runs over all first order neighbors of node i, which are shown in the figure. The radius of curvature of a triangle is calculated as the mean curvature of the three corner points, each weighted by their corresponding Voronoi region in the triangle.

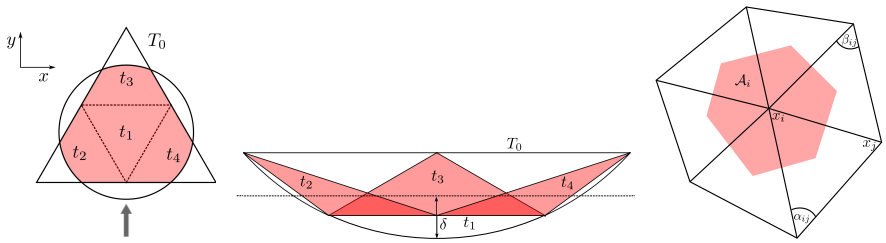

(a) Top view (b) Side view (c) Curvature calculation

Figure 3.1: Geometrical properties of triangulations with local curvatures. The top view **(a)** indicates the line of sight of the side view **(b)**. **(c)** The contact between two shapes is calculated from encompassing spheres over the triangles with a radius of curvature that matches the local surface curvature. The drawing provides the geometrical definition of the Voronoi region area $\mathcal{A}_i$, angles α_{ij}, β_{ij} and points $\mathbf{x}_i, \mathbf{x}_j$ as used in Eq. (3.1).

3.2.2 Pressure formulation of Hertz contact force

For a spherical asperity in contact with a flat elastic half-space, the elastic Hertz pressure associated with a contact of radius a is given as:

$$p_{H,e}(r) = \frac{2\hat{E}}{\pi\hat{R}}\sqrt{a^2 - r^2}, \tag{3.2}$$

with $\hat{R}$ and $\hat{E}$ as defined in Eq. (2.4). Assuming a spherical asperity – and therefore a circular contact area – the total Hertz force can be calculated by integrating Eq. (3.2) over the complete circular contact surface Ω with radius a:

$$F_H = \iint_{\Omega} p_{H,e}(r)\, d\Omega = \frac{4\hat{E}a^3}{3R}, \tag{3.3}$$

Finally, a can be written as a function of the indentation or overlap δ in Hertz' approximation:

$$a = \sqrt{\delta\hat{R}}, \tag{3.4}$$

yielding an often used formula for calculating elastic sphere-sphere or sphere-plane interaction forces:

$$F_H = \frac{4\hat{E}\sqrt{\hat{R}}}{3}\delta^{3/2}. \tag{3.5}$$

This result has been generalized to include damping forces for the contact between viscoelastic particles [164]:

$$F_H = \frac{4\hat{E}\sqrt{\hat{R}}}{3}(\delta^{3/2} + \hat{A}\dot{\delta}\sqrt{\delta}), \tag{3.6}$$

with $\hat{A} = \frac{1}{2}(A_i + A_j)$ the combined damping constant and $\dot{\delta}$ the relative normal velocity between particle i and j. The dissipative pressure $p_{H,d}(r)$ associated with the damping force is then [18]:

$$p_{H,d}(r) = \frac{3\hat{A}\dot{\delta}\hat{E}}{\pi a^2}\sqrt{a^2 - r^2}. \tag{3.7}$$

The total Hertz pressure including normal damping can then be written as:

$$p_H(r) = p_{H,e}(r) + p_{H,d}(r) = \frac{\hat{E}}{\pi}\sqrt{a^2 - r^2}\left(\frac{3\hat{A}\dot{\delta}}{a^2} + \frac{2}{\hat{R}}\right). \tag{3.8}$$

The method demonstrated here uses this pressure formulation of Hertzian contact.

3.2.3 Geometrical contact properties

An effective overlap distance (δ_{eff}) is determined for each pair of triangles selected by the contact detection algorithm (e.g. [63, 79, 82, 140, 144, 149, 210]). If δ_{eff} is larger than zero, a non-zero contact force can be expected. For two spheres i and j with radii r_i and r_j the overlap distance δ is given by:

$$\delta_{\text{eff}} = r_i + r_j - d_{ij}, \tag{3.9}$$

where d_{ij} is the distance between the centers of sphere i and j. Determining the overlap distance between two spheres is trivial, but for rounded triangles, the additional constraint is imposed that the effective contact point $\mathbf{c}_{\text{eff}}$ has to be within the projected triangle in the contact plane. As δ_{eff} is measured going through $\mathbf{c}_{\text{eff}}$, it is different from the simple sphere-sphere overlap distance. The calculation of the effective overlap distance and contact point between two triangles belonging to distinct rounded bodies is explained in A.1. The solution for the simpler case of contact between a triangle from a rounded body and a plane can be easily inferred from this.

Furthermore, an intersection polygon S is constructed (see Fig. 3.2). For contact between a triangle and a sphere, this polygon is simply the projection of the triangle on the contact plane. For contact between two rounded triangles, or a rounded triangle and a finite plane, the polygon is constructed as the intersection between the projected triangle(s) or plane on the contact plane.

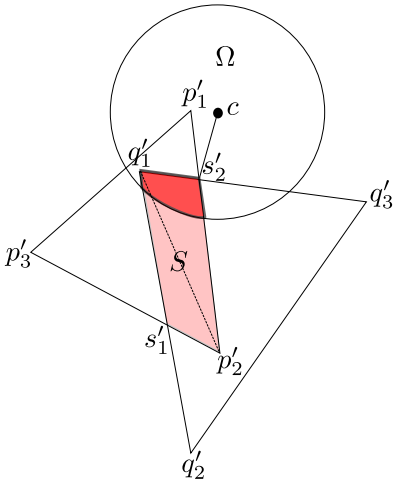

Figure 3.2: Intersection S (in light red) of projected triangles $P' = \{p'_1, p'_2, p'_3\}$ and $Q' = \{q'_1, q'_2, q'_3\}$. The triangle-triangle contact area (in dark red) is the intersection between S and the circle Ω with radius a – see Eq. (3.4).

3.2.4 Normal contact force calculation

If the effective overlap distance is positive, a non-zero contact force can be expected. The intersection polygon (S_{12}, see Section 3.2.3) is either already a triangle or can be trivially subdivided into N_S triangles by connecting one corner point with all edges (see Fig. 3.2). For reasons of computational efficiency, two regimes are distinguished: In the first case, the contact area between the encompassing spheres is a large fraction of the area of the intersection triangle A_j – see below, Eq. (3.13). In this case, a relatively big, well established contact between the two surfaces can be assumed. The contact force is obtained by integrating the Hertz pressure in Eq. (3.8) over the contact area. This integral is approximated using quadrature rules for numerical integration in each j-th sub-triangle of S_{12}. For integrating any function f over a triangle surface A_j, the approximation is of the following form [28, 237]:

$$\iint_{A_j} f(\alpha, \beta, \gamma)\, dA \approx A_j \sum_{i=1}^{N} w_i f(\alpha_i, \beta_i, \gamma_i), \tag{3.10}$$

in which α, β and γ are barycentric coordinates inside the j-th triangle, and w_i are the weights assigned to each quadrature point i.

To calculate both forces and moments caused by a specific pressure/traction in a triangle, the coordinates of the integration test points are determined first.

Using Eq. (3.10) the weighed sum is evaluated, thus approximating the surface integral for the normal contact force on a triangle:

$$\mathbf{F}_n^{\Delta} = \sum_{j=1}^{N_S} \sum_{i=1}^{N_Q} A_j w_{j,i} p\left(r_{j,i}\right) \hat{\mathbf{n}}_{12}, \tag{3.11}$$

where $p\left(r_{j,i}\right)$ is the normal contact pressure according to Eq. (3.8), and $\hat{\mathbf{n}}_{12}$ is the contact normal unit vector – normal to the contact plane and in the direction of the encompassing sphere belonging to rounded body p_2. N_Q is the number of quadrature points and N_S is the number of sub-triangles in S.

The pressure $p\left(r_{j,i}\right)$ is evaluated in the positions corresponding to those quadrature points. Additionally, the moments of each individual force component with respect to the center of the contact plane are summed up:

$$\mathbf{M}_n^{\Delta} = \sum_{j=1}^{N_S} \sum_{i=1}^{N_Q} A_j w_{j,i} p\left(r_{j,i}\right) \mathbf{r}_{j,i} \times \hat{\mathbf{n}}_{12}. \tag{3.12}$$

To ensure sufficient precision at an adequate speed, a 16-point quadrature rule of degree eight [237] is still acceptably fast, since calculations only take place for triangles for which contact has been ascertained.

If the area of contact between the two encompassing spheres is relatively small compared to the typical area of each integration point a bad approximation for force and moment can be expected. Therefore, a different approach is chosen: The integrated Hertz force – Eq. (3.6) – calculated from the total area of contact of the encompassing spheres can be scaled with $A_{S\cap\Omega}/A_{\Omega}$, which is the fraction of the circular contact surface Ω contained in the intersection S of the two triangles (see Fig. 3.2). This total force is then applied to the contact point c, if the point is within the triangle's intersection, or the point closest to it in that intersection polygon. In this case, the moment is still calculated according to Eq. (3.12), although the sum only contains the one force and radius vector. The following criterion is used to decide whether the direct force calculation method is sufficient:

$$\pi a^2 < \gamma \frac{A_j}{N_Q}, \tag{3.13}$$

where γ is the expected number of integration points that are within the contact circle (in the simulations, γ=10).

This second approximation for the forces and the moments one triangle of the body is subject to, is insufficient for bigger overlaps, because the moments generated by the normal pressures described in Eq. (3.8) differ profoundly from that simple approximation. For small overlaps, it is obvious from Eq. (3.12) that the moment is close to $\mathbf{0}$ since the lever length $\mathbf{r}$ is very short, anyway.

3.2.5 Transfer of normal forces and moments to the degrees of freedom

The forces and moments for each triangle are first transferred to the nodes (corners) of the triangle. The reason for this is that it allows to express triangle forces and moments as pure forces at the nodes in a mechanically equivalent fashion. The moment-vector necessarily lies in the contact plane, since the force is defined to be normal to this plane. Let the contact plane without loss of generality be the x-y plane. This implies that $\|\mathbf{F}_n^{\Delta}\| = F^{\Delta z}$ and the position vectors of the $i = (1,2,3)$ nodes w.r.t. the Hertz contact point are $\mathbf{r}_{n_i} = \left(r_{n_i}^x, r_{n_i}^y, 0\right)$. Then, the system of equations can be conveniently written as

$$\left(\begin{array}{rcrcrcl} r_{n_1}^y \cdot F_{n_1}^z & + & r_{n_2}^y \cdot F_{n_2}^z & + & r_{n_3}^y \cdot F_{n_3}^z & = & M^{\Delta x} \\ -r_{n_1}^x \cdot F_{n_1}^z & - & r_{n_2}^x \cdot F_{n_2}^z & - & r_{n_3}^x \cdot F_{n_3}^z & = & M^{\Delta y} \\ F_{n_1}^z & + & F_{n_2}^z & + & F_{n_3}^z & = & F^{\Delta z} \end{array}\right). \tag{3.14}$$

This system can be inverted to find the correct forces on the nodes of the triangle. These point forces are directly transferred to forces and moments acting on the center of mass $\mathbf{x}_{p_1}$ of rounded body p_1:

$$\mathbf{F}_{p_1} = -\sum_{i=1}^{3} F_{n_i}^z \hat{\mathbf{n}}_{12} \tag{3.15}$$

$$\mathbf{M}_{p_1} = -\sum_{i=1}^{3} F_{n_i}^z [(\mathbf{x}_{n_i} - \mathbf{x}_{p_1}) \times \hat{\mathbf{n}}_{12}] \tag{3.16}$$

with $\mathbf{x}_{n_i}$ the position of corner node i in rounded body p_1. Using the nodes in rounded body p_2 and $\hat{\mathbf{n}}_{21} = -\hat{\mathbf{n}}_{12}$, the same method can be applied to obtain the forces and moments on rounded body p_2. It should be noted that the forces and moments on the center of mass of each rounded body can as well be obtained directly – see further in section 4.2.5. However, Eq. 3.14 allows to compute equivalent (pure) forces on each node of the rounded body, which is useful for estimating the stress in each particle, or for describing deformable bodies (see chapter 5).

3.2.6 Tangential forces

To keep matters simple, only dissipative forces are addressed here, and not elastic forces. A simple, widely used Coulomb-friction model was adapted for arbitrary rounded bodies. More complex friction models can be implemented analogously. For

contact between spheres, the two-parameter Coulomb friction force $\mathbf{F}_t$ can be written as [73, 164]:

$$\mathbf{F}_t = -\min(c\,\|\mathbf{v}_t^{\mathrm{r}}\|, \mu\,\|\mathbf{F}_n\|)\frac{\mathbf{v}_t^{\mathrm{r}}}{\|\mathbf{v}_t^{\mathrm{r}}\|}, \tag{3.17}$$

in which c is a viscous damping constant, μ the Coulomb friction coefficient, $\mathbf{F}_n$ the total normal contact force between the spheres and $\mathbf{v}_t^{\mathrm{r}}$ the tangential relative contact velocity.

This formulation has been modified to describe tangential contact forces between contacting rounded triangles. In the sliding regime, the Coulomb friction force $\mathbf{F}_t^{\triangle}$ is calculated as:

$$\mathbf{F}_t^{\triangle} = -\mu\left\|\mathbf{F}_n^{\triangle}\right\|\frac{\mathbf{v}_t^{\mathrm{r}}}{\|\mathbf{v}_t^{\mathrm{r}}\|}, \tag{3.18}$$

where $\mathbf{F}_n^{\triangle}$ is the normal contact force for the given triangle as given in Eq. (3.11). As the sum of all the normal forces $\mathbf{F}_n^{\triangle}$ equals the total normal force of the object $\mathbf{F}_n$, the sliding friction forces will sum up to the total friction force $\mathbf{F}_t$. In the no-slip regime, the tangential force for a triangle is written as:

$$\mathbf{F}_t^{\triangle} = -c\frac{A_{S\cap\Omega}}{A_{\Omega}}\mathbf{v}_t^{\mathrm{r}}. \tag{3.19}$$

In other words, for each contacting triangle, the viscous damping force is weighted with the fraction of the total contact area that is inside the intersection polygon (see also Fig. 3.2). This ensures that the total tangential damping force of the contacting rounded bodies equals $-c\,\mathbf{v}_t^{\mathrm{r}}$.

The slipping threshold for the Coulomb friction model is based on the total normal force $\mathbf{F}_n$ of the two bodies in contact. In order to avoid having to recompute the contact iterations for the whole body, we approximate $\mathbf{F}_n = \mathbf{F}_n^{\mathrm{Hertz}}$ as the Hertz force for a given sphere-sphere overlap – Eq. (3.6). The criterion for sliding then becomes:

$$c\,\|\mathbf{v}_t^{\mathrm{r}}\| > \mu\,\|\mathbf{F}_n\|\,. \tag{3.20}$$

The friction force is acting on the effective contact point $\mathbf{c}_{\mathrm{eff}}$ – see Appendix 1 – between the two rounded triangles and contributes to forces and moments on the center of mass $\mathbf{x}_{p_1}$ of rounded body p_1 as

$$\mathbf{F}_{p_1} = -\mathbf{F}_t^{\triangle} \tag{3.21}$$

$$\mathbf{M}_{p_1} = -(\mathbf{c}_{\mathrm{eff}} - \mathbf{x}_{p_1}) \times \mathbf{F}_t^{\triangle} \tag{3.22}$$

The forces and moments on the center of mass of rounded body p_2 can be obtained analogously, by using the opposite tangential relative contact velocity.

3.2.7 Equation of Motion

The Euler equations of motion for each body p with position vector $\mathbf{r}_p^{\text{dof}}$ and angular velocity $\mathbf{w}_p^{\text{dof}}$ can be written as:

$$m_p \frac{\partial^2 \mathbf{r}_p^{\text{dof}}}{\partial t^2} = \sum \mathbf{F}_p^{\text{dof}} \tag{3.23}$$

$$\hat{\mathbf{I}}_p \frac{\partial \mathbf{w}_p^{\text{dof}}}{\partial t} + \mathbf{w}_p^{\text{dof}} \times (\hat{\mathbf{I}}_p \mathbf{w}_p^{\text{dof}}) = \sum \mathbf{M}_p^{\text{dof}} \tag{3.24}$$

in which $\hat{\mathbf{I}}_p$ is the tensorial moment of inertia in the inertial frame. A leap-frog scheme is used to integrate these equations of motion.

3.3 Results and Discussion

3.3.1 Comparison with perfect sphere

In this section, we show that the approach for computing contact forces on triangulated rounded shapes (see Section 3.2) converges to the known Hertz solution for a spherical shape. For this, a mesh was obtained by subdividing an icosahedron and projecting the nodes on a unit sphere [219] – an example of a threefold subdivided icosahedron is shown in Fig. 3.4(a). In a subdivision, each triangle gets split into four triangles as is illustrated in Fig. 3.1. Here, it is shown how one triangle with an encompassing sphere matching the local curvature of the body is split into four triangles. Since the local curvature is kept, the new triangle nodes are all located on the surface of the same encompassing sphere. Every subdivision of an icosahedron has only twelve nodes with a five-fold connectivity and slightly longer distances to their neighbors; otherwise, the mesh is perfectly regular with six-fold connectivity and is ideal for curvature calculations (see Section 3.2.1) as reported by [233]. The contact forces are compared both in the static and the dynamic case.

Static comparison

Let us bring a meshed sphere in contact with a plane and vary the overlap distance δ. The calculated contact force is then compared with the force according to Hertz theory, Eq. (3.5). The resulting force-indentation curve is shown in Fig. 3.3 with N = 48, 162, 642 the number of nodes in a respectively one-fold, two-fold and three-fold subdivided icosahedron. As can be seen in this curve, the calculated force approaches the Hertz solution quickly as the meshed sphere becomes more refined.

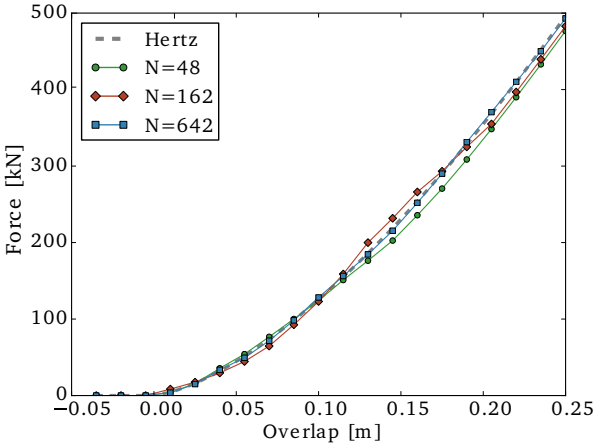

Figure 3.3: Normal elastic force as a function of overlap distance. The normal force is calculated using integration of the Hertz contact pressure over the contact area of a triangulated sphere using different levels of mesh refinements, and is compared to the analytical solution according to Hertz theory.

A more in-depth investigation of the convergence is shown in Fig. 3.4. Here, not only the mesh refinement was varied, but also the level of mesh distortion. The regular mesh based on icosahedron subdivision was artificially distorted by randomly dislocating the nodes and projecting the newly found points back on the spherical surface. The level of mesh distortion is quantified in the parameter D:

$$D = \frac{\sigma(A^{\triangle})}{\langle A^{\triangle} \rangle}, \tag{3.25}$$

which is the ratio of the standard deviation of the triangle areas and the mean triangle area. As D becomes large, the mesh becomes highly irregular – see Fig. 3.4(a). The correspondence with the Hertz solution is quantified by calculating the Normalized Root Mean Square Error (NRMSE) between the Hertz force and the force calculated for the meshed sphere. Fig. 3.4(b) shows the change in NRMSE with mesh refinement for three distinct cases of mesh distortion. Here, the radius of curvature of each triangle was prescribed to be the sphere radius. The solution converges very quickly when the mesh gets more refined, and there is no clear negative effect of the mesh distortion. For Fig. 3.4(c), on the other hand, the radius of curvature was not prescribed, but calculated as described in Section 3.2.1. Only for heavily distorted meshes ($D = 0.7$), the calculated radius of curvature strongly differs from the sphere's radius, giving rise to a large error in the contact force.

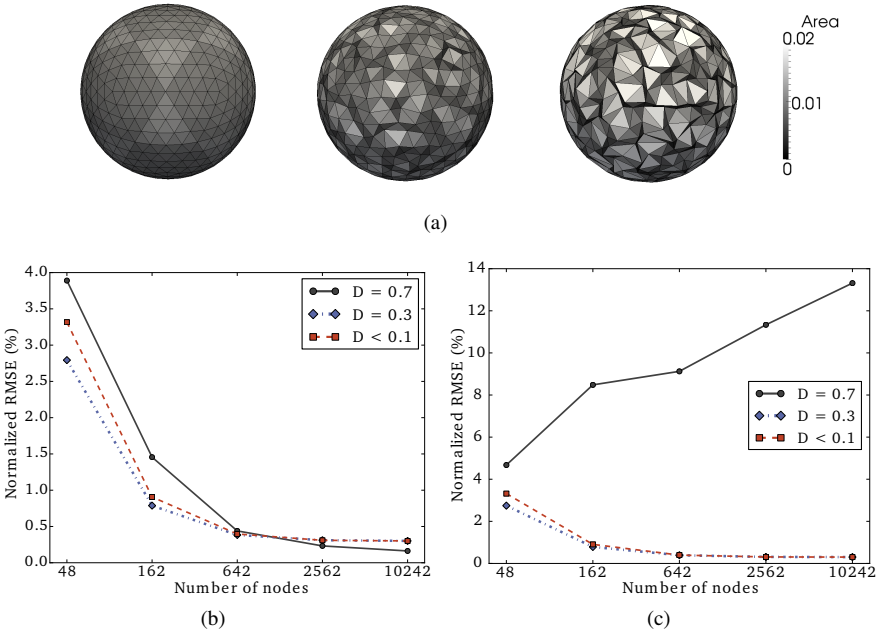

Figure 3.4: Influence of mesh distortion D on convergence of static contact force calculation for different mesh refinements. (a) Mesh of subdivided icosahedron with different levels of mesh distortion D. (b) Change in Normalized Root Mean Square Error (NRMSE) between model and Hertz solution with mesh refinement for different levels of mesh distortion. Triangle curvatures have been set to the curvature of the sphere (=1 m^{-1}). (c) same as (b), but the curvatures of each triangle are calculated according to Section 3.2.1, yielding large errors in curvature for distorted meshes, and corresponding large NRMSE in the contact force calculation.

Dynamic comparison

In order to compare the time dependent behavior with the reference of a perfect sphere the following simple test was constructed: a sphere is dropped from a distance on a flat plane and the height of the sphere is calculated as it bounces on the plane. In Fig. 3.5(a) the change in height is shown over time. The meshed sphere solution corresponds closely to the Hertz solution. For a more refined mesh, the difference remains low even after multiple contact events. Because of contact damping forces, energy is lost each time the sphere hits the plane. The dissipated energy can be easily calculated by comparing the loss in potential energy $\Delta E_p = mg\Delta h$ whenever the sphere reaches its maximal height and has a velocity of zero. The dissipated energy per contact event is shown in Fig. 3.5(b). The NRMSE between the Hertz solution and the solution for a

meshed sphere is calculated from the energy loss curve and shown in Fig. 3.5(c).

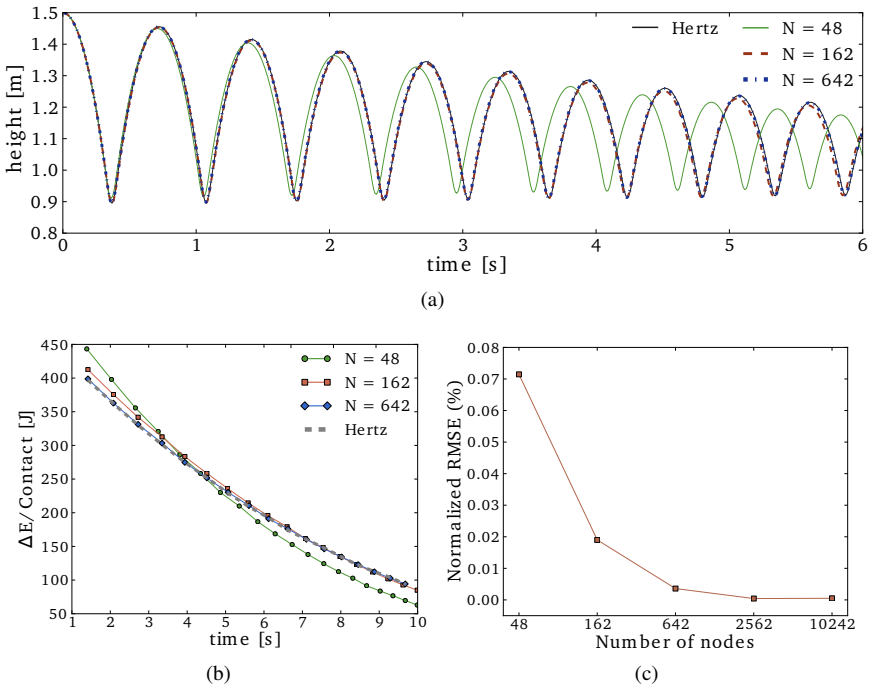

Figure 3.5: Comparison of normal contact dynamics between perfect sphere with Hertzian damping bouncing on a flat plane and meshed sphere for different levels of mesh refinement. (a) Sphere height versus time. (b) Energy dissipated because of normal damping per contact event versus time. (c) Normalized Root Mean Square Error (NRMSE) between model and Hertz solution of energy dissipated per contact event – see (b) – for different levels of mesh refinement.

Finally, it is shown that the model for tangential friction corresponds with the Coulomb force for a perfect sphere, as given in Eq. (3.17). For this, a sphere at rest was placed on top of a horizontal plane. Next, a linearly increasing external horizontal force is applied to the sphere. Initially, the viscous damping force keeps the displacement of the sphere very low[2]. Only after the threshold force $F_{\max} = \mu mg$ is reached, the sphere starts sliding, and experiences a constant friction force. In Fig. 3.6(a) the displacement of the meshed spheres versus time for different levels of mesh refinements is shown. The relative frictional force $F_t/F_{\max}$ as a function of relative applied force $F_A/F_{\max}$ is shown in Fig. 3.6(b). As can be seen in both figures, the solution for the meshed sphere closely

[2]As the force is velocity dependent, the friction will never keep the body completely at rest. This is a limitation of this simplified friction model

follows the Coulomb friction model. It should be noted that the Coulomb friction model is a very simple model that is insufficient for many applications in DEM [164] and is only given as an example. A similar approach could be used for implementing more advanced tangential force models (e.g. [99, 169]).

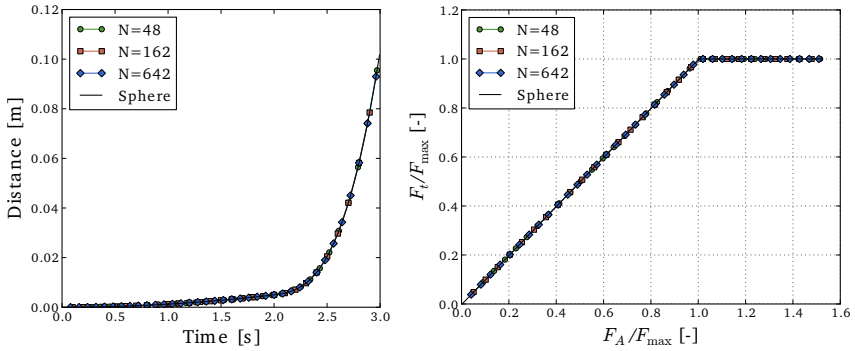

(a) (b)

Figure 3.6: Comparison of tangential friction model between perfect sphere and meshed sphere with different levels of mesh refinement. (a) Displacement versus time for a sphere lying on a flat plane with a linearly increasing applied force. (b) Relative friction force F_t versus relative applied force $F_A/F_{\max}$. Forces are relative to the maximal force of friction $F_{\max} = \mu mg$.

3.3.2 Validity for non-spherical curvatures

In principle, the presented model calculates Hertzian forces correctly for spherical curvatures, i.e. the two principal radii of curvature are equal. In reality, arbitrary shapes can have distinctly different radii of curvature, and an error in contact force magnitude – but not direction – will be made. In order to quantify this error, a force-indentation test between two meshed spheroids with two different radii of curvature was performed (see Section 3.3.1), a and b. For contact between ellipsoids, Hale [74] provided an approximation for the normal elastic Hertz force [239]. In Fig. 3.7, the Normalized Root Mean Square Error (NRMSE) is shown for standard indentation experiments between two spheroids as a function of the principal radii of curvature a/b. For $a/b < 2.5$, the model results correspond well to the approximate solution. However, as a/b becomes large, the error starts to increase rapidly. Typically, the Hertz force is over-estimated compared to the correct solution. In principle, this could be resolved by integrating the Hertz pressure over the real contact ellipse instead of an averaged contact circle.

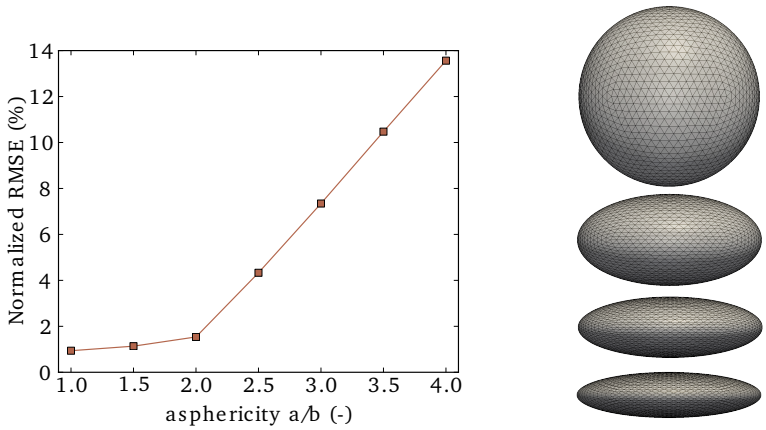

(a) (b)

Figure 3.7: Validity of the contact force model for ellipsoidal contacts. (a) Normalized Root Mean Square Error (NRMSE) on a force-indentation experiment for different ratios of radii of curvature a and b, where $a \geq b$. The maximum indentation was set at 7.5 % of a. (b) top view of spheroids with ratios of a/b of 1, 2, 3 and 4.

In order to estimate the maximal error due to non-spherical curvatures, the extreme case of two contacting cylinders is used. At the hull of a cylinder, the ratio between the two principal radii of curvature is infinite. In a simulation, two triangulated cylinders of equal radius and length L were brought into contact both in parallel – Fig. 3.8(b) – and crossed positions – Fig. 3.8(a). These configurations were chosen because for them an analytical solution is readily available. At the hull, the calculated mean radius of curvature is twice the cylinder radius. For two perpendicular cylinders, the analytical solution can be reduced to the Hertz force for contact between a sphere and an elastic half-space – see Eq. (3.5). Therefore, it is not surprising that the model which uses a sphere-based approximation matches very well with the analytical solution. More interesting is the contact between two parallel cylinders. In this case the contact area is effectively a rectangle, with a linear force-indentation relationship:

$$F_H = \frac{\pi}{4}\hat{E}L\delta. \tag{3.26}$$

As the model assumes a circular contact area, the error in calculated contact force in this extreme case can be very large – Fig. 3.8(b). Although the force increases linearly with overlap, the error in its slope — the effective contact stiffness — is about 23 %.

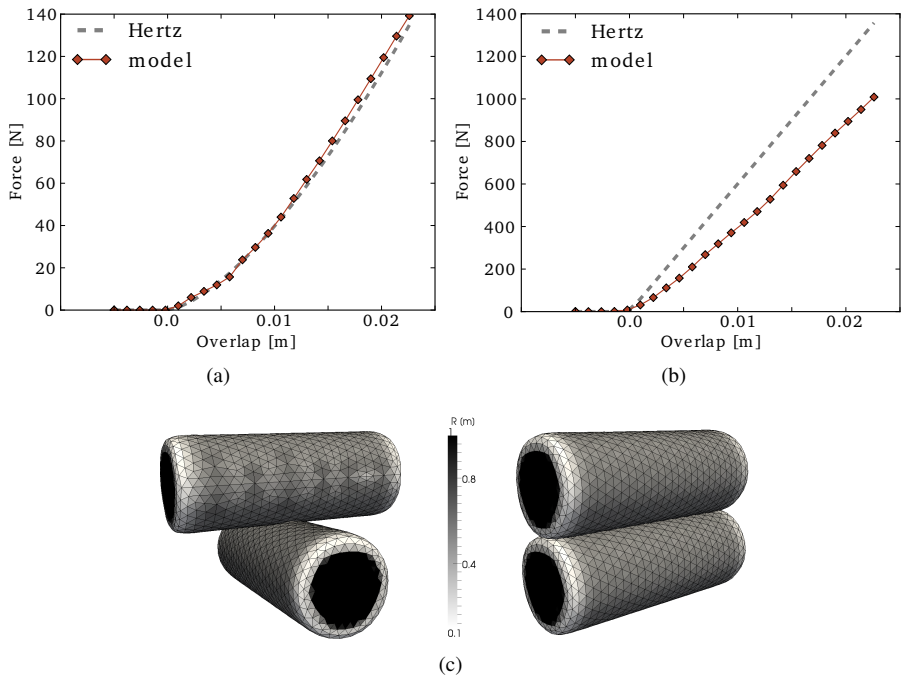

Figure 3.8: Comparison of model with analytical results for extreme cases of (a) contact between two crossed triangulated cylinders and (b) contact between two parallel triangulated cylinders. (c) view on indentation simulations with grayscale indicating the local radius of curvature. Error in effective stiffness: 22.88 %

3.3.3 Comparison with 3D printed non-spherical object

An indentation experiment was performed on a universal testing machine (UTS, see SI in [194]) to validate the correctness of a simulated compression. For this, a mesh of a non-spherical pear-like shape was used, from which a 3D printed object was produced in a rubber-like material. Although rounded, the curvature at the place of contact was non-spherical (ratio of principal radii $a/b \approx 1.6$) and not symmetrical. Measurements were performed on the pear-shaped object as well as on a spherical object made from the same material. The apparent Young's modulus for contact between the rubber-like pear and the compression plate was derived by applying the Hertz model on the force-distance curve obtained on the spherical object and was estimated at $\hat{E} = 26.26\,\text{MPa}$.

The compression experiment on the pear-shaped object was then simulated with this estimated apparent Young's Modulus. The comparison between measured and

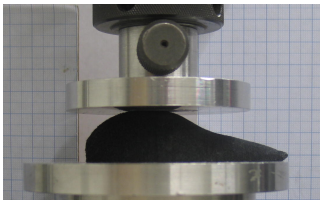

(a) UTS experiment

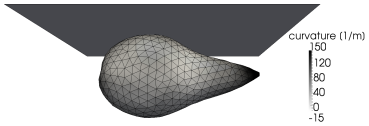

(b) Simulated UTS experiment

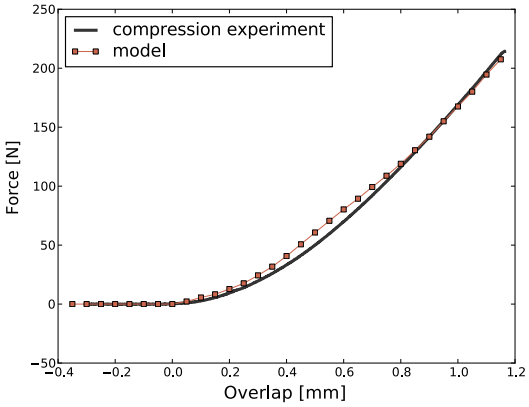

(c) Comparison experiment vs. model

Figure 3.9: (a) Experiment compressing a pear-shaped 3D printed object with a flat indenter. (b) Simulation of compression experiment of the same mesh that was 3D printed (curvature indicated in gray-scale). The position of the simulated pear is kept fixed. (c) Comparison of force-indentation curves between the UTS measurement and the model result. Apparent Young's modulus prescribed in the model 26.26 MPa, obtained by the UTS experiment on a spherical object, see SI in [194].

simulated compression can be found in Fig. 3.9. Without any data fitting, the simulation corresponds well to the measured compression.

In order to correctly attribute the discrepancies between simulation and measurement, the sources of measurement error which can lead to a discrepancy between the simulated and measured curve are briefly summarized:

- Initial contact is especially difficult to define correctly. Here, it was defined as the data point exceeding three times the standard-deviation of the noise level of the sensor closest to the force-maximum. Defining it *a priori* fails, because of the surface roughness (both on top and at the lower support plane) of the tested body. In addition, the 3D printed shapes could only be obtained with a thin black surface coating which seems to be softer than the bulk material – see SI in [194].
- While the manufacturer uses laser sintering to obtain high accuracy of the shape, the precision is limited to 0.5 % of the shape with a lower limit of 0.5 mm. This error has to be considered together with the (rotational) positioning accuracy, which is of comparable magnitude.

- Finally, no physical material can be considered linearly elastic and non-viscous in a large range of forces/velocities, thereby adding a small error in the estimation of the "physical" (apparent) Young's modulus.

While these errors were kept under tight control by the use of 3D printed test objects, they might contribute significantly to the overall small deviation between the simulated model and the measured force-indentation curve.

The presented method for calculating contact forces introduces additional approximations, which could also contribute to the differences between the measured and simulated curves:

- Each triangle represents only one average curvature instead of the two local principal curvatures, and
- the number of quadrature points considered determines the accuracy of the force (and moment) integration. This aspect is kept under control by switching to the direct Hertz solution for overlap areas significantly smaller than a single triangle's area.

When a large number of triangles is in contact, a very accurate integration of the contact pressure can be expected. The accuracy of the method for moderate overlaps can be chosen by increasing the mesh refinement, or by choosing a higher order quadrature rule for integration of the contact pressure. This, however, results in an increased computational cost.

It should be pointed out that the presented model is not expected to be more accurate than Hertz' solution for calculating local contacts at a given curvature. However, it strives to provide a general method for calculating Hertzian contact between arbitrary rounded objects. Therefore, it is crucial to verify that for non-spherical objects (e.g. the pear-shaped object), the calculated contact force does not strongly diverge from the physical contact force.

3.3.4 Example DEM simulation: gravitational packing

To demonstrate the applicability of the presented model, the method was used for a classic DEM simulation where particles are shaken in a box to produce a random stacking. For this, 250 particles were arranged in a – slightly distorted – grid inside a rectangular box. After three sinusoidal oscillations, the particles were allowed to settle. The simulation was repeated for perfect spheres, pears (486 nodes), gummy bears (554 nodes), and triangulated spheres with 12, 48 and 162 nodes per sphere. All particles have the same volume, corresponding to a sphere with radius 0.025 m. The

most important mechanical and geometrical parameters used in these simulations are summarized in Table 3.1.

Parameter	Value	Units
timestep	$1 \cdot 10^{-4}$	s
simulation time	1.35	s
shaking time	0.75	s
settling time	0.60	s
period	0.25	s
amplitude	0.025	m
particle radius	0.025	m
particle density	2000	kg/m^3
particle Young's modulus	$1 \cdot 10^6$	Pa
box Young's modulus	$5 \cdot 10^6$	Pa
normal damping constant	0.01	s
particle Poisson's ratio	0.4	–
box Poisson's ratio	0.4	–
friction constant	0	–

Table 3.1: Simulation parameters and mechanical parameters used in demonstration simulation of particles shaken in a rectangular box (see Fig. 3.10 and Fig. 3.11).

The mean height of the particles during shaking as well as an estimated packing factor have been calculated. For the latter, a rough approximation was used: for different heights, the number of particles N_h under this height h is calculated corresponding to a packing factor P (in percent):

$$P = \frac{N_h V_p}{A_b h} 100 \tag{3.27}$$

with V_p the volume of one particle and A_b the area of the bottom of the box. Note that this is only an approximation of the packing factor as it does not consider the intersections between the particles and the plane at height h. However, for an intersecting particle, the chances of having its center of mass above or under the plane are roughly equal, as long as the plane is fully submerged in particles.

In Fig. 3.10 the configuration of the spheres, pears, gummy bears and meshed spheres at the endpoint of the simulation is illustrated. In Fig. 3.11(a) the evolution in time of the mean height of the particles during shaking is shown. The meshed spheres' simulations closely resemble the solution given by perfect spheres, even for a very coarse mesh of only 12 nodes – effectively an icosahedron. Different height profiles are observed for both pears and gummy bears. Interestingly, the final mean height for the simulated pears is lower than for the spheres and gummy bears. The same can be observed in Fig. 3.11(b), where an estimated packing factor for different heights

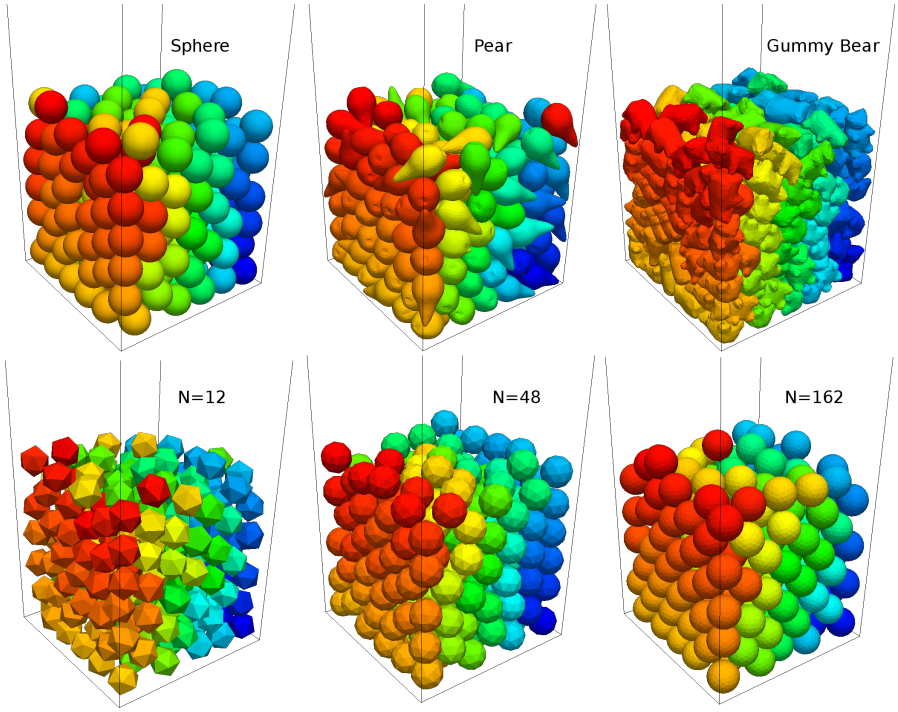

Figure 3.10: Illustration of the stacked particles after three periods of shaking for perfect spheres, pears, gummy bears, and triangulated spheres with 12, 48 and 162 nodes.

is reported following Eq. (3.27). The pear shape seems to result in distinctly denser packings, while the density of packing of the gummy bears closely resembles the density of the sphere's packing. For increased heights, the plane is not fully submerged in particles and Eq. (3.27) does not anymore approximate the packing factor, but the fact that all curves coincide for the "too large" height demonstrates that indeed the total volume of particles was identical for the shown simulations.

Performing simulations with triangulated bodies is computationally more expensive than performing the same simulation with simple spheres due to the fact that there are more 'primitive' particles required to represent a single body. Potentially, the cost per primitive might be higher as well due to the fact that pressures are integrated per triangle. To quantify the additional computational cost and to demonstrate the scaling with growing number of primitive particles, following simulations were constructed: a varying number of bodies – both spheres and triangulated spheres – are shaken in a box for 0.5 s. Timings were registered for contact detection – i.e. generating a list of probable contact candidates – and contact resolution – i.e. determining effective

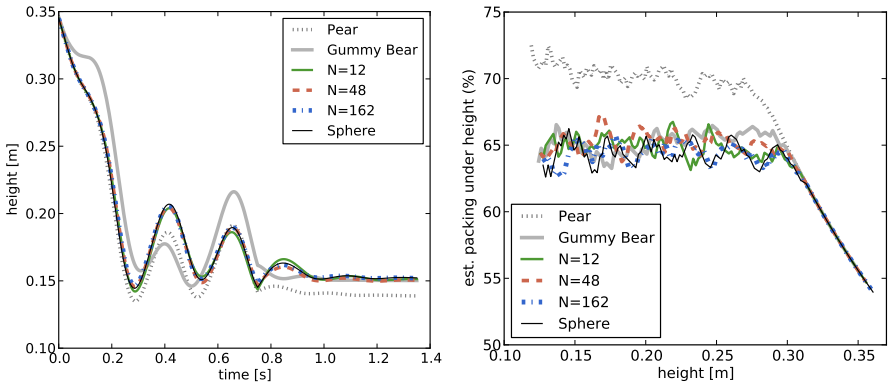

(a) (b)

Figure 3.11: (a) Time evolution of mean height of spheres, triangulated spheres (using 12, 48 and 162 nodes per sphere), pear-shapes and gummy bear-shapes during three shake cycles and subsequent settling time. (b) Estimated packing at endpoint (%) under varying height for the same particle shapes, calculated using Eq. (3.27).

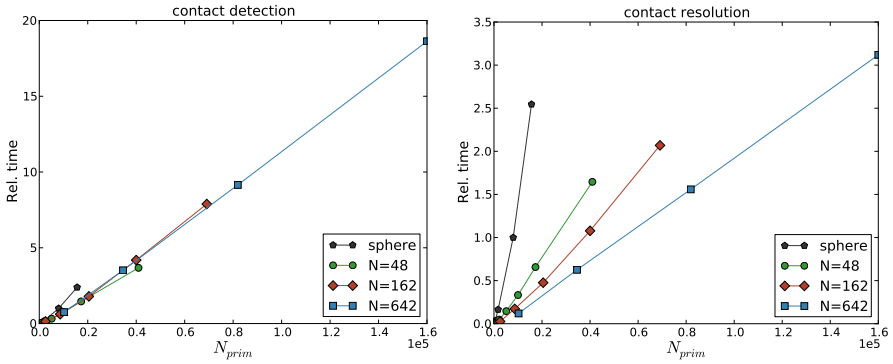

(a) (b)

Figure 3.12: Computational time (relative to sphere simulation with 8000 primitives) as a function of number of primitives N_{prim} for spheres and triangulated spheres with varying mesh refinements for (a) contact detection and (b) contact resolution. For contact detection, a single grid-based algorithm was used [210]. Simulations were performed on Desktop AMD Phenom II X6 1055T.

contacts and calculating the actual contact forces. A single grid-based contact detection algorithm was used, with a grid size slightly larger than the diameter of the contact primitives.

In Fig. 3.12, the relative – compared to a simulation with 8000 spheres – computational time is shown as a function of the number of contact primitives N_{prim}. The computational cost of contact detection scales according to $N_{\text{prim}} \log(N_{\text{prim}})$. For the triangle primitives there is little difference in slope when the increasing number of triangle primitives is caused by either increasing the number of triangles per sphere, or by increasing the number of spheres. For the same number of contact primitives, the time spent in contact resolution decreases as the particle's mesh becomes more refined, because the relative number of effectively contacting primitives goes down. Finally, it can be seen that the cost per primitive is actually lower for the triangle primitives compared to the spheres because the extra cost due to pressure integration is more than compensated by the fact that there will be relatively less triangles in effective contact.

3.4 Conclusion and Outlook

In this chapter, a new method has been presented for DEM simulations using arbitrary rounded shapes. The shape is described as a triangulated surface mesh, in which each triangle is associated with one average radius of curvature. Subsequently, contact forces are computed by integrating repulsive pressure formulations such as Hertz pressure over the contact area between two bodies. By integrating pressures instead of directly calculating contact forces, problems arising due to multiple simultaneous contact points between two contacting bodies [132] are avoided. The contact force is shown to converge upon refinement of the surface mesh. The advantage of using continuum contact models such as Hertz theory is that the known material properties such as the Young's Modulus and Poisson's ratio can be directly used, without parameter tuning. This has been demonstrated with a 3D printed shape in a compression experiment (see Section 3.3.3).

The main limitation of the proposed method is that only one average radius of curvature is considered. For distinctly non-spherical curvatures, this can lead to significant errors in approximating the contact force (see Section 3.3.2). In general, the error made in this regard stays small for ratios between the principal radii of curvature $a/b < 2.5$. Furthermore, it should be stressed that Hertz theory is not applicable for contact between two perfectly flat surfaces ($\hat{R} \to \infty$). When combining Eq. (3.2) with $a \gg r$ and Eq. (3.4), the contact force between two parallel triangulated surfaces with contact area Ω becomes:

$$F_H = \frac{2\Omega\hat{E}}{\pi\sqrt{\hat{R}}}\sqrt{\delta}. \tag{3.28}$$

In other words, the model would calculate a square root force-indentation relationship instead of the correct linear solution.

The method is not limited to describing purely Hertzian contacts. Other contact pressures that have been formulated for contact between spheres can be implemented as well (e.g. adhesive contacts described by a Maugis-Dugdale potential [97, 135]). Also, the model could be improved with a more precise description of frictional forces. While the Coulomb-friction model captures the basic characteristics of a no-slip and a slipping regime, the linear damping regime in the no-slip region fails to correctly describe systems of packed particles which are static or nearly-static. To improve this, a more advanced friction model could be included (e.g. [99, 169]).

Furthermore, it is conceivable to describe contact between bodies, while explicitly calculating the deformation. For this, the connections between nodes can be replaced by (visco-)elastic springs and the nodes themselves become degrees of freedom of the simulation for which the equation of motion is being solved. Alternatively, the elastic spring network could be solved as a linear system and the resulting deformation at each time-step could be imposed on the nodes. An even more involved method could include a full FEM solution of the (visco-)elastic solid, where the pressure in the contact area is prescribed as a boundary condition (similar to multi-body dynamics). The latter two methods assume that equilibration within the material is fast compared to the contact-time. In this case, the repulsive contact pressure should be chosen sufficiently stiff to ensure that the elastic connections undergo the deformation due to contact forces [153].

Acknowledgements

The authors would like to thank Els Herremans for providing a triangulated mesh of high quality representing a realistic pear shape.

This research was funded by the *Agency for Innovation by Science and Technology in Flanders (IWT)*.

Chapter 4

Generalized contact model for arbitrary polyhedra

Adapted from [196]:

Smeets, B., Odenthal, T., Vanmaercke, S., Ramon, H. (2015). Polygon-based contact description for modeling arbitrary polyhedra in the Discrete Element Method. Computer Methods in Applied Mechanics and Engineering.

4.1 Introduction

In granular assemblies, particle shape has been shown to be a determining parameter affecting, among else, a system's response upon loading [150, 158], packing density, stress patterns [24] and ratcheting behaviour [4]. In the Discrete Element Method (DEM), which tries to describe granular systems as assemblies of distinct, explicitly modeled bodies interacting by means of contact forces [164], particle shape is often approximated using a simplified geometrical representation, e.g. spheres. Many applications, however, require a more elaborate description of irregular bodies.

During the last years, many advances are made in shape description for the Discrete Element Method. Instead of spheres, ellipsoids [170, 234, 239], superquadrics [166, 230], and polyhedra [52, 164] have been used to approximate particle shape. Other approaches use composites of more simple shape primitives, such as spheres [49, 53, 127], ellipsoids [160] and spheropolygons [165]. A variation of DEM, the Granular Element Method (GEM), uses Non-Uniform Rational Basis-Splines (NURBS) to

capture grain shape, offering a flexible and robust algorithm to account for arbitrary rounded shapes [6, 122]. Another method for modeling arbitrary rounded shapes is based on triangulated surface meshes in which the local curvature is used for a Hertzian contact force formulation (see chapter 3 and [194]).

In this chapter, we propose a flexible and easy-to-implement algorithm to model irregular polyhedral particles. The presented method represents particles using a surface mesh containing polygonal facets, and formulates contact forces based on individual interactions between two contacting bodies. For each polygon-polygon contact, a linear elastic and dissipative pressure is used which is numerically integrated over the intersection of the two polygons. Because each contact between two polygons is resolved independently, the method benefits from efficient contact detection and can be easily parallelized. In Section 4.2, it is explained how contact forces can be computed between two arbitrarily shaped polyhedra. Next, in Section 4.3, the model is validated by comparing to simulations of gravitational deposition of cubes and further demonstrated by showing analogous deposition of various other polyhedral particles.

4.2 Model description

4.2.1 Contact detection

Contact detection, i.e. the generation of a list of contact candidates, is performed on the level of individual polygonal facets, instead of between two complete polyhedral bodies. Bounding boxes [124] are constructed for each individual polygon. Using these bounding boxes several efficient contact detection methods can be applied, such as (multi-)grid [63, 79, 82, 144] and octree [140, 149] methods.

For each set of two polygons, these algorithms can cheaply determine whether or not their bounding boxes are overlapping, and are therefore likely to have physical contact. With these contact detection methods, the computational effort does not scale with the number of polygons being used in the simulation, but only with the number of polygons that are actually in contact (see section 4.3.4 and [194]).

4.2.2 Geometrical contact properties

Contact pressures are calculated on the contact plane between two polygons P_1 and P_2 with normal vectors $\hat{\mathbf{n}}_1$ and $\hat{\mathbf{n}}_2$. For this, an intersection polygon S_{12} is first determined. In the case of equal material properties, the plane in which S_{12} lies is chosen as the

bisection of the planes of P_1 and P_2. The contact normal unit vector is therefore approximated as:

$$\hat{\mathbf{n}}_{12} = \frac{\hat{\mathbf{n}}_2 - \hat{\mathbf{n}}_1}{\|\hat{\mathbf{n}}_2 - \hat{\mathbf{n}}_1\|} \tag{4.1}$$

If the two contacting bodies have a different stiffness, the contributions of $\hat{\mathbf{n}}_1$ and $\hat{\mathbf{n}}_2$ to $\hat{\mathbf{n}}_{12}$ should in principle be inversely weighted with their stiffness.

All three planes characterized by $\hat{\mathbf{n}}_1$, $\hat{\mathbf{n}}_2$ and $\hat{\mathbf{n}}_{12}$ contain the plane-plane intersection line defined by the vector $\hat{\mathbf{l}}_{12} = \hat{\mathbf{n}}_1 \times \hat{\mathbf{n}}_2$ and a point $\mathbf{s}$ chosen on the intersection line.

Next, P_1 and P_2 are projected on the contact plane along the direction of respectively $\hat{\mathbf{n}}_2$ and $\hat{\mathbf{n}}_1$, yielding the projections P_1' and P_2' – see Fig. 4.1(a) and Fig. 4.1(c). S_{12} is then obtained by computing the side of the intersection between P_1' and P_2' which is in the direction of positive overlap – Fig. 4.1(b).

At a given test point $\mathbf{x}$ inside S_{12}, the overlap distance δ_{12} can be calculated as:

$$\delta_{12}(\mathbf{x}) = 2\tan(\alpha)\left[(\mathbf{x}-\mathbf{s})\cdot(\hat{\mathbf{n}}_{12}\times\hat{\mathbf{l}}_{12})\right] \tag{4.2}$$

with $\cos(\alpha) = \hat{\mathbf{n}}_{12}\cdot\hat{\mathbf{n}}_1$. The contact point $\mathbf{c}$ is approximated as the mean of the corners of S_{12}, weighted by their corresponding overlap distance according to Eq. (4.2).

In every $\mathbf{x} \in S_{12}$, a relative contact velocity is defined as:

$$\begin{aligned}\mathbf{v}_{12}(\mathbf{x}) =& \mathbf{v}_2^{\text{dof}} - \mathbf{v}_1^{\text{dof}} \\ &+\mathbf{w}_2^{\text{dof}} \times (\mathbf{x} - \mathbf{x}_2^{\text{dof}}) \\ &-\mathbf{w}_1^{\text{dof}} \times (\mathbf{x} - \mathbf{x}_1^{\text{dof}}),\end{aligned} \tag{4.3}$$

where $\mathbf{x}_i^{\text{dof}}$, $\mathbf{v}_i^{\text{dof}}$ and $\mathbf{w}_i^{\text{dof}}$ are respectively the center of mass position, velocity and angular velocity of the polyhedron to which polygon P_i belongs.

To deal with issues of numerical accuracy - e.g. exact flat contacts - or efficiency - e.g. early contact reject cases, additional calculations are performed. These are briefly summarized in appendix A.2.

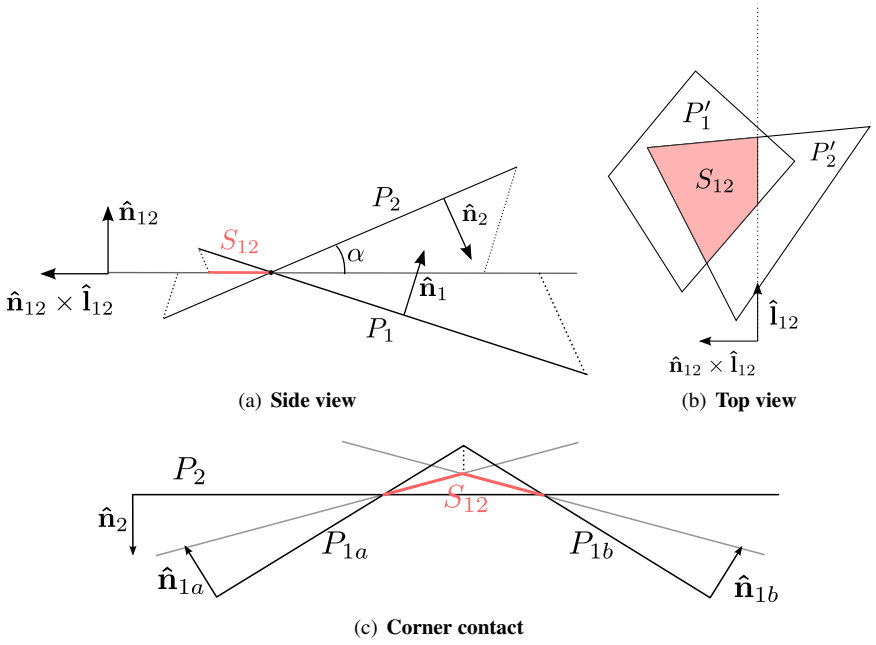

(a) **Side view** (b) **Top view**

(c) **Corner contact**

Figure 4.1: (a) Projection of polygon P_1 and polygon P_2 onto the contact plane according to the normal of the other polygon, yielding P_1' and P_2'. (b) Calculation of S_{12} as the intersection of projected polygons P_1' and P_2', cut off by the plane-plane intersection line $\mathbf{s}$, $\hat{\mathbf{l}}_{12}$. (c) Contact of a corner of body 1 (polygons P_{1a} and P_{1b}) with P_2. By projecting P_{1a} and P_{1b} along $\hat{\mathbf{n}}_2$, S_{12} is continuous and its corresponding overlap volume is equal to the volume of the indenting corner.

4.2.3 Normal contact force calculation

The normal elastic contact pressure $p_{n,e}$ at a test point $\mathbf{x}$ increases linearly with the overlap distance:

$$p_{n,e}(\mathbf{x}) = k_l \, \delta_{12}(\mathbf{x}), \tag{4.4}$$

with k_l the layer stiffness (Pa/m). For a flat linearly elastic layer with thickness h (see also Appendix 1), k_l is related to the bulk modulus K as: $k_l = K/h$ [85].

A normal dissipative (damping) pressure is calculated using the normal relative contact velocity:

$$p_{n,d}(\mathbf{x}) = -c_l\,(\mathbf{v}_{12}(\mathbf{x}) \cdot \hat{\mathbf{n}}_{12}), \tag{4.5}$$

with c_l a layer damping coefficient (kg/(m^{2}s)).

The intersection polygon S_{12} is either already a triangle or can be trivially subdivided into N_S triangles by connecting one corner point with all edges. The contact force between polygons P_1 and P_2 is obtained by integrating the normal pressure over S_{12}, as described in Eq. (3.10).

To calculate both forces and moments caused by a specific pressure/traction in a triangle, the coordinates of the integration test points are determined first. Using Eq. (3.10) the surface integral for the normal contact force on the intersection polygon S_{12} is approximated:

$$\mathbf{F}_n^S = \sum_{j=1}^{N_S} \sum_{i=1}^{N_Q} A_j w_{j,i} p_n\,(\mathbf{x}_{j,i})\,\hat{\mathbf{n}}_{12}, \tag{4.6}$$

where $p_n\,(\mathbf{x}_{j,i})$ is the normal contact pressure according to Eq. (4.4). N_Q is the number of quadrature points and N_S is the number of sub-triangles in S. Additionally, the moments generated by each evaluated pressure with respect to the contact point $\mathbf{c}$ are summed (see also [194]):

$$\mathbf{M}_n^S = \sum_{j=1}^{N_S} \sum_{i=1}^{N_Q} A_j w_{j,i} p_n\,(\mathbf{x}_{j,i})\,[(\mathbf{x}_{j,i} - \mathbf{c}) \times \hat{\mathbf{n}}_{12}]\,. \tag{4.7}$$

4.2.4 Tangential forces

The tangential relative contact velocity $\mathbf{v}_{12}^t$ at $\mathbf{x}$ is calculated as:

$$\mathbf{v}_{12}^t(\mathbf{x}) = \mathbf{v}_{12}(\mathbf{x}) - (\mathbf{v}_{12}(\mathbf{x}) \cdot \hat{\mathbf{n}}_{12})\hat{\mathbf{n}}_{12}. \tag{4.8}$$

A simple two-parameter Coulomb Friction model is used with a viscous damper in the static regime. For a given test point $\mathbf{x}$, the pressure due to friction is expressed as:

$$p_{t,d}(\mathbf{x}) = -\min\left(c_t \left\|\mathbf{v}_{12}^t(\mathbf{x})\right\|, \mu \|p_n(\mathbf{x})\|\right), \tag{4.9}$$

where c_t is a viscous damping constant (kg/(m^{2}s)), μ is the Coulomb friction coefficient (-) and $p_n(\mathbf{x}) = p_{n,e}(\mathbf{x}) + p_{n,d}(\mathbf{x})$ is the total normal contact pressure in $\mathbf{x}$.

Analogous to the normal forces, the tangential contact forces are obtained by numerically integrating these pressures over the sub-triangles of S_{ij}. For a given triangle, the total tangential force becomes:

$$\mathbf{F}_t^S = \sum_{j=1}^{N_S} \sum_{i=1}^{N_Q} A_j w_{j,i} p_t(\mathbf{x}_{j,i}) \frac{\mathbf{v}_{12}^t(\mathbf{x}_{j,i})}{\left\|\mathbf{v}_{12}^t(\mathbf{x}_{j,i})\right\|}, \tag{4.10}$$

and the sum of moments with respect to the contact point:

$$\mathbf{M}_t^S = \sum_{j=1}^{N_S} \sum_{i=1}^{N_Q} A_j w_{j,i} p_t(\mathbf{x}_{j,i}) \left[(\mathbf{x}_{j,i} - \mathbf{c}) \times \frac{\mathbf{v}_{12}^t(\mathbf{x}_{j,i})}{\left\|\mathbf{v}_{12}^t(\mathbf{x}_{j,i})\right\|} \right]. \tag{4.11}$$

4.2.5 Transfer of forces and moments to the rigid body

The triangle forces $\mathbf{F}_n^S$ and $\mathbf{F}_t^S$ can be directly summed up to the center of mass of the triangle's parent body. The rigid body moment is the sum of the triangle's moment and the moment of the triangle forces with respect to the contact point $\mathbf{c}$. For polygon P_1:

$$\mathbf{F}_1^{\text{dof}} = -\mathbf{F}_n^S - \mathbf{F}_t^S, \tag{4.12}$$

$$\mathbf{M}_1^{\text{dof}} = -\mathbf{M}_t^S - \mathbf{M}_n^S - (\mathbf{c} - \mathbf{x}_1^{\text{dof}}) \times (\mathbf{F}_t^S + \mathbf{F}_n^S), \tag{4.13}$$

and for P_2:

$$\mathbf{F}_2^{\text{dof}} = \mathbf{F}_n^S + \mathbf{F}_t^S, \tag{4.14}$$

$$\mathbf{M}_2^{\text{dof}} = \mathbf{M}_t^S + \mathbf{M}_n^S + (\mathbf{c} - \mathbf{x}_2^{\text{dof}}) \times (\mathbf{F}_t^S + \mathbf{F}_n^S), \tag{4.15}$$

4.3 Results and Discussion

In DEM simulations, the objective is generally not to capture individual force-indentation behaviour during collision events in a realistic way. Instead, the aim is to correctly describe the momentum and energy changes of individual collisions in order to simulate the collective dynamics of a particle system. It is common for

simulations to artificially reduce the effective stiffness of particles in order to enable larger time steps and hence a bigger simulation time [26, 27, 224]. Damping coefficients are then changed accordingly, to ensure that the energy exchange during collisions remains unchanged.

In this work, the layer stiffness k_l is chosen large enough to only allow for a very small overlap between the particles, but low enough to use a reasonably high timestep. Wachs et al. [224] suggest to fix the particles' stiffness based on a maximally allowed overlap distance, which should be small relative to the particle size. The normal damping coefficient is subsequently calculated based on k_l and the measured coefficient of restitution e_n, which, for a given collision, is the ratio between the magnitude of the relative velocity before and after the collision.

4.3.1 Validation simulations

To validate the performed method, we compare our simulations to an experimental study by Latham et al. [111, 143], as well as computational results using another method by Wachs et al. [224]. In the first study, 648 wooden cubes were deposited into a rectangular box ($250 \times 250 \times 375$ mm) in a fixed snake-like sequence. With a measured Coulomb friction coefficient μ of 0.5, the authors estimated an average porosity of 33 %.

Parameter	Value [111]	Value [224]	Units
timestep	$4 \cdot 10^{-5}$	$1 \cdot 10^{-5}$	s
simulation time	35.4	10.33	s
cube side length	0.024177	0.00643	m
cube mass	0.00923	0.00031	kg
cube density	653	1163.66	kg/m^3
layer stiffness (k_l)	$30 \cdot 10^6$	$80 \cdot 10^6$	Pa/m
coefficient of restitution (e_n)	0.25	0.85	–
tangential friction coefficient (μ)	0.5	0.5	–
tangential dashpot constant (c_t)	$4 \cdot 10^6$	$4 \cdot 10^6$	kg/(m^{2}s)
number of cubes	648	250	–

Table 4.1: Simulation parameters and mechanical parameters used in validation simulation of gravitational cube deposition for Latham et al. [111] and Wachs et al. [224] simulations (see Fig. 4.2)

In Fig. 4.2(a), the cube deposition process is visualized. Similar to [111], a horizontal plane is shown, which corresponds to the height the cubes would reach if they had the experimentally estimated porosity of 33 %, and is purely a function of the number of cubes in the simulation. As can be visually inspected, the final height of the plane corresponds very well to maximal heights of the cubes. The simulation parameters,

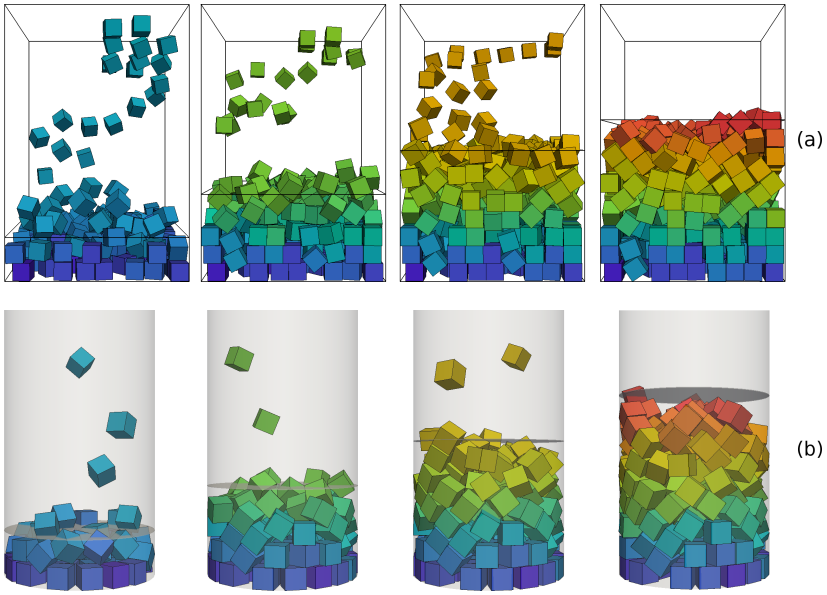

Figure 4.2: Simulated deposition of cubes with friction coefficient of 0.5. **(a)** Deposition based on experiment of Latham et al. [111] in a rectangular container. The volume under the horizontal plane represents a porosity of 33 %. From left to right: 162, 324, 486 and 648 cubes. **(b)** Deposition in a cylindrical container described by Wachs et al. [224]. The volume under the horizontal plane represents a porosity of 42 %. From left to right: 62, 124, 186 and 250 cubes.

listed in Table 4.1, correspond to the experimental settings, only with the cubes' stiffness artificially lowered as explained above. In a second validation simulation, the packing of cubes in a cylindrical container with internal diameter 50 mm and height 130 mm is compared to the simulation results by [224]. There, a porosity of 43.4 % was reported for 250 cubes with a friction coefficient of 0.5 (simulation parameters in Table 4.1). In Fig. 4.2(b), the simulated deposition sequence is visualized, with the horizontal plane corresponding to a porosity of 42 %.

4.3.2 Packing densities of different convex geometries

In order to show the applicability of the model for arbitrary shapes, as well as to investigate the effect of shape on porosity in gravitational deposition, additional simulations were performed for various shapes. First, we consider shapes with triangular facets: tetrahedra, icosahedra, and two levels of subdivided icosahedra

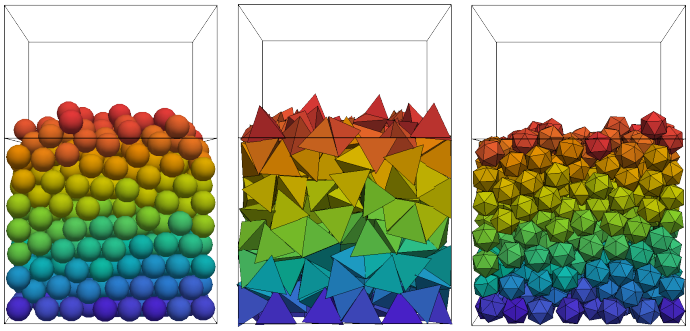

Figure 4.3: Simulated gravitational deposition of (from left to right) spheres, tetrahedra and icosahedra. The plane indicates the level of 33 % porosity as indicated in Fig. 4.2. All shapes have identical volume and mechanical properties as the cubes, described in Table 4.1.

(see also section 5.2.2 and [194]). Apart from the particles' shape, the simulation parameters are identical to the cube deposition as performed by Latham et al. [111], i.e. they have the same volume, mass, and mechanical contact properties. The packing of these shapes is compared to spheres and cubes. For each shape, three different simulation runs are performed – using different initial random orientations of the particles.

In order to make a valid comparison with spheres, the contact model for spheres cannot be considered Hertzian, as the integrated contact force given in Eq. (4.6), would result in a different force-overlap relationship. Instead, it can be shown that for the contact of a sphere with radius R, with a surface consisting of infinitely small facets, the force-indentation relationship would be the following:

$$\mathbf{F}_n = \pi k_l \delta_{12}^2 (R - \frac{\delta_{12}}{2}) \, \hat{\mathbf{n}}_{12}, \tag{4.16}$$

whereas Hertz' force would yield a $F \sim \delta_{12}^{3/2}$ relation. Since this contact force increases as $\sim \delta_{12}^2$ for small indentations ($R \gg \delta_{12}$), Eq. (4.16) has been used to perform the simulations with spheres. This guarantees that discrepancies in packing are truly due the particle's shape and not artifacts due to a slightly different contact force law. It was found that, as long as the particle stiffness is large enough, the final packing density when using Hertz' law does not differ significantly compared to when using Eq. (4.16).

Fig. 4.3 shows the results of gravitational deposition for spheres, tetrahedra and icosahedra in a rectangular box. The horizontal plane indicates a porosity height

of 33 %, similar to Fig. 4.2. In order to quantify packing density more in detail, a packing factor P is calculated as following [194]:

$$P = \frac{N_h V_p}{A_b h} 100, \tag{4.17}$$

with h the height of a horizontal plane submerged in the particle stacking, N_h, the number of particles with a center of mass under h, V_p the volume of one particle and A_b the area of the bottom of the box (250 $\times$ 250 mm). It should be noted that, when h is chosen well within the particle stacking, this measure for the packing factor disregards the loosely packed particles in the upper layers, and hence gives rise to higher packing densities than an average packing density calculated from all particles. On the other hand, because this measure is less influenced by outliers in the top layers, its value is more constant over multiple simulation runs. In this work, an average $\hat{P}$ was calculated as the mean packing factor for 100 planes chosen at h between 140 and 180 mm.

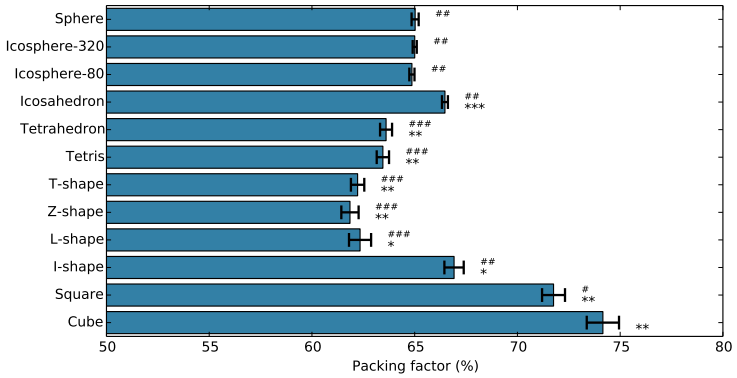

Figure 4.4: Comparison of packing factors for spheres, tetrahedra, icosahedra, cubes, L-shapes, I-shapes, T-shapes, Z-shapes, square shapes and a mixture of the last five. Stars (*) indicate a significant difference from the sphere packing (p-value: 0.05 * 0.01 ** 0.001 ***) using a two-sided Welch's t-test. Hashtags ($^{\#}$) indicate a significant difference from the cube packing (p-value: 0.05 $^{\#}$ 0.01 $^{\#\#}$ 0.001 $^{\#\#\#}$).

Fig. 4.4 shows values and standard deviations of $\hat{P}$ for three simulation runs, indicating significant differences with sphere and cube packings. Interestingly, whereas tetrahedra pack significantly worse than spheres, icosahedra pack significantly better. When subdividing the icosahedron (see [153, 194], subdivided nodes are projected on the sphere surface), one or two times, the packings become identical to the sphere packing. All the triangulated shapes pack significantly worse than cubes. It should be pointed out that these results cannot necessarily be generalized to different shapes and relative sizes of the container.

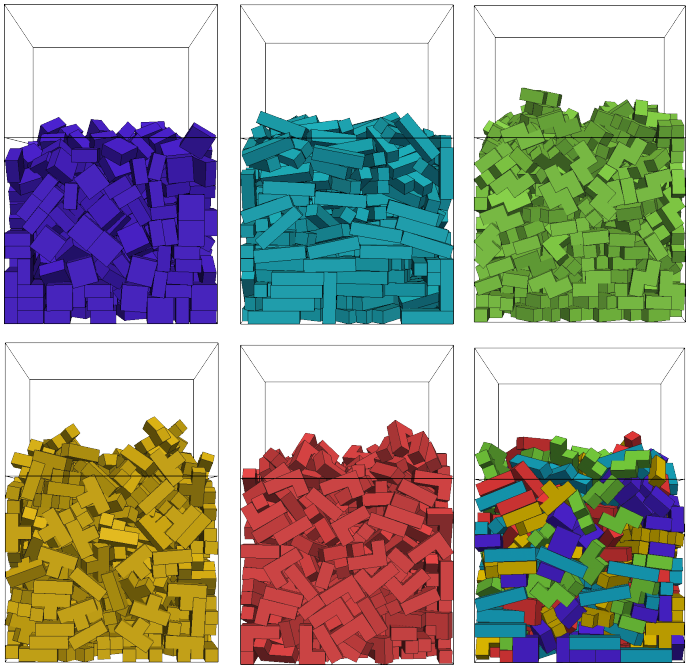

Figure 4.5: Gravitational deposition of tetris blocks. From left to right, top to bottom: square shapes, I-shapes, Z-shapes,T-shapes, L-shapes and a random mixture of all blocks. The plane indicates the level of 33% porosity as indicated in Fig. 4.2. All shapes have identical volume and mechanical properties as the cubes, described in Table 4.1.

It is not surprising that the packing density from gravitational deposition for cubes is higher than for spheres, tetrahedra, or icosahedra, as its theoretical maximal packing density in a rectangular container is much higher. To investigate this further, we performed simulations of gravitational deposition of non-cubical objects with rectangular, orthogonal facets. For this, shapes are introduced which are used in the game “Tetris”. These simulations serve to investigate packing factors from gravitational deposition for objects with very high maximal theoretical packing densities, as well as to demonstrate the applicability of the model to non-convex shaped bodies.

4.3.3 Packing of shapes with concavities

Again, the volume and mass of the shapes is chosen to correspond with the cubes as described by Latham et al. [111]. Simulations are performed with squares, I-shapes,

L-shapes, Z-shapes, and a mixture of these five. Fig. 4.5 shows the final packings of these shapes after gravitational deposition in a rectangular box. Again, the horizontal plane corresponds to a porosity of 33 %. The mean packing factors $\hat{P}$ - see Eq. (4.17) - are summarized in Fig. 4.4. All these shapes pack significantly worse than cubes. Moreover, a clear distinction can be made between the purely convex rectangular shapes (I-shapes and squares), which yield higher packing densities than spheres, and shapes also containing concave regions (Z-shapes, L-shapes and T-shapes) which pack significantly worse than spheres. Although these shapes could theoretically result in very high packing densities in a rectangular container, their concave regions create shielded empty spaces during gravitational deposition, which cannot be filled without fluidizing a large region of particles.

Interestingly, the mixture of all shapes packs better than the concave-shaped particles alone. We hypothesized that a linear combination of the packings densities of each shape, weighted by their fraction in the mixture, could be used as a predictor for the mixture packing factor. However, this would predict a significantly higher packing density. An explanation for this discrepancy could be that the chance of alignment of the rectangular shaped bodies is sharply reduced by the disorder caused by the concave-shaped particles.

4.3.4 Computational performance

In order to assess the computational performance of the proposed method a simulation was constructed of particles in a rotating cylinder ($\varnothing$ =40 cm, angular velocity ω =2 s^{-1}). This set-up was chosen because the system evolves to a steady-state flow in which the average forces, velocity and number of contacts remains conserved. We compare between spheres, cubes and a detailed triangulated mesh of a nut-shape composed out of 444 triangles/particle (see Fig. 4.6). The total number of particles was varied, and the length of the cylinder adapted to roughly conserve the filling height in the cylinder between different particle numbers. Times are reported for simulating steady-state flow during 8000 time steps (timestep: 4×10^{-5} s). Simulations were run single-threaded on a desktop CPU (AMD opteron 6370).

Table 4.2: Total computational time (s) to simulate 3000 spheres, cubes and nuts for 8000 time steps in a rotating drum (see Fig.4.6) on a desktop CPU (AMD Opteron 6378 Processor).

Shape	Spheres	Cubes	Nuts
Time (s)	42.29	$1.43 \cdot 10^3$	$1.23 \cdot 10^4$

Table 4.2 reports the times for systems of 3000 particles. As the particle shape gets more complex, the computational times greatly increase. Fig. 4.7 shows the scaling

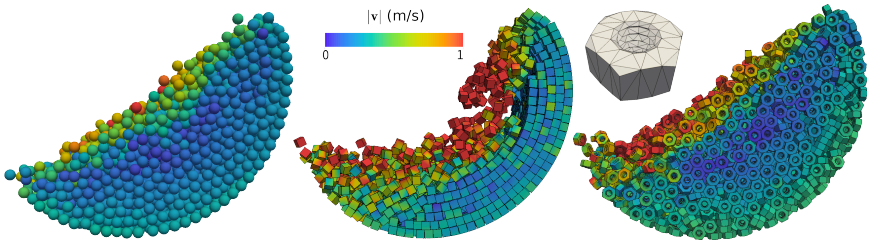

Figure 4.6: Comparison of simulations of 3000 particles in a rotating drum for spheres **(left)**, cubes **(middle)** and a complex "nut" mesh **(right)**, with the color scale indicating magnitude of velocity. Snapshots were made at $t = 10s$.

of the computational cost with the number of contact primitives N_{prim}. For all three shapes, the computational time scales quasi-linearly with N_{prim}. For simple polyhedral shapes, for which the facets span the complete size of the particle, like cubes, the average cost per primitive is higher than for spheres. Indeed, a typical cube-cube collision involves at least four intersecting squares (corner-plane contact). Moreover, the average computational effort per primitive is higher due to the more complicated geometrical calculation – e.g. Eq. (4.6) and Eq. (4.7). Interestingly, however, the calculation time per contact primitive decreases for the more complicated particles. As overlap distances in DEM are typically very small, the number of contacting primitives between two particles only slightly increases when the particle mesh gets more refined. This last point emphasizes the strength of the proposed method. An optimized grid-based contact detection algorithm ensures that only nearly colliding primitives are selected as contact candidates. As illustrated, the simulation of a large number of highly detailed particles is feasible within a reasonable computation time. A study on the computational performance of a similar approach but for rounded bodies can be found in section 3.3.4.

4.4 Conclusion and Outlook

In this chapter, a novel method was presented for simulating arbitrarily-shaped particles consisting of polygonal facets in the Discrete Element Method. Two bodies in contact are simulated as a set of interacting polygon-shaped contact primitives. As these primitives only need to contain local information about the geometry and mechanical properties, the method provides a very flexible framework to simulate contact interactions between particles of any shape and potentially non-uniform mechanical properties. Since there is no need for determining a unique contact point and normal unit vector for the contact between two arbitrary shapes, the method is not restricted to convex bodies and does not require disassembling arbitary shapes into

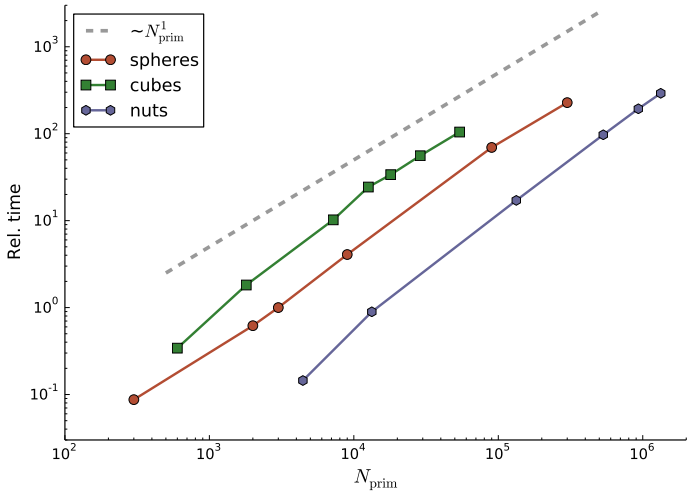

Figure 4.7: Computational time (relative to a simulation of 3000 spheres) as a function of number of contact primitives for spheres, cubes and nut-shapes. The dashed guide-line shows a linear scaling.

sets of convex bodies. It was shown that the computational cost scales quasi linearly with the number of contact primitives / particles and that - although introducing a clear additional overhead for “simple” shapes - the relative computational efficiency scales favorably when the particle shape becomes more complex. Furthermore, because each polygon-polygon contact can be individually resolved without information of the surrounding primitives, the method lends itself very well for parallelization.

The presented method has been validated by comparing to the gravitational deposition of cubes experimentally measured and simulated by Latham et al. [111, 143] and Wachs et al. [224]. After replicating the measured porosity for cubes, we calculated packing factors from simulations of gravitational deposition for various other particles shapes. Moreover, it was verified that the packing density converges to the solution for exact spheres when the polyhedral shapes approaches the sphere.

Conclusions on these packing densities cannot be drawn independent of the (rectangular) shape of the container. Nonetheless, both spheres and tetrahedra have been shown to pack significantly worse than beams. For beams, the packing factor decreases with increasing aspect ratio. It is well known that porosity in packings increases with particle elongation [240]. This has been attributed to the growth of the orientation average excluded volume [109]. When composites of multiple beams contain concave regions, the packing factor is strongly reduced.

In the future this method could be used to investigate the effects mixtures of different

particle shapes have on the geometry and mechanics of packings, heaps and on particle flow behavior. As previous research has pointed out [7, 24, 127, 182], approximating particles in granular materials as spheres is often insufficient to predict stability and dynamics of flow. Having a robust and efficient method available to account for arbitrary particle shapes will help to better simulate and eventually better understand these systems.

Acknowledgements

This research was funded by the *Agency for Innovation by Science and Technology in Flanders (IWT)*, grant nr. 111504.

Chapter 5

Deformable cell model

Adapted from [153]:

Odenthal, T., Smeets, B., Van Liedekerke, P., Tijskens, E., Van Oosterwyck, H., Ramon, H. (2013). Analysis of initial cell spreading using mechanistic contact formulations for a deformable cell model. PLoS Computational Biology, 9 (10), e1003267.

5.1 Introduction

The dynamics of initial cell spreading – that is during the first few minutes – are governed by energy release through binding events of cell surface molecules, rather than by active cellular processes such as e.g. tension generated by stress fibers. These molecular binding events dominate the total adhesion energy of the cell. This adhesion creates a pulling effect that in turn generates strong local forces which result in deformations of the actin cortex. The dynamics of initial cell spreading (the increase of radius of the contact area with time t) universally correspond to an early ($\sim t^{1/2}$), and a later ($\sim t^{1/4}$) power law behavior [29]. It is only at an advanced stage when the cell is already moderately spread out that active pulling of actin stress fibers on focal adhesion complexes will reinforce cell spreading, depending on the cell type in question, see e.g. [93].

The viscoelastic behavior of the cell boundary is determined not so much by the cell membrane itself but by the intracellular cytoskeleton, or, in the case of red blood cells (RBCs), a network of spectrin filaments directly underlying the membrane [50, 51].

A model that can be used for describing cellular mechanics should be able to accurately

describe the mechanical interactions that take place at the cell boundary, i.e. the contact interface with its substrate, the extracellular matrix or surrounding cells. Lattice-free, particle-based methods can describe the interaction forces and the resulting movement and deformation of particles in a natural way. At a point of contact between two particles, contact forces are calculated explicitly based on an appropriate contact force model. From these forces, movement of the particles is calculated by integrating the equation of motion. In the simplest approach, particles are assumed to be spherical. In that case, contact forces can be directly calculated from the sphere-sphere overlap distance $\delta = r_1 + r_2 - \|\mathbf{x}_1 - \mathbf{x}_2\|$ ($r_{1,2}$ are the radii of the spheres and $\mathbf{x}_{1,2}$ the spatial coordinates of their centers). Calculating contact forces for non-spherical shapes is more challenging: approximations have to be made for the contact force model and it is not trivial to calculate a meaningful overlap distance for all cases. Arbitrary shapes have been modeled by using combinations of connected overlapping spheres [127] or by using polyhedra or polyarcs and calculating a contact force proportional to the overlapping volume of the shapes [134, 164]. Besides, the surface of an arbitrary shape can be approximated by sampling points [200]. For each sampling point, a contact force can be calculated based on the indentation in the surface of another object. Disadvantages of using sampling points include that it is hard to directly compare it to a physical contact model such as the Hertz model for spheres, that they generally do not allow to reach complete force equilibrium, and that the precision of the approximation of the contact depends crucially on the local density of nodes, so that the contact parameters need to be re-scaled for different node densities [200].

We present a novel computational framework for describing the mechanical behavior of cells with an emphasis on the interaction between the cell and its environment. Although we only apply this model to cell spreading on a flat surface, the current implementation already allows for more complex settings of interaction with arbitrarily shaped smooth bodies, and cell-cell interaction.

The main novelty of the method developed in this work lies in the fact that we calculate contact between a triangulated surface with "rounded" triangles reflecting the local curvature of a cell and its microenvironment by applying Maugis-Dugdale theory (see section 5.2.1) to all contacting triangles. To apply this adhesive contact model for the triangulated surfaces in our models, we build on the following six ideas (see section 5.2.3):

1. The triangulated surface can locally be approximated by spheres, i.e. a specific curvature is assigned to each triangle, see section 5.2.3.

2. All contact forces are normal to the intersection plane, which is defined by (encompassing) sphere-sphere or sphere-plane intersection. An in-depth discussion is provided in appendix A.1.

3. For the approximation of a spherical surface, the sum of all contact forces on the individual triangles must be equal to the appropriate continuum-mechanics force response and the contact parameters should not depend on the chosen mesh. For details on this, we refer the reader to appendix A.3.

4. To integrate the contact force on each single triangle, quadrature rules can be used to calculate approximate pressures in specific points of the triangle. The details of this are discussed in section 5.2.3.

5. Having thus calculated the force on each triangle, it must be distributed to the nodes of the triangulation. This is done such that total force and moments of the pressure contributions on that triangle are conserved. Details are to be found in section 5.2.3.

6. Finally, an over-damped equation of motion (comparable to [44]) is solved for the nodes of the triangulation, see section 5.2.5.

This novel contact model is combined with a new implementation derived from existing mechanical models for red blood cells, mainly from Fedosov et al. [32, 50]. That model has been previously computed using a dissipative particle dynamics (DPD) solver, a different meso-scale simulation method. The mechanical model of the cortex of the RBC includes finitely extensible nonlinear elastic (FENE) connections and viscous dissipation between the nodes of the triangulation, volume conservation and surface area conservation, as well as bending resistance – see section 5.2.4.

Finally, we apply this newly developed method to an in-depth computational investigation of RBC spreading (see Fig. 5.1 and supplementary Videos S1 and S2 in [153]) as reported by both Hategan et al. [77] and Cuvelier et al. [29] in order to unravel the governing mechanisms.

5.2 Models

To explain the model developed in this work, Maugis-Dugdale theory is briefly summarized. Building on this theory, an in-depth description of the application of this theory to the contact mechanics of a cell with its mechanical microenvironment is given. Finally, we explain the integration of that model with an existing mechanical model for the cortex of a red blood cell.

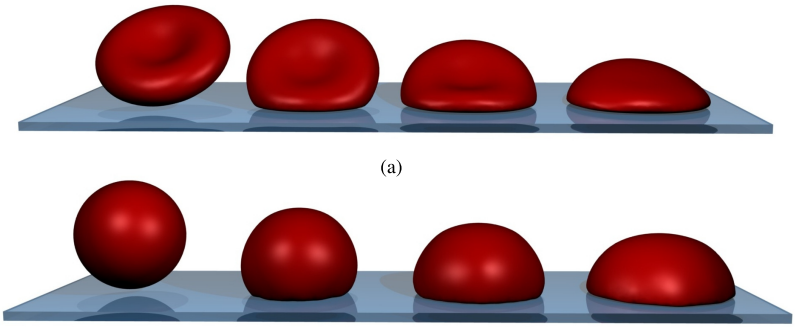

(a)

(b)

Figure 5.1: Simulated cell spreading of the red blood cell at three different time-points. **(a)** biconcave RBC spreading. **(b)** "sphered" RBC spreading. From left to right: no contact at $t = 0\,\mathrm{s}$, early contact at $t = 0.1\,\mathrm{s}$, approximately the cross-over between the two regimes at $t = 0.3\,\mathrm{s}$ and the fully spread cell at $t = 1\,\mathrm{s}$. The biconcave RBC has approximately 40% less volume than the osmotically swollen spherical red blood cell.

5.2.1 Maugis-Dugdale Theory

For two spherical asperities in contact or one asperity in contact with a flat surface (see Fig. 5.2), Maugis-Dugdale (MD) theory can be used to describe the contact mechanics [135]. This theory captures the full range between the Derjaguin-Muller-Toporov (DMT) zone of long reaching adhesive forces and small adhesive deformations to the Johnson-Kendall-Roberts – JKR, see Eq. (2.3) – limit of short interaction ranges and comparatively large adhesive deformations in the transition parameter. The transition parameter λ relates to the Tabor coefficient by a factor of 1.16 [97].

$$\lambda = \sigma_0 \left(\frac{9\hat{R}}{2\pi W \hat{E}^2} \right)^{1/3}. \tag{5.1}$$

In Eq. (5.1), σ_0 is the maximum adhesive tension (measured in Pa) from a Lennard-Jones potential, W (in J/m^2) the adhesion energy, and $\hat{R}$ and $\hat{E}$ are as defined in Eq. (2.4).

The (repulsive) Hertz pressure $p_{H,e}(r)$ associated with a contact of radius a is given by Eq. (3.2). An adhesive stress can be formulated as [99, 135]:

$$p_a(r) = \begin{cases} -\frac{\sigma_0}{\pi} \arccos\left\{ \frac{2a^2 - c^2 - r^2}{c^2 - r^2} \right\}, & 0 \le r \le a, \\ -\sigma_0, & a \le r \le c. \end{cases} \tag{5.2}$$

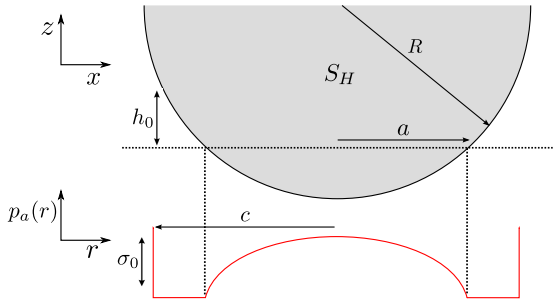

Figure 5.2: Half-sphere S_H with radius R indenting a flat plane and adhesion stress p_a according to the Maugis-Dugdale model.

In the Maugis-Dugdale model, local adhesion tension is assumed to be independent of the overlap until a cut-off distance h_0. If the asperity is further than h_0 away from the flat surface, the adhesive tension drops to zero. Therefore, σ_0 is related to the adhesion energy W as:

$$W = h_0 \sigma_0. \tag{5.3}$$

W is the total work of adhesion, i.e. the work required to move the asperity away from the surface and out of contact. To pull a small area dA out of contact, the required work w is:

$$w = 2W \, \mathrm{d}A. \tag{5.4}$$

The total (global) adhesive force is the integral over the contact zone with radius c, which according to [99] becomes:

$$F_a = -2\sigma_0 \left\{ c^2 \arccos\left(\frac{a}{c}\right) + a\sqrt{c^2 - a^2} \right\}. \tag{5.5}$$

The force in Eq. (5.5) is dependent on a. As Eq. (5.5) expresses the global adhesive force of the complete asperity, it is not a constant force, but through a dependent on the indentation. To calculate the adhesive radius c from the actual geometrical contact area with radius a, the height at the edge of the adhesive zone $h(c) = h_0 = W/\sigma_0$ can be calculated out to be [97]:

$$\begin{aligned} 1 \quad = \quad & \frac{\lambda}{2}\left(\frac{a^3\hat{E}}{3\pi W\tilde{R}}\right)^{2/3} \cdot \left[\left(m^2-2\right)\sec^{-1} m + \sqrt{m^2-1}\right] \\ & + \frac{4\lambda^2}{3}\left(\frac{a^3\hat{E}}{3\pi W\tilde{R}}\right)^{2/3} \cdot \left(\sqrt{m^2-1}\sec^{-1} m - m + 1\right), \end{aligned} \tag{5.6}$$

where $m = c/a \, (\in \mathbb{R}^{>1})$. In general, to calculate both c and a from a given state of the contact, one needs to solve this equation simultaneously with the equation for the net

contact force [97]:

$$\|\mathbf{F}\| = \frac{a^3\hat{E}}{3\pi W\hat{R}^2} - \lambda\left(\frac{a^3\hat{E}}{3\pi W\hat{R}^2}\right)^{2/3}\left(\sqrt{m^2-1} + m^2\sec^{-1}m\right). \tag{5.7}$$

A very well validated contact model for soft, adhesive bodies like cells, the JKR theory [8, 25, 98], is a limiting case of Maugis-Dugdale theory for negligible cutoff-distance for the adhesive interaction h_0 (or $\lambda \gg 1$) . It has therefore a parameter less than MD theory. The adhesive pressure according to JKR – compare to Eq. (5.2) – is

$$p_a(r) = \frac{F_{ij}}{2\pi a_{\mathrm{JKR}}^2}\left(1 - \frac{r^2}{a_{\mathrm{JKR}}^2}\right)^{-\frac{1}{2}}. \tag{5.8}$$

Note that this pressure diverges at $r \equiv a_{\mathrm{JKR}}$.

Summarizing the Maugis-Dugdale theory for an adhesive contact, one considers three distinct zones:

- The Hertz-zone with contact radius a, in which Hertz' theory determines the repulsive pressure. Apart from that, there is also an adhesive tension present in this contact zone.
- A purely adhesive zone with width $c-a$, in which no actual contact is formed but a constant adhesive tension is present. The adhesive force in this zone is determined by comparatively long-range interactions.
- At the edge of that adhesive zone, no interactions take place anymore, and contact pressures and tensions vanish.

5.2.2 Generating triangulated meshes of cells

The meshes used in this work are derived from spherical shapes by subdividing an icosahedron and projecting the nodes on a sphere [219]. In a subdivision, each triangle gets split into four triangles as is illustrated in Fig. 3.1. Here it is shown how one triangle with an encompassing sphere matching the local curvature of the cell is split into four triangles. Since the local curvature is kept, the new triangle nodes are all located on the surface of the same encompassing sphere. Every subdivision of an icosahedron has only twelve nodes with a five-fold connectivity and slightly longer distances to their neighbors; otherwise, the mesh is perfectly regular with six-fold connectivity and is ideal for curvature calculations (see section 5.2.3) as reported by [233].

The bi-concave shape of an RBC can be obtained by reducing the volume of the sphere to approximately 60 %, and letting a system of linear springs with appropriately chosen parameters relax again. This is the reverse process to the well described technique of RBC sphering, see e.g. [59].

We use meshes of either four or five subdivisions of an icosahedron, corresponding to 642 and 2562 nodes, respectively.

5.2.3 Contact mechanics of a triangulated surface

Local curvature of the 3D shape

Interaction between a surface and its surroundings is calculated as the interaction between two spheres, since this is an implicit requirement for Maugis-Dugdale theory. To that end, the encompassing sphere of each surface triangle is used. The outward side of the triangle is defined to be convex. This is a practical consideration: theory only requires $\hat{R}$ to be positive – see Eq. (2.4) – so in cases where particles with only relatively high convex curvature come in contact with particle(s) with relatively lower concave curvature (e.g. cells in a test-tube), this restriction can be relaxed. The radius of the encompassing sphere is calculated to correspond to the local inverse curvature of the triangulated surface. Calculation of of this local curvature is described in detail in section 3.2.1. The radius of curvature changes when the cell deforms, and the local curvature has to computed at each iteration during a simulation.

It should be noted, that a minimum curvature $\frac{1}{2}\|\mathbf{K}\| > 0$ is prescribed to avoid "infinite" radii. This becomes necessary to calculate contact forces in completely flat parts of the contact – here, the contact force is generally close to zero since the contact should be already equilibrated. Although the calculation of the adhesive range c in MD theory loses accuracy by this artificial curvature, the force integration should still be a reasonable approximation, since all integration points (see below) can be expected to be in the "close contact" range a in this case.

Integrating the force on a triangle from the pressure distribution

When two triangulated surfaces come into contact, the contact potential is calculated from the overlap of their respective encompassing spheres. For two contacting spheres, there will be a circular contact area between the two of them, which also defines the direction of "normal" and "tangential" forces for this contact. If the two spheres are physical spheres, the contact point C_{Hertz} will always be located at the center of this circular area since at this point the overlap distance δ – see Fig. 3.1(b) – will be maximal. In the case of contacting triangles, however, only a fragment of the sphere is

physical and it has to be checked that a contact force needs to be calculated – appendix A.1 details how that can be done for any pair of rounded triangles. The cases of a contact with a sphere or a (polygonal) plane are dealt with analogously.

If the check asserts that a contact force can be expected between the triangles (or the triangle and a plane, etc.), for computational reasons we distinguish two regimes: In the first case, the contact area between the encompassing spheres is relatively large (see below, Eq. (5.9)). In this case, we can assume a relatively big, well established contact between the two surfaces. Therefore, we need to integrate the pressures in equations (3.2) and (5.2). This integral is approximated using Eq. (3.10) and Eq. (3.11).

The divergence in the JKR adhesive stress – Eq. (5.8) – makes it difficult to numerically integrate. For this reason and the added flexibility of MD theory, we chose this more general framework. Since the radius of intimate contact, a, is directly known as the radius of the intersection circle of the two encompassing spheres, we only have to solve Eq. (5.6) numerically for m to obtain the adhesive contact radius c – used in Eq. (5.2). The pressure $p(r_i)$ is evaluated in the positions corresponding to those quadrature points. Additionally, we sum up the moments of each individual force component with respect to the center of the contact plane using Eq. (3.12).

If the area of contact between the two encompassing spheres is relatively small compared to the typical area of each integration point:

$$\pi c^2 < 2A_{\triangle}/N_Q, \tag{5.9}$$

we can expect a bad approximation for force and moment. Therefore, a different approach is chosen: The integrated MD force – Eq. (5.7) – calculated from the total area of contact of the encompassing spheres can be scaled with the fraction of the area, which is contained in the intersection of the two triangles. This total force is then applied to the contact point C_{Hertz}, if the point is within the triangle's intersection, or the point closest to it in that intersection polygon. In this case, the moment is still calculated according to Eq. (3.12), although the sum only contains the one force and radius vector.

This second approximation for the forces and the moments one triangle of the body is subject to is insufficient for bigger overlaps, because the moments generated by the repulsive and adhesive pressures described in Eq. (3.2) and Eq. (5.2) differ profoundly from that simple approximation. For small overlaps, it is obvious from Eq. (3.12) that the moment is close to $\mathbf{0}$ since the lever length $\mathbf{r}$ is very short, anyway.

The contact force calculated in this way does not depend on the chosen mesh – see appendix A.3.

Distribution of force to the nodes of the triangulation

Eq. (3.14) in section 3.2.5 explains how a set of contact forces and moments on each triangle can be converted to pure forces on each node. For deformable bodies, these nodes respresent degrees of freedom, and can therefore be directly used in solving the equations of motion.

5.2.4 Elastic model of the cortex

In the deformable cell model, the cortex nodes interact through viscoelastic potentials. In the most simple approach, a linear elastic spring could be used. For a given displacement of nodes i and j, the elastic spring force over a connection is:

$$F_{\text{Linear}} = k_s\,(d_{ij} - d_{ij}^*), \tag{5.10}$$

in which d_{ij} and d_{ij}^* are the actual distance and equilibrium distance between connected node i and j. The linear spring stiffness is called k_s. For red blood cells, two non-linear spring models have been used in literature: the finite extensible non-linear elastic model (FENE) and the worm-like chain model (WLC) [50]. These models express that upon stretching, the biopolymers of the cytoskeleton – a sub-membranous network of spectrin connections for RBCs – first uncoil, providing relatively little resistance, but when completely stretched out, become practically non-extensible.

Between two connected nodes i and j, the FENE attractive potential reads:

$$U_{\text{FENE}} = -\frac{k_s}{2}\,d_{\max}^2\,\log\left[1 - \left(\frac{d_{ij}}{d_{\max}}\right)^2\right], \tag{5.11}$$

where d_{max} is the maximal distance, and k_s the stretching constant. The force derived from this is:

$$F_{\text{FENE}} = -k_s\,d_{ij}\left[1 - \left(\frac{d_{ij}}{d_{\max}}\right)^2\right]^{-1}. \tag{5.12}$$

It is convenient to denote the term $\frac{d_{\max}}{d_{ij}^*}$ by $x_{\max}$, the fraction of maximal extension and equilibrium distance.

FENE springs exert purely attractive forces. In order to account for the (limited) incompressibility of the spectrin, a simple power law is used (power L):

$$F_{\text{POW}} = \frac{k_c}{d_{ij}^L} \tag{5.13}$$

The incompressibility coefficient k_c can be derived for the assumption that the total force must vanish for $d_{ij} \equiv d_{ij}^*$:

$$k_c = k_s \left(d_{ij}^*\right)^{L+1} \left[1 - \left(\frac{d_{ij}^*}{d_{\max}}\right)^2\right]^{-1} \tag{5.14}$$

In the present model, we set $L = 2$, as suggested by [50]. In addition to this purely elastic potential, we also include dissipation as per the Kelvin-Voigt model by adding a parallel dashpot with the damping constant c:

$$F_{\text{Dashpot}} = -c\,\hat{\mathbf{n}}_{ij} \cdot \mathbf{v}_{ij}. \tag{5.15}$$

Here, $\hat{\mathbf{n}}_{ij} \cdot \mathbf{v}_{ij}$ is the projection of the relative velocity of a pair of connected cortex nodes on their connecting axis. The force is also applied in the direction of the connection.

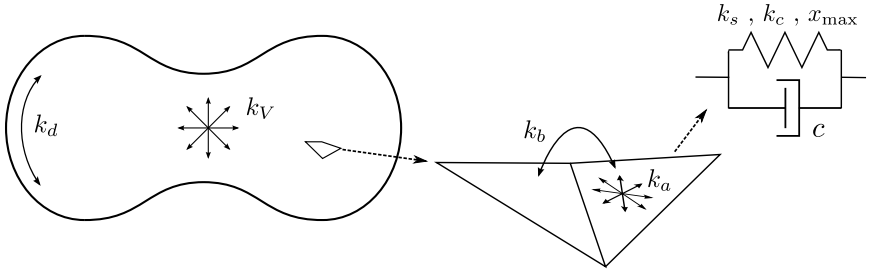

Figure 5.3: Schematic overview of the mechanical representation of the cell's cortex, with relevant mechanical parameters indicated. **Left**: the complete cell is composed out of a closed triangulated mesh with volume conservation (k_V; Eq. 5.2.4) and global area conservation (k_d; Eq. 5.2.4). **Middle**: two adjacent and connected triangles offer a bending resistance when rotating around their common axis (k_b; Eq. 5.2.4) and each triangle tries to conserve its area (k_a; Eq. 5.2.4). **Right**: a connection between two mesh nodes (which are degrees of freedom) acts like a spring-damper, with a linear dashpot (c; Eq. 5.15) and a FENE spring force with stretching coefficient k_s (Eq. 5.12), incompressibility coefficient k_c (Eq. 5.2.4) and maximal spring extension $x_{\max}$ (Eq. 5.12).

Whereas in-plane stretching and compressive forces can be calculated purely based on the distance between two neighboring cortex nodes, bending forces are calculated for two neighboring triangles. The bending moment between two adjacent triangles is given as

$$M = k_b \sin\left(\theta - \theta^*\right). \tag{5.16}$$

Here, k_b is the model parameter determining the bending rigidity, θ is the instantaneous angle and θ^* the spontaneous angle between a pair of triangles with a common edge. A

corresponding force is applied to the non-common points of each of the two triangles, with a compensating force applied to the points on the common edge, ensuring that the total force on the cell remains unchanged. This type of bending-stiffness is commonly found in the literature for RBC models, eg. by [51] and [39] - a more general analysis is provided by [13].

Additionally, both a global and local area constraint[1] is used, making sure that both the individual triangle areas and the total area of the red blood cell can not strongly increase or decrease. As described by [51], this is achieved by a local force with magnitude:

$$F_{A,\text{local}} = k_a \left(A_\triangle - A^*_\triangle\right), \tag{5.17}$$

in which $A_\triangle$ is the triangle area, $A^*_\triangle$ the resting triangle area and k_a the local constraint constant. The magnitude of the global force is formulated as:

$$F_{A,\text{global}} = k_d \left(A_{\text{tot}} - A^*_{\text{tot}}\right), \tag{5.18}$$

where A_{tot} is the total RBC area, A^*_{tot} the total resting area and k_d the global constraint constant. For both constants, values were taken from [50]. These forces are applied in the plane of each triangle in the direction from the barycenter of the triangle.

Finally, we add a volume constraint since for short timescales, the total cytosol volume of the cell can be considered constant. As for the area conservation, the magnitude of the force takes the form

$$F_{\text{volume}} = k_V \left(V - V^*\right), \tag{5.19}$$

with the instantaneous cell volume V and the initial cell volume V^*. This force is applied to each node of the cell in its outward direction as found by the Laplace-Beltrami operator, see Eq. (3.1). The contributions of each mechanical cortex parameter, and the geometry on which they operate are summarized in Fig. 5.3.

5.2.5 Equation of motion

In the low Reynolds number environment in which cells live, motion is dominated by viscous forces [167]. In other words, inertial forces are negligible. For each integration node, Newton's second law (with explicit Stokes' drag)

$$\mathbf{F}^i = m\mathbf{a}^i + \zeta \mathbf{v}^i, \tag{5.20}$$

[1] It should be noted that these are not true "constraints" in the traditional sense of the word, since they are not exactly enforced, but only approximated using a penalty function.

by leaving out the inertial term and specifying all distinct force components, becomes

$$\begin{aligned} & \sum_{\text{triangles } l} \mathbf{F}^{il}_{\text{contact}} + \mathbf{F}^{il}_{A,\text{local}} + \mathbf{F}^{il}_{A,\text{global}} \\ + & \sum_{\text{conn. } k} \mathbf{F}^{ik}_{\text{FENE}} + \mathbf{F}^{ik}_{\text{POW}} + \mathbf{F}^{ik}_{\text{bend}} \\ + & \mathbf{F}^{i}_{\text{volume}} + \mathbf{F}^{i}_{\text{gravity}} + \mathbf{F}^{i}_{\text{random}} \\ = & \sum_{\text{triangles } l} \Gamma^{il}_{\text{substrate}} \mathbf{v}^i + \sum_{\text{conn. } k} c(\mathbf{v}^i - \mathbf{v}^k) + \Gamma^{i}_{\text{liquid}} \mathbf{v}^i. \end{aligned} \tag{5.21}$$

The total force on node i is the sum of all the individual forces: Firstly, the forces that are calculated on the triangles are transferred to the nodes – the contact forces $\mathbf{F}_{\text{contact}}$ only exist for triangles, which are in contact with the substrate. Also, the local and global area constraints for the membrane are added here. Secondly, the cortex connection forces between node i and all fixed connections k are added, and finally the volume constraint and the gravitational force $\mathbf{F}_{\text{gravity}}$ as well as a random force $\mathbf{F}_{\text{random}}$ for taking into account fluctuations of the membrane can be added. Since those fluctuations do not much influence the spreading dynamics in our simulations, we neglect that term for the results presented.

For the right-hand side, we not only discard the term proportional to mass, but we also more explicitly state the components of the constant ζ: Starting with the dissipative/friction term generated from the encompassing sphere - encompassing sphere friction between two contacting triangles $\Gamma_{\text{substrate}}$. This coefficient is weighted by the distance of the node i from the contact point in that triangle. This ensures symmetry of the friction-matrix (see below) and corresponds to the distribution of the contact force. The component of the substrate friction for a triangle is defined as (compare to e.g. [87]) $\Gamma_{\triangle} = A^C_{\triangle} \left[\gamma_n \hat{\mathbf{n}}\hat{\mathbf{n}}^{\mathrm{T}} + \gamma_t \left(\mathbf{I} - \hat{\mathbf{n}}\hat{\mathbf{n}}^{\mathrm{T}}\right)\right]$ where $A^C_{\triangle}$ is the area of contact in that triangle, $\hat{\mathbf{n}}$ is the normalized direction vector between the two encompassing spheres and γ_n, γ_t are, respectively, the normal and tangential friction constants.

Secondly, we have the dissipative dashpot of the connections of this node, and lastly we add the drag coefficient Γ_{liquid} for the whole cell in plasma: here, in a first order approximation, we simply divide the formula from Stokes' law by the number of nodes per cell, thereby recapturing the exact result for a spherical cell in Stokes flow.

For nodes, whose surrounding triangles are all in contact with the substrate, we define a very high friction constant $\Gamma^i_{\text{substrate}}$, effectively fixing those nodes in place. We found that this has no influence on the spreading curves (it can be completely left out), but helps to dampen out small numerical fluctuations in the stiff potential of the contacting plane. This allows us to use bigger time steps Δt when solving this equation of motion.

Eq. (5.21), which is used in essentially the same form by e.g. [61, 87, 88, 105, 171, 218], is a first order differential equation, which couples the movements of all particles together. The whole system can be expressed as:

$$\mathbf{\Gamma} \cdot \mathbf{v} = \mathbf{F}, \tag{5.22}$$

which is identical to Eq. (2.2). However, in this case, the degrees of freedom represent subcellular elements (nodes) and not complete cells. Still, it can be shown [218], that the matrix $\mathbf{\Gamma}$ is positive definite, and therefore we are able to solve the system iteratively for the velocities by using the conjugate gradient method. Subsequently, the nodes' movement is integrated by a forward Euler scheme. For a low Reynolds number environment, the amount of kinetic energy (or motion) directly corresponds to the amount of dissipated energy. Eq. (5.22) shows all dissipative terms in the matrix $\mathbf{\Gamma}$ which dictates the degree of motion induced by the forces $\mathbf{F}$. Identifying all significant dissipative mechanisms is therefore crucial for calculating the dynamics of this system.

5.3 Results

To show the validity of the model assumptions concerning cortex mechanics, we first compare simulated red blood cell stretching to experiments reported in the literature [202]. A combination of FENE potentials with a power law for area incompressibility was used to model the elastic properties of the RBC cortex (see section 5.2.4).

5.3.1 Validation of the RBC cortex model

RBC stretching experiments

Using the deformable cell model, we perform cell stretching simulations in order to validate the elastic constants of the RBC with respect to optical tweezer measurements, in which a red blood cell is attached to two beads on opposite sides. In the experiment, the beads are pulled apart with a set force, and the deformation of the RBC is measured [202].

To simulate the RBC behavior, we pull on the outermost 5 % of the nodes with the same force, and wait until the system is equilibrated. The same parameters as used by [51] in their DPD model yielded comparable results for the presented model – see Table 5.1.

Figure 5.4(b) gives a visualization of the stretched RBC for stretching forces of 0, 50 and 150 pN. In Fig. 5.4(a) the change in both axial diameter D_A and transversal diameter D_T is shown for different cell stretching forces. This curve corresponds well

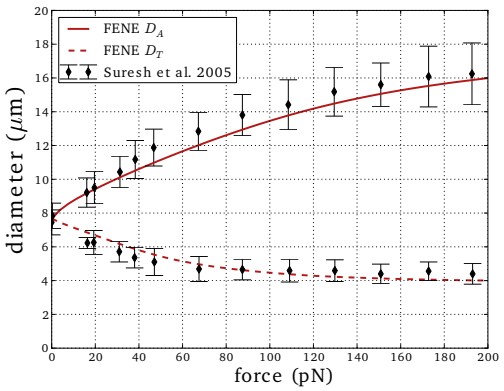

(a) Experiment vs. Simulation

(b) Top: 0 pN, middle: 50 pN, bottom: 150 pN

Figure 5.4: Simulation of cell stretching. **(a)** shows the change of axial diameter D_A and transversal diameter D_T in function of the stretching force, compared to experimental data from Suresh et al. [202]. **(b)** visualizes red blood cells for different stretching forces.

to the computational results presented in the paper of Fedosov et al. [51], who report a maximal axial diameter of 16 µm and a minimal transversal diameter between 4 and 5 µm at a force of 200 pN, as well as experimental data by Suresh et al. [202].

RBC Relaxation

In order to validate the dissipation constants of the cortex itself – see Eq. (5.15) – a relaxation simulation was performed. In this *in-silico* experiment, the cell is first stretched with a fixed force until a constant axial diameter D_A of approximately 8.9 µm is observed. Subsequently, the force is released and the change in D_A over time is monitored. For a liquid viscosity of blood plasma, we found that the cortex damping coefficient c should be chosen in the order of 5×10^{-7} Pa s to match experimentally observed RBC relaxation dynamics (Figure 5.5). In this case, the computational results are in good agreement with experimentally observed RBC relaxation times in the order of 0.1-0.3 s [218].

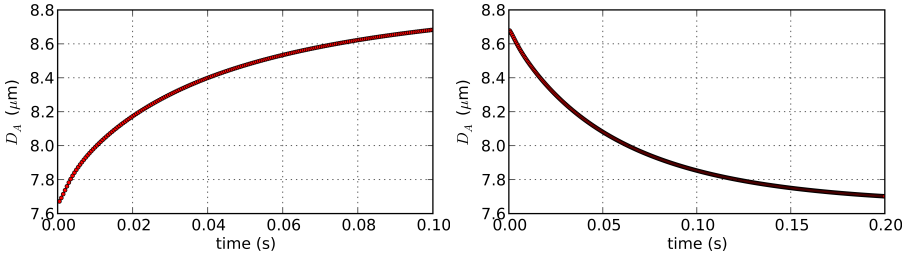

Figure 5.5: Computational results for cell relaxation. Left: cell stretching dynamics. Right: cell relaxation dynamics; cortex damping $c = 5 \times 10^{-7}$ Pa s.

5.3.2 Cell spreading experiments

In the experiments reported by Cuvelier et al. [29], biotinylated RBCs were osmotically swollen to become spherical and the change of the radius of the contact area with time was measured for spreading on a streptavidin coated surface. To compare to the spreading dynamics reported in that paper as well as by Hategan et al. [77] (where the cells spread on a polylysine coated surface), we set up simulations of the described model with the parameters as given in Table 5.1.

Table 5.1: Parameters used for the RBC-spreading model matching data from Hategan et al. [77]. *: Values matching data from Cuvelier et al. [29]: $W = 88 \times 10^{-6}$ J/m^2 (as reported in [29]), $\gamma_n = 200 \times 10^9$ N s/m^3, $\gamma_t = 120 \times 10^9$ N s/m^3, $\Delta t = 50 \times 10^{-6}$ s.

Parameter	Symbol	Value	Units	estimated from:
timestep*	Δt	$6 \cdot 10^{-6}$	s	trial runs
simulation time	T_{end}	1.2	s	[29]
conjugate gradient precision	e_{max}	$10 \cdot 10^{-15}$	N	trial runs
cell radius	r	$3.25 \cdot 10^{-6}$	m	surface area RBC [77]
medium viscosity	η	$0.8 \cdot 10^{-3}$	Pa·s	Blood plasma at 37 °C
Young's modulus cortex	E	$800 \cdot 10^3$	Pa	trial runs
Poisson's ratio	ν	0.4	-	[44]
tangential friction coef.*	γ_t	$6 \cdot 10^9$	N· s/m^3	"fitted", [61],[88]
normal friction coef.*	γ_n	$8 \cdot 10^9$	N· s/m^3	"fitted", [61],[88]
adhesion constant*	W	$1 \cdot 10^{-3}$	J/m^2	[29]
effective adhesive range	h_0	$20 \cdot 10^{-9}$	m	interpolated from [96]
FENE constant (stretch)	k_s	$3.2 \cdot 10^{-6}$	J	[50], [12]
maximal FENE stretch	$x_{\max}$	2.05	[-]	[50]
cortex bending constant	k_b	$240 \cdot 10^{-21}$	Nm	[50], [12]
cortex damping	c	$1.5 \cdot 10^{-6}$	Pa·s	relaxation exp.
local area constraint	k_a	$6 \cdot 10^3$	N/m^2	[50]
global area constraint	k_d	$6 \cdot 10^3$	N/m^2	[50]
volume constraint	k_V	$10 \cdot 10^3$	N/m^3	trial runs conserving V_0

The red blood cell is modeled with a viscoelastic cortex including bending stiffness and Maugis-Dugdale contact interactions. Most parameters in Table 5.1 are taken directly from the literature as indicated. The effective range of interaction h_0 – see Eq. (5.3) – was estimated at 24.8 nm by interpolating from [112] for cells with a radius of $\approx 3\,\mu$m. The cortex Young's modulus used in the Maugis-Dugdale model is the material stiffness of the phospholipid-spectrin complex (the elasticity of the deforming membrane is already taken into account by the FENE potentials). This material stiffness can be assumed to be much higher compared to the whole cell's Young's modulus and is set at a value of 800 kPa. The parameters for the cortex are validated by performing the cell stretching and relaxation experiments explained in the previous section 5.3.1.

5.3.3 Visual and static comparison to data

A view on three stages of the cell spreading for both biconcave and sphered RBCs is presented in Fig. 5.1. Note that the volume of the biconcave RBC is only about 60 % of the volume of the sphered RBC. As a result of that, for the sphered RBC, the final height of the spread-out cell is greater and it has a higher angle of contact compared to the final shape of the initially biconcave RBC.

For this simulation, a triangulation based on a five-fold subdivision of an icosahedron was used – see section 5.2.2. This level of mesh refinement is required to reproduce the final high curvatures at the edge of the contact area when the cell is fully spread out: The triangles at the edge have encompassing spheres with radii of ca. 200 nm, while Hategan et al. [76] report a typical radius of the rim for this situation of 125 ± 40 nm, which is of comparable order of magnitude.

The shape of the final spread-out cell is a spherical cap. By fitting a sphere through the top 95 % of the nodes, the effective contact angle [186] can be estimated. For the modeled RBC, we calculate an effective contact angle of $\approx 65°$, which corresponds reasonably well to the measured effective contact angle of around 60° [76].

5.3.4 Comparison to dynamic data & influence of parameters

Figure 5.6 shows the power-law behavior of the sphered RBC spreading in double logarithmic representation. The "contact radius" of the RBC r_{cc} in these and the following figures is calculated from the sum of all the triangles' areas which are in contact $A^C = \sum_\triangle A^C_\triangle$ by defining $r_{cc} = \sqrt{A^C/\pi}$. The spreading dynamics of the model match the experimentally observed cell spreading [77] very well.

Figure 5.7 summarizes the influence of varying one parameter at a time for the most influential parameters of the model starting from the base parameter set reported in

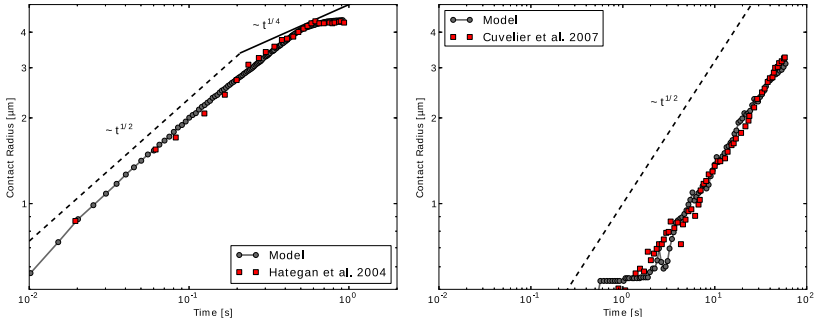

(a) Experiment Hategan et al. (b) Experiment Cuvelier et al.

Figure 5.6: Contact radius vs time for cell spreading simulations: comparison with experimental data from **(a)** Hategan et al. [77] for adhesion strength of 1 mJ/m^2 and with data from Cuvelier et al. **(b)** for adhesion strength of 88 µJ/m^2 – here, we use a coarser mesh with 642 nodes since the cell does not spread completely in the given time-frame and therefore does not exhibit the high local curvatures as in the Hategan et al. experiment.

Table 5.1. Its first sub-Fig. (a) shows simulation results of cell spreading for different values of the cell-substrate adhesion strength W. A lower adhesion strength results in a lower final contact radius, but also makes the spreading slower. However, the $\sim t^{1/2}$ power law behavior as reported by Cuvelier et al. [29] stays well conserved for different adhesion strengths.

The influence of the FENE stretching constant k_s is shown in Fig. 5.7(b). In the range of the RBC FENE constant (in the order of 1×10^{-6} N/m), the influence of k_s on the spreading dynamics is comparatively small. For larger deviations, higher values of k_s limit the final spreading radius to a lower value, or conversely, lower values allow the cell to spread considerably more.

A FENE connection is also characterized by the maximal stretch $x_{\max}$ (Fig. 5.7(c)), which expresses the maximal extension of the spring, at which the FENE force diverges – Eq. (5.12). The initial spreading dynamics are not affected by the precise value of $x_{\max}$, but the final spreading radius is. For higher values of $x_{\max}$, the same tension in the cortex corresponds to a larger extension and therefore a larger radius of the spread out cell.

The effect of the bending stiffness on RBC spreading is shown in Fig. 5.7(d). A higher bending resistance of the cortex speeds up cell spreading, the probable reason being that, through resisting to bending, the cortex keeps the contact angle within the effective range of adhesive interaction close to 180°. This range is of the order of 20 nm for microscopic biomolecular surfaces [112]. It should be noted that for a theoretical vesicle with bending resistance, the actual contact angle is always 180° [186]. However,

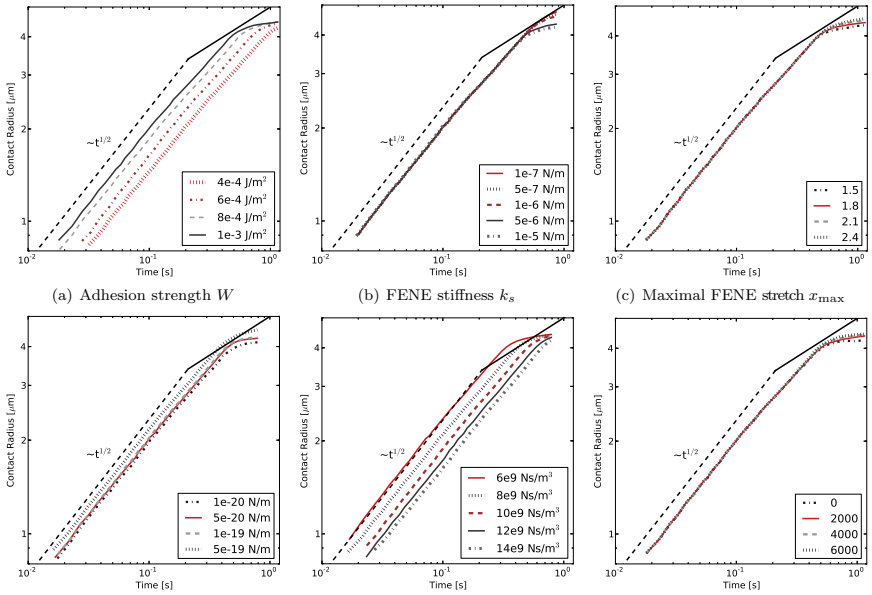

(a) Adhesion strength W (b) FENE stiffness k_s (c) Maximal FENE stretch $x_{\max}$

(d) Bending stiffness k_b (e) Normal friction γ_n (f) Local area constant k_a

Figure 5.7: **Variation of most influential model parameters.** Double-logarithmic plots of cell contact radius r_{cc} versus time. **(a)** varying cell-substrate adhesion strength W yields both a shift in speed and final contact radius. **(b)** varying the FENE stretching constant k_s yields different final contact radii, **(c)** varying the FENE max strain $x_{\max}$ also mostly influences the final contact radii, **(d)** varying bending stiffness k_b influences both spreading speed and final contact radius, **(e)** varying the normal friction coefficient γ_n influences spreading speed and **(f)** varying the local area constraint constant k_a influences the final spreading radius.
For a comparison of spreading rates, see supplementary Figure S1.

for a real RBC, the width of the adhesive spreading front is non-zero and determined by the effective range of interaction h_0. This effective adhesive range is taken into account in Maugis-Dugdale theory – Eq. (5.3) – and relates the maximal adhesive tension at the edge of contact to the total work of adhesion W.

The normal friction coefficient γ_n is determined by the energy dissipation when adhesive contact is initiated. The dissipation is caused by snap-in-contact events when adhesion molecules form bonds, and the hysteresis arising from unbinding stochastically again [112]. In Fig. 5.7(e), the effect of changing γ_n on the RBC spreading dynamics is shown. As could be expected, a lower value of γ_n diminishes the energy dissipation due to adhesion and therefore increases the rate of cell spreading. However it does not change the initial $\sim t^{1/2}$ power law behavior of cell spreading.

Finally, in Fig. 5.7(f), the effect of the local area constraint on the spreading dynamics is shown. When the value of k_a is too low, degenerate triangle shapes can arise with a strongly decreased area. This will result in an underestimation of the final spreading radius. It can be observed that for values of $k_a \geq 2000\,\mathrm{N/m^2}$, the local area of the triangles is sufficiently well conserved and the predicted spreading dynamics are not affected.

5.3.5 Evolution of forces acting on the cell

In Fig. 5.8(a), the outward normal pressure on the nodes is visualized for three distinct phases of the cell spreading process for a sphered RBC. The normal pressure is defined here as the magnitude of the sum of all conservative forces (on the left-hand side in the Equation of motion, (5.21)) in the nodes projected onto the normal in that node – therefore this normal pressure is dominated by contact forces, where adhesive ones yield a positive (outward) pressure in this case. Figure 5.8(b) shows the in-plane tension τ (in $\mathrm{J/m^2}$) of the cortex (further denoted as cortex tension, and not to be confused by the adhesive tension, given by Maugis-Dugdale theory, see Eq. (5.2)) at the same time points. This tension is characterized by the FENE force at the inter nodal connections. Positive forces in these connections correspond to tensile stress in the cortex, while negative values are associated with compressive stress:

$$\tau_i = \frac{1}{N_c^i} \sum_{j \in N_c^i} \sqrt{3} \frac{F_{\mathrm{FENE}}}{d_{ij}}, \tag{5.23}$$

where N_c^i is the number of FENE connections of node i and d_{ij} is the inter-nodal distance (see e.g. [12]).

At $t = 100\,\mathrm{ms}$ the spreading dynamics correspond to the $\sim t^{1/2}$ power law regime. At this stage, adhesive forces are strong especially at the edge of contact, but also in the entire rapidly increasing circular contact area. The elastic energy stored in the membrane at this point in time is very low, as the stretch and bending in the membrane is small. As a result, almost all the energy dissipation (see section 5.2.5) takes place in the contact area.

At $t = 350\,\mathrm{ms}$, a distinct adhesive edge can be observed, in which the magnitude of forces is much stronger than in the inner circle of the contact area, where the contact potential is already nearly minimal. At the edge, the cortex's bending stiffness provides resistance to the strong adhesive tension. Meanwhile, the upper spherical cap is being stretched while at the plane of contact the membrane – together with the substrate it is adhering to – is under compressive stress. At this stage, energy dissipation takes place not only at the substrate interface, but also in the entire stressed cortex. As a result of this, the spreading slows down to a lower rate than the $\sim t^{1/2}$ power law regime.

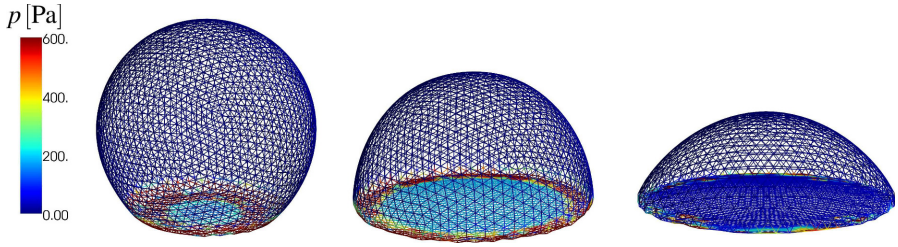

(a) Normal pressure

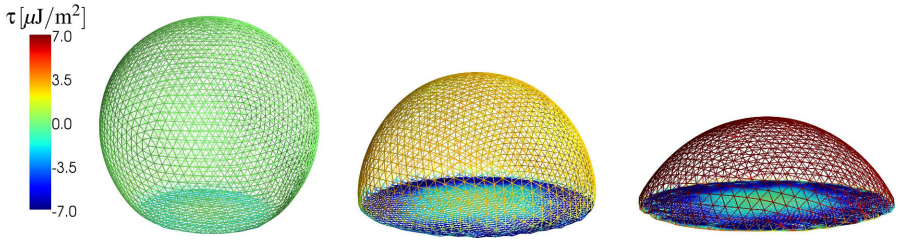

(b) Cortex tension

Figure 5.8: **Normal pressure and cortex tension of a spreading RBC. (a)** Normal pressure (the magnitude of the sum of all conservative forces projected onto the normal in that node) at different time points during cell spreading. left: $t = 100\,\text{ms}$, middle: $t = 350\,\text{ms}$, right: $t = 900\,\text{ms}$. **(b)** Cortex tension (see Eq. (5.23)) averaged at the nodes during cell spreading at the same time points. In the supplementary Video S2 in [153] the sum of all conservative forces acting at each node is indicated by small arrows which are mostly visible for the out-of-plane forces. The distribution of stretch in the cortex is visualized in supplementary Figure S2 in [153].

At $t = 900\,\text{ms}$, spreading has stopped and the cell has reached equilibrium. The forces at the nodes are zero, and the adhesive tension at the edge of contact is being balanced out by the elastic stress in the RBC membrane/cortex. The cortex in the spherical cap is under strong tensile stress and the stretch in the connections is close to its maximal value x_{max}. At the substrate interface, compressive stresses have built up even more. For an elastic substrate, these compressive forces will cause radial inwards deformation of the substrate, as has been observed in traction force microscopy measurements [115, 225] – although these experiments concern late cell spreading.

It should be noted that the maximal normal pressure at the nodes – occurring in the first stage of cell spreading – corresponds to a force in the order of 100 pN, which is in the range of the force applied in the stretching simulations which were used to validate the model parameters of the elastic cortex, see section 5.3.1.

5.4 Discussion

5.4.1 Model performance and limitations

First, with regard to the performance of the newly developed model for a triangulated, deformable cell obeying Maugis-Dugdale contact tractions, we conclude that:

1. We can reproduce the quasi-static cell stretching experiments as analyzed by [50, 51] with nearly identical parameters although the simulation technique used is different (DPD vs. first-order equation of motion inspired by Stokesian dynamics [17]) – see section 5.3.1.
2. The model recapitulates the mechanical behavior of a spreading red blood cell with high precision. From known mechanical parameters it accurately reproduces the cell spreading curves experimentally obtained by [77] and [29].
3. Contact calculations between (rounded) facets of the triangulation show three important advantages over naive node-node based contact calculation schemes:
   (a) Parameters are physically meaningful, well defined and (in principal) measurable;
   (b) using these parameters for different mesh refinements yields very similar results (see also supplementary Text S2 A.3) for cell spreading, and
   (c) the desired accuracy is tunable – both by choosing a finer mesh or more quadrature points for higher accuracy, as needed.
4. The dynamics of both experiments (RBC on polylysine-coated glass, biotinylated RBC on streptavidin substrate, [77], [29]) can be matched by only changing the adhesion energy as given by [29] and adjusting the friction constants γ_n, γ_t (Table 5.1). The contact dissipation cannot be expected to be identical for these two situations, since in the first case, the cell is completely spread within a second, whereas in the second case it takes about a minute. Therefore, rates, numbers and nature of binding/unbinding events will be vastly different, giving rise to different dissipation levels (for a more thorough explanation, see e.g. [96], chapter 9.4).
5. The use of a FENE-like potential is important to consistently obtain these spreading dynamics (data not shown). The same behavior cannot be captured by simple linear springs since they would be either too stiff to allow the initial "fast" spreading phase, or too soft to keep the cell from spreading out too much when the adhesion driven spreading stops. The FENE potential captures this initial softness and final stiffness of the spectrin connections very well (see Fig. 5.4). As a result, the predicted spreading dynamics are very robust – no reasonable change of any parameter yielded anything but an initial $\sim t^{1/2}$ spreading.

6. A five-level subdivision of the icosahedron is required to accurately model the high curvatures occurring when the cell is fully spread out – see section 5.3.3. Using a lower order triangulation yields very similar initial spreading dynamics, but fails to reproduce the final spreading radius of the cell.

7. The model is general enough to allow for simulations in more complex situations – cells interacting with smooth shapes, cells interacting with other cells, etc. It is also well suited for inclusion of cytoskeletal elements (such as the actin network, microtubules, nucleus) in a discrete way.

The modeling technique described in this work has a number of limitations:

- The mesh that is used needs to be refined enough to capture the smallest structures/curvatures that are of interest in the system. This results in comparatively expensive simulations or the additional complication of re-meshing in appropriate regions.

- The linear approximation for the dissipative forces in the equation of motion must be regarded as a first-order approximation of a very complex phenomenon: e.g. [112] notes, that the dissipation upon contact is a time-scale dependent effect, which indicates the limited applicability of the "viscous friction constants" (γ_n, γ_t). This is the reason why we could not match both observed spreading curves in the experiments by Hategan et al. [77] and Cuvelier et al. [29] with the same values for γ_n and γ_t. For cell spreading that happens at the same time scale with similar materials involved, we expect the constants to be very similar.

- The current state of the model does not describe the phenomena affecting late cell spreading which are relevant for other cell types. The dynamics of this active spreading are regulated by cellular processes such as actin polymerization, formation of focal adhesion complexes and stress fibers. Models incorporating the biological effects occurring during late cell spreading have been described [104, 232]. However, they cannot directly relate the initial spreading dynamics to material properties such as adhesion strength and contact dissipation.

5.4.2 Understanding initial cell spreading

Finally, regarding the initial dynamics of cell spreading, we find:

1. The "universal" [29] $\sim t^{1/2}$ power law behavior of initial cell spreading is found consistently. Moreover, this behavior is very robust to changes in model parameters, because it is caused by geometrical properties of the spreading cell. From the simulations we observe that this first spreading phase is characterized

by the absence of tension in the cortical membrane. Since almost no forces are present there, little energy is stored elastically or dissipated in the cortical shell. To understand the $t^{1/2}$ power-law for the radius of contact, we follow the analysis presented by Cuvelier et al. [29]. We conclude that the energy dissipation rate is mainly affected by contact dissipation due to friction. It is therefore proportional to $\gamma_n a^2 \left(\frac{\mathrm{d}a}{\mathrm{d}t}\right)^2$, which can be balanced by the adhesive power. This adhesive power (rate of adhesion-energy gain) is proportional to $Wa\frac{\mathrm{d}a}{\mathrm{d}t}$, yielding for the trivial integration (ignoring all constants)

$$a \sim \sqrt{\frac{2W}{\gamma_n}} t^{1/2}, \tag{5.24}$$

which explains (assuming the given approximations) the characteristic $\sim t^{1/2}$ power law dynamics for the contact radius a. Summarizing, the total energy dissipation per area which is coming into contact with the substrate is constant at this very early stage of cell spreading, yielding the observed dynamics.

2. The first, "fast" slope can only be maintained until the cell's cortex is under tensile stress: In that case, spreading further dissipates more energy – the stretching deformation causes viscous dissipation in the dashpot-like elements, while some is also stored in the (still weak) FENE-like potential. Cuvelier et al. [29] show for several cell types, that in this region a second power law $\sim t^{1/4}$ can be found, but it is least pronounced in the experimental RBC data (see Fig. 5.6(a)). From the simulations we observe that there is no clear second power-law regime, but merely a slowing down of the spreading.

3. The final spread-out phase is characterized by a high tensile, in-plane stress in the spectrin-phospholipid cortical shell. This stress is caused by the balance between adhesion forces that occur at the edge of the spread out cell (in the flattened out center, repulsive and adhesive forces balance out and the contact force is very low) and the FENE connections approaching their maximum extension in the upper spherical cap. The adhesive tension at the edge also causes the membrane-substrate interface to be compressed in a radially inward direction. For a substrate that has shear elasticity, the model therefore predicts that the substrate would deform in a radially inward direction. This prediction is in good agreement with experiments using Traction Force Microscopy [225] – although these experiments are more concerned with the late, active cell-spreading state.

4. Most of the energy dissipation during initial cell spreading occurs due to contact dissipation. The simulations indicate that for a red blood cell, no irreversible deformation in the cortical shell is required to reproduce the experimentally observed spreading dynamics. This means that, should we pull back our cell from the substrate, the cell would re-gain its initial shape, as the equilibrium

lengths of the FENE connections and the equilibrium angles of the bending connections have not been changed. This is contrary to the simpler, conceptual model proposed by Cuvelier et al. [29], which relies on the dissipative "flow" of the cytoskeleton for energy dissipation.

Although the model as shown is restricted to RBC spreading dynamics, we expect that these conclusions can be generalized to other cell types: the same key mechanical components are present in other systems as well, and despite the fact that other cells' cytoskeletons are more complex and the cells can dissipate energy through "active biological processes", we expect the initial cell spreading phase to be still characterized by contact dissipation. Eventually, stress in the membrane / cortex will build up as well and through this, the cell will dissipate energy in the entire cortical shell. However, it is possible that this dissipation involves irreversible deformation in the cortex.

Chapter 6

Immersed Boundary Model of cells in flow

Adapted from:

Guyot, Y., Smeets, B., Odenthal, T., Subramani, R., Luyten, F.P., Ramon, H., Papantoniou, I., Geris, L. (2016) Immersed Boundary Models for quantifying flow-Induced mechanical stimuli on stem cells seeded on 3d scaffolds in perfusion bioreactors.

Submitted to *PLoS Computational Biology*

6.1 Introduction

The culture of stem cell populations in dynamic set-ups, for instance perfusion bioreactors, is of great potential for the production of bone tissue engineered constructs [236]. Amongst others, these systems provide controlled biomechanical stimuli, such as fluid flow-induced shear stresses, that will mimic the *in vivo* environment (bone) contributing to the generation of bone graft substitutes. Shear stress might significantly affect stem cell properties during dynamic culture in bioreactors as it has been associated to early stem cell lineage commitment [198] and osteogenic priming [199] in the absence of inductive growth factors, while it has been observed to promote osteogenic differentiation of bone marrow, periosteum and adipose derived mesenchymal stem cells in the presence of osteoinductive growth factors [58, 68, 138]. Osteogenic differentiation has been further linked to shear stress magnitude

with dose dependent enhancement of extra-cellular matrix deposition and subsequent mineralization by the cultured cells [137, 155, 172, 189].

In order to characterize the dynamic environment throughout cell seeded scaffolds in perfusion bioreactors, many Computational Fluid Dynamics (CFD) model studies have been presented the past decade [15, 84, 130, 154, 162]. However, the majority of these studies considered empty scaffold geometries without incorporating a cell domain. Recently this was addressed by representing the growing neotissue as a porous medium, modeling the effect of neotissue growth on the flow profile [72, 90]. Yet these models predicted the local distribution of shear stresses and pressure through a volume averaged porous domain and did not take into account the local mechanical and geometrical environment of individual cells.

Mechano-transduction of stress induced by shear flow conditions is highly localized at specific areas of the cell's interface with its environment, such as focal adhesions, FAs [188], and primary cilia. The latter have been shown to be involved in the osteogenic response of bone cells to dynamic shear flow conditions [131], as well as in remodeling of the extracellular matrix [229]. The amount of force perceived at the level of FAs as a result of external flow conditions is influenced by the cell's mechanical properties, cell shape and the geometry of its microscopic environment – e.g. location of attachment points, and presence of extracellular matrix (ECM). In this respect, the concept of cell cortical tension has gained a renewed interest in the last years as a mediator of mechano-transduction processes [81]. Cortical tension is created by the cell itself through active acto-myosin contractility, resulting in a pre-stressed cytoskeleton. External flow however, can also contribute to locally elevated levels of cortical tension, especially close to attachment point such as FAs. This passive source of cortical tension, as well as its importance relative to the cell-generated active tension, has not yet been investigated for perfusion cell culture systems. Therefore there is a scaling gap from small scale i.e. "single cell" to the "neotissue/whole scaffold" macro-scale that needs to be bridged and computational models using realistic single cell geometries are a prima candidate for the job [238].

Computational models of cell deformation due to shear flow have been developed considering the cell as a 2D Gaussian interface [113] or a 3D linear elastic solid [31, 192]. The latter uses a mixed Lagrangian-Eulerian formulation to solve the Fluid-Structure interaction (FSI) problem, with a coupling through continuity boundary conditions. For larger deformations, the interaction between cell and fluid has been addressed by means of the level-set method [235]. Alternatively, the Immersed Boundary Method (IBM) is able to explicitly take into account discrete entities in the cell's cortex and, possibly, its internal cytoskeletal structure. It has been used to model the movement and deformation of vesicles, red blood cells and bacteria under flow conditions [129, 237]. An FSI model for osteoblasts attached to scaffold struts

was recently published [238], with a simple rigid single cell consisting of half a sphere with two focal adhesion points. In the work presented in this study, more realistic cell shapes are included, which are not rigid but deformable under the flow. Still, the cytoskeleton constitutes a highly complex material and its mechanical behaviour differs between various temporal and spatial scales, [48]. Hence at present, only a highly simplified mechanical representation of a complete attached cell is computationally feasible.

The main purpose of this study is to use the IBM to investigate fluid-induced mechanical stimuli on progenitor cells (human periosteal derived cells, hPDCs) attached to regular pore scaffolds inside a perfusion bioreactor set-up. Each cell is represented by a simplified model of the cortical shell, similar to [153], supplemented with discrete Focal Adhesions (FAs) and an elastic nucleus. A multi-scale modeling approach is presented, consisting of a CFD analysis at the scaffold macroscopic (tissue) scale in order to determine suitable input boundary conditions at the microscopic scale (single cell scale) where the fluid-structure interaction is modeled via the IBM. The impact on the calculated mechanical stimuli of the spatial location of the cells within the scaffold during flow perfusion was investigated. To illustrate how (location-induced) geometrical differences might affect the biomechanical environment of single cells, three locations and corresponding geometries of cells were chosen: one cell spread along the direction of the flow (A), one facing the flow (F) and one bridging between two struts (B). The present model was furthermore employed to investigate the impact of fluid flow on small clusters of cells attached in the scaffold. In order to investigate some effects of mutual shielding, a 'three cells configuration' (T) facing the flow was presented – Fig. 6.2.

6.2 Methods

Fig. 6.1 provides an overview of the different length scales that were considered in this study and Fig. 6.2 shows the location of the different cells as mentioned above. The following sections explain the deformable cell model and the coupling between the deformable cell and the fluid flow in the scaffold.

6.2.1 Immersed Boundary Method

The IBM has been developed for simulating deformable membranes in fluid flow, based on a combination of an Eulerian and a Lagrangian approach [159]. The deformable object (the cell in this study), is represented by a discretized membrane/cortex $\Gamma_{\text{cell}}(t)$ and is able to move freely through the fixed Eulerian mesh Ω on which the flow is

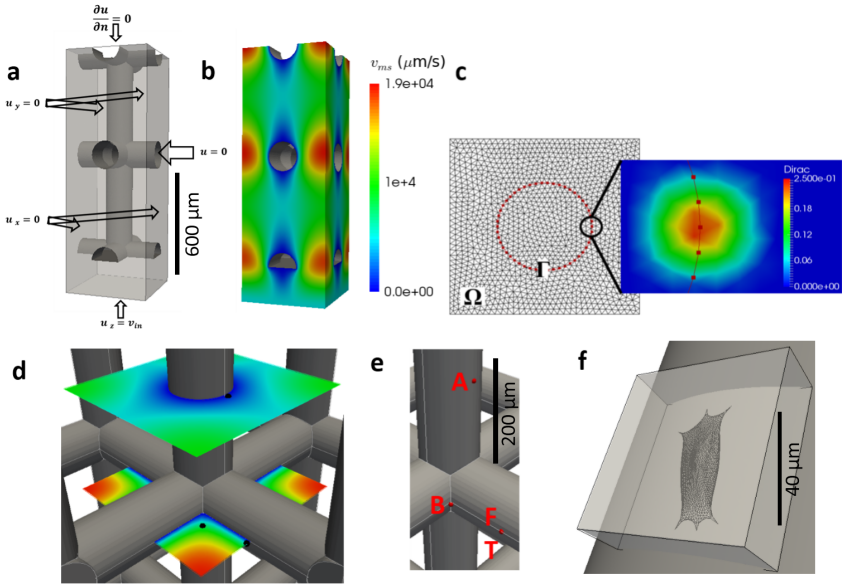

Figure 6.1: Overview of the computational domains. **a)** The computational domain and boundary conditions at the macro-scale. **b)** Computed flow velocity magnitude used as input for the micro-scale models. **c)** Immersed Boundary method representation, Ω and Γ_{cell} are respectively the Eulerian and Lagragian mesh (left), with an illustration of the smoothed dirac δ_p distribution (right). **d)** Black dots represent the three locations where the micro-scale dirichlet boundary conditions for flow velocity are extracted. **e)** Red dots represent the three locations of cells: along flow (A), bridging (B), facing the flow (F) and 'three cell cluster configuration' (T). **f)** Micro-scale domain; the grey cylinder is the scaffold strut, the box is the Eulerian mesh Ω and the cell is the Lagragian mesh Γ_{cell}.

computed – Fig. 6.1(C). The interconnection between both lattices is accomplished by means of a smoothed Dirac function δ_p. In the 3D mesh Ω, the equations for incompressible Stokes flow are solved (as appropriate for the low Reynolds numbers typically encountered in bioreactors), written as

$$\begin{aligned} -\mu\Delta\mathbf{u} + \nabla p &= \mathbf{F} \text{ in } \Omega \\ \nabla \cdot \mathbf{u} &= 0 \text{ in } \Omega \end{aligned} \tag{6.1}$$

with suitable boundary conditions which are explained in following section. In Eq. (6.1), $\mathbf{u}$ represents the fluid velocity, p the pressure and μ the viscosity. The influence of the cell boundary $\Gamma_{\text{cell}}(t)$ immersed in the fluid is taken into account through the

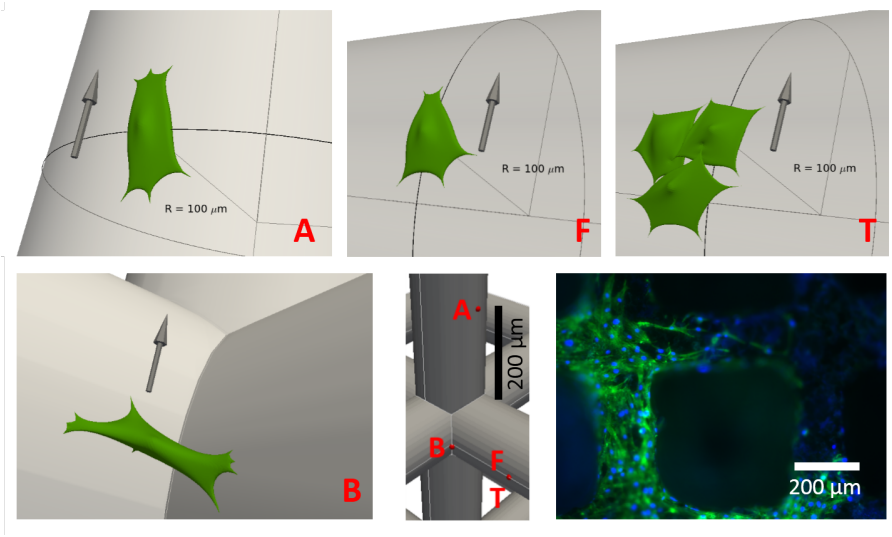

Figure 6.2: Geometrical initial representations of the 4 studied cell configurations. Along the flow (A), facing the flow (F), the three cells clump (T) and the corner bridging cell (B). Bottom right: DAPI/Phaloidin staining of cells attached on scaffold struts.

distributed force density and can be expressed as:

$$\mathbf{F}(\mathbf{x},t) = \int_{\Gamma_{\text{cell}}(t)} f(s,t)\delta_p\left[\mathbf{x}-\mathbf{X}(s,t)\right] \mathrm{d}s \tag{6.2}$$

Here, $\mathbf{x}$ are the Eulerian coordinates and $\mathbf{X}(s,t)$ are the discretized cell membrane coordinates indicating the position of the membrane at time t. As mentioned previously, the interaction between both meshes is realized through the introduction of a dirac function δ_p which is approximated by the following continuous function of the distance r:

$$\delta_p(r) = \begin{cases} \frac{1}{4}\left[1+\cos\left(\frac{\pi r}{2}\right)\right], & |r| \leq 2 \\ 0, & |r| > 2 \end{cases} \tag{6.3}$$

Using Eq. (6.3), Eq. (6.2) can be rewritten in a discrete formulation:

$$\mathbf{F}(\mathbf{x},t) = \sum_{i=1}^{N} f^i(s,t)\delta_p^h(\mathbf{x}-\mathbf{X}(s,t)), \tag{6.4}$$

with N the number of nodes of the cell membrane, h the Eulerian mesh size and

$$\delta_p^h(\mathbf{x}) = \frac{1}{h^3}\delta_p\left(\frac{x}{h}\right)\delta_p\left(\frac{y}{h}\right)\delta_p\left(\frac{z}{h}\right). \tag{6.5}$$

Once the flow is computed, the membrane positions are updated using the following equation of motion:

$$\frac{\mathrm{d}\mathbf{X}(s,t)}{\mathrm{d}t} = \mathbf{U}(\mathbf{X}(s,t),t), \tag{6.6}$$

with $\mathbf{U}$ the interpolated flow velocity on $\Gamma_{\text{cell}}(t)$ which can be expressed as follows:

$$\mathbf{U}(\mathbf{X}(s,t),t) = \int_{\Omega} \mathbf{u}(\mathbf{x},t)\delta_p(\mathbf{x}-\mathbf{X}(s,t))\mathrm{d}\mathbf{x}. \tag{6.7}$$

6.2.2 Mechanical representation of the cell

The mechanical representation of a cell in the Eulerian domain relies on the model represented in Chapter 5 where the underlying mechanisms and assumptions are discussed in detail. Briefly, the model assumes that most of the cytoskeletal material is present in a relatively thin cortical shell and that an elastic description of deformations at short timescales is adequate. The immersed boundary which represents the cell is composed of a triangulated surface with a stretching stiffness k_s and a bending energy k_b – Fig. 6.3. The linear spring force between two connected nodes at distance d^{ij} and

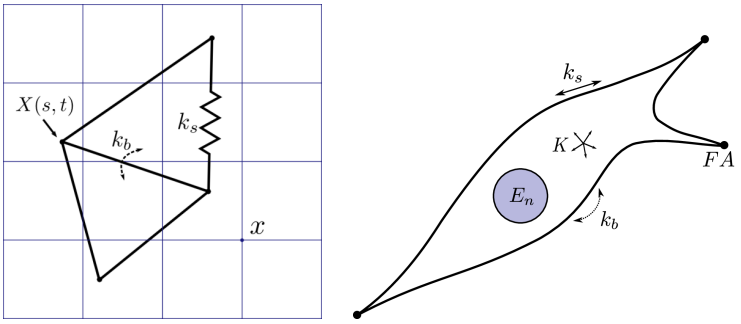

Figure 6.3: Mechanical representation of the cell. Mechanical representation of the cell. **Left:** Lagrangian elastic boundary of the cell with stretching stiffness k_s, bending stiffness k_b and integration points $\mathbf{X}(s,t)$, immersed in an Eulerian lattice with positions $\mathbf{x}$. **Right:** Mechanical representation of a cell attached to a scaffold, approximated through the use of a cortical shell model with stretching and bending stiffness (resp. k_s and k_b), volume compression modulus K and nucleus stiffness E_n. Discrete attachment points representing focal adhesions (FA) connect the cell to the rigid scaffold.

resting length d_0^{ij} is expressed as:

$$f_s^{ij} = k_s(d^{ij} - d_0^{ij}). \tag{6.8}$$

A moment of bending is computed between two adjacent triangles with angle θ^{ij} and resting angle θ_0^{ij}:

$$M_b^{ij} = k_b \sin(\theta^{ij} - \theta_0^{ij}). \tag{6.9}$$

A force corresponding to this moment is applied to the non-common points of each of the two triangles, and a compensating force is applied to the common edge points, ensuring that the total force on the cell remains unchanged. The bending force for each node is denoted as f_b^i. This type of bending stiffness is commonly found in the literature for Red Blood Cell models [50]. The cell's volume is maintained through an effective bulk modulus K. For this, an internal pressure P_v is computed based on a cell's volume V and equilibrium volume V_0:

$$P_v = K \cdot \frac{V_0 - V}{V}. \tag{6.10}$$

Subsequently, a force $f_v^i = P_v A^i n^i$ is obtained for each node i with A^i and n^i respectively the area and outward normal unit vector of each node, both of which are calculated using a discrete version of the Laplace-Beltrami operator. Furthermore, the nucleus is represented as a solid, elastic sphere with Young's modulus E_n for which contact with the cortical nodes is considered Hertzian, i.e.

$$f_n^i = \frac{4E_n\sqrt{R_n}}{3}\delta_n^{i\,2/3}, \tag{6.11}$$

for a nucleus with radius R_n indenting a node i with overlap distance δ_n^i. Discrete attachment points serve as Focal Adhesions (FAs). These points are placed outside of the fluid domain and are therefore not displaced by the fluid. Finally, the total force per node $f^i(s,t)$ is computed as the sum of all aforementioned partial forces:

$$f^i(s,t) = f_s^i + f_b^i + f_v^i + f_n^i. \tag{6.12}$$

6.2.3 Initialization of the cell geometry

In order to obtain realistic shapes of spread-out and stretched-out cells on cylindrical scaffold struts, we perform a separate relaxation simulation. Hereto we start with a spherical geometry, generated from a subdivided icosahedron [153], and slowly translate pre-selected adhesion points towards specific attachment points on the scaffold, which are obtained by displacing the nodes normal to the sphere's surface and subsequently projecting them on the scaffold surface – Fig. 6.4. During this process, the 'free' nodes of the cell relax towards an energy-minimizing equilibrium. The node displacements are calculated in the absence of flow, by solving for the velocity $v(s,t)$:

$$\mathbf{\Gamma} \cdot v(s,t) = f(s,t), \tag{6.13}$$

in which $f(s,t)$ are the internal mechanical forces and $\mathbf{\Gamma}$ is an arbitrary friction matrix. It is clear that this does not simulate the way that real cells obtain their spread out configuration, but it should be pointed out that the fundamental mechanisms of protrusions, contractility and mature focal adhesions will produce very similar shapes with elongated, curvature minimizing surfaces.

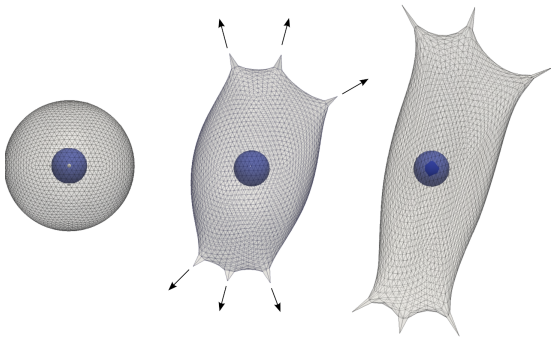

Figure 6.4: Geometrical model of the cell. From **left** to **right**: An example of the procedure for obtaining geometries of cells attached in flow, starting from a perfect sphere. The blue sphere inside the cell represents the nucleus.

6.2.4 Atomic Force Microscopy measurements of cell cortical stiffness

Cell cortical stiffness was measured using Atomic Force Microscopy (AFM). Measurements were performed using a Nanowizard 3 BioScience AFM (JPK) with a working range of $100\times100\times15$ μm mounted on the stage of an inverted microscope (Olympus 1) placed on a vibration-isolation table. A V-shaped gold-coated silicon nitride cantilever with a four-sided pyramidal tip (BudgetSensors) with a nominal tip radius r_{in} of 15 nm and an opening angle θ of 35 degrees was used as the probe. The spring constant k_{spring} of the cantilever was ca. 0.3 Nm^{-1}. Exact values have been calibrated using the thermal fluctuation method. Force curves have been recorded at 5 μm/s approach and retract speed, of which only the approach curves have been analyzed to arrive at the instantaneous Young's modulus using the Sneddon model for forces >200 pN. We neglect the information at low indentations, since according to [178], the Sneddon model is sufficient at higher indentation δ, allowing us to extract the cortical Young's modulus E_c as:

$$F = \frac{E_c \tan(\theta)}{\sqrt{2}(1-\nu^2)}\delta, \tag{6.14}$$

where F is the measured force. Assuming a Poisson's ratio ν of 0.5, we can fit this formula to the typical force-indentation curves obtained by AFM for every pixel on the cell's surface (we use the Levenberg-Marquard algorithm in MINPACK through its python-interface provided by SciPy for curve-fitting). To extract the stiffness of the cortical layer, we select regions on the cell away from the nucleus where the average cell height is very low so that we can assume that the measured stiffness is indeed the compressive stiffness of the cell's cortex and not dominated by effects from bending of the cortical layer or the intra-cellular fluid. The complete selection procedure consists of the following steps [178]:

1. Fit Eq. (6.14) to all the force-distance curves obtained on the cell (typically 16x16 or 32x32). To obtain a robust fit, it has been proven beneficial to estimate the contact-point ($\delta = 0$) at the same time as the apparent cortical Young's modulus.
2. Select thin extensions of the cell.
3. Calculate local slopes of the smoothed surface and reject angles with respect to the vertical $>$20 degrees to minimize artifacts due to tip-sliding or lateral cell movement.
4. Reject bad fits based on a χ^2-statistic (rare).

The remaining apparent cortical Young's moduli are averaged per patch on the cell and the distribution of these is shown in Fig. 6.5d, the global average over all measured cells and all patches is 3.5 ± 2 kPa.

6.2.5 Calibration of cell mechanical model

For a relatively thin cortical 'sheet', and assuming the cortex to consist out of some homogenous elastic material, the stretching stiffness k_s and bending energy k_b can be related to the cortical Young's modulus E_c and the cortical thickness t_c:

$$k_b = \frac{E_c t_c^3}{12(1-\nu_c^2)} \tag{6.15}$$

$$k_s = \frac{2E_c t_c}{\sqrt{3}} \tag{6.16}$$

where we usually assume the Poisson's ratio of the actin cortex ν_c to be 0.5 [41]. Having determined the effective stiffness of the cortical shell and its thickness, these

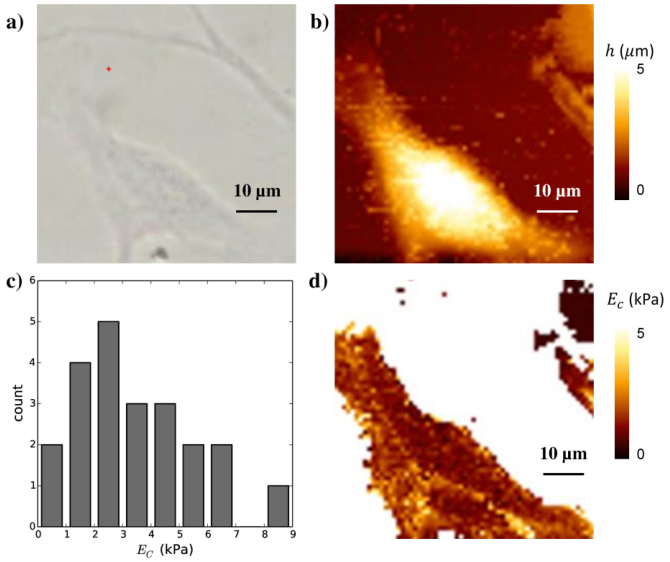

Figure 6.5: AFM measurements of the cell cortical stiffness. **a)** Optical image of the cell, **b)** AFM height map, **c)** histogram of cortical Young's modulus E_c from N=13 cells (in which in total 22 different cortex regions were sampled), **d)** Young's modulus image.

formulas allow us to calculate the parameters of the mechanical cell model. To cross-validate our procedure, these estimated mechanical parameters can be compared to simulated Micropipette Aspiration (MA) experiments. Hereto, a simulation was set up where a spherical cell is aspirated into a thin cylindrical structure with a rounded tip and radius R_p – Fig. 6.6. The relationship between the applied under-pressure in the pipette and the aspirated length L_p of the cell expresses an effective equilibrium Young's Modulus E_∞ which can be compared to experimental values obtained using the same technique [86]:

$$\Delta P = \frac{2\pi}{3} E_\infty \frac{L_p}{R_p} \Phi \tag{6.17}$$

where $\Phi \approx 2.1$ is a scaling factor. The cell's Young's modulus obtained by this procedure – Fig. 6.6 – from the parameter values estimated from the AFM measurements (Table 6.1) compare well to measured values from MSCs; e.g. [191] report Young's moduli in the range of 150-350 Pa.

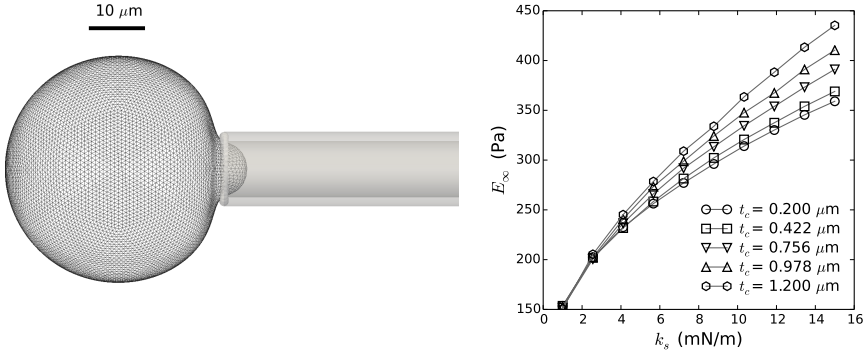

Figure 6.6: Determination of cell stiffness through micropipette aspiration. **Left:** Visualization of simulated micropipette aspiration experiment. **Right:** Equilibrium Young's Modulus E_∞ as a function of stretching stiffness k_s for varying cortical thickness t_c.

6.2.6 Preprocessing and Boundary conditions

The fluid environment around a single cell attached to the scaffold is calculated by solving the immersed boundary problem at the scale of the investigated cell. For this purpose, the Eulerian computational domain Ω corresponds to a box of a few hundreds microns wide/long containing the cell and not the whole scaffold pore – Fig. 6.1(F). In order to have an estimation of the flow magnitude to be used as a Dirichlet boundary condition on domain Ω when solving Eq. (6.1) for the micro-scale problem, Stokes equation was solved on an entire pore of the scaffold – Fig. 6.1(A) and the calculated flow velocity $\mathbf{v}_{ms}$ was used to extract a suitable boundary condition $\mathbf{v}_{ib}$ for the IBM problem. An inlet velocity corresponding to the bioreactor flow rate Q_{in} was set at the entrance of the pore and symmetry boundary conditions were applied on each sides of

Table 6.1: List of parameters used in this study

Parameter	Symbol	Value	Unit	Source
Viscosity	ν	0.001	Pa·s	Water at 293K
Bending energy cortex	k_b	8.5e-17	Nm	AFM; Eq. (6.15)
Cortical stiffness	k_s	2.34e-3	N/m	AFM; Eq. (6.16)
Bulk modulus	K	200	Pa	Assumption
Young's modulus nucleus	E_n	1000	Pa	[69]
Poisson's ratio nucleus	ν_n	0.5	-	[69]

the pore – Fig. 6.1(A).

6.2.7 Implementation

The Immersed Boundary implementation was realized using the Finite Element software FreeFEM++ [80], which solves the Stokes flow problem, with the Lagrangian forces computed in a coupled module implemented in the particle-based simulation platform Mpacts (formerly called DEMeter++) [210].

6.3 Results and Discussion

Four potentially relevant mechanical measures were computed for cells experiencing flow conditions inside a scaffold pore: nodal displacement, cortical tension, normal pressure and local shear stress. Moreover, we compared between four different geometries as illustrated in Fig. 6.2: a cell on a cylindrical strut with flow parallel to the cylinder axis (A), a cell on a cylindrical strut with flow perpendicular to the cylinder axis (F), a small cluster of three interconnected cells on a cylindrical strut with flow perpendicular to the cylinder axis (T) and a single cell attached on a strut junction, forming a bridge between two perpendicular struts (B). All cells were attached with discrete FAs located on the surface of the struts and which did not displace. All aforementioned geometries are regularly encountered in experimental set-ups where cells are attached to titanium scaffold struts – Fig. 6.2. In the following section, we will discuss for each of these geometries the effect of flow on the four mechanical measures.

Fig. 6.7 summarizes the effect of flow on the nodal displacements D. Very low displacements were obtained for flow parallel to the cylindrical strut, while intermediate displacements were found for flow perpendicular to the cylindrical strut and relatively high displacements were observed for the cell forming a bridge at a scaffold corner. For inlet bioreactor flow rates in the order of 1 ml/min, maximal displacements are in the range of 30 nm which have been previously reported as a critical displacement for the detachment of mesenchymal stem cells of bridged morphology from irregular scaffolds [100, 136]. However, these studies were carried out using a one-way fluid–structure interaction (FSI) approach and did not consider the influence of cellular deformation on the surrounding fluid flow, something that in this study was included (two way interaction between cell and fluid).

These deformation value ranges are much smaller than typical deformations of cells in tissue: e.g. for chondrocytes in mature cartilage, strains higher than 20% (i.e. more than 1 μm) have been measured upon tissue compression [71]. It should be stressed that our simulations report the instantaneous elastic response in deformation to a step

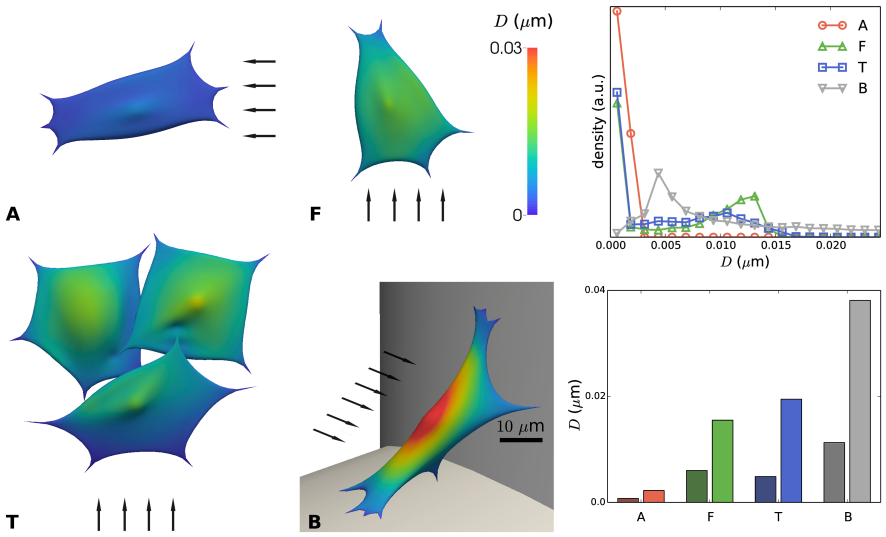

Figure 6.7: Displacement D of the immersed boundary due to flow, relative to the no-flow condition, for distinct configurations (A,F,T and B) of cells on scaffold struts. **Left:** color map showing local displacements. The arrows indicate the direction of the flow; scale bar 10 μm. **Top right:** disitribution of the displacements for A, F, T, B. a.u.: aribitrary units. **Bottom right:** mean nodal displacement (dark color) and maximal nodal displacement for cases A, F, T and B.

increase in flow velocity, and neglect the viscous deformations that might occur when cells are exposed to constant flow conditions for a long time (i.e. days).

In Fig. 6.8, the distribution of cortical tension T is shown for the four different geometrical configurations. Positive values of T indicate tensile conditions, whereas negative values of T indicate compressive stresses in the cortical shell. Unlike the cell deformations, which were maximal for the cell bridging between two struts (B), the maximal tension T occurs for cells on cylindrical struts with flow perpendicular to the strut (F) and (T). Moreover, maximal cortical tensions are observed close to the nucleus and close to FAs, with tensile stresses occurring at the side of incoming flow and compressive stresses at the side of out-going flow. Maximal tensions, which are highly localized, are around 5 μJ/m^2. For comparison, these values are several orders of magnitude below the values for membrane rupture. Other experimental studies have looked at the induction of blebbing, for which they reported that cortical tensions of at least 200 μJ/m^2 [211] were required, while inside blebs, cortical tensions between 10 and 100 μJ/m^2 [161] were measured. The cell's acto-myosin contractility alone creates an average resting cortical tension in the order of 0.5 μJ/m^2 [30]. In other words, the predicted additional cortical tension due to shear flow is relatively low, but it cannot

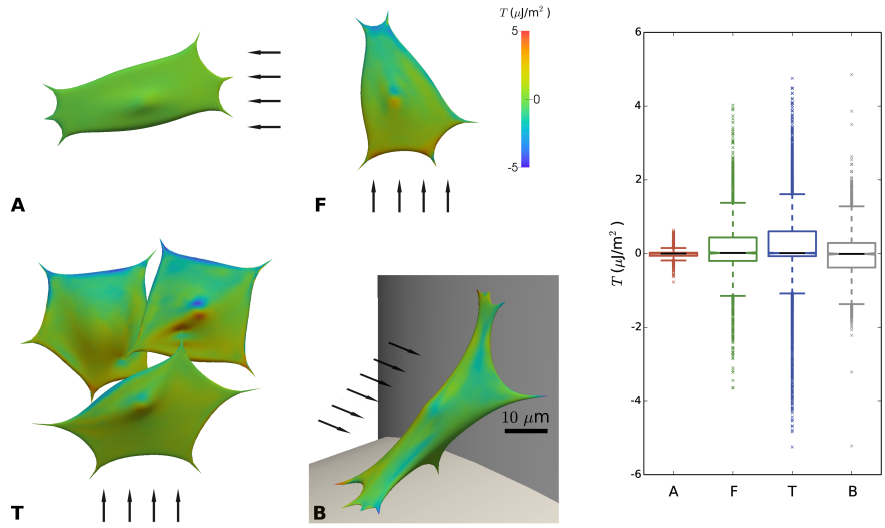

Figure 6.8: Cortical tension T due to imposed flow for distinct configurations (A, F, T and B) of cells on scaffold struts. Positive values indicate tensile conditions, while negative values indicate compressed conditions. **Left:** color map showing local tension. The arrows indicate the direction of the flow; scale bar 10 μm. **Right:** Boxplot showing distribution of tension for cases A, F, T and B.

be excluded that these tensions could result in some conformational changes in the cytoskeleton.

Fig. 6.9 shows the distribution of the fluid pressure P on each cell's surface. Cells located in the configuration where the flow is facing the strut, i.e. where the flow velocity is the highest (F and T), show the largest variation in the pressure distribution, reaching a maximal amplitude of about 0.5 Pa. Contrarily, cells located in (A) and (B) display few pressure differences due to the low velocity magnitude and very small changes in the flow streamlines.

Fig. 6.10 shows the flow induced shear stress τ across the examined cells. While the average value of τ taken over the entire cell-surface (including the 'bottom' of the cells, facing the strut) is generally low due to the reduced flow speed and related shear stress at the bottom of the cell, it is very interesting to compare the maximum wall shear stress values at the top of the cells. Due to their location (F) and (T) configurations show the highest magnitude with a value reaching up to 0.16 Pa while cells located in (A) and (B) show a low value of shear stress, around 0.02-0.03 Pa. *In vivo*, cells in the bone tissue have been found to experience shear stresses of 0.8-3.0 Pa during routine physical

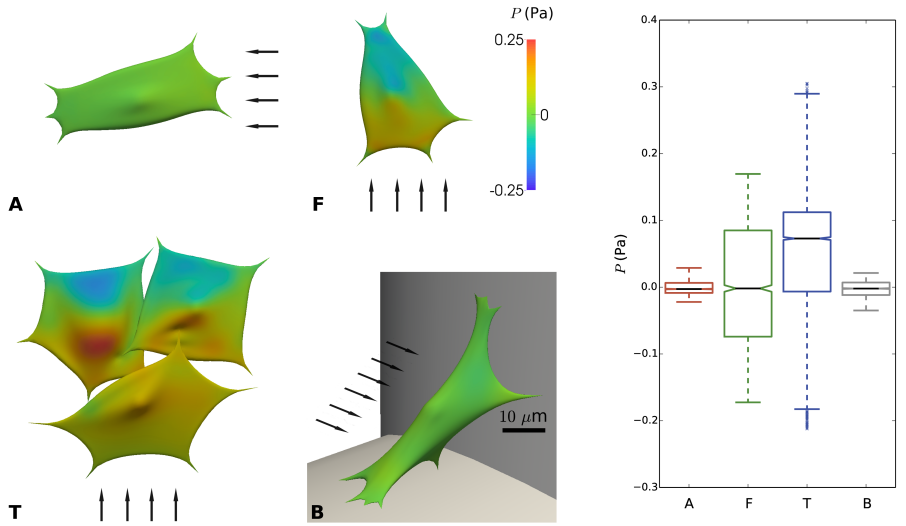

Figure 6.9: Pressure P on the cell surface due to imposed flow for distinct configurations (A, F, T and B) of cells on scaffold struts. **Left:** color maps showing local pressure. The arrows indicate the direction of the flow; scale bar 10 μm. **Right:** boxplot showing distribution of pressure for cases A, F, T and B.

activity [229]. Comparing to the expected wall shear stresses in an empty scaffold, we see that the maximum stresses predicted by the IBM are generally about twice as high, while the average stress over the complete cell surface is significantly lower. This clearly indicates the importance of taking the shape and mechanical response of the cells into account for estimating their relevant wall shear stress. Regarding the (F) and T configurations, as expected, the distribution of shear stress is more homogenous with half of the cell surface exposed to a higher value than 0.015 Pa, while the two other configurations present most of their surface exposed to low shear stress value (below 0.005 Pa). For the flow rate level used in this study, we have previously reported the effect of increasing flow rates resulting in osteogenic priming of hPDCs in the absence of supplementary growth factors [199] with genes such as osterix and bone sialoprotein being slightly upregulated. Additionally, again for similar flow rates and n the presence of osteoinductive medium, hPDCs were seen to secrete higher levels of ECM and to enhance mineralization for increasing flow rates [155]. It has been observed [136] that for a shear stress value exceeding a threshold value of 0.088 Pa, human MSCs can detach from the scaffold surface and by doing so negatively affect the final properties of tissue engineered constructs, resulting in an inhomogenous distribution of neotissue across the scaffold [156]. This illustrates the importance of having a numerical model such as the one presented in this study, to quantify and

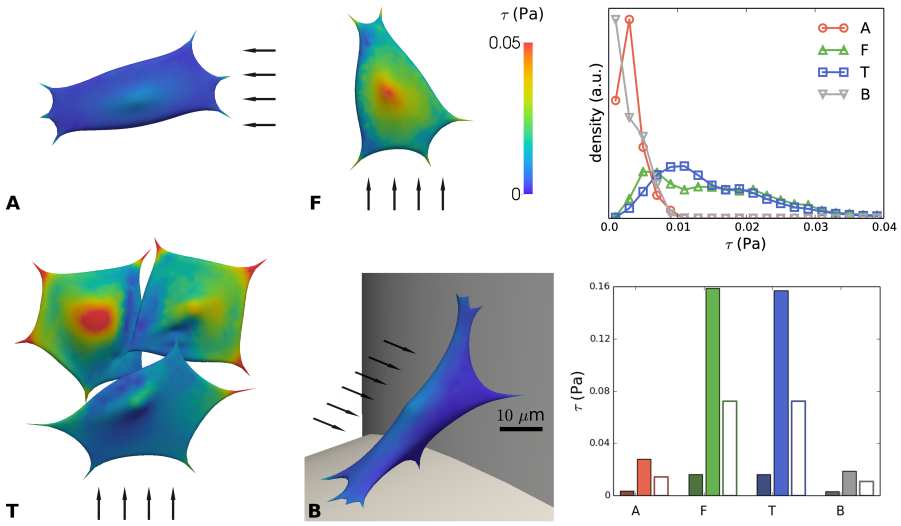

Figure 6.10: Shear stress τ on the cell surface due to imposed flow for distinct configurations (A,F,T and B) of cells on scaffold struts. **Left:** color maps showing local shear stress. The arrows indicate the direction of the flow; scale bar 10 μm. **Top right:** distribution of shear stress for A,F,T,B. **Bottom right:** mean shear stress (dark color) and maximal shear stress (light color) for cases A, F, T and B. The empty bars indicate the shear stress on the empty scaffold strut at the cell's location (computed at the macro-scale).

characterize the mechanical environment that cells experience in novel scaffold designs in order to avoid the development of suboptimal or detrimental mechanical regimes.

Fig. 6.11 shows the results of a parameter study where both the inlet flow velocity Q_{in} and the cortical stiffness k_s were varied for configuration (F). From Q_{in} the Dirichlet boundary conditions in the micro-scale model were determined using a CFD simulation of the complete scaffold pore (Fig. 8.1A). The resulting maximal deformation, pressure, shear stress and cortical tension were quantified. One might notice that the dependence on Q_{in} is linear, which is due to the Stokes flow regime, which would be valid for the investigated range of flow rates. Except for the maximal deformations, the effect of the cells' stiffness is very small.

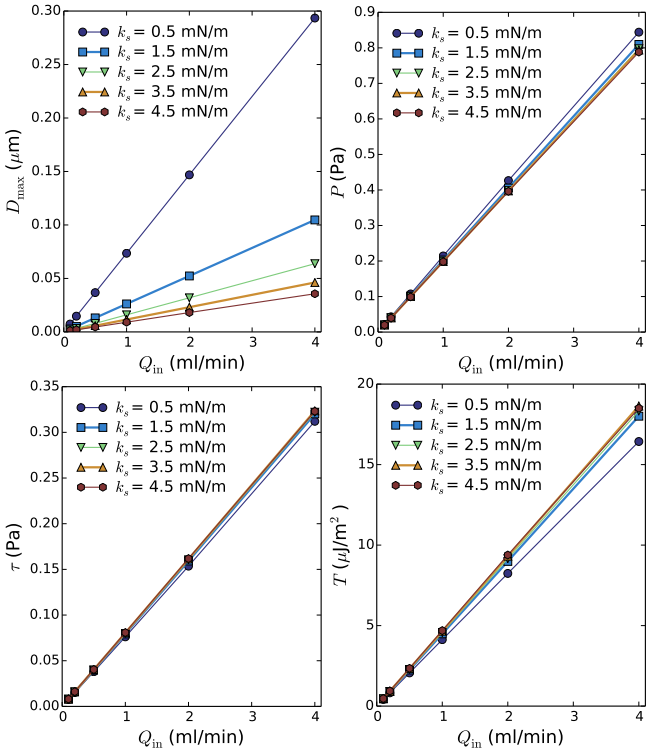

Figure 6.11: Results of a parameter study varying inlet volumetric flow rate and cortex stiffness. **Top left:** maximal local displacement; **Top right:** maximal normal pressure; **Bottom left:** maximal local shear stress and **Bottom right:** maximal local tension.

6.4 Conclusions and outlook

In the presented work, a novel application of the immersed boundary method was developed, representing a deformable cell exposed to microscopic flow and attached to a 3D scaffold inside a perfusion bioreactor. Cells were represented by a deformable Lagrangian surface mesh, which was immersed in an Eulerian fluid domain, with flow in the Stokes regime. We demonstrated the effect of shear flow for multiple realistic geometrical cell configurations and strut locations inside a regular pore scaffold. This tool can be used to estimate shear flow conditions directly on the surface of individual cells, and assess the micro-scale variability of mechanical conditions inside single scaffold pores. The instantaneous cell stiffness was measured using AFM experiments on hPDCs, and the mechanical model was calibrated using micro-pipette aspiration simulations in the range of short term deformations. Simulations confirmed that

mechanical cues originating from the flow are highly dependent on the exact geometry of the cell and its environment. For example, a cell on a cylindrical strut with flow perpendicular to the strut will experience a much larger shear stress than a cell on a similar strut with parallel flow. This should be a major consideration when designing novel scaffold designs.

Moreover, it was found that wall shear stress calculated in the empty scaffold would underestimate the actual maximal wall shear stress experienced by the cells by a factor of two in the investigated cases. Furthermore, the model was used to estimate the additional instanteous flow-induced cell deformation, tension and pressure. Compared to the cell-generated deformation and tension due to acto-myosin activity these values are very small for the applied flow conditions, making it unlikely that they would trigger a biological response, at least for the instantaneous elastic deformation. The effect of shear flow on the long timescale viscous-like deformation of living cells remains to be investigated. This would also require a more elaborate description of the cell's mechanical behavior, which for this study was greatly simplified and limited to linearly elastic deformation. Furthermore, to simulate adhesion and detachment behaviour (e.g. in very high shear flows), the presented methodology has to be extended since adhesion is only implicitely captured by placing FAs out of the fluid domain thereby fixing them in space independently of applied forces. A parameter study showed linear behaviour in the relevant cell-mechanical and flow parameters, showing that the model can be used to inter-/extrapolate to different cell types and flow conditions. For a cell of thickness 5 μm facing flow on a strut of diameter 200 μm, the wall shear stress can be estimated as: $\tau \approx 0.08 Q_{in}$. Evidently, the maximal wall shear stress experienced by a cell does not seem to depend strongly on the cell's mechanics. This implies that even though a cell may undergo structural changes (e.g. migration, re-alignment), it can still reliably "sense" the shear flow (e.g. with its primary cilium). This study constitutes an important step towards model-based control of a cell's biophysical micro-environment (stem cell niche engineering) in a perfusion bioreactor.

Chapter 7

Phase diagram of cells with CIL

Adapted from:

Smeets, B., Alert, R., Pešek, J., Pagonabarraga, I., Ramon, H., Vincent, R. (2016) Emergent structural organizations of 2D motile particles with contact inhibition of locomotion.

Submitted to *Proceedings of the National Academy of Sciences of the United States of America*

7.1 Introduction

Cell colonies exhibit a broad range of phenotypes. In terms of structure, collections of cells can arrange into distributions of single cells, assemble into squamous, columnar, or multi-layered epithelial tissues, or even form 3D agglomerates. In terms of dynamics, cell motility may be simply absent, or produce random, directed or collective motion of cells. The whole phenotype is influenced both by the cell's genotype and environment, and changes of either can drive phenotypic transitions such as the epithelial-mesenchymal transition, multi-layering transitions in epithelia, or the onset of directed motion [126]. Indeed, such changes of the organization of cell collectives are characteristic of morphogenetic remodeling and are also central to tumor growth and dispersal [56, 57, 148, 208]. Therefore, a physical understanding of the phase behavior of cell colonies will shed light into the regulation of many multicellular processes involved in development and growth.

However, a complete physical picture of multicellular organization is not yet available, partly due to the challenge of modeling the complex interactions between cells. Here, we address this problem by simulating self-propelled particles (SPP) endowed with

interactions capturing generic cellular behaviors. Since the seminal work of Vicsek *et al.* [221], models of interacting SPP have been widely used to investigate the collective dynamics of many active matter systems [179], including animal groups [19], human crowds in concerts [190], colonies of bacteria [237] and cell groups. Without committing to the details of a particular system, generic phase behaviors of active matter have been unraveled by studying the simplest model systems. For instance, activity has been shown to induce phase separation above densities of 40% in systems with purely repulsive interactions [55, 174], which is known as motility-induced phase separation (MIPS) [23]. Furthermore, the sole addition of attractive interactions leads to a reentrant phase separation as a function of activity [173].

In addition to a soft excluded-volume repulsion, attractive interactions do exist among cells as a consequence of their active cortical contractility transmitted through cell-cell adhesion complexes, such as the Cadherin junctions. With no additional interactions, this attraction would lead to phase separation at sufficiently high densities [173]. In practice, phase separation is not a generality in cell colonies, may its appearance be cell type dependent. For instance, while epithelial cells tend to form continuous monolayers, mesenchymal cells separate after division despite the presence of adherent junctions [22, 35]. This calls for an extra effective repulsion force to drive the separation, which may have a deep impact on the overall organization of the colony.

Such a repulsive interaction mediated by adhesion is indeed present in many cell types upon cell-cell contact, and is known as contact inhibition of locomotion (CIL) after Abercrombie and Heaysman [3]. Upon a cell-cell collision, the cell front adheres to the colliding cell, which hinders further cell protrusions. Subsequently, repolarization of the cell's cytoskeleton creates a new front away from the adhesion zone, and the two cells thus separate from each other [1, 2]. This interaction has been shown to be crucial in determining the collective behavior of cell groups in several contexts [37, 123]. These range from guiding the directional migration of neural crest cells [22, 231] to ensuring the correct dispersion of Cajal-Retzius cells in the cerebral cortex [222] or of macrophages in the embryo [34].

In this paper, we model cellular interactions via a potential accounting for attractive forces mediated by intercellular adhesion, and soft repulsive forces stemming from cell overlapping. The soft character of the potential allows for cell extrusion under certain conditions. In addition, CIL is modeled as an interaction orienting cell motility away from cell-cell contacts. Such a generic yet minimal model with only five free parameters allows to explore the influence of CIL on the phase behavior of large cell colonies. From simulations, we draw a projection of the phase diagram in the adhesion/CIL plane that showcases five main regions corresponding to clustered, ordered grid-like distribution, near-equilibrium gel, dense polarized active-liquid, and overlapped organizations of the colonies. We also analytically predict some of the transition lines using mean-field arguments. The results may be interpreted in biological terms by associating each phase to common phenotypes, namely grid-like distributions of cells, collectively migrating of

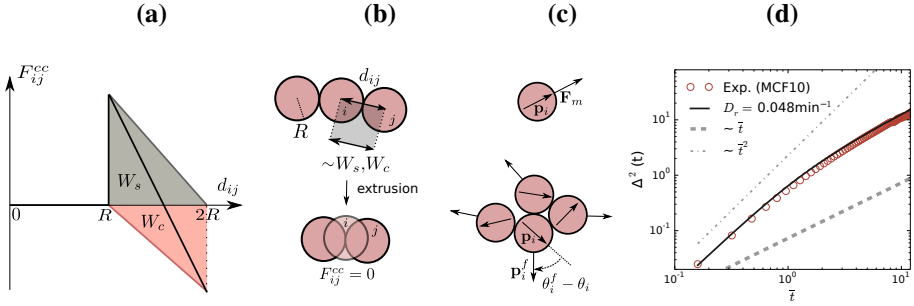

Figure 7.1: A model of self-propelled particles with cell-like interactions. **(a)** Central cell-cell force F_{ij}^{cc} (black) including a soft repulsion due to loss of cell-substrate adhesion area (grey) and attraction due to active contractility through cell-cell adhesions (red). **(b)** Cell extrusion for intercellular distances $d_{ij} < R$, resulting in vanishing cell-cell forces in the plane. **(c)** Cellular self-propulsion force F_m in the direction of the cell's polarity $\mathbf{p}_i$. CIL-like interactions rotate the polarity towards the direction $\mathbf{p}_i^f$ pointing away from cell-cell contacts. **(d)** Evolution of the mean-squared displacement $\Delta^2(t)$ of MCF10a cells in low-density cultures, which is fit by the expression for a persistent random walk (see section 7.5.8) with self-propulsion velocity v_p=1 μm/min and rotational diffusion coefficient D_r=0.048 min^{-1}.

mesenchymal and epithelial tissues, and 3D cellular aggregates, respectively. Particles' softness and CIL-like interactions are key in producing phases akin to the usual phenotypes of cell colonies. In particular, CIL is found to hinder cell extrusion by ensuring tensile stresses in epithelia. We note at last that, surprisingly, cell density does not appear to alter the essence of this phase diagram.

7.2 Methods

We model a 2D colony of cells as a suspension of overdamped self-propelled disks. The equation of motion of cell i with position $\mathbf{x}_i$ and polarity $\mathbf{p}_i = (\cos\theta_i, \sin\theta_i)$ reads (see section 7.5.1):

$$F_m \mathbf{p}_i = \gamma_s \dot{\mathbf{x}}_i + \sum_j^{nn} \left[F_{ij}^{cc} \hat{\mathbf{n}}_{ij} + \Gamma_{ij} (\dot{\mathbf{x}}_i - \dot{\mathbf{x}}_j) \right], \tag{7.1}$$

for contacting neighbor cells j with $\hat{\mathbf{n}}_{ij} = (\mathbf{x}_j - \mathbf{x}_i)/d_{ij}$ and $d_{ij} = ||\mathbf{x}_j - \mathbf{x}_i||$. Note that translational noise is neglected. Here, F_m is the magnitude of the cell's self-propulsion force, γ_s is a cell-substrate friction constant, and the cell-cell friction tensor Γ_{ij} is reduced to a single constant γ (see section 7.5.1).

The central force F_{ij}^{cc} includes a soft repulsion associated to the reduction of the cell-substrate adhesion area whenever two cells are closer than their spread-out size $2R$. The repulsive force is assumed to increase linearly with decreasing intercellular distance d_{ij} up to the maximum value $2W_s/R$ for d_{ij}=R — gray line in Fig. 7.1(a) — with W_s the maximum cell-substrate adhesion energy. At intercellular distances $d_{ij} < R$, no further reduction of the cell-substrate contact area is allowed, and one cell is considered to be extruded from the monolayer plane instead, implying a vanishing in-plane force — see Fig. 7.1(b). In addition, the active contractile force transmitted through cell-cell adhesions is assumed to increase linearly with distance up to $2W_c/R$ for d_{ij}=$2R$ — red line in Fig. 7.1(a) — with W_c the maximum cell-cell adhesion energy. This dependence is suggested by the recently measured linear increase of stress with strain in epithelia [223]. Finally, all these contributions add up to give

$$F_{ij}^{cc}(d_{ij}) = \begin{cases} \frac{2}{R}[W_s - \frac{W_s+W_c}{R}(d_{ij}-R)], & \text{if } R \leq d_{ij} \leq 2R \\ 0, & \text{else.} \end{cases} \tag{7.2}$$

In turn, CIL tends to orient the cellular polarization $\mathbf{p}_i$ in the direction $\mathbf{p}_i^f$ pointing away from the weighted average position of the contacting cells — see Fig. 7.1(c) and section 7.5.4. We model this as a harmonic potential for the polarization angle θ_i that, in addition to rotational noise, yields an Ornstein-Uhlenbeck stochastic process [215] for its dynamics:

$$\dot{\theta}_i = f_{\text{cil}}(\theta_i^f - \theta_i) + \sqrt{2D_r}\,\xi. \tag{7.3}$$

Here, f_{cil} is the inverse of the cellular repolarization time upon cell-cell contact, while $\xi(t)$ is a typified Gaussian white noise, and D_r is the rotational diffusion coefficient.

Upon nondimensionalization (see section 7.5.2), the parameters of the model are reduced to five dimensionless quantities: cell-cell and cell-substrate adhesion energies $\overline{W}_c$ and $\overline{W}_s$, cell-cell friction $\bar{\gamma}$, cell density ϕ, and a repolarization parameter $\psi := f_{\text{cil}}/(2D_r)$ that compares the frequency of cytoskeletal repolarization associated to CIL to the rotational diffusion. A full parameter study shows that all the five aforementioned parameters have a significant effect on the defined phase measures (see Tables B.1-B.3).

Hereafter, we focus on the effects of intercellular adhesion and CIL on the phase behavior of cell colonies, and we thus fix the values of the other three dimensionless parameters. We set a high cell density ϕ=0.85 in order to speed up the relaxation time of all phases. Nevertheless, we provide results at a lower density ϕ=0.4 (see chapter B; Fig. B.1). While density is a key determinant of many phase transitions in colloidal systems, we find that it does not alter much the essence of the present phase diagram; the same phases occur in the same regions of the adhesion/CIL plane as at ϕ=0.85 (see chapter B; Figs B.2, B.3 and B.4(c)).

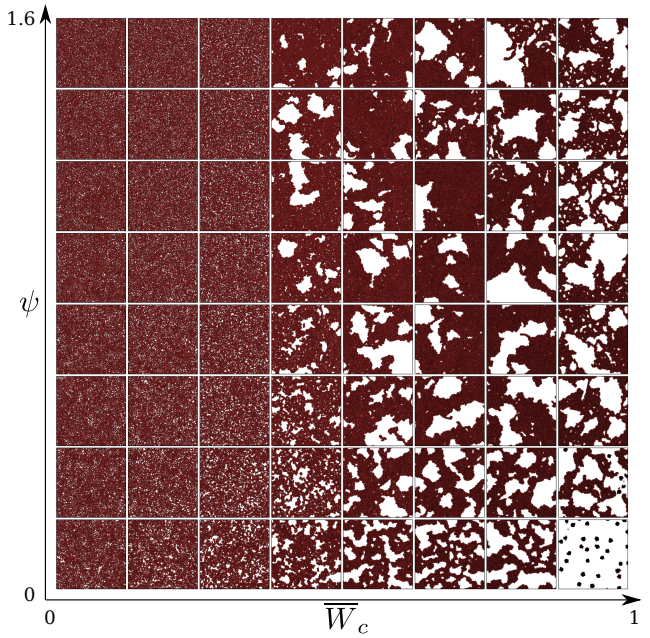

Figure 7.2: Representations of simulated systems for varying adhesive tension $\overline{W}_c$ and contact inhibition of locomotion ψ at high cell-substrate adhesion ($\overline{W}_s$=1.0), high density (ϕ =0.85) and without cell-cell friction ($\bar{\gamma}$=0). Note that the presented images only show a subset of the simulated domains, which contained 1e5 particles.

Cell-cell friction $\bar{\gamma}$ strongly slows down the kinetics of relaxation to stationary states, often leading to frozen non-equilibrium states, impeding access to the study of equilibrium states. Our cell-cell friction parameter effectively corresponds to the intracellular viscosity, which has been shown to have negligible influence on the rheology of tissues at long timescales [133]. In the main text, we thus study the limiting case $\bar{\gamma}$=0, but give more details on the interesting influence of cell-cell friction in section . Finally, we set the cell-substrate adhesion energy to $\overline{W}_s$=1. Additionally, from the Mean-Squared Displacement (MSD) of MCF10a cells in low-density cultures, we estimate typical self-propulsion velocities $v_p = F_m/\gamma_s \sim 1$ μm/min and rotational diffusion coefficients $D_r \sim 0.05$ min^{-1} (see Fig. 7.1(d) and section 7.5.8).

7.3 Results

7.3.1 CIL induces a grid-like phase at low $\overline{W}_c$.

In Fig. 7.2, visualizations are provided of simulated systems in the $\overline{W}_c/\psi$ plane at a density of ϕ=0.85. Simulations at a lower density (ϕ=0.4) are shown in Fig. B.1, for which the essence of most phase transitions is kept.

Focusing first on low cell-cell adhesion, $\overline{W}_c < 0.5$, we adopt a large number fluctuation exponent α_N as used in [55] (see 7.5.3). α_N becomes 0.5 for a randomly distributed phase, and approaches 1 when close to full phase separation. Unsurprisingly, α_N exceeds 0.5 for higher $\overline{W}_c$, demonstrating that the system evolves towards a denser phase – Fig. 7.3(a). A more surprising feature can be observed at lower $\overline{W}_c$ and high enough ψ. There, α_N is smaller than 0.5, implying a phase better distributed than a gas phase. The iso-line α_N=0.5 in Fig. 7.3(a) provides a measure of the structural boundary of this grid-like phase at high ψ.

Next, we examine the dynamics around the grid-like to dense phase transition. Fig. 7.3(b) shows the Mean Square Displacement (MSD), $\Delta^2(t)$, at high ψ=1.5 for increasing $\overline{W}_c$. Remarkably, the MSD at long timescales remains diffusive for a large extent of $\overline{W}_c$, with $\alpha^{\infty}_{\mathrm{MSD}} \approx 1$ for $\overline{W}_c < 0.5$. When increasing adhesion, the MSD drops sharply around $\overline{W}_c \approx 0.25$ — Fig. 7.3(c). The inflection point of this drop can be used as a dynamical indicator of the transition line between the grid-like phase and a dynamic cluster phase, and is located close to the α_N=0.5 iso-line, Fig. 7.7.

We propose a simple argument to formulate a theoretical transition line: a dense phase is stable if the average force due to CIL, $\langle F_{\mathrm{rep}} \rangle$, is lower than the magnitude of the maximal adhesive force. Hence, the transition line can be estimated by:

$$\langle F_{\mathrm{rep}} \rangle - \frac{2}{R} W_c = 0. \tag{7.4}$$

In the limit of large ψ, we obtain:

$$\psi = \frac{-1}{4 \log\left(4\overline{W}_c\right)}. \tag{7.5}$$

Note that at sufficiently high ψ, this phase transition is only a function of cell-cell adhesion and occurs at $\overline{W}_c$=1/4. This analytical phase transition line is in good agreement with the line determined from simulations. Eq. (7.4) provides an upper limit for long-time stability of a stable dense phase, neglecting cooperative effects in the particles' orientation, which would result in a higher effective CIL.

At low ψ and $\overline{W}_c$, α_N is higher than 0.5, signifying a gas with kinetically formed clusters. To better understand this phase, we consider again the MSD, $\Delta^2(t)$, and vary

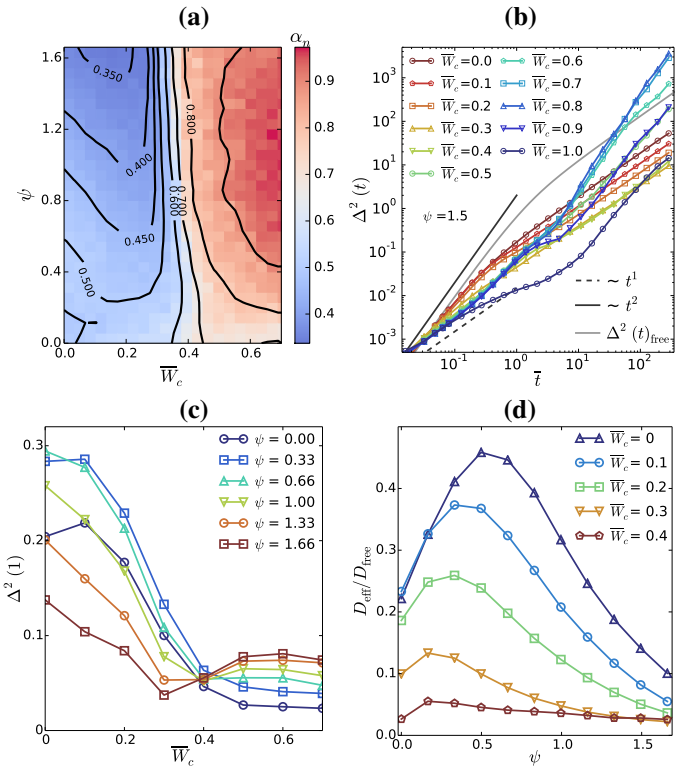

Figure 7.3: **(a)**: Map of large number fluctuation exponent α_N for varying $\overline{W}_c$ and ψ with estimated iso-lines. The iso-line α_N =0.5 indicates the boundary of a grid-like phase. **(b)**: MSD, $\Delta^2(t)$ as a function of time in equilibrium, with guide-lines indicating $\sim t^1$ (diffusive), $\sim t^2$ (ballistic) and the analytical solution for free particles with no contacts. **(c)**: $\Delta^2(1)$, i.e. the MSD at $\bar{t}$=1, as a function of $\overline{W}_c$ for varying ψ. The sharp decrease around $\overline{W}_c$=0.25 indicates a transition towards stable clusters. **(d)**: The effective coefficient of diffusion $D_{\text{eff}}/D_{\text{free}}$, as a function of ψ, for varying $\overline{W}_c$ shows a distinct peak, indicative of transition from a gas to a grid-like distribution.

ψ at low $\overline{W}_c$. Interestingly, the effective diffusivity $D_{\text{eff}}/D_{\text{free}}$ initially increases with ψ — Fig. 7.3(d) and Fig. B.5(a). The presence of CIL stimulates evaporation from kinetically formed clusters, hence preventing jamming and enhancing cell mobility.

Upon further increase of ψ, $D_{\text{eff}}/D_{\text{free}}$ reaches a maximum before decreasing again. In the absence of clusters, the main effect of CIL is now to anticorrelate the cells' orientations, thereby preventing aligned motions that would enhance mixing at high densities, and confining their movement within a local grid structure.

As in Levis *et al.* [119], we use the maximum of $D_{\text{eff}}/D_{\text{free}}$ to define a transition line between a gas and a grid-like phase at lower CIL. This maximum exists up to $\overline{W}_c \approxeq 0.45$, and its location shifts towards lower ψ with increasing $\overline{W}_c$; as such, in the presence of CIL and at low $\overline{W}_c$, more adhesion will paradoxically decrease clustering. This can be rationalized by the fact that adhesion increases the typical duration of contacts, and thus enhances the destabilizing effect of CIL. This effect can be observed as well in Fig. 7.3(a), in which α_N initially decreases with growing $\overline{W}_c$.

7.3.2 Fast phase separation to a polarized active liquid showcasing collective motion and self-healing.

When increasing adhesion at low CIL, clusters become larger and more stable, until a slowly evolving gel-like structure is obtained. Here, the dynamics become sub-diffusive, with adhesion effectively freezing the system in a gel-like structure — Fig. 7.4(a) and Fig. B.6. This phase is the same as the near-equilibrium gel phase at low activity as studied by Redner *et al.* [173]. The transition line from a dynamic cluster phase to an arrested gel can be approximated using the inflection point of α_N for increasing adhesion — Fig. 7.7.

Upon increasing CIL, the large fluctuation exponent α_N approaches 1 for $\overline{W}_c > 0.6$ and the system fully separates — Fig. 7.3(a). As mentioned above, the Peclet number is far too low to induce phase separation through MIPS. Instead, it occurs through coarsening of a gel-like structure and happens simultaneously throughout the whole domain, resembling spinodal decomposition — see Fig. 7.4(e). The dynamics of classical spinodal decomposition are governed by diffusion-like phenomena, which would render the late stage of phase separation a very slow process (e.g. Cahn-Hilliard theory [21]).

Investigating the kinetics of phase separation in more detail, we compute the time evolution of the characteristic lengths $\mathfrak{L}(t)$ (see 7.5.3) — Fig. 7.4(b). For 2D active Brownian particles, its power law exponent $\alpha_{\mathfrak{L}}$ is generally below the diffusive exponent $1/3$ due to the relatively high noise level [174, 201]. Including CIL, however, $\alpha_{\mathfrak{L}}$ surpasses $1/3$, becoming super-diffusive at intermediate times. Eventually, the

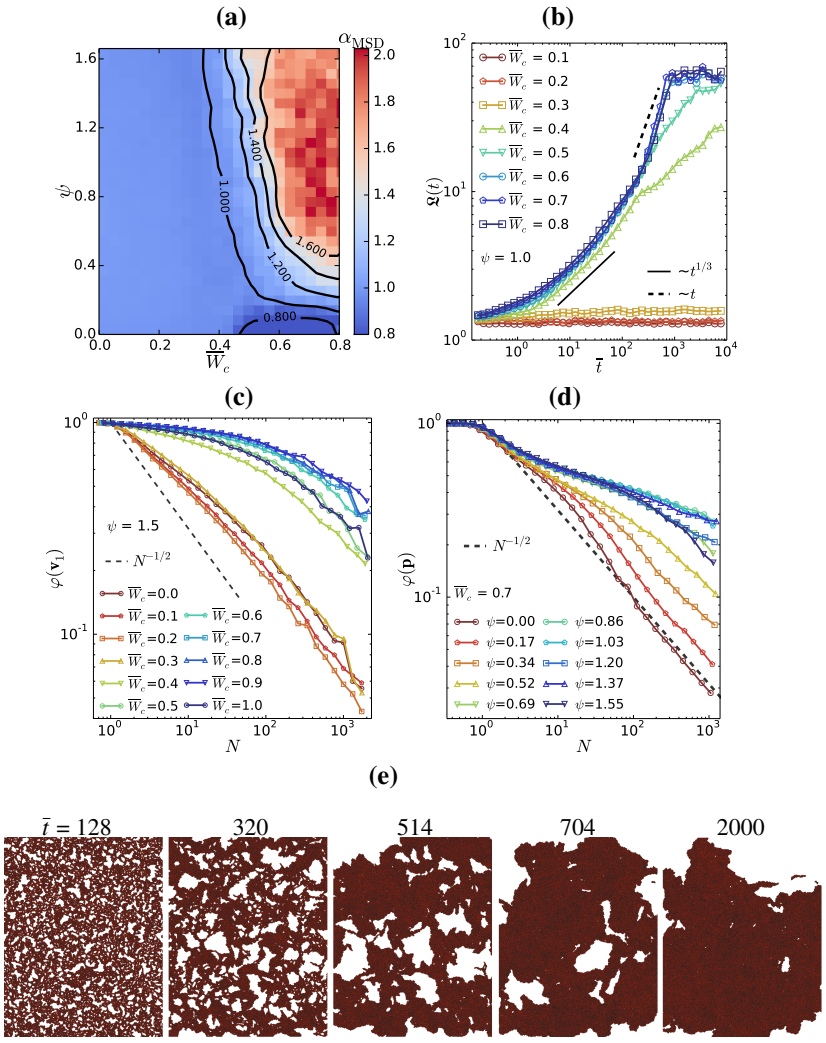

Figure 7.4: **(a)**: Map of the power law exponent of the MSD at long timescales, α_{MSD}, for varying $\overline{W}_c$, and ψ. For low adhesion, α_{MSD} is very close to one. Increasing adhesion and in the absence of CIL, particle motion becomes sub-diffusive due to jamming, while becoming quasi ballistic at ψ=1, indicating large-scale collective motion. **(b)**: Characteristic length scale $\mathfrak{L}(t)$ computed from the static structure factor (see 7.5.3) as a function of time, for varying $\overline{W}_c$ at ψ=1. Due to CIL, the power law exponent $\alpha_{\mathfrak{L}}$ is larger than $\approx$ 1/4, the subdiffusive exponent which is typically observed in spinodal decomposition in 2D systems, and with increasing time surpasses the diffusive exponent 1/3 due to increasing cell alignment. At high $\overline{W}_c$ and large times, the system collapses to polarized fluid at a super-linear rate, thereby completing phase separation. **(c)**: Spatial velocity correlation measure $\varphi(\mathbf{v})$ as a function N for changing $\overline{W}_c$, with velocities measured on a time interval of 1. In the presence of high CIL (ψ=1.5), the particle velocities become highly aligned. **(d)**: Spatial polarization correlation measure $\varphi(\mathbf{p})$ as a function of N for varying ψ at $\overline{W}_c$=0.7. At sufficiently high ψ, the point where $\varphi(\mathbf{p})$ bends back towards $N^{-1/2}$ diverges. **(e)**: Progression of a fast phase separating system with 85.000 cells at ψ=1 and $\overline{W}_c$=0.7, showcasing initial coarsening due to spinodal decomposition, followed by a collapse into a gigantic cluster, which moves collectively and has very large correlation lengths. See also Fig. B.8.

system collapses at a super-linear rate and phase separation is accomplished in a surprisingly short time, when $\mathfrak{L}(t)$ reaches a plateau.

Remarkably, the precise timing of this plateau is influenced very little by the system's size and the dynamics are affected little by the system's density — see Fig. B.4(b-c). These very fast phase separation dynamics resemble spinodal decomposition in the presence of convective transport and viscoelastic stresses [108]. At sufficient CIL, large fluctuations of collective cell movement can be observed, which grow in size and are eventually only limited by the characteristic lengths of the domains — Fig. B.8. Indeed, the existence of large-scale collective motion (convection) is evident in the MSD — Fig. 7.3(b) — which for $\overline{W}_c > 0.4$ scales ballistically ($\sim t^2$) at large timescales, and even surpasses the total displacement of free particles ($\Delta^2(t)_{\text{free}}$). As shown in Fig. 7.4(a), while elevated levels of $\overline{W}_c$ cause sub-diffusive behavior due to jamming at low CIL, α_{MSD} quickly approaches 2 when increasing ψ — see also Fig. B.5(b).

To investigate this collective behavior in more detail, we show the spatial velocity correlation function $\varphi(\mathbf{v})$ in Fig. 7.4(c). (see 7.5.3). For uncorrelated velocities, i.e. a gas, $\varphi(\mathbf{v})$ will scale as $\sim 1/\sqrt{N}$, while for rigid body-like translations, $\varphi(\mathbf{v})$=1 up to the size of the largest unconnected cluster. Initially, $\overline{W}_c$ decreases velocity correlation, since clusters are de-stabilized (see earlier), while around $\overline{W}_c$=0.4 a sharp shift towards high correlation occurs. For $\overline{W}_c$=0.7, the bending point of $\varphi(\mathbf{v})$ occurs at $N > 100$, exemplifying convective motion on large spatial scales.

This collective motion is not caused by a polarization at the edge of clusters, but by strongly aligned polarizations throughout the dense phase. Fig. 7.4(d) shows the spatial correlation function for the cell polarizations: $\varphi(\mathbf{p})$. Upon increasing ψ, the value of N where $\varphi(\mathbf{p})$ bends back towards $N^{-1/2}$ diverges, showing strong polarization allignment at large lengthscales. The sharp shift in this bending point provides a delineation for the polarized liquid region — see Fig. 7.7. We note that this phase resembles the state observed by Szabo *et al.* [204].

7.3.3 CIL prevents monolayer de-wetting.

De-wetting occurs when the repulsive energy barrier provided by cell-substrate adhesion (W_s) is not high enough to prevent a dense phase from collapsing due to multi-cellular contractility (W_c). Individual cells are squeezed out of the 2D monolayer, giving rise to 3D cell aggregates. De-wetting constitutes a limiting case of the presented model's scope, which due to its inherent 2D formulation only predicts its occurrence but not the precise dynamics and structure inside the de-wetted phase.

Fig. 7.5(a) shows a map of the average inter-particle distance $\langle \overline{d}_{ij} \rangle$ between contacting cells as a function of $\overline{W}_c$ and ψ. When de-wettting, a sharp downward shift in $\langle \overline{d}_{ij} \rangle$ occurs. The value of $\overline{W}_c$ at which the de-wetting transition happens is dependent on ψ,

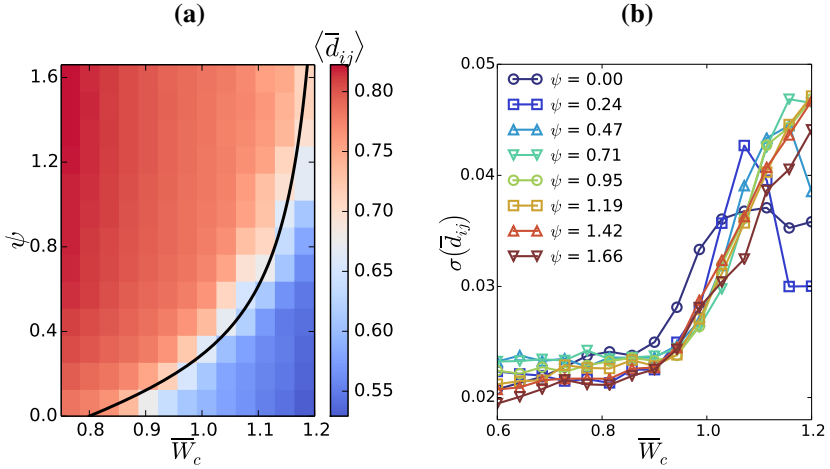

Figure 7.5: **(a)**: Map of the mean inter-particle distance $\langle \overline{d}_{ij} \rangle$ for all contacting cells i and j, at high $\overline{W}_c$ for varying ψ. De-wetting is associated with a sharp shift to lower $\langle \overline{d}_{ij} \rangle$. The indicated analytical line is obtained from the force balance $\langle F_{cc} + F_{\text{rep}} \rangle = 0$. **(b)**: Standard deviation of the inter-particle distance $\sigma(\overline{d}_{ij})$, as a function of $\overline{W}_c$, for varying ψ. At high ψ, large fluctuations in the dense phase increase $\sigma(\overline{d}_{ij})$, causing de-wetting for lower $\overline{W}_c$, than obtained from the force balance — see **(a)**.

appearing at higher W_c for large ψ. Indeed, CIL improves the wetting capability of a monolayer of contractile particles by orienting them towards the free space, thereby increasing the total cell-substrate adhesion energy.

An analytical de-wetting transition line can be derived by considering the average intercellular force for cells with intercellular distance r between R and $2R$:

$$\langle F_{cc} \rangle = \frac{1}{3\pi R^2} \int_0^{2\pi} d\theta \int_R^{2R} r F_{cc}(r)\, dr = \frac{2}{9R} \left(4W_s - 5W_c\right), \tag{7.6}$$

The wetting transition is then obtained from the force balance:

$$\left\langle F_{\text{cc}} + F_{\text{rep}} \right\rangle = 0. \tag{7.7}$$

In the limit $\psi \gg 1/2\pi$, the de-wetting line can be approximated to yield:

$$\psi = -\frac{1}{4 \ln\left(\frac{4}{9}\left(5\overline{W}_c - 4\overline{W}_s\right)\right)}, \tag{7.8}$$

This de-wetting line, Eq. (7.7), is shown in Fig. 7.5(a), and is in close agreement with the location of a sharp shift in $\langle \overline{d}_{ij} \rangle$, calculated from simulations. In these simulations,

de-wetting follows a distinct pattern, contracting small regions of characteristic spacing — irrespective of the initial cluster size — into a semi-stable network-like structure, which itself collapses with much slower dynamics. In the case of large ψ, when F_{rep} approaches F_m, the de-wetting transition will occur at $\overline{W}_c$=1.25 when $\overline{W}_s$=1, and at $\overline{W}_c$=0.45 when $\overline{W}_s$=0.

It can be seen from Fig. 7.5(a), that the analytical de-wetting line obtained from the force balance (Eq. (7.7)), underestimates the de-wetting transition for larger ψ: a small number of de-wetted cells is counted in simulations, even below the transition line. A possible explanation for this is that the analytical de-wetting line neglects the effect of large density fluctuations occurring in the dense phase, which thereby give rise to co-operative compressive forces that can locally result in de-wetting. In Fig. 7.5(b) the standard deviation on the inter-particle distances $\sigma(d_{ij})$, is shown as a function of $\overline{W}_c$ and for varying ψ. At high ψ, in the dense phase, the variation in d_{ij} becomes very high due to large-scale fluctuations — see also Fig. B.9.

7.3.4 The effect of single cell viscosity

Previously, phases were described for a cell-cell friction constant $\bar{\gamma}$=0. In the following, the repercussions of a non-negligible tissue viscosity will be discussed. For low adhesion W_c and ψ, the effect of γ is small, since clusters remain small, motion is uncorrelated and contact times are relatively short. For larger W_c, however, the impact of γ, especially on the dynamics, is significant.

Fig. 7.6(a) shows the temporal evolution of α_N, starting from a uniform cell distribution, at $\overline{W}_c$=0.7 and ψ=1.0. At zero viscosity the system will rapidly phase separate resulting in an active, liquid-like dense phase (see previous). Increasing $\bar{\gamma}$ sharply decreases the rate of phase separation, even at small values of $\bar{\gamma}$=0.2. Furthermore, the decrease in the power law exponent of the time evolution of α_N suggests a change in the mechanism of phase separation.

Fig. 7.6(b) depicts the MSD, $\Delta^2(t)$, as a function of time, at ψ=1.5 and $\overline{W}_c$=0.4, for varying levels of $\bar{\gamma}$ — see also Fig. B.10(a). This is located just at the edge of the phase separating region of the $\psi/\overline{W}_c$ plane. Here, $\Delta^2(t)$ still scales diffusive (t^1) for large timescales. When increasing $\bar{\gamma}$, the MSD greatly decreases, with a peculiar plateau — and even a drop — around $\bar{t}$=1/ψ. Such a drop with increasing time is an uncommon feature, which might be explained by the existence of oscillations or waves with a common period.

To examine this in more detail, we computed the Fourier power spectrum $S(\overline{f})$ of the orientations θ — Fig. 7.6(d) — at $\overline{W}_c$=0.7 and ψ=1 (see also Fig. B.11(c) and B.10(b)). Interestingly, at high $\bar{\gamma}$, a peak in the power spectrum appears at $\overline{f}$=ψ=1, i.e. a standing wave exists in the cell orientations. Increasing $\bar{\gamma}$ shifts the peak towards lower

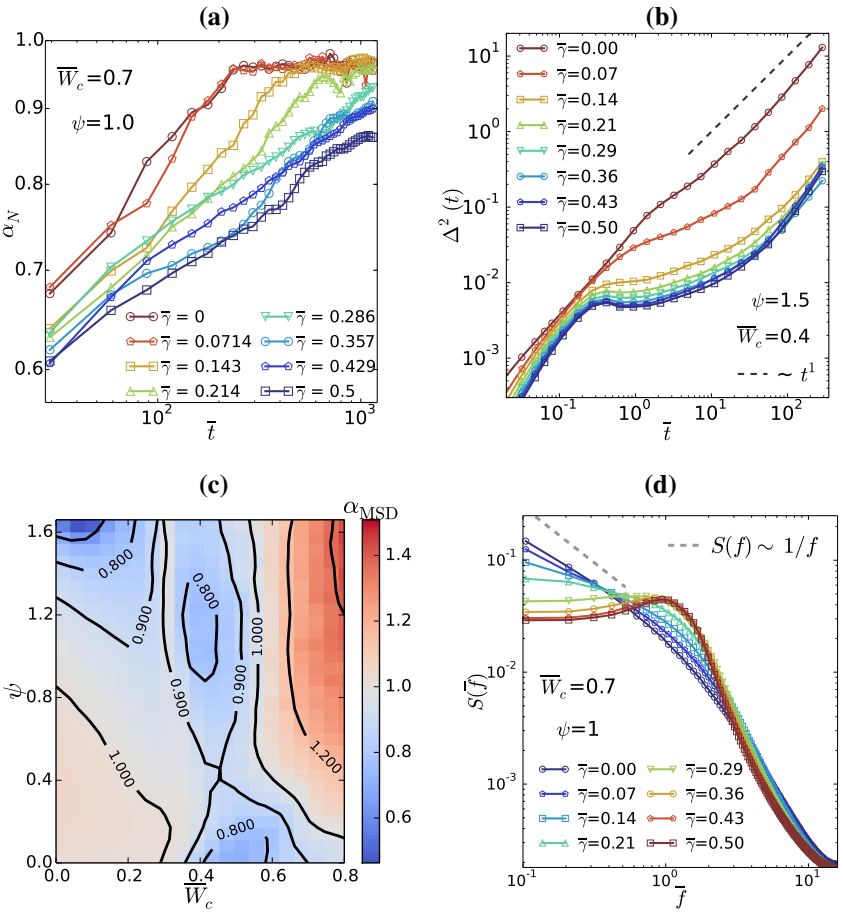

Figure 7.6: Influence of single cell viscosity $\bar{\gamma}$ on the phases observed in the $\overline{W}_c/\psi$ plane. **(a)**: Large number fluctuation exponent α_N, as a function of time, for varying viscosity $\bar{\gamma}$ at ψ=1 and $\overline{W}_c$=0.7. Viscosity causes a sharp reduction in both slope and exponent of phase separation dynamics. **(b)**: MSD, $\Delta^2(t)$, as a function of time, for varying $\bar{\gamma}$, at ψ=1.5 and $\overline{W}_c$=0.4. Viscosity greatly reduces $\Delta^2(t)$, creating a semi-equilibrium frozen gel phase, and introduces a remarkable plateau around $\bar{t}$=$1/\psi$, caused by standing waves in the cells' orientations. **(c)**: Map of the power law exponent of the MSD at long timescales, α_{MSD}, for varying $\overline{W}_c$, and ψ at viscosity $\bar{\gamma}$=0.2. For medium $\overline{W}_c$, a large sub-diffusive zone appears, corresponding to a frozen gel-like phase — compare to Fig. 7.4(b). Similarly, at low $\overline{W}_c$ and high ψ, a crystalline phase arises which is frozen due to jamming at high density. **(d)**: Fourier power spectrum $S(\bar{f})$ of the orientations, for varying $\bar{\gamma}$ at $\overline{W}_c$=0.7 and ψ=1. A peak occurs at $\bar{f} = \psi = 1$ at high $\bar{\gamma}$, and its location shifts towards zero when $\bar{\gamma}$ approaches zero. Notice the $\sim 1/f$ scaling when $\bar{\gamma} \to 0$.

frequencies, as the waves grow in size, eventually resulting in large-scale convective motion for $\bar{\gamma}$=0, and a characteristic $\sim 1/f$ scaling in the power spectrum at low frequencies — see also Fig. B.11(b). Since γ limits the size of these waves, they can not grow and amplify the dynamics of spinodal decomposition. Instead, a non-equilibrium frozen gel-like phase is obtained which phase separates extremely slowly; many times slower than feasible to compute in simulations and than of biological relevance. At lower $\overline{W}_c$=0.4, the peak in $S(\overline{f})$ becomes most prominent — see Fig. B.11(a) — alluding to a gel phase centered around $\overline{W}_c \approx 0.4$ at high ψ.

The effect of adding viscosity on the phase diagram can be clearly seen in Fig. 7.6(c), which gives a map of the power law exponent of the MSD, α_{MSD}, for varying $\overline{W}_c$ and ψ. Around $\overline{W}_c$=0.4 and at large ψ, a large sub-diffusive region appears, which corresponds to a non-equilibrium frozen gel-like phase. Moreover, the phase separating region decreases in size and within it, α_{MSD} is lower, suggesting a dwindling contribution of convective flow to the dynamics of phase separation. At low $\overline{W}_c$ and high ψ, another sub-diffusive zone arises. Here, a strongly jammed crystalline phase exists, which now freezes due to cell-cell friction. It should be noted that the latter phase is only present at sufficiently high density, since its existence is the result of the lack of void space.

7.4 Discussion

We used particle simulations to study the phase organization of self-propelled particles with biologically relevant properties for cell populations in 2D. We stress that using soft particles simulations allows in the same scheme the existence of disperse, confluent and dewetting phases. We find that an interplay in between cell-cell adhesion and CIL interaction provides a rich generic 2D phase landscape, the use of cell-substrate adhesion adding an extra transition to the third dimension. We quantify both structurally and dynamically the different phases, and provide analytical transition lines for the disperse-confluent transition and for the dewetting transition. Importantly, the density is seen to affect little the essence of the phase diagram.

We took special care to use quantities which are accessible experimentally. In order to challenge the predictions of the present model, we estimate that *in vitro* experiments would need the recording of multi-day time-lapses of field of views including at least $\approx 50,000$ cells in order to obtain robust phase characterizations. While this would be very impractical with conventional microscopes, recent technologies of lens-free microscopes [103] should render such experiments feasible. The reader shall remark that a cell division parameter, which will results in exploring the density axis in the phase landscape, was not included in the model. We performed simulations including exponential cell growth, Fig. B.12. Clearly, processes such as phase separation are not completed due to a lack of time, but the essence of the phases and their transitions is

seen to be well conserved. Comparing such simulations to experiments as a function of increasing density and which phases are crossed over should help to the comparison experiments/theory.

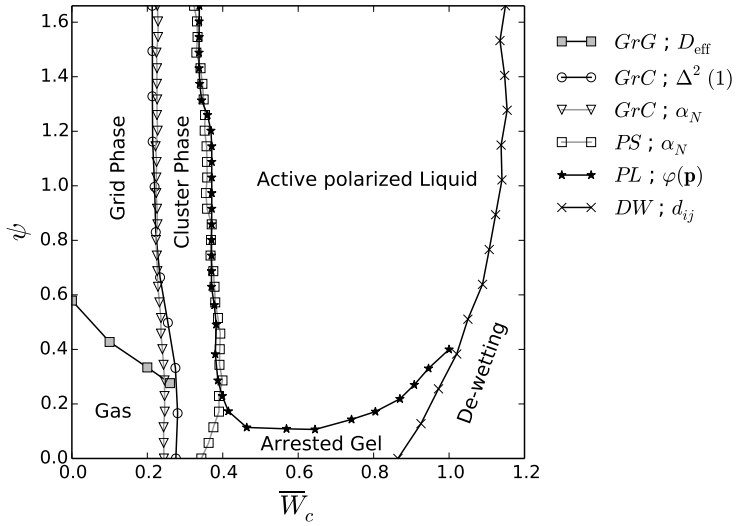

Figure 7.7: Phase diagram in the $\overline{W}_c/\psi$ plane at $\overline{W}_s$=1, $\bar{\gamma}$=0 and ϕ=0.85, with numerically estimated phase transition lines indicated. *GrG*: Grid-like to gas phase transition line, based on the location of the peak of D_{eff} — see Fig. 7.3(d). *GrC*: Grid-like to cluster phase transition based on the inflection point in $\Delta^2(1)$ — dynamical, see Fig. 7.3(c) — and the iso-line of α_N=0.5 — structural, see Fig. 7.3(a). *PS*: Phase separation line, based on the inflection point in α_N, see Fig. 7.3(a). *PL*: delineation of the active polarized liquid inside the phase separation zone based on $\varphi(\mathbf{p})$, see Fig. 7.4(c). *DW*: De-wetting line estimated from the inflection point in the inter-particle distance d_{ij} with increasing $\overline{W}_c$ — see Fig. 7.5. The details on how each transition line was calculated numerically are provided in the section 7.5.9.

This work gives a very general description of the phase organization of large populations of cell-like particles. It could be argued that many key biological transitions in development, disease and healing constitute fundamental physical phase transitions. Indeed, the minimal presented model includes phases resembling a large range of existing cell and tissue phenotypes; for instance, the state of stable epithelium is highly relevant to many tissues. We note that the kinetics of phase separation are very fast compared to the ones of typical spinodal decompositions. Practically, the phase separation process we observe corresponds to a fast closing of the holes present in the populations. While the exact mechanism speeding up the process is unclear, this resembles the capacity of epithelia to rapidly close wounds to ensure quick regeneration.

From the state of stable epithelium, decreasing the cell-cell adhesive tension would

drive the population to a disperse state. For cells, this is exemplified in the Epithelial-Mesenchymal Transition (EMT), which has long been associated with a down-regulation of Cadherin proteins [101, 121]. In more recent *in-vitro* experiments, EMT has been observed when a down-regulation of Cadherins is induced [9, 42], connected with a decrease of monolayer tension [9]. In the latter study, this decrease in monolayer tension leading to EMT was not abrupt — less than 50 % — in agreement with the idea of a sharp transition between the two phases — Fig. 7.3(a). *In-vivo*, a well studied case of EMT is neuron dispersal, which has been associated to the presence of strong CIL [22] and a decrease of cell-cell adhesion. In [34], an EMT towards a grid-like distribution of neurons has been observed *in-vivo*, tightly connected to the presence of CIL.

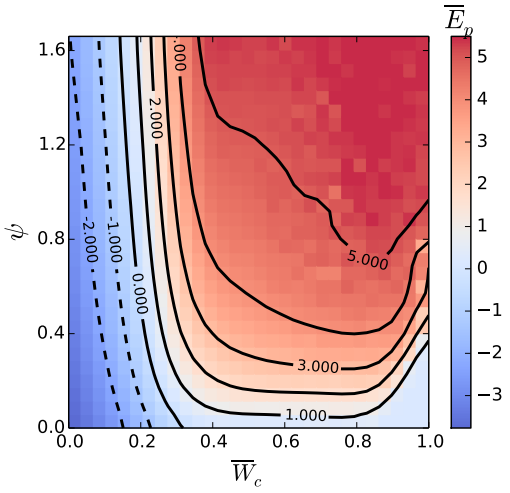

Figure 7.8: Map of average potential energy $\overline{E}_p$, computed using virial theorem, for varying $\overline{W}_c$ and ψ, at $\overline{W}_s$=1 and $\bar{\gamma}$=0. Note that ψ generally ensures tensile conditions ($\overline{E}_p > 0$), particularly in the active-liquid region. At low $\overline{W}_c$, kinetic clustering induces average compressive stresses. The effects of introducing viscosity on the mechanical state are discussed briefly in SI Fig. B.7

An intermediate decrease of cell-cell adhesion has been connected to the elusively termed partial-EMT [128, 209] in which groups of cells escape collectively from a confluent tissue by combining their strength, contrary to pure EMT, where one single cell is able to escape by itself. It could be speculated that this state of partial-EMT corresponds to the cluster phase at intermediate adhesion exhibited by the present model, which indeed occurs at medium cell-cell adhesion.

From a stable epithelium, the de-wetting phase can be reached by increasing W_c and/or by decreasing ψ. It has been known since many years that cancer cells lose their CIL behavior [1, 3, 176], which would correspond to a transition from a stable epithelium

towards de-wetting, the latter corresponding to a passage from a 2D geometry to a 3D cell aggregate. Another route towards de-wetting is by decreasing cell-substrate adhesion W_s, which was studied in [42]. As shown in Eq. (7.8), increasing W_s favors wetting by translating the de-wetting line towards larger W_c. When an explant lands on an adhesive surface, a distinct wetting process of the spheroid takes place [75]. This common phenomenon was studied using concepts from wetting physics more recently in [43].

Finally, we point out the importance of CIL on mechanics. Fig. 7.8 shows the average virial energy ($\overline{E}_p$; a measure for the pressure in the system, see 7.5.2) in the $\overline{W}_c/\psi$ plane. Positive values of E_p correspond to an environment with average tensile intercellular stresses, whereas negative values of E_p correspond to compressive stresses. It should be noted that from the 2D simulations, we can only report intercellular stress in the 2D monolayer, i.e. very similar to what can be computed from Traction Force Microscopy measurements [213]. CIL is seen to ensure tensile intercellular stresses in the stable monolayer phase. This tension corresponds the surface tension measured in [223], and is necessary to maintain the wetting of the monolayer when $W_s < W_c$.

This work opens similar research for cell populations living in 3D scaffolds, for which the free parameters of the simulations would have to be adjusted. Inherently, this will lead to a different phase landscape, which will supplement the knowledge of what happens in the de-wetting phase of the present study, leading to a global view of cell population organizations in 1D, 2D and 3D, and of the transition in between the different phases and dimensions.

More generally, asymmetric contact repulsions analogous to CIL may be relevant interactions in other fields such as the structure of bacterial colonies [11], the organization of social animals [120, 125], and more generally in population distribution ecology. This may include human social behavior such as the distribution of people on a crowded beach [197].

7.5 Supplementary Information

7.5.1 Solving the equation of motion

The overdamped system (Eq. (7.1)) can be written as:

$$F_m \begin{pmatrix} \cos\theta_i \\ \sin\theta_i \end{pmatrix} - \sum_j^{nn} F_{ij}^{cc} \hat{\mathbf{n}}_{ij} = \gamma_s \dot{\mathbf{x}}_i + \sum_j^{nn} \Gamma_{ij} (\dot{\mathbf{x}}_i - \dot{\mathbf{x}}_j) \tag{7.9}$$

For contact between two cells i and j, the combined friction constant Γ_{ij} is defined as:

$$\Gamma_{ij} = \gamma_{\parallel} (\hat{\mathbf{n}}_{ij} \otimes \hat{\mathbf{n}}_{ij}) + \gamma_{\perp} (\hat{\mathbf{I}} - \hat{\mathbf{n}}_{ij} \otimes \hat{\mathbf{n}}_{ij}) \tag{7.10}$$

in which $\mathbf{I}$ denotes the identity matrix. $\gamma_{\parallel}$ is the effective internal viscosity of the cell for deformations over long time-scales, and $\gamma_{\perp}$ a sliding friction coefficient. The equation of motion for the complete collection of N particles can be expressed as $\mathbf{F} = \boldsymbol{\Gamma} \cdot \dot{\mathbf{x}}$, with $\mathbf{F}$ a vector with all non-dissipative forces and $\boldsymbol{\Gamma}$ a $N \times N$ friction matrix with (2×2) sub-matrices which are non-zero for diagonal components and for (i, j) of contacting cells i and j, and zero otherwise [195]. Note that this is identical to Eq. (2.1). It can be shown that $\boldsymbol{\Gamma}$ is positive definite, and therefore we are able to solve the system iteratively for the velocities by using the conjugate gradient method – see [218]. Finally, the new cell positions are computed using an explicit Euler time integration scheme. It should be noted that CIL imposes an additional upper limit to the simulation time step Δt:

$$\Delta t < \frac{1}{f_{\text{cil}}}. \tag{7.11}$$

See also further in section 7.5.11.

7.5.2 Parameter non-dimensionalization

To reduce the size of the parameter set, the following normalizations are introduced:

$$2\overline{R} = 1, \qquad \overline{F}_m = 1 \quad \text{and} \quad \overline{v}_m = 1 \tag{7.12}$$

Hence, the energy of motility W_m and the substrate friction γ_s become:

$$\overline{W}_m = \frac{W_m}{2F_m R} = 1 \qquad \text{and} \qquad \overline{\gamma}_s = \frac{\gamma_s}{F_m / v_m} = 1. \tag{7.13}$$

Based on these, the following non-dimensionalized simulation parameters are defined:

$$\begin{aligned} \overline{\gamma}_{\parallel} &= \gamma_{\parallel}/\gamma_s \qquad \text{and} \qquad \overline{\gamma}_{\perp} = \gamma_{\perp}/\gamma_s, \\ \overline{W}_s &= W_s/W_m \qquad \text{and} \qquad \overline{W}_c = W_c/W_m, \\ \overline{f}_{\text{cil}} &= f_{\text{cil}} \frac{2R}{v_m} \qquad \text{and} \qquad \overline{D}_r = D_r \frac{2R}{v_m}. \end{aligned} \tag{7.14}$$

In practice, we usually assume that $\overline{\gamma}_{\parallel} = \overline{\gamma}_{\perp} = \overline{\gamma}_c$. Adding the cell density ϕ and combining $\overline{f}_{\text{cil}}$ and $\overline{\omega}_r$ into ψ, we end up with 5 real parameters which define the dynamics of this system. The measure for potential energy E_p is normalized as:

$$\overline{E}_p = E_p / W_m. \tag{7.15}$$

Wave vectors $\mathbf{q}$ are normalized as:

$$\overline{\mathbf{q}} = 2R\,\mathbf{q}. \tag{7.16}$$

7.5.3 Phase measures

In order to quantify the organization of large populations of particles, robust static and dynamic phase measures are required. The following phase measures are employed throughout this chapter:

The *large fluctuations exponent* (α_N); The standard deviation ΔN of the fluctuations in the number of particles in a sub-region of size l^2, containing a total mean number of N particles, follows a power law $\Delta N \sim N^{\alpha_N}$, with α_N a large fluctuations exponent. $\alpha_N = 1$ for a dense system, $\alpha_N = 1/2$ for a randomly distributed population (gas-like), and $\alpha_N < 1/2$ for a grid-like structure.

The *Mean Squared Displacement* as a function of time, $\Delta^2(t)$, from which is defined the ratio $D_{\text{eff}}/D_{\text{free}}$ of the effective coefficient of diffusion at long timescale D_{eff} over the effective coefficient of diffusion at long timescale of the isolated particles D_{free}.

The *Static Structure Factor*, $S(\mathbf{q})$. For each wave vector $\mathbf{q}$:

$$S(\mathbf{q}) = \frac{1}{N}\left\langle \left\| \sum_{j=0}^{N} \mathrm{e}^{-i\mathbf{q}\mathbf{x}_j} \right\|^2 \right\rangle, \tag{7.17}$$

From $S(q)$, the characteristic length scale $\mathfrak{L}(t)$ is computed as:

$$\mathfrak{L}(t) = 2\pi \frac{\int_{q_{\min}}^{q_c} S(q,t)\,\mathrm{d}q}{\int_{q_{\min}}^{q_c} S(q,t)\,q\,\mathrm{d}q}, \tag{7.18}$$

in which $q_{\min} = 2\pi/L$, with L, the domain length (excluding the boundary) and q_c a cut-off value which we choose $2\,q_c R = 6$ to ensure the inclusion of all large wavelength contributions.

The *spatial correlation measure* φ. For windows of increasing size N, $\varphi(\mathbf{v})$ is computed as:

$$\varphi(\mathbf{v}) = \left\| \sum_{i=1}^{N} \mathbf{v}_i \right\| / \sum_{i=1}^{N} \|\mathbf{v}_i\|, \tag{7.19}$$

i.e. the ratio between the magnitude of the sum of the velocities and the sum of the magnitudes of the velocities. When motion between particles is perfectly uncorrelated, φ scales like $\sim 1/\sqrt{N}$ for $N > 1$ while for perfectly correlated rigid body-like tranlation, φ=1, regardless of N. It should be stressed that $\varphi(\mathbf{v})$ only estimates translational spatial correlations, neglecting correlations due to rotational motion of clusters. For $\mathbf{v}$, the average was taken over a (small) time interval, $\bar{t}$=1. By substituting the velocities $\mathbf{v}_i$ with the particles' polarization vectors $\mathbf{p}_i$, the polar correlation measure $\varphi(\mathbf{p})$ is

obtained.

The *mean inter-particle distance* $\overline{d}_{ij}$ decreases when the system contracts due to W_c, but greatly drops when the energy barrier for de-wetting is overcome, thereby providing a clear measure of the de-wetting transition. For each cell i, $\overline{d}_{ij}$ is computed by averaging over its nearest neighbors *nn*:

$$\overline{d}_{ij} = \frac{1}{2R} \left\langle \sum_{j}^{nn} ||\mathbf{x}_i - \mathbf{x}_j|| \right\rangle \tag{7.20}$$

The average *potential energy*, E_p, is a measure for the local mechanical stress due to contacts that individual cells experience. An estimate for the potential energy can be obtained using the virial theorem which states that:

$$E_p = \left\langle \sum_{j}^{nn} \left[F_{ij}^{cc} \hat{\mathbf{n}}_{ij} \cdot (\mathbf{x}_i - \mathbf{x}_j) \right] \right\rangle. \tag{7.21}$$

where the sum iterates over all contacting neighbor (*nn*) cells j of cells i.

The *mean cluster size* $\langle N_c \rangle$ is a useful structural measure for non-percolated systems at low density — see Fig. B.3(a).

The ratio of the number of single (unbound) particles over the size N_s/N gives an indication of the presence of a gas-like phase for non-percolated systems at low density — see Fig. B.3(b).

7.5.4 Free direction for CIL

CIL causes the cells to polarize away from contact. To model this, we define a free direction vector $\mathbf{p}_i^f$ which points away from the closest neighboring cells. The following formulation is valid for contact between disk-like walkers in 2D but is equally applicable for contact between spherical particles in 3D:

$$\mathbf{p}_i^f = -\sum_{j}^{nn} \left[\frac{2a_{ij}^2}{d_{ij}^3} (\mathbf{c}_{ij} - \mathbf{x}_i) \right], \tag{7.22}$$

Note that the contribution of each neighbor to $\mathbf{p}_i^f$ is weighted using the contact radius a_{ij}. In other words, if a cell has a large contact area with cell i, its contribution to the free direction vector is bigger. $\mathbf{c}_{ij}$ is the contact point, which in the general case of two spheres with radii R_i and R_j is calculated as:

$$\mathbf{c}_{ij} = \mathbf{x}_i + \hat{\mathbf{n}}_{ij} \frac{R_i^2 - R_j^2 + d_{ij}^2}{2d_{ij}}. \tag{7.23}$$

In 2D, $\hat{\mathbf{p}}_i^f = \mathbf{p}_i^f / ||\mathbf{p}_i^f||$ is related to the free orientation angle θ_i^f as:

$$\hat{\mathbf{p}}_i^f = \begin{pmatrix} \cos\theta_i^f \\ \sin\theta_i^f \end{pmatrix}. \tag{7.24}$$

Should a cell i not have any contacts, $\hat{\mathbf{p}}_i^f$ is set to $\hat{\mathbf{p}}_i$, hence CIL has no effect on the cell's polarization (see Eq. (7.3)).

7.5.5 Effective repulsive force due to CIL

The net effect of CIL is a long-range repulsive potential. Here we try to derive an analytical formulation for this effective repulsive force for an idealized system. The orientation θ follows an Ornstein-Uhlenbeck process, for which, the probability distribution satisfies the Fokker-Planck equation. With periodic boundary conditions $P(-\pi) = P(\pi)$, and assuming $\theta_f = 0$, the stationary solution for the probability distribution P is given by:

$$P(\theta) = \sqrt{\frac{\psi}{\pi}} \frac{\exp\left(-\psi\theta^2\right)}{\mathrm{erf}(\pi\sqrt{\psi})}. \tag{7.25}$$

The average repulsive force can be expressed as:

$$\langle \mathbf{F}_{\mathrm{rep}} \rangle = F_m \langle \mathbf{p} \rangle \tag{7.26}$$

$$= F_m \left\langle \begin{pmatrix} \cos\theta \\ \sin\theta \end{pmatrix} \right\rangle. \tag{7.27}$$

Due to symmetry, $\langle \sin\theta \rangle = 0$. Hence, the magnitude of the effective mean repulsive force can be calculated by integrating from $-\pi$ to π:

$$\left\langle F_{\mathrm{rep}} \right\rangle = \frac{F_m}{\mathrm{erf}(\pi\sqrt{\psi})} \sqrt{\frac{\psi}{\pi}} \int_{-\pi}^{\pi} \cos(\theta) \exp\left(-\psi\theta_i^2\right) \mathrm{d}\theta_i, \tag{7.28}$$

which has a solution:

$$\left\langle F_{\mathrm{rep}} \right\rangle = \frac{i F_m \exp\left(-\frac{1}{4\psi}\right)}{2\,\mathrm{erf}(\pi\sqrt{\psi})} \left[\mathrm{erf}\left(\frac{i + 2\pi\psi}{2\sqrt{\psi}} \right) - \mathrm{erf}\left(\frac{i - 2\pi\psi}{2\sqrt{\psi}} \right) \right]. \tag{7.29}$$

For $\psi \gg 1/2\pi$, i.e. the effect of CIL is non-negligible, the integral in Eq. (7.28), can be approximated to:

$$\left\langle F_{\mathrm{rep}} \right\rangle \approx F_m \sqrt{\frac{\psi}{\pi}} \int_{-\infty}^{\infty} \cos\left(\theta\right) \exp\left(-\psi\theta_i^2\right) \mathrm{d}\theta_i, \tag{7.30}$$

which has a solution:

$$\left\langle F_{\text{rep}} \right\rangle \approx F_m \exp\left(-\frac{1}{4\psi}\right). \tag{7.31}$$

In the opposite limit, $\psi \ll 1/\pi^2$, Eq. (7.29) can be simplified to:

$$\left\langle F_{\text{rep}} \right\rangle \approx \frac{4\sqrt{\pi} F_m \psi^{3/2}}{(1+4\pi^2\psi^2)\,\text{erf}(\pi\sqrt{\psi})} \exp\left(-\pi^2\psi\right) \tag{7.32}$$

$$\approx \frac{4\sqrt{\pi} F_m \psi^{3/2}}{\text{erf}(\pi\sqrt{\psi})}. \tag{7.33}$$

Finally, the mean repulsive force due to CIL can be written as:

$$\left\langle \mathbf{F}_{\text{rep}} \right\rangle = \langle F_{\text{rep}} \rangle \mathbf{p}^f. \tag{7.34}$$

7.5.6 De-wetting line

An analytical de-wetting transition line can be obtained by considering the average cell-cell force for cells with intercellular distance r between R and $2R$:

$$\langle F_{\text{cc}} \rangle = \frac{1}{R} \int_R^{2R} F_{\text{cc}}(r)\, \mathrm{d}r = \frac{W_s - W_c}{R}. \tag{7.35}$$

The wetting transition is then given by:

$$\left\langle F_{\text{cc}} + F_{\text{rep}} \right\rangle = 0. \tag{7.36}$$

In the limit $\psi \ll 1/\pi^2$, the de-wetting line has the shape:

$$\psi = \left[\frac{\overline{W}_c - \overline{W}_s}{2\sqrt{\pi}}\right]^{2/3}. \tag{7.37}$$

In the opposite limit, assuming that ψ is much larger than $1/2\pi$, we use expression (7.31) to obtain:

$$\psi = \frac{-1}{4\log\left[2(\overline{W}_c - \overline{W}_s)\right]}. \tag{7.38}$$

The previous equation provides a demarcation beyond which any given contact between two cells will ultimately de-wet - regardless of the surrounding cells. However, in a dense phase, individual cells might de-wet much earlier since $\langle F_{\text{cc}} \rangle$ is the combined

force of all surrounding cells. A modified transition line for a dense phase can be obtained by computing the average potential cell-cell force using polar coordinates:

$$\langle F_{cc}\rangle = \frac{1}{3\pi R^2}\int_0^{2\pi} d\theta \int_R^{2R} rF_{cc}(r)\,dr = \frac{2}{9R}\left(4W_s - 5W_c\right), \tag{7.39}$$

where the prefactor $3\pi R^2$ is the area of the circular corona where potential interactions exist, $r \in [R, 2R]$. This value of the average potential force must be used instead of $\langle F_{cc}\rangle = (W_s - W_c)/R$, which was obtained using rectangular coordinates. Hence, the line for the extrusion transition in the limit of ψ much larger than $1/2\pi$ now reads:

$$\psi = -\frac{1}{4\ln\left(\frac{4}{9}\left(5\overline{W}_c - 4\overline{W}_s\right)\right)}. \tag{7.40}$$

7.5.7 Clustering line

Beyond the clustering line, persistent clusters will be stable, i.e. the average repulsive force due to contact inhibition of locomotion will be lower than the magnitude of the maximal tensile force. Hence, the transition line can be estimated by:

$$\langle F_{\text{rep}}\rangle - \frac{2}{R}W_c = 0. \tag{7.41}$$

In the limit of large ψ, using Eq. (7.31) yields a transition line which has the form:

$$\psi = \frac{-1}{4\log\left(4\overline{W}_c\right)}. \tag{7.42}$$

From this, one can easily see that for large ψ, formation of clusters is only a function of the adhesive tension and will occur at $\overline{W}_c$=1/4.

7.5.8 Long time-scale coefficient of diffusion

Given an equation of motion of the form:

$$v_p \cdot \mathbf{p} = \mathbf{v}, \tag{7.43}$$

where the velocities $\mathbf{v}$ are linked to the polarizations $\mathbf{p} = (\cos\theta, \sin\theta)$ through an instantaneous walking velocity v_p, and where the orientations undergo a random walk:

$$\frac{d\theta}{dt} = \sqrt{2D_r}\xi, \tag{7.44}$$

with ξ a Gaussian noise with mean 0 and standard deviation 1, Fürth (1920) derived an expression for the mean squared displacement $\Delta^2(t)$:

$$\Delta^2(t) = \frac{2v_p^2}{D_r^2}\left(\mathrm{e}^{-D_r t} - 1 + D_r t\right), \tag{7.45}$$

which at long time scales can be approximated by the diffusion-like process with:

$$\Delta^2(t) \approx \frac{2v_p^2}{D_r} t, \tag{7.46}$$

i.e. the effective long-time scale coefficient of diffusion is given by

$$D_\infty = \frac{v_p^2}{2D_r}. \tag{7.47}$$

7.5.9 Phase transition lines

A full phase diagram with estimated transition lines was provided in Fig. 7.7. Here, we provide the full details on how each of these lines was numerically determined:

- *GrG*: As mentioned in the text, this transition line is given by the value ψ^{LC} at which the peak in D_{eff} occurs for each $\overline{W}_c$. To get a robust estimate of the location of this peak, it was estimated by its first moment:

$$\psi^{LC} = \frac{\int_0^{\psi_c} D_{\text{eff}}\,\psi\, d\psi}{\int_0^{\psi_c} D_{\text{eff}}\, d\psi}, \tag{7.48}$$

  with ψ_c the cross-over value, i.e. where $D_{\text{eff}}(\psi_c) = D_{\text{eff}}(0)$.

- *GrC*; $\Delta^2(1)$ is computed as the value of $\overline{W}_c$ where the inflection point occurs in the drop of the MSD at $\bar{t} = 1$: $\Delta^2(1)$ — see Fig. 7.3(c). For this we calculate the minimum of the gradient $\partial\Delta^2(1)/\partial\overline{W}_c$, again by estimating its first moment, integrating between $\overline{W}_c$=0 and $\overline{W}_c$=0.4.

- *GrC*; α_N is computed as the interpolated value of $\overline{W}_c$ at which α_N=0.5, and this for each ψ.

- *PS* is computed as the value of $\overline{W}_c$ where the inflection point occurs in the increase of α_N. For this, we calculate the maximum of the gradient $\partial\alpha_N/\partial\overline{W}_c$, estimated from its first moment by integrating between $\overline{W}_c$=0.2 and $\overline{W}_c$=0.5.

- *PL*: For computing the polarized liquid transition line we determine the measure $\sqrt{N}\varphi(\mathbf{p})$ for varying N. For non-aligned polarities, this measure would be 1 for all N. For systems which have a local alignment, it will be above one for intermediate N and finally lower back to 1 at large N. Hence, the position of the maximum in $\sqrt{N}\varphi(\mathbf{p})$ provides a heuristic measure on the length-scales at which the polar properties in the dense phase are present. The phase line is generated by computing the 2D interpolated values of $\overline{W}_c$ and ψ at which the position of this maximum exceeds $N = 75$. It should be noted that the location of the transition line is not sensitive to the exact choice of this cross-over value, since it sharply increases towards very large N.

- *DW*, finally, is calculated by the downward inflection point in $\langle d_{ij} \rangle$ with increasing $\overline{W}_c$. For this the minimum of the gradient $\partial \langle d_{ij} \rangle / \partial \overline{W}_c$ is estimated from its first moment, by integrating between $\overline{W}_c$=0.7 and $\overline{W}_c$=1.2.

7.5.10 A rudimentary cell cycle

In this chapter, a full phase diagram was constructed in the absence of cell division, in order to obtain a "pure" phase description which contains equilibrium phases at densities below confluency. In reality, of course, most *in vitro* experiments are complicated by the fact that cells are continuously dividing, thereby changing the phase properties and bringing the system out of equilibrium. In the discussion section, the effect of including cell division was briefly mentioned — see also Fig. B.12. Here, we quickly elaborate on the details of these simulations.

Cell growth is considered exponential, with no inhibiting factors, and the cell cycle is described from a purely morphological point of view. For the average cell cycle we assume a time of 20.93 hours, of which 40 minutes are spent in cytokinesis, as was experimentally determined on MCF10a epithelial cells. The full details of the cell cycle model can be found in section 2.2.3. The main assumptions of this cell cycle model are that the total volume of a dividing cell remains constant during cytokinesis, and that the cells' volumetric growth rate is constant during the growth phase, which is the remaining time during the cell cycle in which cells are not dividing. Cytokinesis itself is force controlled — see section 2.2.3 — but we assume that the total force cells can generate is always sufficient to complete cytokinesis in the pre-set time (i.e. 40 minutes).

7.5.11 Implementation details

To limit computation times, as well as disk space, the total number of particles was varied between different simulations — depending on the minimum number

of cells required to obtain a robust estimate of a given phase measure. Minimally, this constituted 25×10^3 particles for estimating the MSD, going up to 10^5 particles for simulations to obtain the large fluctuation exponent α_N.

The simulation time step was determined numerically by means of a convergence analysis at $\Delta t = 30$s (i.e. $\Delta\bar{t}$=0.016), which was used for all simulations. It should be noted that in the presence of γ, a significantly larger Δt would be possible. The conjugate gradient method was used for obtaining the particle velocities (see earlier), and the maximal residual in the forces was determined at $\overline{F}_{\text{res}}=2 \times 10^{-6}$, or $F_{\text{res}}=10^{-13}$N. An explicit Euler scheme was used to update the positions. The stochastic differential equation for the orientations was integrated using the Euler-Maruyama method. In order to efficiently compute contact interactions, a grid-based contact detection algorithm was used, which was executed every second step, and ignored contact candidates i and j when $\overline{d}_{ij} > 1.1R$.

The system's boundary was enclosed by means of a stiff, repulsive potential. To prevent any boundary effects in the computation of phase measures, only particles sufficiently far away from the boundary (at least 2.5 cell diameters) were included in the computations.

All simulations were performed in the flexible particle-based simulation framework Mpacts (formerly called DEMeter++).

Acknowledgements

We acknowledge Elsa Bazelières for experimental help, Xavier Trepat for discussions and encouragements, and Tim Odenthal and Simon Vanmaercke for help with implementation as well as proofreading the manuscript. H.R. and B.S. acknowledge support from the Agency for Innovation by Science and Technology in Flanders (IWT), Grant nr. 111504. R.A. acknowledges support from Fundació "La Caixa", the Spanish Ministry of Economy and Competitiveness (FIS2013-41144-P), and Generalitat de Catalunya (2014-SGR-878).

Authors contributions

B.S. and R.V. conceived the project. B.S. implemented the model, performed simulations and did numerical analyses. R.A., B.S. and R.V. provided analytical derivations. B.S., R.A., J.P., I.P., H.R. and R.V. discussed and interpreted the results. B.S. R.A., and R.V. wrote the manuscript. All the authors commented on the manuscript.

Chapter 8

Conclusions and future perspectives

During this project, an extensive effort was made to develop and extend a computational platform for meshless, individual cell-based modeling of cellular aggregates. This resulted in total in 41392 lines of C++ code and 17262 lines of Python code, spread over 730 commit operations in the code versioning system. Together with previous implementations by T. Odenthal and S. Vanmaercke, this lead to a powerful and flexible platform for particle-based simulations, dealing with various spatial scales, particle shapes and application fields. The previous chapters, each of which adapted from a journal publication, showcase this diverse applicability. However, next to methodological and software developments, the objective in this doctoral project was to advance biological insights concerning the interplay between active cell behavior, cell mechanics and the cell culture environment.

While individual cell-based modeling techniques now exist for more than 20 years [45] and already have resulted in some important findings and explanations of biological phenomena, their widespread use is still lacking. A possible reason for this is the "complexity gap" that exists between models and reality. Unavoidably, a modeler has to make educated decisions on which system aspects will be included in a model. Not only does this require a large integrative knowledge of cell biology, it often leads to "model element creep": the tendency of models to become ever more complicated with new mechanisms and parameters, sometimes without convincing evidence of their necessity. Instead of providing clear insights, such models will often make inconclusive predictions, or will just be tweaked with until results meet the biased modeler's expectations. This tendency of "model element creep" is often caused by wrong expectations about the purpose of mechanistic, mathematical models of

(complex) biological systems. It's often assumed that these models should act like carbon copies of reality and hence should provide quantitative predictions of biological outcomes, regardless of the spatial, temporal or biological scope. Rather, I'm convinced that a model should provide a de-complicated base system in which the effects of fundamental mechanisms can be tested. In this PhD work, I tried to rely as much as possible on fundamental physics, and only represent complex biological mechanisms through their effective mechanical or morphological consequences. This leads to models with relatively few parameters for which even the entire parameter space can be exhaustively explored.

In chapter 2, the influence of the most fundamental mechanical properties of cell and substrate on the mechanical microenvironment was investigated for cell cultures on microcarriers. Upon increase of cell density due to cell growth, an abrupt rise in compressive stress (i.e. the mechanical microenvironment) was observed in simulations. Interestingly, this sudden change in mechanical conditions is typical of a "jamming" transition, which has very recently been experimentally observed [205]. An elaborate sensitivity analysis showed that cell substrate adhesion strength and cell stiffness were the mechanical properties that most affect this rapid stress increase upon reaching confluence. Moreover, the shown simulations provide a proof-of-concept of the method and implementation for solving the equations of motion as a system using the Conjugate Gradient Method, as was proposed and implemented by [152].

Similar models of active cellular systems have shown surprisingly complex aggregate behavior, which naturally arises through emergence. In chapter 7, it was demonstrated that the presence of a well described and established biological mechanism, contact inhibition of locomotion, dramatically alters the phase behavior of two-dimensional cell aggregates, and gives rise to large-scale collective and organized cell behavior. The fact that precisely this contact inhibition of locomotion is omnipresent in most mammalian cells, but not in tumor cells, is by itself intriguing. Depending on the magnitude of cell-cell contractile energy, a grid-like phase or an active polarized liquid have been shown to occur. Moreover, a distinct de-wetting transition line could be identified, which should prove useful to help modulate the amount of cell aggregation for artificial cell culture systems. In an in-depth analysis of the effect of single cell viscosity, it was demonstrated that a non-equilibrium frozen gel-like phase can emerge. Finally, contact inhibition of locomotion was seen to ensure large tensile stresses, which are ubiquitous in "wound healing" sheet expansion experiments using epithelial cells [213]. By classifying multicellular structures in physical phases, we provide the groundwork of a structured framework for explaining the emergence of complex *in vitro* and *in vivo* tissue architectures. Analogously, interpreting phenotypical transformations as physical phase transitions can help shed light on important biological processes such as embryonic development and tumorigenesis.

In the context of tissue engineering, these mechanistic, physical models will help identify the characteristic aggregate phenotypes which occur in *in vitro* culture systems

and can be compared to *in vivo* systems. Due to the strong connection between the cell's physical microenvironment and its eventual differentiation pathway, these characteristic phenotypes might be directly related to key developmental processes which tissue engineering technologies try to emulate.

One important future prospect will be the explicit inclusion of particle shape in models that describe large-scale behavior of cell aggregates. Doing this will expose the effects of nematics – i.e. the geometrical alignment of elongated cells – which can have a dramatic impact on the phase behavior of large cellular systems. As was indicated in Fig. 1.3, the development of new methodologies to represent arbitrary shapes in individual cell-based modeling, and in DEM in general, constituted an important research pillar in this PhD project.

In chapter 3, a novel mechanistic method to account for mechanical contact between arbitrary rounded shapes was presented. These shapes were represented by means of triangulated surface meshes, on which the local radius of curvature can be computed for each triangle. Subsequently, contact forces were obtained by integrating the pressure distribution from Hertz theory over the contact area shared between two colliding bodies. The limitations of the method were explored, and convergence upon mesh refinement was demonstrated with respect to well understood reference cases. Finally, its applicability was studied by performing a series packing simulations with various particle shapes. This technique is especially suited for relatively soft bodies, such as cells on the microscopic scale, or fruits/food products on the macroscopic level, since the contact force will still be accurately represented even for large indentations.

A generalization of this method for arbitrary polyhedra — losing the restriction that the bodies should have rounded shapes — was presented in chapter 4. Here, an intersection polygon is computed in the contact plane between two colliding bodies. In this polygon, a geometrical "overlap distance" can be obtained at every location. Hence, by integrating a pressure that is scaled with this overlap distance, a continuous, stable and robust contact force can be obtained for any two arbitrary triangulated shapes. A disadvantage of this method is that it cannot anymore directly rely on the material properties of the particles, i.e. it is not fully mechanistic. Only a detailed model that also represents internal mechanical stress, e.g. the Finite Element Method, would generate a (near) exact solution for any arbitrary polyhedral shape. Still, Discrete Element Method simulations are generally not strongly influenced by the precise shape of the elastic contact potential, and it is common practice to artificially lower the contact stiffness for very rigid bodies, even when using spherical particles.

By adding a mechanical description of cytoskeletal behavior, and a proper model of adhesive tractions, a deformable cell model was obtained (see chapter 5). For the mechanical representation, an existing cortical model for the mechanics of red blood cells was implemented and validated based on experiments using optical tweezers. Next, the procedure for computing contact forces described in chapter 3 was combined

with a pressure formulation from Maugis-Dugdale theory to compute the forces of cell adhesion. The combined model was then validated by comparing with experiments of initial cell spreading. Using simulations, we could determine the factors that influence the scaling laws for initial cell spreading, which have been shown to remain conserved across many different cell types. Meanwhile, exploratory simulations have already shown the potential of deformable cell representations in modeling small aggregates of cells in microwell cultures, as well as in small epithelial monolayers.

Subsequently, the deformable cell model was coupled with a model for Computational Fluid Dynamics (chapter 6). For this, we made use of the Immersed Boundary Method, which realizes the coupling between a Lagrangian discretized domain (i.e. the deformable cell model) and an Eulerian volume mesh (i.e. the grid used for CFD computation) by distributing (Lagrangian) forces using a smoothened Dirac distribution. Using this method, we quantified the mechanical effects of microscopic flow on stem cells seeded in perfusion bioreactors which are used for Tissue Engineering purposes. The mechanical behavior of the stem cells was calibrating by comparing to Atomic Force Microscopy experiments. It was shown that mechanical signals such as the shear stress can vary strongly depending on the precise geometry of the cell. Therefore, it was concluded that reservations should be made when merely estimating such properties based on CFD simulations in empty scaffolds.

Finally, the scientific world has made some remarkable progress in the last five years in the fields of tissue engineering, mechanobiology and in general in cell biology. Emerging technologies such as micro-fluidics and bioprinting allow precise control of aggregate architecture and open the path to custom designed cell microenvironments. As experimental techniques such as traction force microscopy and atomic force microscopy start to mature, they will provide unprecedented, quantitative information on the physics of cells and their constituents. Moreover, the use of methods from fundamental physics to study biological systems has become more and more prominent in the last few years. From flocks of birds, over self-assembling colonies of cells to swarms of biomolecules, these exponents of living systems all share a common feature: they are composed out of “active matter”, for which a fundamental and unifying theory is still lacking [163]. In this regard, particle-based computational models will help unravel the foundations of active matter behavior, and through this they might drastically change our understanding of the emergence and organization of multicellularity, the progression of diseases, and of life in general.

Appendix A

Geometric contact properties

A.1 Contact point and effective overlap distance for rounded triangles

Here, the effective (geometrical) overlap distance and effective contact point between two triangles which each have an encompassing sphere are derived. It can be assumed that the actual contact point $\mathbf{c}_{\text{eff}}$ must be somewhere within the contact plane of the triangles' encompassing spheres. Any other position of the contact point would "favor" one sphere over the other for no apparent reason. Therefore, the corner points of both triangles $P = \{p_1, p_2, p_3\}$ and $Q = \{q_1, q_2, q_3\}$ are orthogonally projected on the contact plane of the spheres, as illustrated in Fig. A.1.

The two projected triangles $P' = \{p'_1, p'_2, p'_3\}$ and $Q' = \{q'_1, q'_2, q'_3\}$ are all located in the same plane (see also Section 3.2, Fig. 3.2). The triangles are effectively in contact when the intersection between the sphere-sphere contact circle, P' and Q' is not empty (indicated by the dark red area in Fig. 3.2). As the overlap distance between the encompassing spheres decreases monotonously when going away from c, the contact point where the overlap between the encompassing spheres is maximal must be the point in the dark red area that is closest to the center of the contact circle c. This point is also the point in the light red area that is closest to c.

The light red area is the polygon $S = \{q'_1, s'_1, p'_2, s'_2\}$. The number of corner points of this polygon can vary between 3 and 6, dependent on the relative positions of the two triangles. In order to calculate this polygon the intersection points (in this case s_1 and s_2) have to be determined. The intersection s between two lines defined by four points

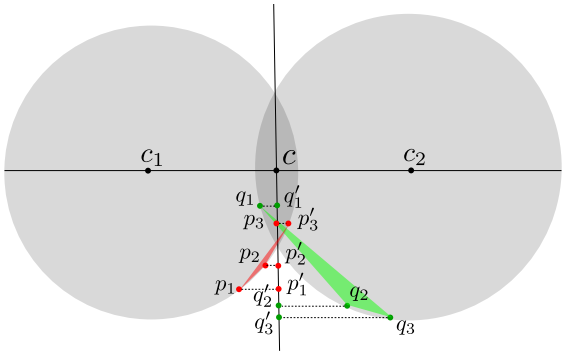

Figure A.1: Triangles P and Q, which belong to two rounded bodies in contact are projected onto the contact plane of their encompassing spheres.

x_1, x_2, x_3 and x_4 can be found as:

$$s = x_1 + u\frac{(w \times v) \cdot (u \times v)}{\|u \times v\|^2} \tag{A.1}$$

with $u = x_2 - x_1$, $v = x_4 - x_3$ and $w = x_3 - x_1$. Of course an intersection between two lines within a plane can always be found. Furthermore, it is verified whether s is effectively on the triangle segment. For a triangle segment between p_1 and p_2, this is the case if:

$$\|p_1 - s\|^2 < \|p_1 - p_2\|^2 \tag{A.2}$$

and

$$\|p_2 - s\|^2 < \|p_1 - p_2\|^2 . \tag{A.3}$$

In order to determine all intersection points between two triangles P' and Q', equations A.1, A.2 and A.3 have to be evaluated nine times (three times for each side of P').

The polygon S is the collection of all intersection points and all corner points of the triangles P' that are within triangle Q' and corner points of triangle Q' that are within triangle P'. Next, each point p_i from $\{p_2 \dots p_n\}$ is sorted according to the dot product with p_1, yielding a set of counter-clockwise sorted elements. Then, the closest distance from this sorted polygon S to the center of the contact circle c is calculated, giving the closest point $\mathbf{c}_{\text{eff}}$ as the effective contact point and the squared distance h^2. If c is within S, the distance between S and c is zero and the contact point will be c itself. From h^2, the effective overlap δ_{eff} is calculated in the case that c is not in S:

$$\delta_{\text{eff}} = \delta_s - R_1 - R_2 + \sqrt{R_1^2 - h^2} + \sqrt{R_2^2 - h^2} \tag{A.4}$$

with $h = \|c - c_p\|^2$ and δ_s being the overlap for a sphere-sphere contact – Eq. (3.9).

Additionally, it has to be checked whether one of the two triangles actually is on the opposite side of the sphere. Contacts only need to be calculated between triangles which are facing each other with their "outside" direction. The threshold angle for this is defined to be 90 °, i.e. for angles of more than 90 ° between any triangle and the contact plane, the triangles do not face each other and no contact should be calculated:

$$n_1 \cdot (c_2 - c_1) > 0 \quad \wedge \quad n_2 \cdot (c_1 - c_2) > 0 \tag{A.5}$$

in which n_1 and n_2 are normal vectors on triangle 1 (P) and triangle 2 (Q). If Eq. (A.5) holds, the triangles are facing each other. In the implementation, this check is performed at the start of contact resolution, because the contact can be immediately discarded if this simple check does not hold.

A.2 Contact resolution between polygons

To avoid calculating unnecessary contacts, as well as to ensure sufficient accuracy in almost flat contacts – see chapter 4, the implementations includes a few additional calculations, which are discussed in this section.

Contact rejection cases

A few simple checks can be performed to reject potential contact candidates and therefore avoid unnecessary calculations. A first requirement for two contacting polygons is that their normals face towards each other. For this the following rejection criterion is employed:

$$\hat{\mathbf{n}}_1 \cdot \hat{\mathbf{n}}_2 > 0. \tag{A.6}$$

Without additional information about the shape of the complete body, it is impossible to distinguish two valid contact candidates from contact candidates on opposite sides of two shapes (see Fig. A.2). This is resolved by also taking into account the local layer thicknesses h_1 and h_2. For each polygon these are defined as the cross diameter of the body normal to the polygon and can be (pre-)computed by shooting a ray from the center of a given polygon in the direction opposite to its outward normal vector. The distance between the first polygon intersection of this ray and the center of the polygon determines the layer thickness.

Let $\mathbf{x}_i^c$ be the center point of polygon P_i with layer thickness h_i. The interior point $\mathbf{x}_i^s$ (see also Fig. A.2) is calculated as:

$$\mathbf{x}_i^s = \mathbf{x}_i^c - \frac{1}{2} h_i \hat{\mathbf{n}}_i \tag{A.7}$$

For two polygons P_1 and P_2, the rejection criterion becomes:

$$(\mathbf{x}_1^s - \mathbf{x}_2^s) \cdot \hat{\mathbf{n}}_{12} < |(\mathbf{x}_1^c - \mathbf{x}_2^c) \cdot \hat{\mathbf{n}}_{12}| \tag{A.8}$$

The implication of this rejection criterion is that this method does not allow for indentations which are bigger than $\min(0.5h_1, 0.5h_2)$. For relatively stiff particles this is generally not a concern in DEM simulations, but this might pose a constraint for simulating very thin (sheet-like) particle shapes.

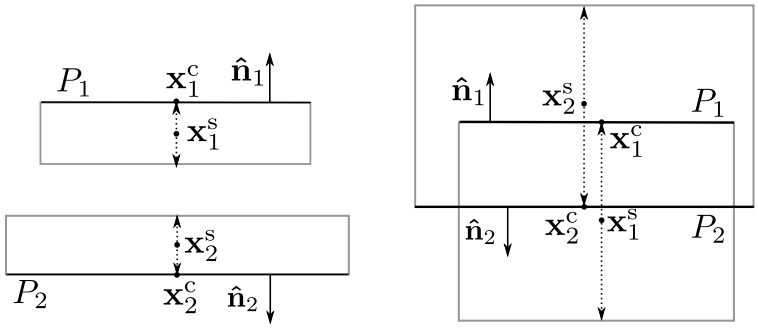

(a) **no physical contact** (b) **physical contact**

Figure A.2: (a) P_1 and P_2 have opposite normals and would have a non-empty intersection in the contact plane, but this configuration does not represent a physical contact. $\|\mathbf{x}_1^s - \mathbf{x}_2^s\| < \|\mathbf{x}_1^c - \mathbf{x}_2^c\|$. (b) P_1 and P_2 have opposite normals, a non empty intersection in the contact plane and represent a physical contact condition: $\|\mathbf{x}_1^s - \mathbf{x}_2^s\| > \|\mathbf{x}_1^c - \mathbf{x}_2^c\|$.

A trivial third criterion is used when S_{ij} has been computed: P_1 and P_2 have no intersection area where the overlap distance would be positive:

$$S_{ij} = \emptyset \tag{A.9}$$

Approximate flat contacts

When P_1 and P_2 are almost exactly parallel, their planes' intersection line $\hat{\mathbf{l}}_{ij}$ cannot be calculated correctly and the contact calculations can be greatly simplified. The criterion used for two parallel planes is:

$$\|\hat{\mathbf{n}}_1 \times \hat{\mathbf{n}}_2\| < \sin(\alpha_{\max}) \tag{A.10}$$

with $\alpha_{\max}$ the maximum angle allowed between the two planes for which they are still considered parallel. In this study, $\alpha_{\max}$ was chosen at $0.001°$.

If P_1 and P_2 are parallel, S_{12} is simply the complete intersection between their projections: P_1' and P_2'. The contact point is the center point of S_{12}, and the overlap distance δ_{12} is calculated as:

$$\delta_{12} = (\mathbf{x}_1^c - \mathbf{x}_2^c) \cdot \hat{\mathbf{n}}_{12} \tag{A.11}$$

A.3 Convergence of integrated pressures upon mesh refinement

Meshed bouncing ball

As a proof-of-principle problem, we let a soft, but rigid (with only six degrees of freedom) ball bounce on a soft flat substrate. The only acting forces are gravity and a velocity dependent drag force as body forces on the ball, and Hertz' contact force between the ball and the substrate.

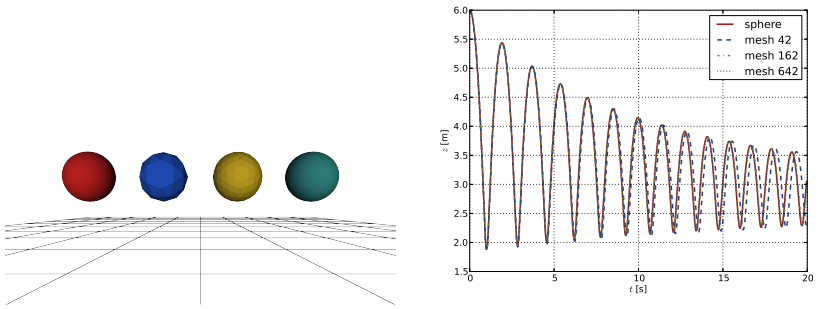

(a) (b)

Figure A.3: **Bouncing ball simulation.** (a) gives a view on the starting point of the simulation. (b) shows the time evolution of the z-coordinate of the center of mass for all four representations of the ball. For the coarsest mesh with 42 nodes, deviations at the end of the simulation are visible.

We solve Newton's equations of motion:

$$\mathbf{F}_{\text{ball}} = m \cdot \mathbf{g} - c \cdot \mathbf{v} + \frac{4\hat{E}a^3}{3\hat{R}} \cdot \hat{n} = m \cdot \mathbf{a}, \tag{A.12}$$

using an explicit leap-frog time integration method [210]. Here $\hat{n}$ is the normal vector to the contact plane. Figure A.3 shows the result of that simulation with the rigid

sphere, but also with three differently coarse meshes, using the algorithm explained in the previous sections.

As Figure A.3 illustrates, the newly developed contact model achieves the same results for this situation as the well-known Hertz' model (red sphere). On top of that, the outcome of the simulations does not depend on the refinement of the chosen mesh: Only minor deviations can be seen after approximately ten "bounces" for the coarsest mesh.

Meshed sphere adhesion

We show convergence with mesh refinement by simulating an adhesive triangulated sphere ($R = 3\mu$m, $W = 1$mJ/m^2) that is being loaded onto a flat plane. Five different mesh refinements are considered, all based on regular subdivisions of the icosahedron yielding 48 to 20242 nodes. Figure A.4(a) shows force versus penetration depth for subdivisions with 48, 642 and 10242 nodes, calculated by integrating the MD pressure for a Tabor coefficient (μ) of 0.1, compared to the solution of Hertz (no adhesion), JKR, MD and DMT. Figure A.4(b) shows the change in normalized Root Mean Square Error (RMSE) with mesh refinement for different Tabor coefficents μ. For high values of μ (close to the JKR limit), the error in the calculated forces is larger as the adhesive tension diverges near the edge of the contact radius (compare to equations 5.2 and 5.8).

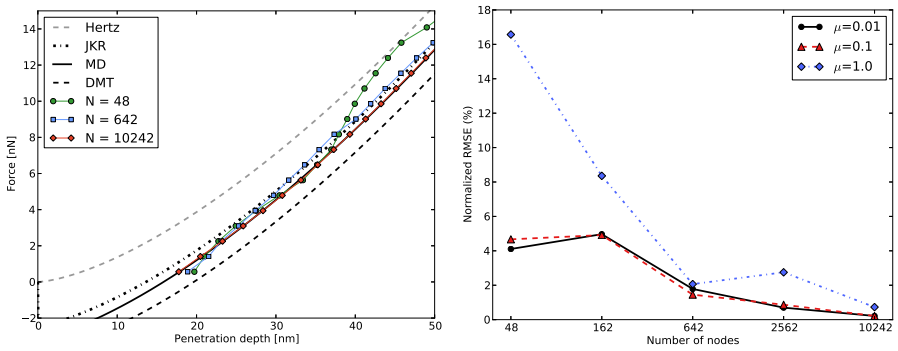

(a) (b)

Figure A.4: **Adhesive sphere simulation.** (a): Force versus penetration depth for adhesive meshed sphere (MD, $\mu = 0.1$) with different mesh refinements, compared with analytical solutions for Hertz, JKR, MD and DMT. (b): Root Mean Square Error (RMSE), normalized as a percentage of the maximal force, for prediction of the analytical MD solution as a function of mesh refinement for different Tabor coefficients μ.

Appendix B

Supplementary Figures

Phase diagram of cells with CIL: extra figures

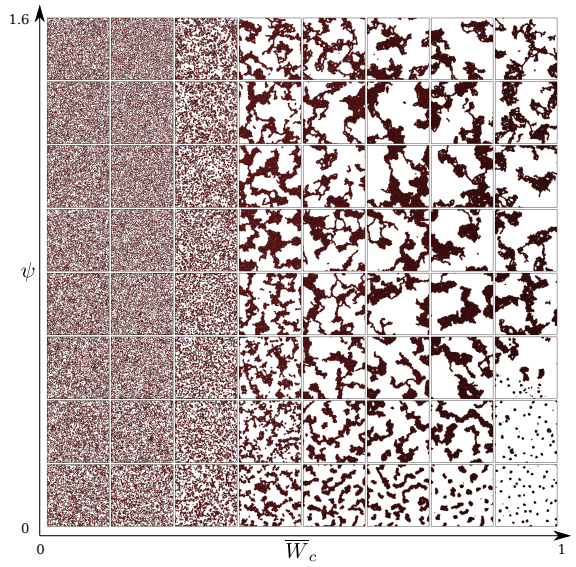

Figure B.1: Representations of simulated systems for varying $\overline{W}_c$ and ψ at $\overline{W}_s$=1, $\bar{\gamma}$=0 and low density ϕ=0.4. The majority of phases described for ϕ =0.85 is conserved, including a cluster phase, de-wetting, an active-liquid phase and a grid-like phase. Note that the presented images only show a subset of the simulated domains, which contained 1e5 particles. With respect to Fig. 7.2, the zoom level has been changed to show a similar number of particles per frame.

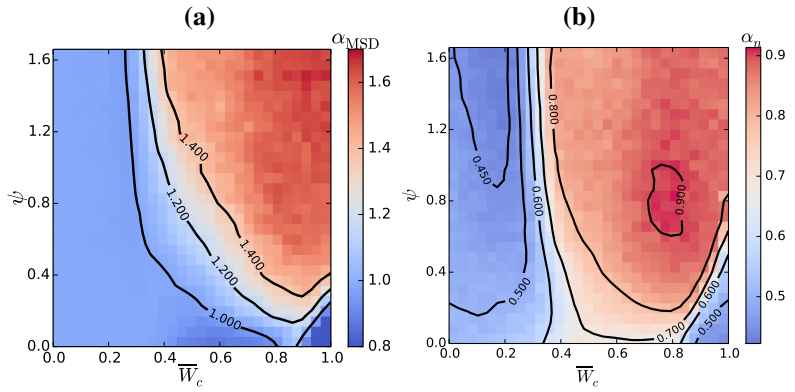

Figure B.2: Maps showing dynamical and structural properties for varying $\overline{W}_c$ and ψ at low density ϕ=0.4, $\overline{W}_s$=1 and $\bar{\gamma}$=0. The total size of the system N=25.000 and $\bar{t}$=765. **(a)**: Map of the power law exponent of the MSD (α_{MSD}) at long timescales. Compared to Fig. 7.4(b), the essence of the phase landscape is conserved with at high $\overline{W}_c$ a jammed cluster phase for low ψ, and fast phase separation at high ψ. Due to smaller cluster sizes at lower density, the exponent is generally closer to diffusive, and the phases evolve more slowly. Note the small de-wetted region in the bottom right corner, in which α_{MSD} again becomes very low. **(b)**: Map of the large fluctuation exponent α_N. Compared to a higher density ϕ=0.85, the structural transition lines remain highly conserved — see Fig. 7.3(a). In the de-wetted zone, $\alpha_N \approx 0.5$, i.e. a random distribution of de-wetted clusters is obtained.

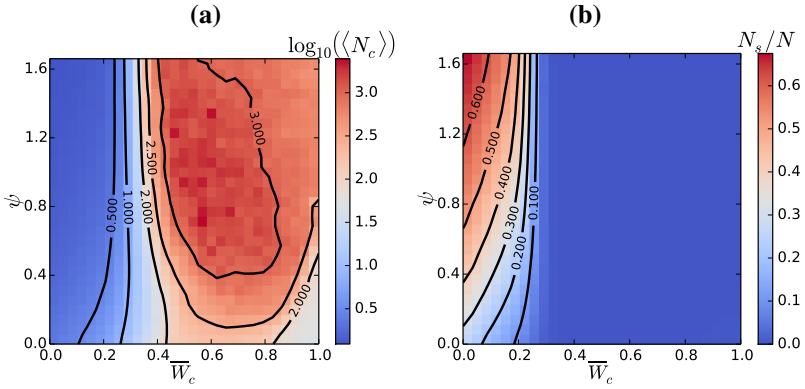

Figure B.3: Cluster analysis for varying $\overline{W}_c$ and ψ at $\overline{W}_s$=1 and low density ϕ=0.4. The total size of the system N=25.000 and $\bar{t}$=765. **(a)**: Map of mean cluster size $\langle N_c \rangle$. Percolated and active-liquid regions correspond to high values of $\log_{10}(\langle N_c \rangle)$, which will approach the system's size when $\bar{t} \to \infty$. **(b)**: Map of the ratio of single particles N_s ("gas" phase) to the size of the system N. Since co-operative effects are small at such low densities, the iso-lines correspond well to the analytical clustering line as given in Eq. (7.4). An analysis of cluster sizes like this is only meaningful at reasonably low density, hence was not provided in the main manuscript, where we focus at ϕ=0.85.

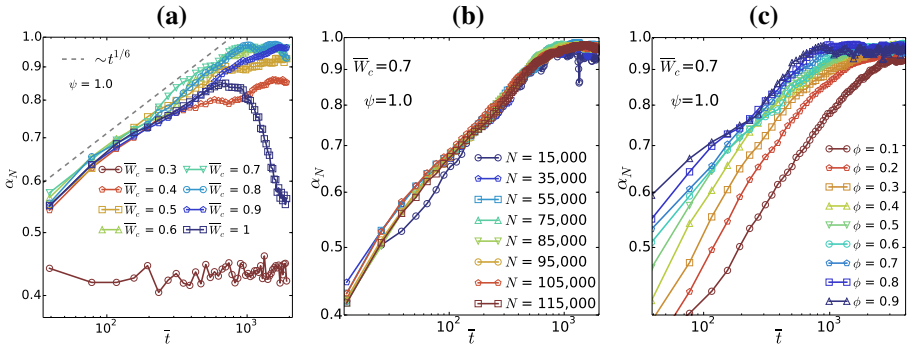

Figure B.4: Change of large fluctuation exponent α_N as a function of time. **(a)**: Varying $\overline{W}_c$ at ψ=1. From $\overline{W}_c \approx 0.4$, phase separation follows $\alpha_N \sim t^{1/6}$ power law dynamics, occurring most quickly for $\overline{W}_c \approx 0.7$, after which it slows down as the dense phase contracts, eventually collapsing catastrophically in the limit of de-wetting. **(b)**: Varying the total system size N, at $\overline{W}_c$=0.7 and ψ=1. Phase separation dynamics are independent of the system's size. **(c)**: Varying density ϕ. Systems phase separate at all densities, but the dynamics of phase separation are severely affected by density in a non-trivial way. For $\phi \gtrapprox 0.5$, systems first reach a percolated phase — with a slower timing for lower ϕ — and then phase separate using similar dynamics. For $\phi \lessapprox 0.5$, systems will first reach a cluster phase, with clusters acting as single particles with more persistent random walk — i.e. a much higher effective Peclet number — which coagulate into large clusters. An in-depth characterization of the phase separation dynamics and its dependence on density (e.g. comparing to [55]) falls outside the scope of this work.

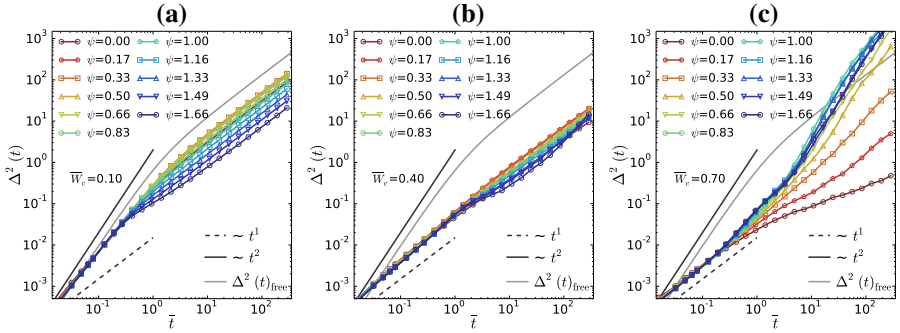

Figure B.5: **(a)**: MSD, $\Delta^2(t)$, as a function of time for varying ψ at low $\overline{W}_c$=0.1 and $\overline{\gamma}$=0. Guide-lines are given for $\Delta^2(t) \sim \bar{t}$ (random walk) and $\Delta^2(t) \sim \bar{t}^2$ (ballistic walk). As ψ increases, the MSD initially increases when still in the gas phase, as ψ breaks down clusters which inhibit particle movement. Later, within the grid-like phase, kinetic clusters are rare, and ψ decreases persistent motion at high density, thereby lowering the MSD. At long time scales, the MSD scales like diffusion — see also Fig. 7.3(d). **(b)**: MSD as a function of time for varying ψ at medium $\overline{W}_c$=0.4 and $\overline{\gamma}$=0. A dense, percolated cluster phase is present in which the dynamics are affected relatively little by CIL and scale diffusive at long timescales. **(c)**: MSD as a function of time for varying ψ at high $\overline{W}_c$=0.7. For low ψ, MSD at long timescales is sub-diffusive due to jamming effects. As ψ grows, MSD increases greatly and becomes ballistic at long timescales due to convective motion. Note that $\Delta^2(t)$ reaches a maximum at ψ=1, when the repolarization timescale of CIL equals the characteristic time of the persistent random walk.

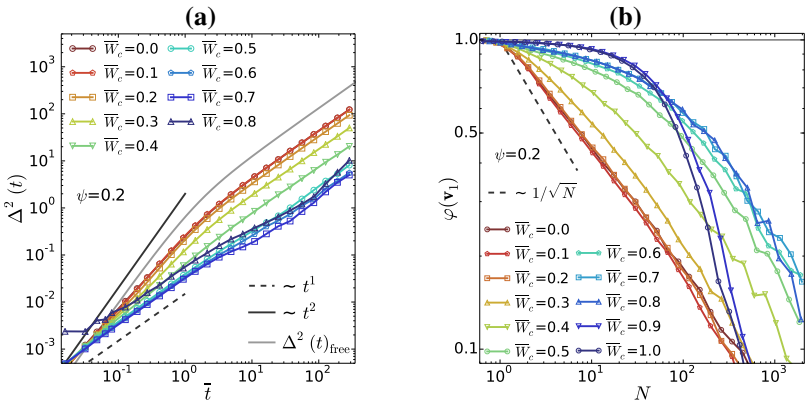

Figure B.6: **(a)**: MSD, $\Delta^2(t)$ as a function of time for varying $\overline{W}_c$ at low CIL ψ=0.2 and $\bar{\gamma}$=0. Unlike at high ψ, no abrupt change in MSD is present upon phase separation, but a gradual decrease, as clusters progressively grow, and cell movement slows down to an arrested gel-like phase. Moreover, the slope of the MSD ≈ 1, i.e. particle movement remains diffusive. When de-wetting, at high $\overline{W}_c$, MSD at small timescales increases greatly, with displacements generated not by the migration force, but by the mechanical potential. **(b)**: Spatial velocity correlation φ — see Fig. 7.4(d) — for varying $\overline{W}_c$ at low ψ=0.2. As $\overline{W}_c$ grows, a continuous shift towards more correlated — but not collective — motion occurs, until φ sharply drops when de-wetting, with the bending point signifying the size of the de-wetted aggregates.

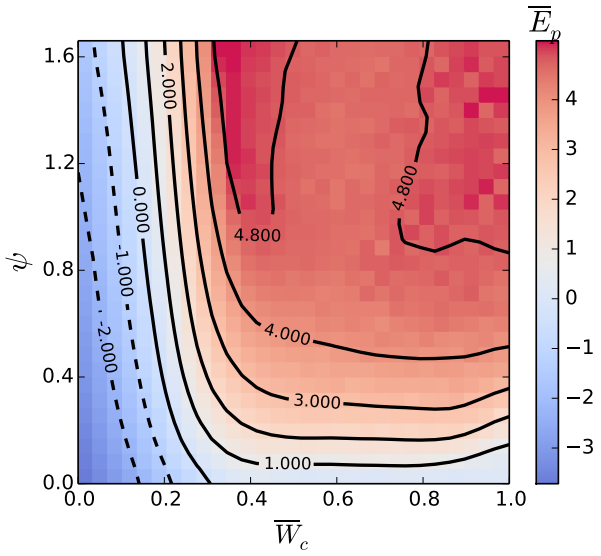

Figure B.7: Map of average potential energy $\overline{E}_p$, computed using virial theorem, for varying $\overline{W}_c$ and ψ, at $\overline{W}_s$=1 and $\bar{\gamma}$=0.2. Note that the frozen gel-like phase at $\overline{W}_c$=0.4 displays large tensile stresses, while the stresses in the active-liquid region at higher $\overline{W}_c$ are attenuated compared to the situation at $\bar{\gamma}$=0 — see Fig. 7.8.

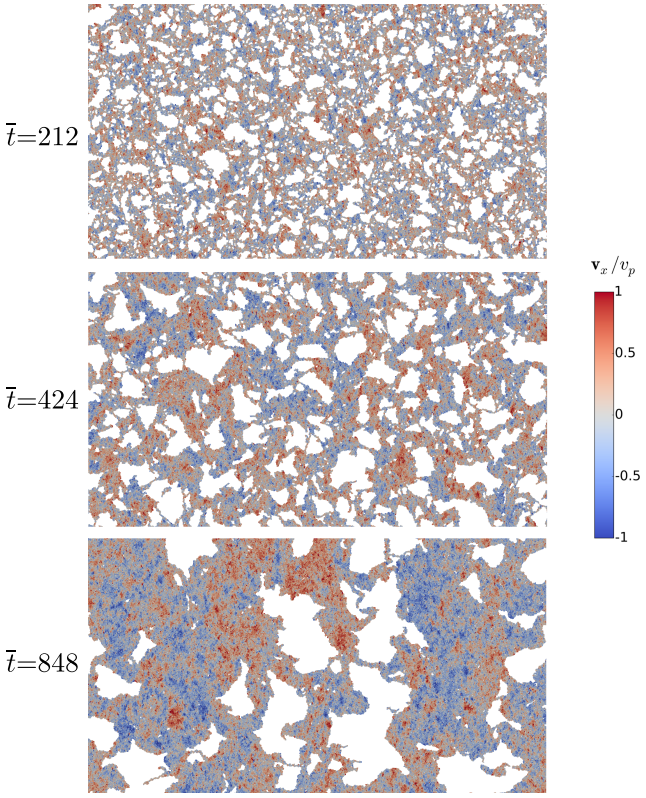

Figure B.8: Visualizations of simulation progression at three different timepoints with $\overline{W}_c$=0.7 and ψ=1, showing fast phase separation due to spinodal decomposition sped up by convective motion. The color scale indicates the x-component of the cell velocities $\mathbf{v}_x$, relative to the instantaneous velocity of "free" cells v_p, illustrating the magnification of oscillations as the strut size thickens. Initially, at $\tilde{t}$=0, the cells were distributed in a hexagonal uniform grid. The total simulation contained 500.000 cells, of which roughly 200.000 are visible in the shown rectangular window.

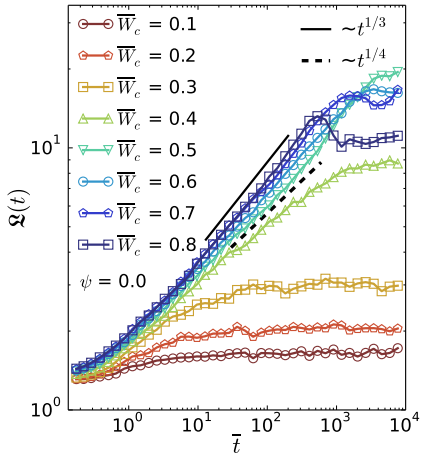

Figure B.9: Characteristic length scale $\mathfrak{L}(t)$ computed from the static structure factor as a function of time, for varying $\overline{W}_c$ at ψ=0. At sufficient $\overline{W}_c$, spinodal decomposition with a power law exponent $\alpha_{\mathfrak{L}} \approx 0.25$, consistent with reported simulation using active Brownian particles [174, 201]. At large $\overline{W}_c$, domain sizes grow until the dense phase reaches a critical size, with de-wetting occurring at the center. Note that this mechanism is different then at $\overline{W}_c > \overline{W}_s$, when clusters will de-wet rapidly without any strut coarsening, thereby resulting in de-wetted clusters of much smaller size. The exponent $\alpha_{\mathfrak{L}}$ at high $\overline{W}_c$ is closer to the diffusive exponent 1/3, suggesting that large $\overline{W}_c$ reduces the contribution of noise in 2D spinodal decomposition with soft particles.

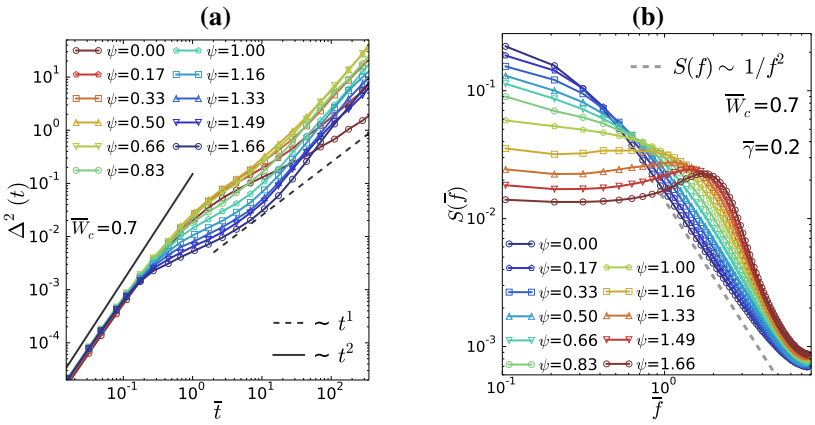

Figure B.10: Varying ψ at $\overline{W}_s$=1, $\overline{W}_c$=0.7, and $\overline{\gamma}$=0.2 **(a)**: MSD, $\Delta^2(t)$ as a function of time with guide lines indicating $\Delta^2(t) \sim \bar{t}$ (random walk) and $\Delta^2(t) \sim \bar{t}^2$ (ballistic walk). A sharp decrease in MSD occurs around $\bar{t}$=1 when increasing ψ. At long timescales, the MSD still scales super-diffusive, but the power law α_{MSD} is lower than two, i.e. γ the contribution of convection to the cell displacements. Compare also to Fig. B.5(c), which shows the same situation at $\overline{\gamma}$=0. **(b)**: Fourier power spectrum $S(\bar{f})$ of the orientation trajectories, with the guide-line indicating $1/f^2$ decay in the noise. Due to CIL, a peak appears that shifts towards higher frequencies with increasing ψ.

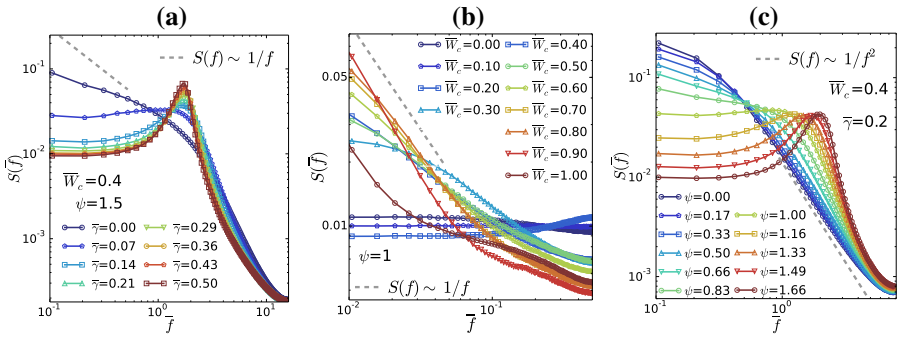

Figure B.11: Fourier power spectra $S(\overline{f})$ of the orientation trajectories **(a)** Varying cell-cell friction $\overline{\gamma}$ at ψ=1.5 and $\overline{W}_c$=0.4, with the guide-line indicating $1/f$ decay in the noise. At high $\overline{\gamma}$, a strong peak is present at $\overline{f} = \psi$, and a plateau is present at low frequencies. **(b)**: Varying $\overline{W}_c$ at ψ=1 and $\overline{\gamma}$=0, with the guide-line indicating $1/f$ decay in the noise. At low frequencies, $S(\overline{f})$ sharply shifts upward above $\overline{W}_c$=0.4, reaching $1/f$ scaling as $\overline{W}_c$ approaches 0.7. Later, when the dense phase collapses, $S(\overline{f})$ strongly decreases again. **(c)**: Varying ψ at $\overline{W}_c$=0.4, and $\overline{\gamma}$=0.2. A sharp peak at medium frequencies appears when increasing ψ, and $S(\overline{f})$ greatly decreases at low frequencies, indicative of an arrested frozen phase in which the polarizations oscillate with a frequency $\overline{f} \approx \psi$.

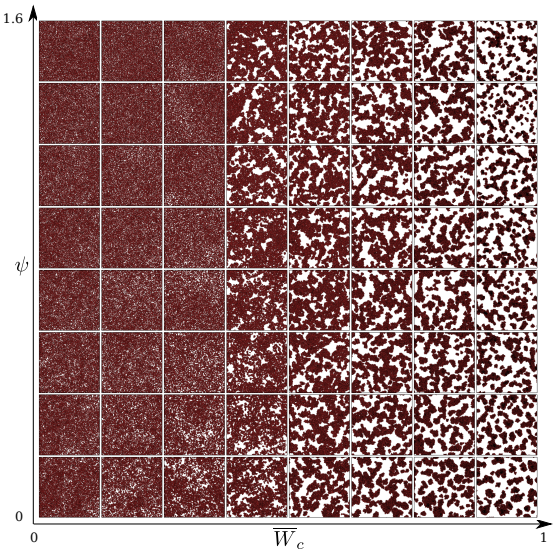

Figure B.12: Representations of non-equilibrium intermediate states for varying $\overline{W}_c$ and ψ at $\overline{W}_s$=1 and $\overline{\gamma}$=0, including exponential cell growth starting at a density of ϕ=0.15. The systems are shown after a growth time of $\overline{t}$=115 at which the density is roughly equal to 0.85. Initially, the cells were randomly distributed inside a square domain. Below the active-liquid line, where phases reach equilibrium very fast, the structural landscape remains conserved. At high $\overline{W}_c$, however, phase separation could not complete fully — see e.g. Fig. B.4 — and cluster-rich phases are observed, even at high ψ.

Table B.1: Coefficients of the linear model: $\alpha_N = a_0 + a_1 \log_{10}(\psi) + a_2\phi + a_3\overline{W}_s + a_4\overline{W}_c + a_5\bar{\gamma}_c$, with α_N the exponent $\Delta N \sim N^{\alpha_N}$.

i	Coefficient	Estimate (a_i)	Std. Error	T value	P ($>|t|$)	$p < 0.001$
0	Intercept	0.364534	0.013904	26.218	$<$ 2e-16	*
1	$\log_{10}(\psi)$	-0.113836	0.002881	-39.512	$<$ 2e-16	*
2	ϕ	0.113456	0.010816	10.489	$<$ 2e-16	*
3	$\overline{W}_s$	0.007302	0.012270	0.595	0.5519	
4	$\overline{W}_c$	0.030216	0.007262	4.161	3.4e-05	*
5	$\bar{\gamma}_c$	0.013187	0.004521	2.917	0.0036	

Table B.2: Coefficients of the linear model: $N_c/N = a_0 + a_1 \log_{10}(\psi) + a_2\phi + a_3\overline{W}_s + a_4\overline{W}_c + a_5\bar{\gamma}$, with N_c/N the ratio of the number of clusters N_c and the number of cells N.

i	Coefficient	Estimate (a_i)	Std. Error	T value	P ($>|t|$)	$p < 0.001$
0	Intercept	0.498514	0.027863	17.892	$<$ 2e-16	*
1	$\log_{10}(\psi)$	-0.011801	0.005774	-2.044	0.0412	
2	ϕ	-0.422278	0.021676	-19.481	$<$ 2e-16	*
3	$\overline{W}_s$	-0.000967	0.024588	-0.039	0.9686	
4	$\overline{W}_c$	-0.239999	0.014554	-16.491	$<$ 2e-16	*
5	$\bar{\gamma}$	-0.002649	0.009061	-0.292	0.7701	

Table B.3: Coefficients of the linear model: $N_{\mathrm{dw}}/N = a_0 + a_1 \log_{10}(\psi) + a_2\phi + a_3\overline{W}_s + a_4\overline{W}_c + a_5\bar{\gamma}$, with N_{dw}/N the ratio of the number of dewetted cells N_{dw} and the number of cells N.

i	Coefficient	Estimate (a_i)	Std. Error	T value	P ($>|t|$)	$p < 0.001$
0	Intercept	0.0130311	0.0061012	2.136	0.032895	
1	$\log_{10}(\psi)$	0.0002573	0.0012642	0.204	0.838774	
2	ϕ	0.0124584	0.0047464	2.625	0.008780	
3	$\overline{W}_s$	-0.0239943	0.0053841	-4.456	9.11e-06	*
4	$\overline{W}_c$	0.0123958	0.0031868	3.890	0.000106	*
5	$\bar{\gamma}$	-0.0023109	0.0019840	-1.165	0.244344	

Bibliography

[1] M. Abercrombie. „Contact inhibition and malignancy.” In: *Nature* 281.5729 (1979), pp. 259–262 (cit. on pp. 122, 136).

[2] M. Abercrombie and E. Ambrose. „Interference microscope studies of cell contacts in tissue culture”. In: *Experimental cell research* 15.2 (1958), pp. 332–345 (cit. on p. 122).

[3] M. Abercrombie and J. E. Heaysman. „Observations on the social behaviour of cells in tissue culture: II. "Monolayering" of fibroblasts”. In: *Experimental cell research* 6.2 (1954), pp. 293–306 (cit. on pp. 122, 136).

[4] F. Alonso-Marroquin and H. Herrmann. „Ratcheting of granular materials”. In: *Physical review letters* 92.5 (2004), p. 054301 (cit. on p. 63).

[5] A. R. Anderson, M. A. J. Chaplain, K. A. Rejniak, and W. Alt, eds. *Single-Cell-Based Models in Biology and Medicine*. Mathematics and Biosciences. Birkhaeuser Verlag AG, 2007 (cit. on pp. 3, 9, 19).

[6] J. E. Andrade, K.-W. Lim, C. F. Avila, and I. Vlahinić. „Granular element method for computational particle mechanics”. In: *Computer Methods in Applied Mechanics and Engineering* 241 (2012), pp. 262–274 (cit. on p. 64).

[7] A. K. Ashmawy, B. Sukumaran, and V. V. Hoang. „Evaluating the influence of particle shape on liquefaction behavior using discrete element modeling”. In: *Proc. Offshore and Polar Engineering Conference*. 2003, pp. 542–550 (cit. on p. 77).

[8] E. Barthel. „Adhesive elastic contacts: JKR and more”. In: *Journal of Physics D: Applied Physics* 41.16 (2008), p. 163001 (cit. on p. 84).

[9] E. Bazellières, V. Conte, A. Elosegui-Artola, X. Serra-Picamal, M. Bintanel-Morcillo, P. Roca-Cusachs, J. J. Muñoz, M. Sales-Pardo, R. Guimerà, and X. Trepat. „Control of cell–cell forces and collective cell dynamics by the intercellular adhesome”. In: *Nature cell biology* 17.4 (2015), pp. 409–420 (cit. on pp. 10, 136).

[10] D. A. Beller, M. A. Gharbi, and I. B. Liu. „Shape-controlled orientation and assembly of colloids with sharp edges in nematic liquid crystals". In: *Soft matter* 11.6 (2015), pp. 1078–1086 (cit. on p. 9).

[11] E. Ben-Jacob. „Harnessing Bacterial Intelligence: A Pre-Requisite for Human Habitation of Space". In: *Beyond Earth: The Future of Humans in Space* (2006) (cit. on p. 137).

[12] D. Boal. *Mechanics of the Cell*. 2nd ed. Cambridge University Press, 2012 (cit. on pp. 93, 97).

[13] D. H. Boal and M. Rao. „Topology changes in fluid membranes". In: *Physical Review A* 46 (6 Sept. 1992), pp. 3037–3045 (cit. on p. 89).

[14] N. Borghi, M. Sorokina, O. G. Shcherbakova, W. I. Weis, B. L. Pruitt, W. J. Nelson, and A. R. Dunn. „E-cadherin is under constitutive actomyosin-generated tension that is increased at cell–cell contacts upon externally applied stretch". In: *Proceedings of the National Academy of Sciences* 109.31 (2012), pp. 12568–12573 (cit. on p. 36).

[15] F. Boschetti, M. T. Raimondi, F. Migliavacca, and G. Dubini. „Prediction of the micro-fluid dynamic environment imposed to three-dimensional engineered cell systems in bioreactors". In: *Journal of biomechanics* 39.3 (2006), pp. 418–425 (cit. on p. 104).

[16] H.-J. Boxberger and T. F. Meyer. „A new method for the 3-D in vitro growth of human RT112bladder carcinoma cells using the alginate culture technique". In: *Biology of the Cell* 82.2–3 (1994), pp. 109–119 (cit. on p. 21).

[17] J. Brady and G. Bossis. „Stokesian Dynamics". In: *Anuual Review of Fluid Mechanics* 20 (1988), pp. 111–157 (cit. on pp. 22, 99).

[18] N. V. Brilliantov, F. Spahn, J.-M. Hertzsch, and T. Pöschel. „Model for collisions in granular gases". In: *Physical review E* 53.5 (1996), p. 5382 (cit. on p. 43).

[19] J. Buhl, D. J. Sumpter, I. D. Couzin, J. J. Hale, E. Despland, E. Miller, and S. J. Simpson. „From disorder to order in marching locusts". In: *Science* 312.5778 (2006), pp. 1402–1406 (cit. on p. 122).

[20] H. Byrne and D. Drasdo. „Individual-based and continuum models of growing cell populations: a comparison". In: *Mathematical Biology* 58 (2009), pp. 657–680 (cit. on p. 9).

[21] J. W. Cahn and J. E. Hilliard. „Free energy of a nonuniform system. I. Interfacial free energy". In: *The Journal of chemical physics* 28.2 (1958), pp. 258–267 (cit. on p. 128).

[22] C. Carmona-Fontaine, H. K. Matthews, S. Kuriyama, M. Moreno, G. A. Dunn, M. Parsons, C. D. Stern, and R. Mayor. „Contact inhibition of locomotion in vivo controls neural crest directional migration". In: *Nature* 456.7224 (2008), pp. 957–961 (cit. on pp. 122, 136).

[23] M. E. Cates and J. Tailleur. „Motility-Induced Phase Separation". In: *Annual Review of Condensed Matter Physics* 6 (2015), pp. 219–244 (cit. on p. 122).

[24] G.-C. Cho, J. Dodds, and J. C. Santamarina. „Particle shape effects on packing density, stiffness, and strength: natural and crushed sands". In: *Journal of Geotechnical and Geoenvironmental Engineering* 132.5 (2006), pp. 591–602 (cit. on pp. 63, 77).

[25] Y. S. Chu, S. Dufour, J. P. Thiery, E. Perez, and F. Pincet. „Johnson-Kendall-Roberts Theory Applied to Living Cells". In: *Physical Review Letters* 94.2 (2005), p. 028102 (cit. on pp. 21, 84).

[26] P. W. Cleary. „DEM prediction of industrial and geophysical particle flows". In: *Particuology* 8.2 (2010), pp. 106–118 (cit. on p. 69).

[27] P. W. Cleary. „Large scale industrial DEM modelling". In: *Engineering Computations* 21.2/3/4 (2004), pp. 169–204 (cit. on p. 69).

[28] G. R. Cowper. „Gaussian quadrature formulas for triangles". In: *International Journal for Numerical Methods in Engineering* 7.3 (1973), pp. 405–408 (cit. on p. 44).

[29] D. Cuvelier, M. Thery, Y.-S. Chu, S. Dufour, J.-P. Thiery, M. Bornens, P. Nassoy, and L. Mahadevan. „The universal dynamics of cell spreading". In: *Current Biology* 17 (2007), pp. 694–699 (cit. on pp. 22, 79, 81, 93, 95, 99–102).

[30] J. Dai, H. P. Ting-Beall, R. M. Hochmuth, M. P. Sheetz, and M. A. Titus. „Myosin I contributes to the generation of resting cortical tension". In: *Biophysical journal* 77.2 (1999), pp. 1168–1176 (cit. on p. 115).

[31] H. Dailey, H. Yalcin, and S. Ghadiali. „Fluid-structure modeling of flow-induced alveolar epithelial cell deformation". In: *Computers & structures* 85.11 (2007), pp. 1066–1071 (cit. on p. 104).

[32] M. Dao, J. Li, and S. Suresh. „Molecularly based analysis of deformation of spectrin network and human erythrocyte". In: *Materials Science and Engineering: C* 26.8 (Sept. 2006), pp. 1232–1244 (cit. on p. 81).

[33] J. T. Daub and R. M. Merks. „A cell-based model of extracellular-matrix-guided endothelial cell migration during angiogenesis". In: *Bulletin of mathematical biology* 75.8 (2013), pp. 1377–1399 (cit. on p. 7).

[34] J. R. Davis, C.-Y. Huang, J. Zanet, S. Harrison, E. Rosten, S. Cox, D. Y. Soong, G. A. Dunn, and B. M. Stramer. „Emergence of embryonic pattern through contact inhibition of locomotion". In: *Development* 139.24 (2012), pp. 4555–4560 (cit. on pp. 122, 136).

[35] O. De Wever, W. Westbroek, A. Verloes, N. Bloemen, M. Bracke, C. Gespach, E. Bruyneel, and M. Mareel. „Critical role of N-cadherin in myofibroblast invasion and migration in vitro stimulated by colon-cancer-cell-derived TGF-β or wounding". In: *Journal of cell science* 117.20 (2004), pp. 4691–4703 (cit. on p. 122).

[36] J. Demol, D. Lambrechts, L. Geris, J. Schrooten, and H. V. Oosterwyck. „Towards a quantitative understanding of oxygen tension and cell density evolution in fibrin hydrogels". In: *Biomaterials* 32 (2010), pp. 107–118 (cit. on p. 18).

[37] R. A. Desai, S. B. Gopal, S. Chen, and C. S. Chen. „Contact inhibition of locomotion probabilities drive solitary versus collective cell migration". In: *Journal of The Royal Society Interface* 10.88 (2013), p. 20130717 (cit. on p. 122).

[38] A. Deutsch and S. Dormann. *Cellular Automaton Modeling of Biological Pattern Formation: Characterization, Applications, and Analysis (Modeling and Simulation in Science, Engineering and Technology)*. Birkhaeuser Verlag AG, 2004 (cit. on p. 6).

[39] D. E. Discher, D. H. Boal, and S. K. Boey. „Simulations of the Erythrocyte Cytoskeleton at Large Deformation. II. Micropipette Aspiration". In: *Biophysical Journal* 75 (1998), pp. 1584–1597 (cit. on p. 89).

[40] D. E. Discher, P. Janmey, and Y.-l. Wang. „Tissue Cells Feel and Respond to the Stiffness of Their Substrate". In: *Science* 310 (2005), pp. 1139–1143 (cit. on p. 37).

[41] D. Docheva, D. Padula, C. Popov, W. Mutschler, H. Clausen-Schaumann, and M. Schieker. „Researching into the cellular shape, volume and elasticity of mesenchymal stem cells, osteoblasts and osteosarcoma cells by atomic force microscopy". In: *Journal of cellular and molecular medicine* 12.2 (2008), pp. 537–552 (cit. on p. 111).

[42] S. Douezan and F. Brochard-Wyart. „Dewetting of cellular monolayers". In: *The European Physical Journal E* 35.5 (2012), pp. 1–6 (cit. on pp. 136, 137).

[43] S. Douezan, K. Guevorkian, R. Naouar, S. Dufour, D. Cuvelier, and F. Brochard-Wyart. „Spreading dynamics and wetting transition of cellular aggregates". In: *Proceedings of the National Academy of Sciences* 108.18 (2011), pp. 7315–7320 (cit. on p. 137).

[44] D. Drasdo, S. Hoehme, and M. Block. „On the Role of Physics in the Growth and Pattern Formation of Multi-Cellular Systems: What can we Learn from Individual-Cell Based Models". In: *Journal of Statistical Physics* 128 (2007), pp. 287–345 (cit. on pp. 19, 20, 22, 81, 93).

[45] D. Drasdo, R. Kree, and J. S. McCaskill. „Monte Carlo approach to tissue-cell populations". In: *Physical Review E* 52.6 (Dec. 1995), pp. 6635–6657 (cit. on pp. 8, 9, 147).

[46] R. C. Dutta and A. K. Dutta. „Cell-interactive 3D-scaffold; advances and applications". In: *Biotechnology Advances* 27.4 (2009), pp. 334–339 (cit. on p. 18).

[47] A. Engler, S. Sen, H. Sweeney, and D. Discher. „Matrix Elasticity Directs Stem Cell Lineage Specification". In: *Cell* 126 (2006), pp. 677–689 (cit. on pp. 9, 18).

[48] B. Fabry, G. N. Maksym, J. P. Butler, M. Glogauer, D. Navajas, and J. J. Fredberg. „Scaling the microrheology of living cells". In: *Physical review letters* 87.14 (2001), p. 148102 (cit. on pp. 10, 105).

[49] J. Favier, M. Abbaspour-Fard, M. Kremmer, and A. Raji. „Shape representation of axi-symmetrical, non-spherical particles in discrete element simulation using multi-element model particles". In: *Engineering Computations* 16.4 (1999), pp. 467–480 (cit. on pp. 40, 63).

[50] D. A. Fedosov, B. Caswell, and G. E. Karniadakis. „Systematic coarse-graining of spectrin-level red blood cell models". In: *Computer Methods in Applied Mechanics and Engineering* 199.29–32 (2010), pp. 1937–1948 (cit. on pp. 79, 81, 87–89, 93, 99, 109).

[51] D. A. Fedosov, H. Lei, B. Caswell, S. Suresh, and G. E. Karniadakis. „Multiscale Modeling of Red Blood Cell Mechanics and Blood Flow in Malaria". In: *PLoS Comput. Biol.* 7.12 (2011), e1002270 (cit. on pp. 79, 89, 91, 92, 99).

[52] Y. Feng, K. Han, and D. Owen. „Energy-conserving contact interaction models for arbitrarily shaped discrete elements". In: *Computer Methods in Applied Mechanics and Engineering* 205–208 (2012). Special Issue on Advances in Computational Methods in Contact Mechanics dedicated to the memory of Professor J.A.C. Martins, pp. 169–177 (cit. on pp. 40, 63).

[53] J.-F. Ferellec and G. R. McDowell. „A method to model realistic particle shape and inertia in DEM". In: *Granular Matter* 12.5 (2010), pp. 459–467 (cit. on pp. 40, 63).

[54] J. Fidorra, T. Mielke, J. Booz, and L. Feinendegen. „Cellular and nuclear volume of human cells during the cell cycle". In: *Radiation and environmental biophysics* 19.3 (1981), pp. 205–214 (cit. on p. 22).

[55] Y. Fily and M. C. Marchetti. „Athermal phase separation of self-propelled particles with no alignment". In: *Physical review letters* 108.23 (2012), p. 235702 (cit. on pp. 122, 126, 159).

[56] P. Friedl and D. Gilmour. „Collective cell migration in morphogenesis, regeneration and cancer". In: *Nature reviews Molecular cell biology* 10.7 (2009), pp. 445–457 (cit. on p. 121).

[57] P. Friedl and K. Wolf. „Tumour-cell invasion and migration: diversity and escape mechanisms". In: *Nature Reviews Cancer* 3.5 (2003), pp. 362–374 (cit. on p. 121).

[58] M. Fröhlich, W. L. Grayson, D. Marolt, J. M. Gimble, N. Kregar-Velikonja, and G. Vunjak-Novakovic. „Bone grafts engineered from human adipose-derived stem cells in perfusion bioreactor culture". In: *Tissue Engineering Part A* 16.1 (2009), pp. 179–189 (cit. on p. 103).

[59] Y. Fung and P. Tong. „Theory of the sphering of red blood cells". In: *Biophysical journal* 8.2 (1968), pp. 175–198 (cit. on p. 85).

[60] J. Galle, M. Hoffmann, and G. Aust. „From single cells to tissue architecture - a bottom-up approach to modelling the spatio-temporal organisation of complex multi-cellular systems". In: *Mathematical Biology* 58 (2008), pp. 261–283 (cit. on p. 19).

[61] J. Galle, M. Loeffler, and D. Drasdo. „Modeling the effect of deregulated proliferation and apoptosis on the growth dynamics of epithelial cell populations in vitro". In: *Biophysical journal* 88.1 (2005), pp. 62–75 (cit. on pp. 8, 91, 93).

[62] J. Galle, L. Preziosi, and A. Tosin. „Contact inhibition of growth described using a multiphase model and an individual cell based model". In: *Applied Mathematics Letters* 22 (2009), pp. 1483–1490 (cit. on p. 23).

[63] A. Garcia-Alonso, N. Serrano, and J. Flaquer. „Solving the collision detection problem". In: *Computer Graphics and Applications, IEEE* 14.3 (1994), pp. 36–43 (cit. on pp. 43, 64).

[64] M. Gardner. „Mathematical games: The fantastic combinations of John Conway's new solitaire game "Life"". In: *Scientific American* 223.4 (1970), pp. 120–123 (cit. on p. 6).

[65] T. D. Gatzke and C. M. Grimm. „Estimating curvature on triangular meshes". In: *International journal of shape modeling* 12.01 (2006), pp. 1–28 (cit. on p. 41).

[66] P. M. Gilbert, K. L. Havenstrite, K. E. G. Magnusson, A. Sacco, N. A. Leonardi, P. Kraft, N. K. Nguyen, S. Thrun, M. P. Lutolf, and H. M. Blau. „Substrate Elasticity Regulates Skeletal Muscle Stem Cell Self-Renewal in Culture". In: *Science* 329.5995 (2010), pp. 1078–1081 (cit. on p. 18).

[67] F. Graner and J. A. Glazier. „Simulation of Biological Cell Sorting Using a Two-Dimensional Extended Potts Model". In: *Physical Review Letters* 69 (1992), pp. 2013–2016 (cit. on p. 6).

[68] W. L. Grayson, D. Marolt, S. Bhumiratana, M. Fröhlich, X. E. Guo, and G. Vunjak-Novakovic. „Optimizing the medium perfusion rate in bone tissue engineering bioreactors". In: *Biotechnology and bioengineering* 108.5 (2011), pp. 1159–1170 (cit. on p. 103).

[69] F. Guilak, J. Tedrow, and R. Burgkart. „Viscoelastic properties of the cell nucleus". In: *Biochemical and biophysical research communications* 269.3 (2000), pp. 781–786 (cit. on p. 113).

[70] F. Guilak, D. M. Cohen, B. T. Estes, J. M. Gimble, W. Liedtke, and C. S. Chen. „Control of Stem Cell Fate by Physical Interactions with the Extracellular Matrix". In: *Cell Stem Cell* 5.1 (2009), pp. 17–26 (cit. on p. 14).

[71] F. Guilak, A. Ratcliffe, and V. C. Mow. „Chondrocyte deformation and local tissue strain in articular cartilage: a confocal microscopy study". In: *Journal of Orthopaedic Research* 13.3 (1995), pp. 410–421 (cit. on p. 114).

[72] Y. Guyot, F. Luyten, J. Schrooten, I. Papantoniou, and L. Geris. „A Three-Dimensional Computational Fluid Dynamics Model Of Shear Stress Distribution During Neotissue Growth In A Perfusion Bioreactor". In: *Biotechnology and bioengineering* 112.12 (2015), pp. 2591–2600 (cit. on p. 104).

[73] P. Haff and B. Werner. „Computer simulation of the mechanical sorting of grains". In: *Powder Technology* 48.3 (1986), pp. 239–245 (cit. on p. 47).

[74] L. C. Hale. *Principles and techniques for designing precision machines*. Tech. rep. Lawrence Livermore National Lab., CA (US), 1999 (cit. on p. 52).

[75] R. G. Harrison, M. Greenman, F. P. Mall, and C. Jackson. „Observations of the living developing nerve fiber". In: *The Anatomical Record* 1.5 (1907), pp. 116–128 (cit. on p. 137).

[76] A. Hategan, R. Law, S. Kahn, and D. E. Discher. „Adhesively-Tensed Cell Membranes: Lysis Kinetics and Atomic Force Microscopy Probing". In: *Biophysical Journal* 85.4 (2003), pp. 2746–2759 (cit. on p. 94).

[77] A. Hategan, K. Sengupta, S. Kahn, E. Sackmann, and D. E. Discher. „Topographical Pattern Dynamics in Passive Adhesion of Cell Membranes". In: *Biophysical Journal* 87.5 (2004), pp. 3547–3560 (cit. on pp. 81, 93–95, 99, 100).

[78] J. Haycock. „3D Cell Culture: A Review of Current Approaches and Techniques". In: *Methods in Molecular Biology* 695 (2011), pp. 1–15 (cit. on p. 18).

[79] K. He, S. Dong, and Z. Zhou. „Multigrid contact detection method". In: *Phys. Rev. E* 75.3 (Mar. 2007), p. 036710 (cit. on pp. 22, 43, 64).

[80] F. Hecht. „New development in freefem++". In: *Journal of Numerical Mathematics* 20.3-4 (2012), pp. 251–266 (cit. on p. 114).

[81] C.-P. Heisenberg and Y. Bellaiche. „Forces in tissue morphogenesis and patterning". In: *Cell* 153.5 (2013), pp. 948–962 (cit. on p. 104).

[82] M. Held, J. T. Klosowski, and J. S. Mitchell. „Evaluation of collision detection methods for virtual reality fly-throughs". In: *Canadian Conference on Computational Geometry*. Citeseer. 1995, pp. 205–210 (cit. on pp. 43, 64).

[83] H. Hertz. „Ueber die Beruehrung fester elastischer Koerper". In: *Journal fuer die reine und angewandte Mathematik* 91 (1881), pp. 156–171 (cit. on p. 39).

[84] L. A. Hidalgo-Bastida, S. Thirunavukkarasu, S. Griffiths, S. H. Cartmell, and S. Naire. „Modeling and design of optimal flow perfusion bioreactors for tissue engineering applications". In: *Biotechnology and bioengineering* 109.4 (2012), pp. 1095–1099 (cit. on p. 104).

[85] G. Hippmann. „An algorithm for compliant contact between complexly shaped surfaces in multibody dynamics". In: *Multibody Dynamics, Jorge AC Ambrosio (Ed.), IDMEC/IST, Lisbon, Portugal, July* 14 (2003) (cit. on p. 66).

[86] R. Hochmuth. „Micropipette aspiration of living cells". In: *Journal of Biomechanics* 33 (2000), pp. 15–22 (cit. on pp. 25, 112).

[87] S. Hoehme and D. Drasdo. „A single-cell-based model of tumor growth in vitro: monolayers and spheroids". In: *Physical Biology* 2 (2005), pp. 133–147 (cit. on pp. 8, 90, 91).

[88] S. Hoehme, M. Brulport, A. Bauer, E. Bedawy, W. Schormann, M. Hermes, V. Puppe, R. Gebhardt, S. Zellmer, M. Schwarz, E. Bockamp, T. Timmel, J. G. Hengstler, and D. Drasdo. „Prediction and validation of cell alignment along microvessels as order principle to restore tissue architecture in liver regeneration". In: *Proceedings of the National Academy of Sciences* 107.23 (2010). Including Supporting information, pp. 10371–10376 (cit. on pp. 8, 91, 93).

[89] D. Höhner, S. Wirtz, H. Kruggel-Emden, and V. Scherer. „Comparison of the multi-sphere and polyhedral approach to simulate non-spherical particles within the discrete element method: Influence on temporal force evolution for multiple contacts". In: *Powder Technology* 208.3 (2011), pp. 643–656 (cit. on p. 40).

[90] M. S. Hossain, D. Bergstrom, and X. Chen. „Prediction of cell growth rate over scaffold strands inside a perfusion bioreactor". In: *Biomechanics and modeling in mechanobiology* 14.2 (2014), pp. 333–344 (cit. on p. 104).

[91] H. Huang, R. Kamm, and R. Lee. „Cell mechanics and mechanotransduction: pathways, probes, and physiology". In: *American Journal of Physiology- Cell Physiology* 287.1 (2004), p. C1 (cit. on p. 18).

[92] N. Huebsch, P. R. Arany, A. S. Mao, D. Shvartsman, O. A. Ali, S. A. Bencherif, and J. R.-F. D. J. Mooney. „Harnessing traction-mediated manipulation of the cell/matrix interface to control stem-cell fate". In: *Nature Materials* 9 (2010), pp. 518–526 (cit. on p. 18).

[93] S. Huveneers and E. H. J. Danen. „Adhesion signaling–crosstalk between integrins, Src and Rho". In: *Journal of Cell Science* 122 (2009), pp. 1059–1069 (cit. on p. 79).

[94] D. E. Ingber. „Cellular mechanotransduction: putting all the pieces together again". In: *The FASEB Journal* 20.7 (2006), pp. 811–827 (cit. on p. 18).

[95] D. E. Ingber. „Tensegrity I. Cell structure and hierarchical systems biology". In: *Journal of Cell Science* 116 (2003), pp. 1157–1173 (cit. on p. 20).

[96] J. N. Israelachvili. *Intermolecular and surface forces*. third edition. Academic press, 2011 (cit. on pp. 93, 99).

[97] K. L. Johnson and J. A. Greenwood. „An Adhesion Map for the Contact of Elastic Spheres". In: *Journal of colloid and interface science* 192 (1997), pp. 326–333 (cit. on pp. 21, 61, 82–84).

[98] K. L. Johnson, K. Kendall, and A. Roberts. „Surface energy and the contact of elastic solids". In: *Proceedings of the royal society* 324 (1971), pp. 301–313 (cit. on pp. 21, 84).

[99] K. Johnson. „Adhesion and friction between a smooth elastic spherical asperity and a plane surface". In: *Proceedings of the Royal Society of London. Series A: Mathematical, Physical and Engineering Sciences* 453.1956 (1997), pp. 163–179 (cit. on pp. 52, 61, 82, 83).

[100] C. Jungreuthmayer, M. J. Jaasma, A. A. Al-Munajjed, J. Zanghellini, D. J. Kelly, and F. J. O'Brien. „Deformation simulation of cells seeded on a collagen-GAG scaffold in a flow perfusion bioreactor using a sequential 3D CFD-elastostatics model". In: *Medical engineering & physics* 31.4 (2009), pp. 420–427 (cit. on p. 114).

[101] R. Kalluri and R. A. Weinberg. „The basics of epithelial-mesenchymal transition". In: *The Journal of clinical investigation* 119.6 (2009), p. 1420 (cit. on p. 136).

[102] J. Kerkhofs, S. Roberts, F. Luyten, H. Van
bibnamedelimb Oosterwyck, and L. Geris. „Relating the chondrocyte gene network to growth plate morphology; from genes to phenotype". In: *PLoS One* 4 (2012), e34729 (cit. on p. 17).

[103] S. V. Kesavan, F. Momey, O. Cioni, B. David-Watine, N. Dubrulle, S. Shorte, E. Sulpice, D. Freida, B. Chalmond, J. Dinten, et al. „High-throughput monitoring of major cell functions by means of lensfree video microscopy". In: *Scientific reports* 4 (2014), p. 5942 (cit. on p. 134).

[104] M.-C. Kim, D. M. Neal, R. D. Kamm, and H. H. Asada. „Dynamic modeling of cell migration and spreading behaviors on fibronectin coated planar substrates and micropatterned geometries". In: *PLOS Computational Biology* 9.2 (2013), e1002926 (cit. on p. 100).

[105] A. Krinner, M. Hoffmann, M. Loeffler, D. Drasdo, and J. Galle. „Individual fates of mesenchymal stem cells in vitro". In: *BMC Systems Biology* 4 (2010), pp. 1–9 (cit. on pp. 19, 25, 91).

[106] A. Krinner, M. Zscharnak, A. Bader, D. Drasdo, and J. Galle. „Impact of oxygen environment on mesenchymal stem cell expansion and chondrogenic differentiation". In: *Cell Proliferation* 42 (2009), pp. 471–484 (cit. on pp. 8, 25).

[107] W. H. Kruskal and W. A. Wallis. „Use of ranks in one-criterion variance analysis". In: *Journal of the American statistical Association* 47.260 (1952), pp. 583–621 (cit. on p. 24).

[108] V. Kumaran and G. Fredrickson. „Early stage spinodal decomposition in viscoelastic fluids". In: *The Journal of chemical physics* 105.18 (1996), pp. 8304–8313 (cit. on p. 130).

[109] A. V. Kyrylyuk and A. P. Philipse. „Effect of particle shape on the random packing density of amorphous solids". In: *physica status solidi (a)* 208.10 (2011), pp. 2299–2302 (cit. on p. 76).

[110] R. Langer and J. Vacanti. „Tissue engineering". In: *Science* 260 (1993), pp. 920–926 (cit. on p. 2).

[111] J. Latham and A. Munjiza. „The modelling of particle systems with real shapes". In: *Philosophical Transactions of the Royal Society of London Series A Mathematical Physical and Engineering Sciences* 362 (2004), pp. 1953–1972 (cit. on pp. 69–71, 73, 76).

[112] D. Leckband and J. Israelachvili. „Intermolecular forces in biology". In: *Quarterly Reviews of Biophysics* 34(2) (2001), pp. 105–267 (cit. on pp. 22, 94–96, 100).

[113] A. Lee, M. Berny-Lang, S. Liao, E. Kanso, P. Kuhn, O. McCarty, and P. Newton. „A low-dimensional deformation model for cancer cells in flow". In: *Physics of Fluids (1994-present)* 24.8 (2012), p. 081903 (cit. on p. 104).

[114] K. Y. Lee and D. Mooney. „Alginate: Properties and biomedical applications". In: *Progress in Polymer Science* 37 (2012), pp. 106–126 (cit. on pp. 25, 31).

[115] W. Legant, C. Choi, J. Miller, L. Shao, L. Gao, E. Betzig, and C. Chen. „Multidimensional traction force microscopy reveals out-of-plane rotational moments about focal adhesions". In: *PNAS* 110(3) (2013), pp. 881–886 (cit. on p. 98).

[116] D. S. Lemons and A. Gythiel. „Paul Langevin's 1908 paper "on the theory of Brownian motion"["Sur la théorie du mouvement brownien," CR Acad. Sci. (Paris) 146, 530–533 (1908)]". In: *American Journal of Physics* 65.11 (1997), pp. 1079–1081 (cit. on pp. 5, 8).

[117] P. Lenas, M. Moos, and F. Luyten. „Developmental engineering: a new paradigm for the design and manufacturing of cell-based products. Part I: from three-dimensional cell growth to biomimetics of *in vivo* development". In: *Tissue Engineering: Part B* 15(4) (2009), 381:394 (cit. on pp. 1, 2, 17).

[118] P. Lenas, M. Moos, and F. Luyten. „Developmental engineering: a new paradigm for the design and manufacturing of cell-based products. Part II. From genes to networks: tissue engineering from the viewpoint of systems biology and network science". In: *Tissue Engineering: Part B* 15(4) (2009), pp. 395–422 (cit. on p. 2).

[119] D. Levis and L. Berthier. „Clustering and heterogeneous dynamics in a kinetic Monte Carlo model of self-propelled hard disks". In: *Physical Review E* 89.6 (2014), p. 062301 (cit. on p. 128).

[120] L. Li, H. Peng, J. Kurths, Y. Yang, and H. J. Schellnhuber. „Chaos–order transition in foraging behavior of ants". In: *Proceedings of the National Academy of Sciences* 111.23 (2014), pp. 8392–8397 (cit. on p. 137).

[121] J. Lim and J. P. Thiery. „Epithelial-mesenchymal transitions: insights from development". In: *Development* 139.19 (2012), pp. 3471–3486 (cit. on p. 136).

[122] K.-W. Lim and J. E. Andrade. „Granular element method for three-dimensional discrete element calculations". In: *International Journal for Numerical and Analytical Methods in Geomechanics* 38.2 (2014), pp. 167–188 (cit. on p. 64).

[123] B. Lin, T. Yin, Y. I. Wu, T. Inoue, and A. Levchenko. „Interplay between chemotaxis and contact inhibition of locomotion determines exploratory cell migration". In: *Nature communications* 6 (2015), p. 6619 (cit. on p. 122).

[124] M. C. Lin, D. Manocha, and J. Cohen. „Collision detection: Algorithms and applications". In: (1996) (cit. on p. 64).

[125] Q.-X. Liu, A. Doelman, V. Rottschäfer, M. de Jager, P. M. Herman, M. Rietkerk, and J. van de Koppel. „Phase separation explains a new class of self-organized spatial patterns in ecological systems". In: *Proceedings of the National Academy of Sciences* 110.29 (2013), pp. 11905–11910 (cit. on p. 137).

[126] H. Lodish. *Molecular cell biology*. Macmillan, 2008 (cit. on p. 121).

[127] M. Lu and G. McDowell. „The importance of modelling ballast particle shape in the discrete element method". In: *Granular Matter* 9 (2007), pp. 69–80 (cit. on pp. 40, 63, 77, 80).

[128] M. Lu, M. K. Jolly, H. Levine, J. N. Onuchic, and E. Ben-Jacob. „MicroRNA-based regulation of epithelial–hybrid–mesenchymal fate determination". In: *Proceedings of the National Academy of Sciences* 110.45 (2013), pp. 18144–18149 (cit. on p. 136).

[129] E. Lushi, H. Wioland, and R. E. Goldstein. „Fluid flows created by swimming bacteria drive self-organization in confined suspensions". In: *Proceedings of the National Academy of Sciences* 111.27 (2014), pp. 9733–9738 (cit. on p. 104).

[130] F. Maes, P. Van Ransbeeck, H. Van Oosterwyck, and P. Verdonck. „Modeling fluid flow through irregular scaffolds for perfusion bioreactors". In: *Biotechnology and bioengineering* 103.3 (2009), pp. 621–630 (cit. on p. 104).

[131] A. M. Malone, C. T. Anderson, P. Tummala, R. Y. Kwon, T. R. Johnston, T. Stearns, and C. R. Jacobs. „Primary cilia mediate mechanosensing in bone cells by a calcium-independent mechanism". In: *Proceedings of the National Academy of Sciences* 104.33 (2007), pp. 13325–13330 (cit. on p. 104).

[132] D. Markauskas, R. Kačianauskas, A. Džiugys, and R. Navakas. „Investigation of adequacy of multi-sphere approximation of elliptical particles for DEM simulations". In: *Granular Matter* 12.1 (2010), pp. 107–123 (cit. on pp. 40, 60).

[133] P. Marmottant, A. Mgharbel, J. Käfer, B. Audren, J.-P. Rieu, J.-C. Vial, B. Van Der Sanden, A. F. Marée, F. Graner, and H. Delanoë-Ayari. „The role of fluctuations and stress on the effective viscosity of cell aggregates". In: *Proceedings of the National Academy of Sciences* 106.41 (2009), pp. 17271–17275 (cit. on pp. 4, 125).

[134] H. Matuttis, S. Luding, and H. Herrman. „Discrete element simulations of dense packings and heaps made of spherical and non-spherical particles". In: *Powder Technology* 108 (2000), pp. 278–292 (cit. on p. 80).

[135] D. Maugis. „Adhesion of spheres: The JKR-DMT transition using a Dugdale model". In: *J. Colloid Interface Sci.* 150.1 (1992), pp. 243–269 (cit. on pp. 61, 82).

[136] R. J. McCoy, C. Jungreuthmayer, and F. J. O'Brien. „Influence of flow rate and scaffold pore size on cell behavior during mechanical stimulation in a flow perfusion bioreactor". In: *Biotechnology and bioengineering* 109.6 (2012), pp. 1583–1594 (cit. on pp. 114, 117).

[137] R. J. McCoy and F. J. O'Brien. „Influence of shear stress in perfusion bioreactor cultures for the development of three-dimensional bone tissue constructs: a review". In: *Tissue Engineering Part B: Reviews* 16.6 (2010), pp. 587–601 (cit. on p. 104).

[138] L. Meinel, V. Karageorgiou, S. Hofmann, R. Fajardo, B. Snyder, C. Li, L. Zichner, R. Langer, G. Vunjak-Novakovic, and D. L. Kaplan. „Engineering bone-like tissue in vitro using human bone marrow stem cells and silk scaffolds". In: *Journal of Biomedical Materials Research Part A* 71.1 (2004), pp. 25–34 (cit. on p. 103).

[139] M. Meyer, M. Desbrun, P. Schröder, and A. H. Barr. „Discrete Differential-Geometry Operators for Triangulated Manifolds". In: *Visualization and Mathematics* 3.7 (2002), pp. 35–57 (cit. on p. 41).

[140] M. Moore and J. Wilhelms. „Collision detection and response for computer animation". In: *ACM Siggraph Computer Graphics*. Vol. 22. 4. ACM. 1988, pp. 289–298 (cit. on pp. 43, 64).

[141] P. Moreo, J. M. Garcia-Aznar, and M. Doblaré. „Modeling mechanosensing and its effect on the migration and proliferation of adherent cells". In: *Acta Biomaterialia* 4.3 (2008), pp. 613–621 (cit. on p. 18).

[142] V. T. Moy, Y. Jiao, T. Hillmann, H. Lehmann, and T. Sano. „Adhesion Energy of Receptor-Mediated Interaction Measured by Elastic Deformation". In: *Biophysical Journal* 76.3 (1999), pp. 1632–1638 (cit. on p. 21).

[143] A. Munjiza and J. Latham. „Comparison of experimental and FEM/DEM results for gravitational deposition of identical cubes". In: *Engineering Computations* 21.2/3/4 (2004), pp. 249–264 (cit. on pp. 69, 76).

[144] A. Munjiza, E. Rougier, and N. W. M. John. „MR linear contact detection algorithm". In: *International Journal for Numerical Methods in Engineering* 66.1 (2006), pp. 46–71 (cit. on pp. 43, 64).

[145] S. Na, O. Collin, F. Chowdhury, B. Tay, M. Ouyang, Y. Wang, and N. Wang. „Rapid signal transduction in living cells is a unique feature of mechanotransduction". In: *Proceedings of the National Academy of Sciences* 105.18 (2008), pp. 6626–6631 (cit. on p. 37).

[146] T. J. Newman. „Modeling multicellular systems using subcellular elements". In: *Mathematical Biosciences and Engineering* 2.3 (2005), pp. 613–624 (cit. on p. 9).

[147] B. Nguyen, Q. Wang, N. Kuiper, A. E. Haj, C. Thomas, and Z. Zhang. „Strain-dependent viscoelastic behaviour and rupture force of single chondrocytes and chondrons under compression". In: *Biotechnology Letters* 10 (2009), pp. 1–8.118935 (cit. on p. 25).

[148] M. A. Nieto. „Epithelial plasticity: a common theme in embryonic and cancer cells". In: *Science* 342.6159 (2013), p. 1234850 (cit. on p. 121).

[149] H. Noborio, S. Fukuda, and S. Arimoto. „Fast interference check method using octree representation". In: *Advanced robotics* 3.3 (1988), pp. 193–212 (cit. on pp. 43, 64).

[150] C. Nouguier-Lehon, B. Cambou, and E. Vincens. „Influence of particle shape and angularity on the behaviour of granular materials: a numerical analysis". In: *International Journal for Numerical and Analytical Methods in Geomechanics* 27.14 (2003), pp. 1207–1226 (cit. on p. 63).

[151] A. C. Oates. „What's all the noise about developmental stochasticity?" In: *Development* 138.4 (2011), pp. 601–607 (cit. on p. 4).

[152] T. Odenthal. „A Computational Framework for Individual Cell-based Models from Yeast Sorting to Red Blood Cell Mechanics and Beyond". PhD thesis. KU Leuven, 2013 (cit. on pp. 3, 12, 148).

[153] T. Odenthal, B. Smeets, P. Van Liedekerke, E. Tijskens, H. Van Oosterwyck, and H. Ramon. „Analysis of initial cell spreading using mechanistic contact formulations for a deformable cell model". In: *PLoS computational biology* 9.10 (2013), e1003267 (cit. on pp. 61, 72, 79, 81, 98, 105, 109).

[154] A. L. Olivares, È. Marsal, J. A. Planell, and D. Lacroix. „Finite element study of scaffold architecture design and culture conditions for tissue engineering". In: *Biomaterials* 30.30 (2009), pp. 6142–6149 (cit. on p. 104).

[155] I. Papantoniou, Y. C. Chai, F. P. Luyten, and J. Schrooten. „Process quality engineering for bioreactor-driven manufacturing of tissue-engineered constructs for bone regeneration". In: *Tissue Engineering Part C: Methods* 19.8 (2013), pp. 596–609 (cit. on pp. 104, 117).

[156] I. Papantoniou, Y. Guyot, M. Sonnaert, G. Kerckhofs, F. P. Luyten, L. Geris, and J. Schrooten. „Spatial optimization in perfusion bioreactors improves bone tissue-engineered construct quality attributes". In: *Biotechnology and bioengineering* 111.12 (2014), pp. 2560–2570 (cit. on p. 117).

[157] P. Pathmanathan, J. Cooper, A. Fletcher, G. Mirams, L. Montahan, P. Murray, J. Osborne, J. Pitt-Francis, A. Walter, and S. J. Chapman. „A computational study of discrete mechanical tissue models". In: *Physical Biology* 6(3) (2009), p. 036001 (cit. on p. 21).

[158] A. Pena, R. Garcia-Rojo, and H. Herrmann. „Influence of particle shape on sheared dense granular media". In: *Granular Matter* 9.3-4 (2007), pp. 279–291 (cit. on p. 63).

[159] C. S. Peskin. „The immersed boundary method". In: *Acta numerica* 11 (2002), pp. 479–517 (cit. on p. 105).

[160] J. F. Peters, M. A. Hopkins, R. Kala, and R. E. Wahl. „A poly-ellipsoid particle for non-spherical discrete element method". In: *Engineering Computations* 26.6 (2009), pp. 645–657 (cit. on pp. 39, 63).

[161] J. Peukes and T. Betz. „Direct measurement of the cortical tension during the growth of membrane blebs". In: *Biophysical journal* 107.8 (2014), pp. 1810–1820 (cit. on p. 115).

[162] J. T. Podichetty, P. R. Bhaskar, A. Khalf, and S. V. Madihally. „Modeling pressure drop using generalized scaffold characteristics in an axial-flow bioreactor for soft tissue regeneration". In: *Annals of biomedical engineering* 42.6 (2014), pp. 1319–1330 (cit. on p. 104).

[163] G. Popkin. „The physics of life." In: *Nature* 529.7584 (2016), pp. 16–18 (cit. on pp. 8, 150).

[164] T. Pöschel and T. Schwager. *Computational Granular Dynamics*. Springer, 2005 (cit. on pp. 40, 43, 47, 52, 63, 80).

[165] L. Pournin and T. M. Liebling. „A generalization of distinct element method to tridimensional particles with complex shapes". In: *P&G05* 2 (2005), pp. 1375–1378 (cit. on p. 63).

[166] D. S. Preece, R. P. Jensen, E. D. Perkins, and J. R. Williams. *Sand production modeling using superquadric discrete elements and coupling of fluid flow and particle motion*. Tech. rep. Albuquerque, NM (US); Sandia National Labs, 1999 (cit. on pp. 39, 63).

[167] E. Purcell. „Life at low Reynolds-number". In: *American Journal of Physics* 45 (1977), pp. 3–11 (cit. on pp. 8, 89).

[168] Z. Qu, J. N. Weiss, and W. R. MacLellan. „Coordination of cell growth and cell division: a mathematical modeling study". In: *Journal of Cell Science* 117 (2004), pp. 4199–4207 (cit. on p. 22).

[169] L. Vu-Quoc and X. Zhang. „An accurate and efficient tangential force–displacement model for elastic frictional contact in particle-flow simulations". In: *Mechanics of materials* 31.4 (1999), pp. 235–269 (cit. on pp. 52, 61).

[170] L. Vu-Quoc, X. Zhang, and O. Walton. „A 3-D discrete-element method for dry granular flows of ellipsoidal particles". In: *Computer methods in applied mechanics and engineering* 187.3 (2000), pp. 483–528 (cit. on pp. 39, 63).

[171] I. Ramis-Conde, M. A. J. Chaplain, A. R. A. Anderson, and D. Drasdo. „Multi-scale modelling of cancer cell intravasation: the role of cadherins in metastasis". In: *Physical Biology* 6 (2009), p. 016008 (cit. on p. 91).

[172] J. Rauh, F. Milan, K.-P. Günther, and M. Stiehler. „Bioreactor systems for bone tissue engineering". In: *Tissue Engineering Part B: Reviews* 17.4 (2011), pp. 263–280 (cit. on p. 104).

[173] G. S. Redner, A. Baskaran, and M. F. Hagan. „Reentrant phase behavior in active colloids with attraction". In: *Physical Review E* 88.1 (2013), p. 012305 (cit. on pp. 122, 128).

[174] G. S. Redner, M. F. Hagan, and A. Baskaran. „Structure and dynamics of a phase-separating active colloidal fluid". In: *Physical review letters* 110.5 (2013), p. 055701 (cit. on pp. 122, 128, 162).

[175] T. Re'em and S. Cohen. „Microenvironment Design for Stem Cell Fate Determination". In: *Advances in Biochemical Engineering/Biotechnology* 126 (2012), pp. 227–262 (cit. on pp. 14, 18).

[176] G. Reig, E. Pulgar, and M. L. Concha. „Cell migration: from tissue culture to embryos". In: *Development* 141.10 (2014), pp. 1999–2013 (cit. on p. 136).

[177] K. A. Rejniak and L. J. McCawley. „Current trends in mathematical modeling of tumor–microenvironment interactions: a survey of tools and applications". In: *Experimental Biology and Medicine* 235 (2010), pp. 411–423 (cit. on p. 19).

[178] F. Rico, P. Roca-Cusachs, N. Gavara, R. Farré, M. Rotger, and D. Navajas. „Probing mechanical properties of living cells by atomic force microscopy with blunted pyramidal cantilever tips". In: *Physical Review E* 72.2 (2005), p. 021914 (cit. on pp. 110, 111).

[179] P. P. Romanczuk. *Active Brownian Particles: From Individual to Collective Stochastic Dynamics; Dedicated to the Late Frank Edward Moss (1934-2011)*. EDP Sciences, 2012 (cit. on p. 122).

[180] S. Rusinkiewicz. „Estimating curvatures and their derivatives on triangle meshes". In: *3D Data Processing, Visualization and Transmission, 2004. 3DPVT 2004. Proceedings. 2nd International Symposium on*. IEEE. 2004, pp. 486–493 (cit. on p. 41).

[181] A. Saltelli, K. Chan, and E. M. Scott, eds. *Sensitivity Analysis*. Wiley, 2000 (cit. on pp. 24, 25).

[182] J. Santamarina and G. Cho. „Soil behaviour: The role of particle shape". In: *Advances in geotechnical engineering: The skempton conference*. Vol. 1. Thomas Telford. 2004, pp. 604–617 (cit. on p. 77).

[183] U. S. Schwarz and M. L. Gardel. „United we stand–integrating the actin cytoskeleton and cell–matrix adhesions in cellular mechanotransduction". In: *Journal of cell science* 125.13 (2012), pp. 3051–3060 (cit. on p. 9).

[184] U. S. Schwarz and S. A. Safran. „Physics of adherent cells". In: *Reviews of Modern Physics* 85.3 (2013), p. 1327 (cit. on p. 13).

[185] M. Scianna and L. Preziosi. *Cellular Potts models: multiscale extensions and biological applications*. CRC Press, 2013 (cit. on p. 7).

[186] U. Seifert and R. Lipowsky. „Adhesion of vesicles". In: *Physical Review A* 42(8) (1990), pp. 4768–4771 (cit. on pp. 94, 95).

[187] X. Serra-Picamal, V. Conte, R. Vincent, E. Anon, D. Tambe, E. Bazellieres, J. Butler, J. Fredberg, and X. Trepat. „Mechanical waves during tissue expansion". In: *Nature Physics* 8 (2012), pp. 628–634 (cit. on p. 36).

[188] T. Shemesh, B. Geiger, A. D. Bershadsky, and M. M. Kozlov. „Focal adhesions as mechanosensors: a physical mechanism". In: *Proceedings of the National Academy of Sciences of the United States of America* 102.35 (2005), pp. 12383–12388 (cit. on p. 104).

[189] V. Sikavitsas, G. Bancroft, J. van den Dolde, T. Sheffield, J. Jansen, C. Ambrose, and A. Mikos. „Fluid flow increases mineralized matrix deposition in three-dimensional perfusion culture of marrow stromal osteoblasts in a dose-dependent manner". In: *Engineering in Medicine and Biology, 2002. 24th Annual Conference and the Annual Fall Meeting of the Biomedical Engineering Society EMBS/BMES Conference, 2002. Proceedings of the Second Joint*. Vol. 1. IEEE. 2002, pp. 884–885 (cit. on p. 104).

[190] J. L. Silverberg, M. Bierbaum, J. P. Sethna, and I. Cohen. „Collective motion of humans in mosh and circle pits at heavy metal concerts". In: *Physical review letters* 110.22 (2013), p. 228701 (cit. on p. 122).

[191] K. Sliogeryte, S. D. Thorpe, D. A. Lee, L. Botto, and M. M. Knight. „Stem cell differentiation increases membrane-actin adhesion regulating cell blebability, migration and mechanics". In: *Scientific Reports* 4 (Dec. 2014), p. 7307 (cit. on p. 112).

[192] N. Slomka and A. Gefen. „Confocal microscopy-based three-dimensional cell-specific modeling for large deformation analyses in cellular mechanics". In: *Journal of biomechanics* 43.9 (2010), pp. 1806–1816 (cit. on p. 104).

[193] B. Smeets. „Individuele-cel modellen van gistkolonies: een discrete-elementen benadering". MA thesis. KU Leuven, 2010 (cit. on pp. 12, 23).

[194] B. Smeets, T. Odenthal, J. Keresztes, S. Vanmaercke, P. Van Liedekerke, E. Tijskens, W. Saeys, H. Van Oosterwyck, and H. Ramon. „Modeling contact interactions between triangulated rounded bodies for the discrete element method". In: *Computer Methods in Applied Mechanics and Engineering* 277 (2014), pp. 219–238 (cit. on pp. 39, 54, 55, 64, 67, 71, 72).

[195] B. Smeets, T. Odenthal, E. Tijskens, H. Ramon, and H. Van Oosterwyck. „Quantifying the mechanical micro-environment during three-dimensional cell expansion on microbeads by means of individual cell-based modelling". In: *Computer methods in biomechanics and biomedical engineering* 16.10 (2013), pp. 1071–1084 (cit. on pp. 17, 31, 138).

[196] B. Smeets, T. Odenthal, S. Vanmaercke, and H. Ramon. „Polygon-based contact description for modeling arbitrary polyhedra in the Discrete Element Method". In: *Computer Methods in Applied Mechanics and Engineering* 290 (2015), pp. 277–289 (cit. on p. 63).

[197] H. Smith. „Territorial spacing on a beach revisited: A cross-national exploration". In: *Social Psychology Quarterly* 44.2 (1981), pp. 132–137 (cit. on p. 137).

[198] M. J. Song, D. Dean, and M. L. K. Tate. „Mechanical modulation of nascent stem cell lineage commitment in tissue engineering scaffolds". In: *Biomaterials* 34.23 (2013), pp. 5766–5775 (cit. on p. 103).

[199] M. Sonnaert, I. Papantoniou, V. Bloemen, G. Kerckhofs, F. Luyten, and J. Schrooten. „Human periosteal-derived cell expansion in a perfusion bioreactor system: proliferation, differentiation and extracellular matrix formation". In: *Journal of tissue engineering and regenerative medicine* (2014) (cit. on pp. 103, 117).

[200] J. Spillmann and M. Teschner. „Contact surface computation for coarsely sampled deformable objects". In: *In Proc. Vision, Modeling, Visualization*. 2005 (cit. on p. 80).

[201] J. Stenhammar, D. Marenduzzo, R. J. Allen, and M. E. Cates. „Phase behaviour of active Brownian particles: the role of dimensionality". In: *Soft Matter* 10.10 (2014), pp. 1489–1499 (cit. on pp. 128, 162).

[202] S. Suresh, J. Spatz, J. Mills, A. Micoulet, M. Dao, C. Lim, M. Beil, and T. Seufferlein. „Connections between single-cell biomechanics and human disease states: gastrointestinal cancer and malaria". In: *Acta Biomaterialia* 1.1 (2005), pp. 15–30 (cit. on pp. 91, 92).

[203] A. Szabó and R. M. Merks. „Cellular potts modeling of tumor growth, tumor invasion, and tumor evolution". In: *Front Oncol* 3.87.10 (2013), p. 3389 (cit. on p. 7).

[204] B. Szabo, G. Szöllösi, B. Gönci, Z. Jurányi, D. Selmeczi, and T. Vicsek. „Phase transition in the collective migration of tissue cells: experiment and model". In: *Physical Review E* 74.6 (2006), p. 061908 (cit. on p. 130).

[205] D. T. Tambe and J. J. Fredberg. „And I hope you like jamming too". In: *New Journal of Physics* 17.9 (2015), p. 091001 (cit. on p. 148).

[206] D. T. Tambe, C. C. Hardin, T. E. Angelini, K. Rajendran, C. Y. Park, X. Serra-Picamal, E. H. Zhou, M. H. Zaman, J. P. Butler, D. A. Weitz, et al. „Collective cell guidance by cooperative intercellular forces". In: *Nature materials* 10.6 (2011), pp. 469–475 (cit. on p. 36).

[207] S.-Y. Tee, J. Fu, C. S. Chen, and P. A. Janmey. „Cell shape and substrate rigidity both regulate cell stiffness". In: *Biophysical journal* 100.5 (2011), pp. L25–L27 (cit. on p. 37).

[208] J. P. Thiery, H. Acloque, R. Y. Huang, and M. A. Nieto. „Epithelial-mesenchymal transitions in development and disease". In: *cell* 139.5 (2009), pp. 871–890 (cit. on p. 121).

[209] X.-J. Tian, H. Zhang, and J. Xing. „Coupled reversible and irreversible bistable switches underlying TGFβ-induced epithelial to mesenchymal transition". In: *Biophysical journal* 105.4 (2013), pp. 1079–1089 (cit. on p. 136).

[210] E. Tijskens, H. Ramon, and J. D. Baerdemaeker. „Discrete element modelling for process simulation in agriculture”. In: *Journal of Sound and Vibration* 266.3 (2003). First International ISMA Workshop on Noise and Vibration in Agricultural and Biological Engineering, pp. 493–514 (cit. on pp. 19, 43, 59, 114, 155).

[211] J.-Y. Tinevez, U. Schulze, G. Salbreux, J. Roensch, J.-F. Joanny, and E. Paluch. „Role of cortical tension in bleb growth”. In: *Proceedings of the National Academy of Sciences* 106.44 (2009), pp. 18581–18586 (cit. on p. 115).

[212] X. Trepat, L. Deng, S. S. An, D. Navajas, D. J. Tschumperlin, W. T. Gerthoffer, J. P. Butler, and J. J. Fredberg. „Universal physical responses to stretch in the living cell”. In: *Nature* 447 (2007), pp. 592–595 (cit. on p. 10).

[213] X. Trepat, M. R. Wasserman, T. E. Angelini, E. Millet, D. A. Weitz, J. P. Butler, and J. J. Fredberg. „Physical forces during collective cell migration”. In: *Nature physics* 5.6 (2009), pp. 426–430 (cit. on pp. 137, 148).

[214] M. Turelli. „Random environments and stochastic calculus”. In: *Theoretical population biology* 12.2 (1977), pp. 140–178 (cit. on p. 8).

[215] G. E. Uhlenbeck and L. S. Ornstein. „On the theory of the Brownian motion”. In: *Physical review* 36.5 (1930), p. 823 (cit. on p. 124).

[216] F. Ulloa-Montoya, C. Verfaillie, and W.-S. Hu. „Culture systems for pluripotent stem cells”. In: *Journal of Bioscience and Bioengineering* 100(1) (2005), pp. 12–27 (cit. on p. 17).

[217] P. Van Liedekerke, M. Palm, N. Jagiella, and D. Drasdo. „Simulating tissue mechanics with agent-based models: concepts, perspectives and some novel results”. In: *Computational Particle Mechanics* 2.4 (2015), pp. 401–444 (cit. on p. 3).

[218] P. Van Liedekerke, B. Smeets, T. Odenthal, E. Tijskens, and H. Ramon. „Solving microscopic flow problems using Stokes equations in SPH”. In: *Computer Physics Communications* 184 (2013), pp. 1686–1696 (cit. on pp. 91, 92, 138).

[219] P. Van Liedekerke, E. Tijskens, H. Ramon, P. Ghysels, G. Samaey, and D. Roose. „Particle-based model to simulate the micromechanics of biological cells”. In: *PHYSICAL REVIEW E* 81.6, Part 1 (June 2010), pages (cit. on pp. 48, 84).

[220] L. Verlet. „Computer" experiments" on classical fluids. I. Thermodynamical properties of Lennard-Jones molecules”. In: *Physical review* 159.1 (1967), p. 98 (cit. on p. 7).

[221] T. Vicsek, A. Czirók, E. Ben-Jacob, I. Cohen, and O. Shochet. „Novel type of phase transition in a system of self-driven particles”. In: *Physical review letters* 75.6 (1995), p. 1226 (cit. on pp. 8, 122).

[222] V. Villar-Cervino, M. Molano-Mazón, T. Catchpole, M. Valdeolmillos, M. Henkemeyer, L. M. Martínez, V. Borrell, and O. Marín. „Contact repulsion controls the dispersion and final distribution of Cajal-Retzius cells". In: *Neuron* 77.3 (2013), pp. 457–471 (cit. on p. 122).

[223] R. Vincent, E. Bazellières, C. Pérez-González, M. Uroz, X. Serra-Picamal, and X. Trepat. „Active Tensile Modulus of an Epithelial Monolayer". In: *Physical Review Letters* 115.24 (2015), p. 248103 (cit. on pp. 10, 124, 137).

[224] A. Wachs, L. Girolami, G. Vinay, and G. Ferrer. „Grains3D, a flexible DEM approach for particles of arbitrary convex shape. Part I: Numerical model and validations". In: *Powder Technology* 224 (2012), pp. 374–389 (cit. on pp. 40, 69, 70, 76).

[225] N. Wang, E. Ostuni, G. Whitesides, and D. Ingber. „Micropatterning Tractional Forces in Living Cells". In: *Cell Motility and the Cytoskeleton* 52 (2002), pp. 97–106 (cit. on pp. 98, 101).

[226] N. Wang, I. M. Toli-Nrrelykke, J. Chen, S. M. Mijailovich, J. P. Butler, J. J. Fredberg, and D. Stamenovic. „Cell prestress. I. Stiffness and prestress are closely associated in adherent contractile cells". In: *American Journal of Physiology - Cell Physiology* 282.3 (2002), pp. C606–C616 (cit. on p. 37).

[227] Y. Wang, E. L. Botvinick, Y. Zhao, M. W. Berns, S. Usami, R. Y. Tsien, and S. Chien. „Visualizing the mechanical activation of Src". In: *Nature* 434.7036 (2005), pp. 1040–1045 (cit. on p. 37).

[228] Y. Wang, F. Meng, and F. Sachs. „Genetically encoded force sensors for measuring mechanical forces in proteins". In: *Communicative & integrative biology* 4.4 (2011), pp. 385–390 (cit. on p. 36).

[229] S. Weinbaum, S. Cowin, and Y. Zeng. „A model for the excitation of osteocytes by mechanical loading-induced bone fluid shear stresses". In: *Journal of biomechanics* 27.3 (1994), pp. 339–360 (cit. on pp. 104, 117).

[230] C. Wellmann and P. Wriggers. „A two-scale model of granular materials". In: *Computer Methods in Applied Mechanics and Engineering* 205–208 (2012). Special Issue on Advances in Computational Methods in Contact Mechanics dedicated to the memory of Professor J.A.C. Martins, pp. 46–58 (cit. on pp. 39, 63).

[231] M. L. Woods, C. Carmona-Fontaine, C. P. Barnes, I. D. Couzin, R. Mayor, and K. M. Page. „Directional Collective Cell Migration Emerges as a Property of Cell Interactions". In: *Plos One* 9.9 (2014), e104969 (cit. on p. 122).

[232] Y. Xiong, P. Rangamani, M.-A. Fardin, A. Lipshtat, B. Dubin-Thaler, O. Rossier, M. P. Sheetz, and R. Iyengar. „Mechanisms controlling cell size and shape during isotropic cell spreading". In: *Biophysical journal* 98.10 (2010), pp. 2136–2146 (cit. on p. 100).

[233] G. Xu. „Discrete Laplace–Beltrami operator on sphere and optimal spherical triangulations". In: *International Journal of Computational Geometry & Applications* 16 (2006), pp. 75–93 (cit. on pp. 48, 84).

[234] B. Yan, R. A. Regueiro, and S. Sture. „Three-dimensional ellipsoidal discrete element modeling of granular materials and its coupling with finite element facets". In: *Engineering Computations* 27.4 (2010), pp. 519–550 (cit. on pp. 39, 63).

[235] L. Yang, J. C. Effler, B. L. Kutscher, S. E. Sullivan, D. N. Robinson, and P. A. Iglesias. „Modeling cellular deformations using the level set formalism". In: *BMC systems biology* 2.1 (2008), p. 68 (cit. on p. 104).

[236] A. B. Yeatts and J. P. Fisher. „Bone tissue engineering bioreactors: Dynamic culture and the influence of shear stress". In: *Bone* 48.2 (Feb. 2011), pp. 171–181 (cit. on p. 103).

[237] L. Zhang, T. Cui, and H. Liu. „A set of symmetric quadrature rules on triangles and tetrahedra". In: *J. Comput. Math* 27 (2009), pp. 89–96 (cit. on pp. 44, 45, 104, 122).

[238] F. Zhao, T. J. Vaughan, and L. M. Mcnamara. „Multiscale fluid–structure interaction modelling to determine the mechanical stimulation of bone cells in a tissue engineered scaffold". In: *Biomechanics and modeling in mechanobiology* 14.2 (2015), pp. 231–243 (cit. on pp. 104, 105).

[239] Q. Zheng, Z. Zhou, and A. Yu. „Contact Forces between Viscoelastic Ellipsoidal Particles". In: *Powder Technology* 248 (2013), pp. 25–33 (cit. on pp. 39, 52, 63).

[240] R. Zou and A. Yu. „Evaluation of the packing characteristics of mono-sized non-spherical particles". In: *Powder technology* 88.1 (1996), pp. 71–79 (cit. on p. 76).

Publications

Journal Articles & full Proceedings

[1] L. Geris, P. Van Liedekerke, B. Smeets, E. Tijskens, and H. Ramon. „A cell based modelling framework for skeletal tissue engineering applications". In: *Journal of Biomechanics* 10 (2009), p. 1016.

[2] Y. Guyot, B. Smeets, T. Odenthal, R. Subramani, F. Luyten, H. Ramon, I. Papantoniou, and L. Geris. „Immersed Boundary Models for quantifying flow-Induced mechanical stimuli on stem cells seeded on 3d scaffolds in perfusion bioreactors". In: *PLOS Computational Biology* (submitted) (2016).

[3] T. Leblicq, B. Smeets, H. Ramon, and W. Saeys. „A discrete element approach for modelling the compression of crop stems". In: *Computers and Electronics in Agriculture* 123 (2016), pp. 80–88.

[4] T. Odenthal, B. Smeets, J. Christiaens, K. Verstrepen, E. Tijskens, and H. Ramon. „Evolution of Adhesion Properties in Yeast". In: *Proceedings of the 10^{th} International Symposium on Computer Methods in Biomechanics and Biomedical Engineering*. Arup, Apr. 2012, pp. 431–437.

[5] T. Odenthal, B. Smeets, P. Van Liedekerke, E. Tijskens, H. Van Oosterwyck, and H. Ramon. „Analysis of initial cell spreading using mechanistic contact formulations for a deformable cell model". In: *PLoS computational biology* 9.10 (2013), e1003267.

[6] J. Pešek, P. Baerts, B. Smeets, C. Maes, and H. Ramon. „Mathematical model suitable for efficient simulation of thin semi-flexible polymers in complex environments". In: *Soft matter* 12 (2016), pp. 3360–3387.

[7] B. Smeets, R. Alert, J. Pesek, I. Paganobarraga, H. Ramon, and R. Vincent. „Emergent structural organisations of 2D motile particles with contact inhibition of locomotion". In: *PNAS* (submitted) (2016).

[8] B. Smeets, T. Odenthal, J. Keresztes, S. Vanmaercke, P. Van Liedekerke, E. Tijskens, W. Saeys, H. Van Oosterwyck, and H. Ramon. „Modeling contact interactions between triangulated rounded bodies for the discrete element method". In: *Computer Methods in Applied Mechanics and Engineering* 277 (2014), pp. 219–238.

[9] B. Smeets, T. Odenthal, E. Tijskens, H. Ramon, and H. Van Oosterwyck. „Quantifying the mechanical micro-environment during three-dimensional cell expansion on microbeads by means of individual cell-based modelling". In: *Computer methods in biomechanics and biomedical engineering* 16.10 (2013), pp. 1071–1084.

[10] B. Smeets, T. Odenthal, H. Van Oosterwyck, and H. Ramon. „Characterizing the mechanical microenvironment of 3d cell cultures using individual-based models". In: *Proceedings of the 10th International Symposium on Computer Methods in Biomechanics and Biomedical Engineering*. Arup, 2012, pp. 135–141.

[11] B. Smeets, T. Odenthal, S. Vanmaercke, and H. Ramon. „Polygon-based contact description for modeling arbitrary polyhedra in the Discrete Element Method". In: *Computer Methods in Applied Mechanics and Engineering* 290 (2015), pp. 277–289.

[12] P. Van Liedekerke, P. Ghysels, E. Tijskens, G. Samaey, B. Smeets, D. Roose, and H. Ramon. „A particle-based model to simulate the micromechanics of single-plant parenchyma cells and aggregates". In: *Physical Biology* 7 (2010), p. 026006.

[13] P. Van Liedekerke, B. Smeets, T. Odenthal, E. Tijskens, and H. Ramon. „Solving microscopic flow problems using Stokes equations in SPH". In: *Computer Physics Communications* 184 (2013), pp. 1686–1696.

International conferences

[1] T. Heck, T. Odenthal, B. Smeets, P. Van Liedekerke, A. Izquierdo-Alvarez, A. Jorge Peñas, H. Ramon, and H. Van Oosterwyck. „A Mechanical Model of Single Cell Migration on a Viscoelastic Substrate". In: *Congress of the European Society of Biomechanics*. Prague, May 2015.

[2] T. Heck, T. Odenthal, B. Smeets, P. Van Liedekerke, A. Jorge Penas, A. Izquierdo-Alvarez, H. Ramon, and H. Van Oosterwyck. „Mechanical modeling of single cell migration on a deformable viscoelastic extracellular matrix". In: *European Cellular Mechanics Meeting*. Barcelona, Dec. 2015.

[3] T. Heck, T. Odenthal, B. Smeets, P. Van Liedekerke, H. Ramon, and H. Van Oosterwyck. „Mechanical modeling of single cell-extracellular matrix coupling". In: *International Symposium on Computer Methods in Biomechanics and Biomedical Engineering*. Amsterdam, 13-15 October 2014.

[4] T. Heck, T. Odenthal, B. Smeets, P. Van Liedekerke, S. Vanmaercke, H. Ramon, and H. Van Oosterwyck. „Computational modeling of cell migration and cell-matrix interaction". In: *IEEE-EMBS Benelux Chapter*. Luik, 26 November 2015.

[5] J. Leijten, L. Moreira Teixeira, J. Bolander, B. Smeets, W. Ji, T. Odenthal, D. Lambrechts, H. Van Oosterwyck, and F. Luyten. „Macromolecular Crowding Drives Cartilage Formation in Chondrogenic Stem Cell Microtissues". In: *Tissue Engineering Part A: vol. 21. 4th TERMIS World Congress*. Boston: MA, Sept. 2015, S89–S89.

[6] T. Odenthal, T. Heck, B. Smeets, P. Van Liedekerke, H. Ramon, and H. Van Oosterwyck. „Coupling of a cell migration model with an (N)SPH substrate to investigate dynamic generation of cellular tractions". In: *International Conference on Particle-based Methods*. Barcelona, 28-30 September 2015.

[7] T. Odenthal, B. Smeets, T. Heck, H. Van Oosterwyck, and H. Ramon. „Cell Migration Investigated by a Mechanistic 3D Deformable Cell Model". In: *International Symposium on Computer Methods in Biomechanics and Biomedical Engineering*. Amsterdam, 13-15 October 2014.

[8] T. Odenthal, B. Smeets, H. Ramon, and H. Van Oosterwyck. „Initial cell spreading investigated by a deformable cell model with mechanistic contact interactions". In: *International Conference on Particle-based Methods*. Stuttgart, 18-20 September 2013.

[9] T. Odenthal, B. Smeets, K. Sliogeryte, P. Van Liedekerke, and E. Tijskens. „DEM in Biological Physics: Simulating Yeast Colony Growth." In: *International PhD & Research Day of the International Fine Particles Reasearch Institute (IFPRI)*. Luik, 30th June 2010.

[10] T. Odenthal, B. Smeets, K. Sliogeryte, P. Van Liedekerke, E. Tijskens, and H. Ramon. „DEM in Biological Physics: Individual-cell Based Models." In: *European Cell Mechanics Meeting.* Amsterdam, 17-19 October 2011.

[11] T. Odenthal, B. Smeets, P. Van Liedekerke, E. Tijskens, V. Oosterwyck, and H. Ramon. „A deformable cell model and its application to investigate initial cell spreading". In: *International Symposium on Computer Methods in Biomechanics and Biomedical Engineering.* Best Student Poster Presentation Prize. Salt Lake City, UT, Mar. 2013.

[12] T. Odenthal, B. Smeets, P. Van Liedekerke, E. Tijskens, and H. Ramon. „Particle based simulation of cell growth and cell colony growth." In: *Statistical Physics and Biology of Collective Motion*. Dresden, Aug. 2010.

[13] T. Odenthal, B. Smeets, P. Van Liedekerke, E. Tijskens, H. Ramon, and H. Van Oosterwyck. „Inital cell spreading investigated by a new deformable cell model". In: *International Conference on Computational Bioengineering*. Leuven, Nov. 2013.

[14] T. Odenthal, B. Smeets, P. Van Liedekerke, E. Tijskens, H. Van Oosterwyck, and H. Ramon. „Particle-based Methods for Simulating Tissue." In: *Belgian Symposium on Tissue Engineering*. Leuven, 17-18 September 2012.

[15] B. Smeets, J. Leijten, T. Odenthal, L. Teixeira, F. Luyten, H. Van Oosterwyck, and H. Ramon. „Dynamic simulation of in vitro micro-tissue formation using a particle-based deformable cell model". In: *International Conference on Particle-based Methods*. Barcelona, 28-30 September 2015.

[16] B. Smeets, L. Moreira Teixeira, J. Leijten, T. Odenthal, F. Luyten, H. Ramon, and H. Van Oosterwyck. „A cell-based model of the dynamics of in vitro micro-aggregation". In: *International Symposium on Computer Methods in Biomechanics and Biomedical Engineering*. Amsterdam, 13-15 October 2014.

[17] B. Smeets, T. Odenthal, J. Leijten, L. Teixeira, H. Van Oosterwyck, and H. Ramon. „Quantifying the effect of mechanical properties on cell micro-aggregation dynamics using a deformable cell-based model". In: *European Cell Mechanics Meeting*. Barcelona, 13-15 May 2015.

[18] B. Smeets, T. Odenthal, H. Ramon, and H. Van Oosterwyck. „Individual-based Modeling of Microcarrier Cell Expansion: A Sensitivity Analysis". In: *Belgian Symposium on Tissue Engineering*. Leuven, Belgium, 17-18 September 2012.

[19] B. Smeets, T. Odenthal, H. Ramon, and H. Van Oosterwyck. „Particle-based methods for Tissue Engineering". In: *Belgian Symposium on Tissue Engineering*. Leuven, Belgium, 24-25 October 2013.

[20] B. Smeets, T. Odenthal, H. Ramon, and H. Van Oosterwyck. „Quantifying mechanical heterogeneity in microbead cell expansion using individual-cell based models". In: *International Conference on Particle-based Methods*. Stuttgart, Germany, 18-20 September 2013.

[21] B. Smeets, T. Odenthal, K. Sliogeryte, P. Van Liedekerke, and H. Ramon. „Differential Adhesion and Socio-Evolution in Yeast". In: *European Cell Mechanics Meeting*. P37. Amsterdam, Netherlands, 17-19 October 2011.

[22] B. Smeets, T. Odenthal, E. Tijskens, H. Ramon, and H. Van Oosterwyck. „Individual-based modelling of the mechanical microenvironment". In: *International Conference on Computational Bioengineering*. Leuven, Belgium, Nov. 2013.

[23] B. Smeets, T. Odenthal, E. Tijskens, H. Ramon, and H. Van Oosterwyck. „The microenvironment for microbead cell expansion: mechanical characterization employing an individual-cell based model". In: *Congress of the European Society of Biomechanics*. Congress of the European Society of Biomechanics. Patras, Greece, 25-28 August 2013.

[24] B. Smeets, T. Odenthal, E. Tijskens, S. Roberts, W. Tam, P. Van Liedekerke, H. Van Oosterwyck, and H. Ramon. „Influence of mechanics on microcarrier cell expansion: a computational study." In: *Journal of Tissue Engineering and Regenerative Medicine: vol. 6. TERMIS World Congress.* Vienna, May 2012.

[25] B. Smeets, T. Odenthal, P. Van Liedekerke, E. Tijskens, H. Ramon, and H. Van Oosterwyck. „Individual-cell based model for characterizing the mechanical microenvironment in microcarrier cell expansion". In: *Computer Methods in Biomechanics and Biomedical Engineering*. Salt Lake City, UT, Mar. 2013.

[26] B. Smeets, T. Odenthal, P. Van Liedekerke, E. Tijskens, H. Van Oosterwyck, and H. Ramon. „Mechanical stress in microcarrier cell expansion investigated with a deformable cell model". In: *European Cell Mechanics Meeting*. Obergurgl, Austria, 28 September - 2 October 2013.

[27] P. Van Liedekerke, T. Odenthal, B. Smeets, E. Tijskens, and H. Ramon. „Solving microscopic flow problems using stokes equations in sph". In: *International Conference on Computational Bioengineering*. Leuven, Nov. 2013.

[28] H. Van Oosterwyck, T. Odenthal, B. Smeets, T. Heck, and H. Ramon. „Particle-Based Models for Cell Mechanics and Mechanobiology." In: *7th World Congress of Biomechanics*. Boston, June 2014.

[29] H. Van Oosterwyck, T. Odenthal, B. Smeets, and H. Ramon. „Quantifying cell mechanical forces as determinants of stem cell fate". In: *Quantifying cell mechanical forces as determinants of stem cell fate. Virtual Physiological Human Conference*. Trondheim, Sept. 2014.

[30] S. Vanmaercke, B. Smeets, T. Odenthal, J. Keresztes, and H. Ramon. „Using Arbitrary Triangulated Shapes in DEM Simulations. Contact models and applications". In: *International Conference on Particle-based Methods*. Barcelona, 28-30 September 2015.